



Delft University of Technology

Forward-Looking Ultra-Wideband Synthetic Array Imaging

Wang, Jianping

DOI

[10.4233/uuid:a2dacf4c-c10f-4800-81ca-5cf7e55be736](https://doi.org/10.4233/uuid:a2dacf4c-c10f-4800-81ca-5cf7e55be736)

Publication date

2018

Document Version

Final published version

Citation (APA)

Wang, J. (2018). *Forward-Looking Ultra-Wideband Synthetic Array Imaging*. [Dissertation (TU Delft), Delft University of Technology]. <https://doi.org/10.4233/uuid:a2dacf4c-c10f-4800-81ca-5cf7e55be736>

Important note

To cite this publication, please use the final published version (if applicable).
Please check the document version above.

Copyright

Other than for strictly personal use, it is not permitted to download, forward or distribute the text or part of it, without the consent of the author(s) and/or copyright holder(s), unless the work is under an open content license such as Creative Commons.

Takedown policy

Please contact us and provide details if you believe this document breaches copyrights.
We will remove access to the work immediately and investigate your claim.

Forward-Looking Ultra-Wideband Synthetic Array Imaging

Jianping Wang

Forward-Looking Ultra-Wideband Synthetic Array Imaging

Dissertation

for the purpose of obtaining the degree of doctor
at Delft University of Technology
by the authority of the Rector Magnificus prof.dr.ir. T.H.J.J. van der Hagen
chair of the Board for Doctorates
to be defended publicly on
Thursday 5 April 2018 at 10:00 o'clock

by

Jianping WANG

Master of Science in Information & Communication Engineering,
Beijing Institute of Technology, China,
born in Lvliang, Shanxi, China.

This dissertation has been approved by the
promotor: Prof. DSc. A.G. Yarovoy

Composition of the doctoral committee:

Rector Magnificus, chairman
Prof. DSc. A.G. Yarovoy, Delft University of Technology

Independent members:

Prof. dr. W.A. Mulder,	Delft University of Technology
Prof. dr. ir. E.C. Slob,	Delft University of Technology
Prof. dr. ir. G.J.T. Leus,	Delft University of Technology
Prof. ir. P. Hoogeboom,	Delft University of Technology
Prof. dr. M. Sato,	Tohoku University, Japan
Prof. dr. C. Craeye,	Université catholique de Louvain, Belgium



This research was supported by the NeTTUN project funded by the European Commission through the FP-7 framework under Grant 280712.

ISBN 978-94-028-1007-3

Copyright © 2018 by Jianping Wang

All rights reserved. No part of the material protected by this copyright notice may be reproduced or utilized in any form or by any means, electronic or mechanical, including photocopying, recording or by any information storage and retrieval system, without the prior permission of the author.

An electronic version of this dissertation is available at
<http://repository.tudelft.nl/>.

To my family

Contents

1	Introduction	1
1.1	Overview of Synthetic Aperture Radar Techniques	3
1.2	Research Objectives	5
1.3	Novelties and Main Results	6
1.4	Outline of the Thesis	8
	References	10
2	Fundamentals of Microwave Imaging	13
2.1	Maxwell's Equations	13
2.2	Wave Equations	16
2.2.1	Vector Wave Equations	16
2.2.2	Scalar Wave Equations	17
2.3	Electromagnetic Scattering	18
2.4	Born Approximation Model.	20
2.5	Imaging Reconstruction Methods	21
2.5.1	Radar-based Approaches	21
2.5.2	Inversion-based Approaches	25
2.6	Conclusion	27
	References	27
3	Rotated Arrays for Fully Polarimetric Imaging	29
3.1	Introduction	29
3.2	Scattering Formulation	30
3.3	Wavefield Extrapolator for Rotated Antennas	32
3.4	Rotated Antenna Arrays Design	37
3.4.1	Array Topologies	37
3.4.2	Sampling Criteria	38
3.5	Numerical Simulation	39
3.5.1	Full-polarimetric Imaging with Rotated Arrays and Traditional Polarimetric Arrays	43
3.5.2	Polarimetric Imaging vs Scalar-wave-based Processing . . .	52

3.6	Experimental Results	55
3.7	Conclusion	62
	References	63
4	Linear Inversion of Polarization-Varied EM Data	65
4.1	Introduction	65
4.2	Signal Model.	67
4.3	Full-wave Green's Functions of Rotated Antennas.	70
4.3.1	Free-space Dyadic Green's Function.	70
4.3.2	Half-space Green's Functions	71
4.4	Simulations	76
4.4.1	Green's Function Computation.	76
4.4.2	Imaging with Rotated Antenna Array	78
4.5	Experiments	82
4.6	Conclusion	84
	References	87
5	Three-Dimensional Array Design and Optimization	89
5.1	Introduction	89
5.1.1	Prior Works and Existing Theories.	89
5.1.2	Our Contributions.	91
5.2	Signal Model.	92
5.2.1	Linear Inversion Problem.	92
5.2.2	Problem Statement	94
5.3	Clustered FrameSense.	96
5.3.1	Frame Potential	96
5.3.2	The Algorithm	96
5.4	Clustered Maximal Projection on Minimal Eigenspace	98
5.4.1	MPME.	98
5.4.2	CMPME Algorithm.	99
5.4.3	Efficient Implementation	100
5.5	Imaging Examples.	102
5.5.1	Planar Array Imaging.	102
5.5.2	Optimization of the E-RadSAR	111
5.6	Discussion of 3-D Imaging Array.	115
5.7	Conclusion	117
	References	117

6 Signal Fusion for Enhanced Imaging	121
6.1 Introduction	121
6.2 <i>k</i> -space Signals for Array Based Imaging	122
6.3 <i>k</i> -space Signal Fusion	127
6.3.1 Signal Incoherence Compensation	128
6.3.2 Subband Signal Fusion	132
6.3.3 More Remarks on the Implementation.	133
6.4 Numerical Simulations	136
6.4.1 Point Targets	136
6.4.2 Extended Object	138
6.5 Experimental Results	145
6.6 Conclusion	150
References	150
7 Conclusions	153
7.1 Results and Novelties of the Research	153
7.2 Recommendations	155
References	157
List of Acronyms	159
Summary	161
Samenvatting	163
Acknowledgements	167
List of Publications	169
About the Author	171

1

Introduction

In the past decades, microwave imaging has attracted the attention of numerous researchers from various fields due to its advantages over some existing imaging instruments. Microwave imaging systems typically emit electromagnetic (EM) waves by transmitting antennas to illuminate the imaging scene and then collect the reflected or scattered signals by receiving antennas. So compared to the optical imaging systems, they avoid the operating limitations such as night-time scenarios or non-illuminated areas. Moreover, due to the relatively long wavelength, microwave signals can penetrate the barriers or opaque media (e.g., smoke and fog) to sense the imaging scene. This feature has made microwave imaging popular for subsurface imaging, through-wall imaging, concealed weapon detection, remote sensing, etc. As a non-intrusive imaging tool, microwave imaging equipment has no health risk on the human body as long as a safe level of microwave radiation is used, which is different from computed tomography (CT) that exposes the human body to ionizing X-ray radiation. Many studies have also been performed with attempt to investigate the potential of microwave imaging in medical applications, for instance, breast cancer detection [1, 2].

With the expansion of microwave imaging application areas, images with increasingly higher resolution and higher quality are required, especially for short-range imaging. In order to meet these requirements, many microwave imaging systems have been developed by fully exploiting the Ultra-wideband (UWB), array and polarimetry techniques. As the down-range resolution is inversely proportional to the operational frequency bandwidth, a wideband or even UWB signal with fractional bandwidth larger than 20% [3] is generally used to increase the re-

solving capability of the imaging system in the down-range direction. To improve the cross-range resolution, the typical approaches are to exploit array techniques: phased arrays, synthetic aperture radar (SAR) and Multiple-Input-Multiple-Output (MIMO) arrays [4]. The phased array uses a great number of antennas to construct a large array aperture, thus forming a narrow beamwidth in the cross-range direction(s). Although it provides the capability for real-time imaging, a phased array is usually very expensive, which is not attractive or even not affordable for civilian applications. By contrast, both synthetic aperture and MIMO array techniques enable to significantly reduce the number of antennas needed to build a large aperture and provide an affordable/cheap solution to the array system. Synthetic aperture techniques translate a single antenna/small array in space to synthesize a large aperture while MIMO array techniques exploit the spatial diversity of the transmitting and receiving antennas' locations to generate a large virtual array. However, to synthesize a virtual large aperture array with N antenna elements, MIMO arrays still require at least $2\sqrt{N}$ antennas, while synthetic aperture techniques provide the potential to further reduce the number of antennas needed, in the extreme case, down to one. Therefore, in scenarios with tight cost and/or space constraints, the synthetic aperture (or combined with MIMO array) technique is probably the most desirable option to build large virtual arrays. Moreover, accounting for the vector nature of EM waves, differently polarized signals scattered from targets can be

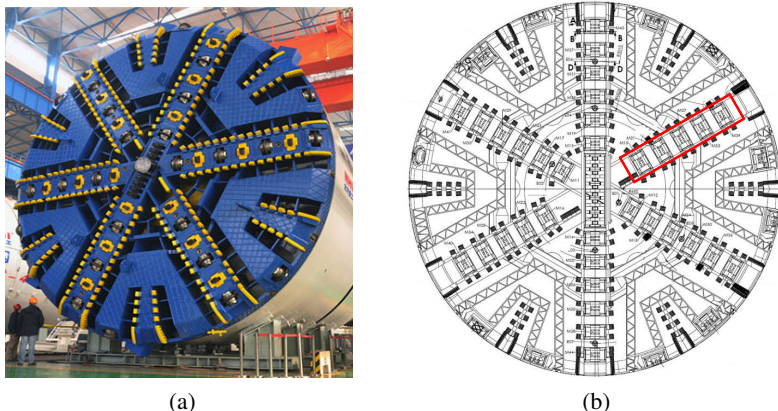


Figure 1.1: (a) Cutter-head of a tunnel boring machine, (b) the frontal view of the cutter head of a six-arm tunnel boring machine, where the red rectangle indicates the possible slots for ground penetrating radar (GPR) antennas.

acquired. Taking advantage of the imaging and polarimetry technique, different polarimetric images are reconstructed; those contain rich scattering information about the targets and significantly benefit the target detection, classification as well as recognition [5].

The motivation of this research is to develop a forward-looking Ground Penetrating Radar (GPR) system to predict ground properties ahead of a tunnel boring machine (TBM) which is a very powerful and important piece of equipment for tunnel excavation (as illustrated in Figure 1.1(a) [6]). In this scenario, the GPR antennas are embedded in a few slots on the cutter-head of a TBM, for instance, as illustrated in Figure 1.1(b) for a six-arm TBM [7]. In order to minimize or avoid the influence of the slots made for the GPR antennas on the robustness of the mechanical structures of the cutter-head of a TBM, the number of antennas should be as small as possible. Thus, the synthetic aperture technique seems to be the most attractive solution in this circumstance.

1.1 Overview of Synthetic Aperture Radar Techniques

Synthetic aperture radar techniques have been widely used for both remote sensing (in the far field of the sensor) and short-range imaging applications. In remote sensing applications, the radar system is typically mounted on a moving platform, for instance, an airplane or a satellite, and the EM signals are collected with its translation along a (quasi-) linear trajectory. Thus, a large aperture is synthesized, which leads to high resolution in the cross-range direction. By steering the antenna beam during the data acquisition with respect to the illuminated area, different operational modes have been designed, including Stripmap, ScanSAR, Spotlight, Sliding spotlight, and so on [8]. These operational modes of SAR systems generally achieve a relatively vast area survey. To observe a small region of interest from full 360° aspects, Circular SAR (CSAR) [9] has been proposed by moving the radar system over a circular trajectory above the illuminated area. Furthermore, CSAR is extended by utilizing the synthetic aperture technique in the elevation (i.e., down-range) direction as well in order to improve the height (down-range) resolution, which is referred as Elevation CSAR (E-CSAR) [10].

Besides the aforementioned SAR modalities, some other SAR configurations are also introduced in the short-range imaging applications, in particular for 3-D imaging. According to their implementation, these synthetic aperture techniques can be mainly divided into three categories [11]: (1) rectilinear scanning system, (2) cylindrical scanning system, and (3) Radial-scanning SAR (Rad-SAR) system.

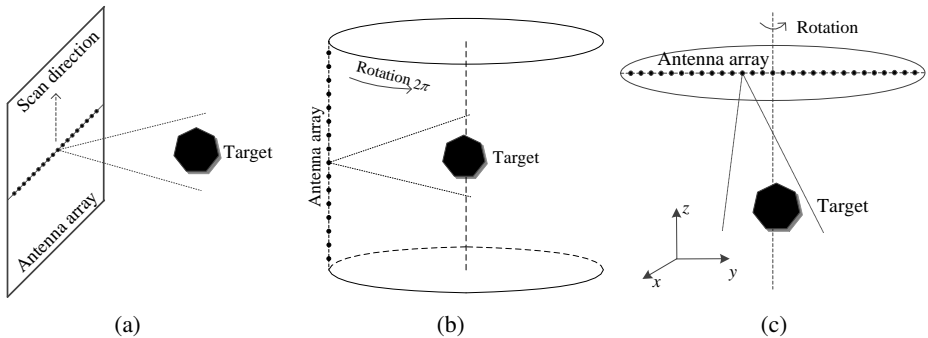


Figure 1.2: Geometrical configurations of near-field 3-D SAR imaging systems. (a) Rectilinear scanning system, (b) Cylindrical scanning system, and (c) Rad-SAR system.

Their imaging geometries are shown in Figure 1.2. In the rectilinear scanning system, a linear array is moved along its perpendicular direction for signal acquisition, thus synthesizing a 2-D planar array. This configuration has been widely used for subsurface survey with array-based GPR system, through-wall imaging, etc. Meanwhile, the cylindrical scanning system rotates a linear array around an axis to illuminate targets, and a cylindrical array is formed around the targets. So it is suitable to the circumstance where targets are located within a certain volume and accessible from all 360° aspects around them. In practice, one of its application examples is the human body scanner used for security check in airports or other public checkpoints. By contrast, in the Rad-SAR system, a linear array is rotated around a point in the array to form a planar circular array. It is easy to implement and provides great potential for forward-looking short-range imaging applications. Some other scanning/synthetic aperture geometries, for example the spherical scanning configuration, are also proposed, and some of them are already used for near-field antenna measurement. However, these have been scarcely employed for building imaging systems for practical applications so far.

Considering the GPR system used for a TBM, a large aperture array is synthesized with the rotation of its cutter-head where GPR antennas are installed. So it naturally forms a RadSAR-type configuration in this circumstance. Although the RadSAR-type configuration has already been investigated for near-field imaging [11] and subsurface sensing [12], the EM waves were tackled as the scalar waves in these studies. That is to say, the impact of the rotation of antenna orientations on the acquired signals was neglected. So considering the vector nature of EM waves, the possibility of the RadSAR for polarimetric imaging is still not clear. Moreover,

UWB signals can be used to get high-resolution in the down-range direction and also provides the potential for sparse spatial sensing without causing aliasing. In the open literature, the combination of UWB and the RadSAR techniques is not yet discussed. Therefore, further research has to be carried out to fully explore the capability of the RadSAR for high-resolution short-range imaging and to develop proper imaging algorithms for high-quality image reconstruction.

1.2 Research Objectives

The research objective of this thesis is to develop a high-resolution, high-quality Rad-SAR imaging system by fully exploiting the synthetic aperture radar, UWB and polarimetry techniques. The primary focus of the work lies in the investigation of the capabilities of the UWB Rad-SAR and the development of an advanced imaging algorithm. Considering the aforementioned motivation and the particular features of the Rad-SAR, some related research questions should be addressed to achieve the main research objective.

The Rad-SAR system implements the synthetic array by rotating a linear array/antennas around a point over the aperture. For linearly polarized antennas which are typically used in subsurface imaging systems, the rotation constantly changes the antenna polarizations with respect to targets, thus acquiring scattered EM signals with varying polarizations. However, the imaging algorithms developed for seismic/acoustic waves based on the scalar wave assumption are generally used for image reconstruction. To be utilized for the EM field, the antenna polarizations within the imaging array are typically assumed to be coherent, i.e., aligned. Otherwise, the utilization of the traditional imaging algorithms would decrease the image quality. Moreover, traditional polarimetric-imaging techniques also assume that the differently polarized signals/images are acquired separately at first, and the polarimetry techniques are applied for polarimetric information processing. Therefore, the fact that antenna polarizations of the Rad-SAR are constantly varying during the signal acquisition naturally leads to the following research questions.

Q1: How can we tackle the effects of the variations of antenna polarizations over the aperture of the Rad-SAR on the imaging performance?

Q2: Can we take advantage of the Rad-SAR for fully polarimetric imaging?

Considering the highly tight constraint on the space for the antenna installation in the TBM application, it is expected that the number of antennas used can be as

small as possible. The antennas are installed on the cutter-head of a TBM. With the rotation of the cutter head, a Rad-SAR is implemented. As during the operation the cutter head does not only rotate but also advances with the progress of the excavation, a synthetic aperture in the down-range direction can also be synthesized. Moreover, according to the UWB theory, using an UWB signal could also lead to sparse arrays, thus reducing the number of antennas needed. Then the following questions arise.

Q3: Can we reduce the imaging system complexity, i.e., the number of antennas needed, by exploiting the Rad-SAR with its down-range movement? If yes, how would the spatial samples be properly taken for high-resolution, high-quality imaging?

Q4: How should the spatial samples of the Rad-SAR be taken when UWB signals are used by the imaging system?

Finally, to utilize UWB techniques, RF front-ends that work in the UWB spectrum are required. However, in practice it is quite often that the UWB antennas are not available due to the technological difficulties in antenna design, especially for subsurface imaging, like in the TBM application. Then an alternative solution is to divide the UWB spectrum into several relatively narrow band segments, and narrowband antennas are used to work at each segment so as to cover the whole UWB spectrum. So to get an equivalent UWB signal for high-resolution imaging, the narrowband data should be processed by addressing the following question:

Q5: How could we properly and coherently fuse the multiband data/images to achieve an equivalent UWB imaging?

The above questions cover the main aspects of Rad-SAR imaging, and some of them are of general interest in UWB microwave imaging and go beyond the Rad-SAR as well as beyond the GPR imaging system in the TBM application.

1.3 Novelties and Main Results

By addressing the aforementioned research questions, some novelties and results have been obtained and are presented in the thesis as follows:

- Two novel approaches to design rotating antenna arrays for fully polarimetric imaging have been proposed. The proposed approaches overcome the effects

of the variations of antenna polarizations of the Rad-SAR on the imaging performance via designing specific rotating antenna arrays. The designed rotating arrays allow retrieving the fully polarimetric signals from their measurements acquired by antennas with spatially varying polarizations. It benefits the traditional scalar-wave based imaging algorithms to be applied for image reconstruction without degrading the image quality. Moreover, the proposed approaches also provide a cost-efficient solution to fully polarimetric imaging with a Rad-SAR system, which is a novel array-based imaging.

- A linear inversion based approach is applied to address the effects of the variations of antenna polarizations of the Rad-SAR from the aspect of imaging. The proposed approach considers the full-wave (including near-, intermediate- and far-field) contributions to the radiation characteristic of antennas. To accelerate the linear inversion approach, two computationally efficient methods, i.e., an interpolation based method and a Nonuniform fast Fourier transform (NUFFT) based method, are suggested to compute the accurate Green's functions for the observation matrix construction. The proposed linear inversion approach significantly improves the image quality compared to those traditional scalar-wave based imaging algorithms.
- A new multi-dimensional sampling model by accounting for the integral impact of spatial- (i.e., array technique), frequency- (i.e., UWB technique) and polarization diversity on image focusing is established based on an abstract matrix formulation. Based on this model, the trade-offs among the spatial-, frequency and polarization sampling can be to some extent made for imaging system design. It not only extends the traditional narrow/wide array theory but also lays the theoretical foundations for designing 3-D sampling schemes/arrays, frequency-modulated arrays, etc.
- The Clustered FrameSense (CFS) algorithm has been developed to implement the multidimensional sampling design. This algorithm sequentially optimizes the sample selection by evaluating the “orthogonality” of a group of samples associated with a sampling position with respect to the selected ones through the inner product. It is computationally efficient and an appealing algorithm for huge sample selection problems, for instance, sampling design for imaging systems.
- The Clustered Maximum Projection onto Minimum Eigenspace (CMPME) algorithm has also been developed for sampling design for linear inversion

problems. It evaluates both the “orthogonality” and the contribution of the new samples with respect to the selected ones. As CMPME is a forward selection algorithm, it is very efficient when the number of selected samples is much smaller than that of the candidate ones.

- A novel fusion approach is developed to coherently process the multiband data in the wavenumber domain to achieve an equivalent UWB high-resolution imaging. It not only integrates the data from different frequency subbands but also extrapolates the missing data between them. As the fusion operation is performed in the wavenumber domain, the proposed approach can be applied to fuse multiband data acquired with both collocated and non-collocated arrays in different frequency bands.

The research presented in this thesis has been performed within the NeTTUN project which is funded by the European Commission within FP-7 Programme under Grant 280712. Part of the project is to develop an advanced ground prediction system used for TBM. Within the frame of the project, we are responsible for the development of a high-resolution ground penetrating radar system and related signal processing approaches. The antenna array topologies and algorithms developed have been discussed within the NeTTUN consortium.

1.4 Outline of the Thesis

The remaining of the thesis is organized in three parts by covering the exploration of polarization, spatial and frequency diversities associated with array-based forward-looking UWB imaging. In the first part, the effects of the variations of the antenna orientations caused by the rotation of the array during the signal acquisition on the image reconstruction will be discussed, which will be tackled from both system design (i.e., array design) and image formation aspects. In the second part, the potential of exploiting three-dimensional spatial sampling to reduce the number of antennas needed for 3-D imaging will be investigated through a sampling selection strategy. In the third part, multiband signal fusion to achieve an equivalent UWB imaging will be studied and a wavenumber domain fusion approach will be presented. The content of the chapters to follow are briefly described as follows:

Chapter 2 presents some mathematical fundamentals related to microwave imaging. The propagation of EM waves and their interactions with media are governed by the Maxwell's equations. Considering the assumption of the

sources used for microwave imaging, in this chapter we divide the traditional microwave imaging algorithms into two categories: scalar-wave based approaches and vector-wave based approaches. Scalar-wave based approaches assume that the electromagnetic sources radiate isotropically like an acoustic source and all the EM sources radiate equally for array-based imaging systems by assuming they are polarization coherent. On the other hand, the vector-wave based approaches consider the full vectorial nature of the EM waves and different polarized components of the scattered EM waves are included in the image formation. In this chapter, some typical imaging algorithms in these two categories are presented and their differences are analyzed as well. Through a mathematical discussion of these imaging approaches, it lays the foundations for properly selecting/developing the imaging algorithms in Chapters 3-5 and also indicates some implications for the imaging system design.

Chapter 3 tackles the effects of the variations of the antenna polarizations of the rotating antenna array in the image formation and proposes two approaches to design rotating arrays to overcome these effects. In this chapter, the effects of the rotation of the antenna orientation on the acquired EM signals are investigated through the scattering process formulation. Some relationship equations between the fully polarized signals in two sets of different polarization bases are derived. Based on the derived relationship equations, two approaches are proposed for rotating array design for fully polarimetric imaging. Two design examples for the rotating arrays are given to demonstrate the effectiveness and accuracy of the proposed approaches by comparing with the traditional fully polarimetric imaging arrays. Finally, the performance of the previously designed rotating arrays for fully polarimetric imaging is verified through experimental measurements.

Chapter 4 focuses on the same problem as in Chapter 3 but addresses it through *image formation processing* instead by considering the vectorial nature of the EM waves. In this chapter, a linear inversion approach based on the “exact” radiation patterns is applied to reconstruct images from the EM data acquired using antennas with spatially varying orientations within the aperture. To accelerate the proposed algorithm, two approaches, i.e., an interpolation based approach and a Nonuniform fast Fourier transform (NUFFT) based approach, are proposed to efficiently compute the accurate Green’s functions (GF) of rotated antennas, thus obtaining full-wave radiation patterns. The efficiency and

accuracy of the two approaches for GF computation are examined via a numerical example. Imaging experiments are also carried out to demonstrate the performance of the proposed linear inversion algorithm.

Chapter 5 extends the two-dimensional (2-D) circular synthetic array to a three-dimensional (3-D) one by combining both the cross-range rotation and the forward motion of a linear array. The aim of this chapter is to investigate the 3-D spatial sampling of the synthetic array so as to examine the possibility to reduce the number of antennas needed in the linear array. Following Chapter 4, the imaging problem is formulated as an estimation problem, and the 3-D spatial sampling design of the UWB synthetic array is converted to be an observation selection problem by discretizing the signal acquisition aperture. Two greedy algorithms are developed to sequentially select the discrete sensing vectors associated with each spatial sampling position over the operational bandwidth. Their performance to select (near) optimal observations are demonstrated and compared with other existing algorithms. Finally, an imaging example to illustrate the performance of the selected 3-D array is given.

Chapter 6 is dedicated to multiband signal fusion to achieve an equivalent UWB imaging result when either a dedicated UWB front-end or continuous UWB spectrum is unavailable. A wavenumber domain (i.e., k -space) fusion algorithm based on the Matrix-Pencil Approach (MPA) is presented. Compared to the traditional time(frequency)-space domain fusion approaches, the proposed fusion approach is applicable to the multiband signals acquired with both collocated and non-collocated antennas in different frequency subbands.

Chapter 7 summarizes the main achievements presented in this dissertation and also provides some recommendations for further research.

References

- [1] D. Byrne, M. Sarafianou, and I. J. Craddock, “Compound radar approach for breast imaging,” *IEEE Transactions on Biomedical Engineering*, vol. 64, pp. 40–51, Jan 2017.
- [2] M. J. Burfeindt, J. D. Shea, B. D. V. Veen, and S. C. Hagness, “Beamforming-enhanced inverse scattering for microwave breast imaging,” *IEEE Transactions on Antennas and Propagation*, vol. 62, pp. 5126–5132, Oct 2014.

- [3] J. Taylor, *Introduction to Ultra-Wideband Radar Systems*. Taylor & Francis, 1994.
- [4] X. Zhuge, *Short Range Ultra-Wideband Imaging with Multiple-Input Multiple-Output Arrays*. PhD dissertation, Delft University of Technology, 2010.
- [5] J.-S. Lee and E. Pottier, *Polarimetric radar imaging: from basics to applications*. CRC press, 2009.
- [6] “Dual mode TBM.” <http://nhi-sy.com/75/DualModeTBM.html>.
- [7] J. P. De Sloovere and A. Taboulet, “End user requirements for the NeTTUN ground prediction radar system,” NeTTUN deliverable D3.1, Dec 2012.
- [8] A. Moreira, P. Prats-Iraola, M. Younis, G. Krieger, I. Hajnsek, and K. P. Papathanassiou, “A tutorial on synthetic aperture radar,” *Geoscience and Remote Sensing Magazine, IEEE*, vol. 1, no. 1, pp. 6–43, 2013.
- [9] M. Soumekh, *Synthetic Aperture Radar Signal Processing with MATLAB Algorithms*. Wiley, 1999.
- [10] M. L. Bryant, L. L. Gostin, and M. Soumekh, “3-D E-CSAR imaging of a T-72 tank and synthesis of its SAR reconstructions,” *Aerospace and Electronic Systems, IEEE Transactions on*, vol. 39, no. 1, pp. 211–227, 2003.
- [11] Z. Li, J. Wang, J. Wu, and Q. H. Liu, “A fast radial scanned near-field 3-d sar imaging system and the reconstruction method,” *Geoscience and Remote Sensing, IEEE Transactions on*, vol. 53, no. 3, pp. 1355–1363, 2015.
- [12] S. Zhu, W. Jian, L. Yu, S. Yi, and M. Sato, “A circular measurement for linearly polarized ground penetrating radar to map subsurface crossing cylinders,” in *Geoscience and Remote Sensing Symposium (IGARSS), 2013 IEEE International*, pp. 1426–1429.

2

Fundamentals of Microwave Imaging

In this chapter, some mathematical fundamentals of microwave imaging are briefly presented, which include the signal model, scattering approximations and image reconstruction approaches that are used in the following chapters.

2.1 Maxwell's Equations

Maxwell's equations govern the electromagnetic (EM) field by a set of experimental laws, which connects the EM field vectors to the sources [1, 2]. In the differential form, Maxwell's equations are given by

$$\nabla \times \mathbf{E}(\mathbf{r}, t) = -\frac{\partial \mathbf{B}(\mathbf{r}, t)}{\partial t} \quad (2.1)$$

$$\nabla \times \mathbf{H}(\mathbf{r}, t) = \frac{\partial \mathbf{D}(\mathbf{r}, t)}{\partial t} + \mathbf{J}(\mathbf{r}, t) \quad (2.2)$$

$$\nabla \cdot \mathbf{D}(\mathbf{r}, t) = \rho(\mathbf{r}, t) \quad (2.3)$$

$$\nabla \cdot \mathbf{B}(\mathbf{r}, t) = 0 \quad (2.4)$$

Here the notations are listed as follows.

\mathbf{r} — the position vector [in meters (m)];

t — the time [in seconds (s)];

$\mathbf{E}(\mathbf{r}, t)$ — Electric field [in volts per meter (V/m)];

- $\mathbf{H}(\mathbf{r}, t)$ — Magnetic field [in amperes per meter (A/m)];
 $\mathbf{D}(\mathbf{r}, t)$ — Electric field flux [in coulombs per square meter (C/m^2)];
 $\mathbf{B}(\mathbf{r}, t)$ — Magnetic field flux [in webers per square meter, or Tesla (Wb/m^2 , or T)];
 $\mathbf{J}(\mathbf{r}, t)$ — Electric current density [in amperes per square meter (A/m^2)];
 $\rho(\mathbf{r}, t)$ — volume electric charge density [in coulombs per cubic meter (C/m^3)].
 $\nabla \times, \nabla \cdot$ — curl and divergence operators, respectively.

Equations (2.1)-(2.4) give the relationships between the field vectors \mathbf{E} , \mathbf{H} , \mathbf{D} and \mathbf{B} with their sources \mathbf{J} and ρ . They can be simplified if we assume the vector fields are time-harmonic. A time-harmonic field can be represented by

$$\mathbf{F}(\mathbf{r}, t) = \text{Re} [\mathbf{F}(\mathbf{r}) e^{j\omega t}] \quad (2.5)$$

where $j = \sqrt{-1}$ is the complex unit, ω is the angular frequency, and $\mathbf{F}(\mathbf{r})$ is a complex vector. $\text{Re}[\cdot]$ takes the real part of an argument. Using the time-harmonic form in (2.5) for the vector fields and taking the Fourier transform of (2.1)-(2.4) with respect to time, the time-harmonic form of Maxwell's equations is obtained

$$\nabla \times \mathbf{E}(\mathbf{r}) = -j\omega \mathbf{B}(\mathbf{r}) \quad (2.6)$$

$$\nabla \times \mathbf{H}(\mathbf{r}) = j\omega \mathbf{D}(\mathbf{r}) + \mathbf{J}(\mathbf{r}) \quad (2.7)$$

$$\nabla \cdot \mathbf{D}(\mathbf{r}) = \rho(\mathbf{r}) \quad (2.8)$$

$$\nabla \cdot \mathbf{B}(\mathbf{r}) = 0 \quad (2.9)$$

Maxwell's equations can also be represented in their integral form. By integrating (2.6)-(2.7) over a regular open surface S and using Stokes' theorem, one can derive

$$\oint_C \mathbf{E}(\mathbf{r}) d\mathbf{l} = -j\omega \int_S \mathbf{B}(\mathbf{r}) \cdot \hat{\mathbf{n}} ds \quad (2.10)$$

$$\oint_C \mathbf{H}(\mathbf{r}) d\mathbf{l} = j\omega \int_S \mathbf{D}(\mathbf{r}) \cdot \hat{\mathbf{n}} ds + \int_S \mathbf{J}(\mathbf{r}) \cdot \hat{\mathbf{n}} ds \quad (2.11)$$

where C is the contour line of the surface S , $\hat{\mathbf{n}}$ is its normal at \mathbf{r} and ds denotes the related differential area. Similarly, integrating (2.8) and (2.9) over a volume bounded by surface S_c and applying Gauss' theorem, one obtains

$$\oint_{S_c} \mathbf{D}(\mathbf{r}) \cdot \hat{\mathbf{n}} dr = \int_V \rho(\mathbf{r}) dr = Q \quad (2.12)$$

$$\oint_{S_c} \mathbf{B}(\mathbf{r}) \cdot \hat{\mathbf{n}} dr = 0 \quad (2.13)$$

where Q is the total charge in volume V . Equations (2.10) to (2.13) form the integral representation of Maxwell's equations, which give the relations among field vectors and sources within a given region.

Moreover, to consider the effect of media on the EM field, Maxwell's equations should be supplemented by the constitutive relations which characterize the EM properties of the media via three parameters: permittivity ϵ , permeability μ , and conductivity σ . In general, these three parameters can be a tensor/scalar, and also a function of frequency. Accounting for the research background, media that are linear, locally and instantaneously acting, isotropic and inhomogeneous are considered in this thesis. Then the three EM parameters of the media can be represented by scalar functions. The constitutive relations are expressed as

$$\mathbf{D}(\mathbf{r}) = \epsilon(\mathbf{r})\mathbf{E}(\mathbf{r}) \quad (2.14)$$

$$\mathbf{B}(\mathbf{r}) = \mu(\mathbf{r})\mathbf{H}(\mathbf{r}) \quad (2.15)$$

$$\mathbf{J}(\mathbf{r}) = \sigma(\mathbf{r})\mathbf{E}(\mathbf{r}) \quad (2.16)$$

For homogeneous media, the permittivity, permeability and conductivity functions are spatially shift-invariant. For example, the EM properties of vacuum are described by $\epsilon = \epsilon_0 \approx 8.85 \times 10^{-12} \text{F/m}$, $\mu = \mu_0 = 4\pi \times 10^{-7} \text{H/m}$, and $\sigma = 0$.

In addition, in a linear, isotropic and conducting medium, (2.7) is also generally expressed as

$$\nabla \times \mathbf{H} = j\omega\epsilon(\mathbf{r})\mathbf{E}(\mathbf{r}) + \sigma(\mathbf{r})\mathbf{E}(\mathbf{r}) + \mathbf{J}_0(\mathbf{r}) = j\omega\epsilon_0 \left(\epsilon_r(\mathbf{r}) - j\frac{\sigma(\mathbf{r})}{\omega\epsilon_0} \right) \mathbf{E}(\mathbf{r}) + \mathbf{J}_0(\mathbf{r}) \quad (2.17)$$

where $\epsilon_r(\mathbf{r}) = \epsilon(\mathbf{r})/\epsilon_0$ is defined as the relative permittivity of the medium, and $\mathbf{J}_0(\mathbf{r})$ denotes the impressed current. In the derivation of (2.17), equations (2.14)-(2.16) have been used. If we introduce the effective dielectric permittivity as

$$\epsilon_e(\mathbf{r}) = \epsilon_0 \left(\epsilon_r(\mathbf{r}) - j\frac{\sigma(\mathbf{r})}{\omega\epsilon_0} \right) = \epsilon'(\mathbf{r}) - j\epsilon''(\mathbf{r}) = \epsilon_0 (\epsilon'_r(\mathbf{r}) - j\epsilon''_r(\mathbf{r})) \quad (2.18)$$

then equation (2.17) can be written as

$$\nabla \times \mathbf{H} = j\omega\epsilon_e(\mathbf{r})\mathbf{E}(\mathbf{r}) + \mathbf{J}_0(\mathbf{r}) \quad (2.19)$$

In (2.19), only the impressed current \mathbf{J}_0 explicitly appears in the right-hand side. So by defining the complex-valued permittivity, the conducting media can be treated in the same way as the dielectric media. Consequently, (2.16) is not explicitly listed in the constitutive relations in some literature. For simplification of notation, we omit the subscript of ϵ_e to denote the effective permittivity in the following text.

2.2 Wave Equations

2.2.1 Vector Wave Equations

Considering a homogeneous medium, the dielectric permittivity and permeability are characterized as ϵ and μ . Taking the curl of (2.6) and substituting it for $\nabla \times \mathbf{H}$ in (2.7), the *vector wave equation* for the electric field can be obtained

$$\nabla \times \nabla \times \mathbf{E}(\mathbf{r}) - k^2 \mathbf{E}(\mathbf{r}) = -j\omega\mu\mathbf{J}_0(\mathbf{r}) \quad (2.20)$$

where $k = \omega\sqrt{\mu\epsilon}$ denotes the wavenumber of the medium where EM waves propagate.

In order to get a unique solution to the above vector wave equation, some boundary conditions and the radiation conditions satisfied by the electric and magnetic fields are required, which are provided by the uniqueness theorem. For instance, in the lossy region of interest V bounded by a closed surface S , the conditions imposed on the tangential component $\hat{\mathbf{n}} \times \mathbf{E}(\mathbf{r})$ [or $\hat{\mathbf{n}} \times \mathbf{H}(\mathbf{r})$] are sufficient to determine the EM field inside V . In addition, unique solutions for the EM field can also be obtained by assigning mixture boundary conditions of the tangential components on S , i.e., $\hat{\mathbf{n}} \times \mathbf{E}(\mathbf{r})$ on one part and $\hat{\mathbf{n}} \times \mathbf{H}(\mathbf{r})$ on the other part of S .

For an unbounded medium, the radiation conditions should be assigned to guarantee the uniqueness of the solution to (2.20), which can be written as

$$\hat{\mathbf{r}} \times \mathbf{E}(\mathbf{r}) = \eta \mathbf{H}(\mathbf{r}) + o\left(\frac{1}{r}\right) \quad (2.21)$$

$$\mathbf{H}(\mathbf{r}) \times \hat{\mathbf{r}} = \frac{1}{\eta} \mathbf{E}(\mathbf{r}) + o\left(\frac{1}{r}\right) \quad (2.22)$$

where $\hat{\mathbf{r}} = \mathbf{r}/r$ is the unit vector and $\eta = \sqrt{\mu/\epsilon}$ is the intrinsic impedance of the medium. Then taking advantage of the wave equation (2.20) and the radiation conditions (2.21) and (2.22), the EM field in an unbounded medium (e.g., free space) generated by the impressed current \mathbf{J}_0 can be determined as

$$\mathbf{E}(\mathbf{r}) = j\omega\mu \int_V \mathbf{J}_0(\mathbf{r}') \bar{\mathbf{G}}(\mathbf{r}, \mathbf{r}') d\mathbf{r}' \quad (2.23)$$

where $\bar{\mathbf{G}}(\mathbf{r}, \mathbf{r}')$ is the free-space dyadic Green's tensor given by [3]

$$\bar{\mathbf{G}}(\mathbf{r}, \mathbf{r}') = \left[\bar{\mathbf{I}} + \frac{1}{k^2} \nabla \nabla \right] G(\mathbf{r} - \mathbf{r}') = -\frac{1}{4\pi} \left[\bar{\mathbf{I}} + \frac{1}{k^2} \nabla \nabla \right] \frac{e^{-jk|\mathbf{r}-\mathbf{r}'|}}{|\mathbf{r} - \mathbf{r}'|}. \quad (2.24)$$

In (2.24), $\bar{\mathbf{I}}$ is the 3×3 identity dyadic and the scalar Green's function

$$G(\mathbf{r} - \mathbf{r}') = -\frac{e^{-jk|\mathbf{r}-\mathbf{r}'|}}{4\pi|\mathbf{r}-\mathbf{r}'|} \quad (2.25)$$

is the solution to the inhomogeneous *scalar wave equation*

$$[\nabla^2 + k^2] G(\mathbf{r} - \mathbf{r}') = \delta(\mathbf{r} - \mathbf{r}'). \quad (2.26)$$

The dyadic Green's tensor $\bar{\mathbf{G}}(\mathbf{r}, \mathbf{r}')$ corresponds to the EM fields generated by the elementary source and is the solution to the following equation

$$\nabla \times \nabla \times \bar{\mathbf{G}}(\mathbf{r}, \mathbf{r}') - k^2 \bar{\mathbf{G}}(\mathbf{r}, \mathbf{r}') = \bar{\mathbf{I}} \delta(\mathbf{r} - \mathbf{r}'). \quad (2.27)$$

It should be noted that (2.24) is obtained by using the vector field identities $\nabla \times \nabla \times \bar{\mathbf{G}} = \nabla \nabla \cdot \bar{\mathbf{G}} - \nabla^2 \bar{\mathbf{G}}$ and $\nabla \cdot \bar{\mathbf{G}} = \rho/\epsilon = (\nabla \cdot \bar{\mathbf{I}})/(-j\omega\epsilon)$. Moreover, (2.23) gives the electric field radiated by a bounded source. Without loss of generality, its form for the electric field still holds in other situations, for instance, half-space scenario, as long as a proper dyadic Green's tensor is used.

2.2.2 Scalar Wave Equations

In a homogeneous, isotropic and *source-free* medium, the vector wave equation in (2.20) can be modified as

$$\nabla \times \nabla \times \mathbf{E}(\mathbf{r}) - k^2 \mathbf{E}(\mathbf{r}) = 0 \quad (2.28)$$

Taking advantage of the vector field identities $\nabla \times \nabla \times \mathbf{E}(\mathbf{r}) = \nabla \nabla \cdot \mathbf{E}(\mathbf{r}) - \nabla^2 \mathbf{E}(\mathbf{r})$ and $\nabla \cdot \mathbf{E}(\mathbf{r}) = 0$, (2.28) can be rewritten as

$$\nabla^2 \mathbf{E}(\mathbf{r}) + k^2 \mathbf{E}(\mathbf{r}) = 0. \quad (2.29)$$

In Cartesian coordinates, the electric field $\mathbf{E}(\mathbf{r}) = \hat{x}E_x + \hat{y}E_y + \hat{z}E_z$, where \hat{x} , \hat{y} and \hat{z} are the unit vector for the three components. Therefore, (2.29) consists of three homogeneous scalar wave equations

$$(\nabla^2 + k^2) \psi(\mathbf{r}) = 0 \quad (2.30)$$

where $\psi(\mathbf{r})$ can be any one of the components E_x , E_y or E_z . However, the solution of (2.29) is only admissible to (2.30) when it is solved with the condition $\nabla \cdot \mathbf{E}(\mathbf{r}) = 0$. So only two of the three equations in (2.28) are independent [2]. Nevertheless, the equation (2.30) derived from electromagnetics lays the foundation for microwave image reconstruction with scalar-wave imaging algorithms, which will be introduced later in this chapter.

2.3 Electromagnetic Scattering

Let us consider the scattering problem of a bounded contrast domain occupied by scatterers embedded in an unbounded homogeneous medium. Assume the contrast domain is V^s and the dielectric permittivity and permeability of the scatterers are $\hat{\epsilon}^s(\mathbf{r})$ and $\hat{\mu}^s(\mathbf{r})$, respectively. For the unbounded homogeneous medium, it is characterized by the permittivity $\hat{\epsilon}(\mathbf{r})$ and the permeability $\hat{\mu}(\mathbf{r})$. With the presence of the contrast domain, the EM fields radiated by the sources, which are indicated as the incident fields $\{\hat{\mathbf{E}}^i(\mathbf{r}), \hat{\mathbf{H}}^i(\mathbf{r})\}$, are perturbed and the resulting EM fields (i.e., perturbed fields) are denoted by $\{\hat{\mathbf{E}}(\mathbf{r}), \hat{\mathbf{H}}(\mathbf{r})\}$. Obviously, the differences between the perturbed fields and the incident fields lead to the scattered fields $\{\hat{\mathbf{E}}^s(\mathbf{r}), \hat{\mathbf{H}}^s(\mathbf{r})\}$ which are ascribed to the presence of the contrast domain, i.e., to the interaction between the contrast scatterers and the incident fields. Therefore, their relations can be written as

$$\hat{\mathbf{E}}(\mathbf{r}) = \hat{\mathbf{E}}^i(\mathbf{r}) + \hat{\mathbf{E}}^s(\mathbf{r}) \quad (2.31)$$

$$\hat{\mathbf{H}}(\mathbf{r}) = \hat{\mathbf{H}}^i(\mathbf{r}) + \hat{\mathbf{H}}^s(\mathbf{r}) \quad (2.32)$$

As both the perturbed fields and the incident fields satisfy Maxwell's equations, so we can get, according to (2.10) and (2.11), the following equations

$$\oint_C \hat{\mathbf{E}}(\mathbf{r}) d\mathbf{l} = -j\omega \int_S \hat{\mu}^s(\mathbf{r}) \hat{\mathbf{H}}(\mathbf{r}) \cdot \hat{\mathbf{n}} ds \quad (2.33)$$

$$\oint_C \hat{\mathbf{H}}(\mathbf{r}) d\mathbf{l} = j\omega \int_S \hat{\epsilon}^s(\mathbf{r}) \hat{\mathbf{E}}(\mathbf{r}) \cdot \hat{\mathbf{n}} ds + \int_S \mathbf{J}_0(\mathbf{r}) \cdot \hat{\mathbf{n}} ds \quad (2.34)$$

and

$$\oint_C \hat{\mathbf{E}}^i(\mathbf{r}) d\mathbf{l} = -j\omega \int_S \hat{\mu}(\mathbf{r}) \hat{\mathbf{H}}^i(\mathbf{r}) \cdot \hat{\mathbf{n}} ds \quad (2.35)$$

$$\oint_C \hat{\mathbf{H}}^i(\mathbf{r}) d\mathbf{l} = j\omega \int_S \hat{\epsilon}(\mathbf{r}) \hat{\mathbf{E}}^i(\mathbf{r}) \cdot \hat{\mathbf{n}} ds + \int_S \mathbf{J}_0(\mathbf{r}) \cdot \hat{\mathbf{n}} ds \quad (2.36)$$

where S is a regular open surface with the contour line C . Subtracting (2.35) and (2.36) from (2.33) and (2.34), respectively, one can obtain

$$\oint_C [\hat{\mathbf{E}}(\mathbf{r}) - \hat{\mathbf{E}}^i(\mathbf{r})] d\mathbf{l} = -j\omega \int_S [\hat{\mu}^s(\mathbf{r}) \hat{\mathbf{H}}(\mathbf{r}) - \hat{\mu}(\mathbf{r}) \hat{\mathbf{H}}^i(\mathbf{r})] \cdot \hat{\mathbf{n}} ds \quad (2.37)$$

$$\oint_C [\hat{\mathbf{H}}(\mathbf{r}) - \hat{\mathbf{H}}^i(\mathbf{r})] d\mathbf{l} = j\omega \int_S [\hat{\epsilon}^s(\mathbf{r}) \hat{\mathbf{E}}(\mathbf{r}) - \hat{\epsilon}(\mathbf{r}) \hat{\mathbf{E}}^i(\mathbf{r})] \cdot \hat{\mathbf{n}} ds \quad (2.38)$$

Taking advantage of (2.31) and (2.32), the above equations can be rewritten as

$$\oint_C \hat{\mathbf{E}}^s(\mathbf{r}) d\mathbf{l} = -j\omega \int_S \{[\hat{\mu}^s(\mathbf{r}) - \hat{\mu}(\mathbf{r})] \hat{\mathbf{H}}(\mathbf{r}) + \hat{\mu}(\mathbf{r}) \hat{\mathbf{H}}^s(\mathbf{r})\} \cdot \hat{\mathbf{n}} ds \quad (2.39)$$

$$\oint_C \hat{\mathbf{H}}^s(\mathbf{r}) d\mathbf{l} = j\omega \int_S \{[\hat{\epsilon}^s(\mathbf{r}) - \hat{\epsilon}(\mathbf{r})] \hat{\mathbf{E}}(\mathbf{r}) + \hat{\epsilon}(\mathbf{r}) \hat{\mathbf{E}}^s(\mathbf{r})\} \cdot \hat{\mathbf{n}} ds \quad (2.40)$$

If we introduce the equivalent sources

$$\mathbf{M}_{eq}(\mathbf{r}) = j\omega [\hat{\mu}^s(\mathbf{r}) - \hat{\mu}(\mathbf{r})] \hat{\mathbf{H}}(\mathbf{r}), \quad (2.41)$$

$$\mathbf{J}_{eq}(\mathbf{r}) = j\omega [\hat{\epsilon}^s(\mathbf{r}) - \hat{\epsilon}(\mathbf{r})] \hat{\mathbf{E}}(\mathbf{r}), \quad (2.42)$$

then (2.39) and (2.40) are rearranged as

$$\oint_C \hat{\mathbf{E}}^s(\mathbf{r}) d\mathbf{l} = -j\omega \int_S \hat{\mu}(\mathbf{r}) \hat{\mathbf{H}}^s(\mathbf{r}) \cdot \hat{\mathbf{n}} ds - \int_S \mathbf{M}_{eq}(\mathbf{r}) \cdot \hat{\mathbf{n}} ds \quad (2.43)$$

$$\oint_C \hat{\mathbf{H}}^s(\mathbf{r}) d\mathbf{l} = j\omega \int_S \hat{\epsilon}(\mathbf{r}) \hat{\mathbf{E}}^s(\mathbf{r}) \cdot \hat{\mathbf{n}} ds + \int_S \mathbf{J}_{eq}(\mathbf{r}) \cdot \hat{\mathbf{n}} ds \quad (2.44)$$

From (2.43) and (2.44), one can observe that the scattered fields can be considered as the radiated fields generated by the equivalent sources which are dependent on the electromagnetic properties of the scatterers. These two equations show the volume equivalence theorem.

Using the equivalence sources, one can express the scattered electric and magnetic fields as [2]

$$\hat{\mathbf{E}}^s(\mathbf{r}) = j\omega \hat{\mu} \int_V \mathbf{J}_{eq}(\mathbf{r}') \cdot \bar{\mathbf{G}}(\mathbf{r}, \mathbf{r}') d\mathbf{r}' + \int_V \nabla \times \mathbf{M}_{eq}(\mathbf{r}') \cdot \bar{\mathbf{G}}(\mathbf{r}, \mathbf{r}') d\mathbf{r}' \quad (2.45)$$

$$\hat{\mathbf{H}}^s(\mathbf{r}) = j\omega \hat{\epsilon} \int_V \mathbf{M}_{eq}(\mathbf{r}') \cdot \bar{\mathbf{G}}(\mathbf{r}, \mathbf{r}') d\mathbf{r}' - \int_V \nabla \times \mathbf{J}_{eq}(\mathbf{r}') \cdot \bar{\mathbf{G}}(\mathbf{r}, \mathbf{r}') d\mathbf{r}' \quad (2.46)$$

As the nonmagnetic media, i.e., $\hat{\mu} = \hat{\mu}^s = \mu_0$, are considered in the study presented in this thesis, $\mathbf{M}_{eq} = 0$ can be obtained. Then the scattered electric and magnetic fields can be simplified as

$$\hat{\mathbf{E}}^s(\mathbf{r}) = j\omega \mu_0 \int_V \mathbf{J}_{eq}(\mathbf{r}') \cdot \bar{\mathbf{G}}(\mathbf{r}, \mathbf{r}') d\mathbf{r}' \quad (2.47)$$

$$\hat{\mathbf{H}}^s(\mathbf{r}) = - \int_V \nabla \times \mathbf{J}_{eq}(\mathbf{r}') \cdot \bar{\mathbf{G}}(\mathbf{r}, \mathbf{r}') d\mathbf{r}'. \quad (2.48)$$

In practice, microwave imaging systems only acquire the electric field measurements for image reconstruction. Hence, we can mainly focus on the discussion of the electric field relation, i.e., (2.47), in the following.

Substituting (2.41) into (2.47) and (2.48), we obtain

$$\hat{\mathbf{E}}^s(\mathbf{r}) = j\omega\hat{\mu} \int_V \tau(\mathbf{r}') \hat{\mathbf{E}}(\mathbf{r}') \cdot \bar{\mathbf{G}}(\mathbf{r}, \mathbf{r}') d\mathbf{r}' \quad (2.49)$$

where

$$\tau(\mathbf{r}) = j\omega [\hat{\varepsilon}^s(\mathbf{r}) - \hat{\varepsilon}] \quad (2.50)$$

is called the object function or contrast function. In (2.49), both the object function $\tau(\mathbf{r})$ and the perturbed electric field $\hat{\mathbf{E}}(\mathbf{r})$ are unknown. Meanwhile, the perturbed electric field $\hat{\mathbf{E}}(\mathbf{r})$ is also related to the permittivity of scatterers. Therefore, to reconstruct the object function based on some measurements outside of the region of interest becomes a very difficult problem. However, in some circumstances, (2.49) can be linearized by introducing some approximation models, which will alleviate the inversion/image reconstruction processing.

2.4 Born Approximation Model

When the scatterer has a small contrast relative to the background medium, the Born approximation can be applied. The simplest (i.e., the first order) Born approximation assumes that the perturbed electric field in the integrand in (2.49) can be approximated by the incident one

$$\begin{aligned} \hat{\mathbf{E}}^s(\mathbf{r}) &= j\omega\hat{\mu} \int_V \tau(\mathbf{r}') \hat{\mathbf{E}}(\mathbf{r}') \cdot \bar{\mathbf{G}}(\mathbf{r}, \mathbf{r}') d\mathbf{r}' \\ &\approx j\omega\hat{\mu} \int_V \tau(\mathbf{r}') \hat{\mathbf{E}}^i(\mathbf{r}') \cdot \bar{\mathbf{G}}(\mathbf{r}, \mathbf{r}') d\mathbf{r}' \end{aligned} \quad (2.51)$$

As the incident field $\hat{\mathbf{E}}^i(\mathbf{r}')$ is independent from the scatterers, equation (2.51), compared to (2.49), is linearized with respect to the object function. Meanwhile, the object function becomes the only unknown in (2.51) which is easy to solve. The condition for the first-order Born approximation to be valid for weak scatterers can be expressed as

$$k_b a \sup_{|\mathbf{r}|<a} |\varepsilon_r(\mathbf{r}) - 1| < 2\pi\zeta \quad (2.52)$$

where k_b is the wavenumber of the EM signal in the background medium, a is the radius of the minimum circle that can enclose the object cross section, and ζ is a

constant. In [4], Slaney *et al.* set $\zeta = 0.25$ by investigating a plane wave impinging onto a cylindrical object and requiring the phase differences between the incident wave and the wave traveling through the object to be less than π .

Some other Born approximations (e.g., the second-order Born approximation and extended Born approximation) have been developed and provide a better reconstruction of scatterers. However, considering the computational simplicity, we still use the first-order Born approximation for the algorithm development in this thesis.

2.5 Imaging Reconstruction Methods

Based on the above formulation, many different imaging algorithms have been developed for microwave imaging, such as delay-and-sum, filtered back projection, Kirchhoff migration, Range migration algorithm (RMA), linear inversion algorithms, etc. In principle, we can divide these algorithms into two categories: (1) Radar-based (or scalar-wave based) approaches and (2) Inverse-based approaches. The radar-based approaches typically treat the EM signals as the scalar wave for image formation, especially for those algorithms initially developed for seismic/acoustic imaging. These approaches are usually computationally efficient and provide the potential for real-time/near real-time imaging. By contrast, the inverse-based approaches take into account the vector nature of the EM signals and significantly improve image qualities at the expense of much higher computational cost. Moreover, the inversion-based approaches are to some extent applicable to more general imaging configurations. For convenience, a few algorithms used in the later chapters are briefly introduced below.

2.5.1 Radar-based Approaches

As presented above, each of the electric field components in Cartesian coordinates satisfies the scalar wave equation (2.30). Hence, for the same polarized signals acquired over a measurement surface, they can be back-propagated to the time zero to reconstruct the image of scatterers by exploiting the exploding reflector model (ERM) which assumes that the reflected signals can be considered as the radiated signals from a virtual source placed at the scatterer's position but propagating with half of the real speed in the practical medium. This back propagation process can be implemented in either spatial-time domain or frequency-wavenumber domain and accordingly different imaging algorithms are developed. Two examples of such algorithms are Kirchhoff migration and range migration.

2.5.1.1 Kirchhoff Migration

Kirchhoff migration, which was an approach originally proposed to the migration of seismic data based on the scalar wave equation, utilizes the Kirchhoff integral to backpropagate the acquired signals to the time zero to reconstruct the image of scatterers [5]. The Kirchhoff integral can be derived from Green's theorem that relates the wavefield in the interior of a closed surface and the observations on the surface [6], which is given by¹

$$U(\mathbf{r}, t) = - \int dt_0 \int_{S_0} dS_0 \left[G(\mathbf{r}, \mathbf{r}_0, t, t_0) \frac{\partial U}{\partial \mathbf{n}}(\mathbf{r}_0, t_0) - U(\mathbf{r}_0, t_0) \frac{\partial G}{\partial \mathbf{n}}(\mathbf{r}, \mathbf{r}_0, t, t_0) \right] \quad (2.53)$$

where $U(\mathbf{r}, t)$ is the wave field in a volume bounded by the surface S_0 , and \mathbf{r} is the vector from the origin to a wavefield point. \mathbf{r}_0 is the vector from the origin to a point on the surface of integration S_0 . t_0 is the time at which the wavefield is observed, and \mathbf{n} is the unit vector normal to the surface S_0 . $G(\mathbf{r}, \mathbf{r}_0, t, t_0)$ is the Green's function that is a solution to the scalar wave equation for a point source at \mathbf{r} , which is the time domain counterpart of the Green's function in (2.25).

To evaluate the integral in (2.53), both the wave field $U(\mathbf{r}_0, t_0)$ and its derivative in the direction normal to the surface S_0 are required. To circumvent the requirement for the derivatives of $U(\mathbf{r}_0, t_0)$ in the normal direction \mathbf{n} , the Kirchhoff approximation can be introduced, which specifies the Green's function on the surface S_0 by

$$G = 0, \quad \frac{\partial G}{\partial \mathbf{n}} = 2 \frac{\partial G_{fs}}{\partial \mathbf{n}} \quad (2.54)$$

and

$$G_{fs} = -\frac{\delta(t - t_0 - R/v)}{4\pi R}, \quad R = |\mathbf{r} - \mathbf{r}_0|.$$

where v is the propagation velocity of EM waves in the medium. Then (2.53) can be simplified as

$$U(\mathbf{r}, t) = -\frac{1}{2\pi} \int dt_0 \int U(\mathbf{r}_0, t_0) \frac{\partial}{\partial \mathbf{n}} \left[\frac{\delta(t - t_0 - R/v)}{R} \right] dS_0 \quad (2.55)$$

Equation (2.55) is the so-called Kirchhoff integral. After some algebraic manipulations, it can be explicitly written as

$$U(\mathbf{r}, t) = \frac{1}{2\pi} \int dS_0 \frac{\partial R}{\partial n} \left[\frac{\partial U(\mathbf{r}_0, t - R/v)}{\partial t} \frac{1}{Rv} + \frac{U(\mathbf{r}_0, t - R/v)}{R^2} \right] \quad (2.56)$$

¹Here the factor $-\frac{1}{4\pi}$ is included in the Green's function $G(\mathbf{r}, \mathbf{r}_0)$ compared to that in Reference [6].

Based on (2.56), the Kirchhoff migration algorithm for image reconstruction is obtained by setting $t = 0$, which is expressed as

$$f(\mathbf{r}) = U(\mathbf{r}, 0) = \frac{1}{2\pi} \int \frac{\partial R}{\partial n} \left[\frac{\partial U(\mathbf{r}_0, t - R/v)}{\partial t} \frac{1}{Rv} + \frac{U(\mathbf{r}_0, t - R/v)}{R^2} \right] dS_0|_{t=0} \quad (2.57)$$

2.5.1.2 Range Migration

Range migration is another kind of popular imaging algorithm which processes the image reconstruction in the spatial Fourier (i.e., wavenumber) domain. It has been widely used for synthetic aperture radar [7], seismic imaging, computed tomography. Similar to Kirchhoff migration, range migration algorithms can also be derived from the scalar wave equation. However, as the range migration algorithm can take advantage of the fast Fourier transform in the implementation, it is more efficient than Kirchhoff migration which performs the image reconstruction in the spatial-time domain.

Considering the scalar wave equation (2.26), it can be explicitly expressed in a Cartesian coordinate system as

$$\left[\frac{\partial^2}{\partial x^2} + \frac{\partial^2}{\partial y^2} + \frac{\partial^2}{\partial z^2} + k^2 \right] U(\mathbf{r}, \mathbf{r}_0, \omega) = \delta(\mathbf{r} - \mathbf{r}_0) \quad (2.58)$$

Taking the Fourier transform with respect to x and z (i.e., cross-range variables) on both sides of (2.58), we obtain

$$\left[-k_x^2 - k_z^2 + \frac{\partial^2}{\partial y^2} + k^2 \right] U(k_x, k_z, y, k) = 0 \quad (2.59)$$

where k_x and k_z represent the wavenumber-domain counterparts of x and z , respectively. Note that in the above derivation the velocities of wave propagation in the cross-range directions are assumed to be constant. (2.59) is a second-order differential equation with respect to y . Utilizing the ERM and considering only the incoming wave field, one can get the solution to (2.59) as

$$U(k_x, k_z, y, k) = U(k_x, k_z, y = 0, k) e^{-jk_y y} \quad (2.60)$$

where

$$k_y = \sqrt{k^2 - k_x^2 - k_z^2} \quad (2.61)$$

and $k = 2\omega/v$, in which the factor “2” results from half of the velocity of wave propagation in the ERM model. Taking the inverse Fourier transform of (2.60), the

migrated image in space is obtained

$$f(x, y, z, t = 0) = \iiint U(k_x, k_z, y = 0, k) e^{-j(k_x x + k_y y + k_z z)} dk_x dk_z d\omega \quad (2.62)$$

In (2.62), the wave field is extrapolated through a phase-shift [see (2.60)] before the inverse FT. So it is also known as Gazdag's phase-shift migration, which can tackle the variations of the propagation velocities in the down-range direction. In a homogeneous medium, the wave propagation velocity is constant. Hence, the integral element $d\omega$ in (2.62) can be converted into dk_y . According to the dispersion relation (2.61), one can get

$$d\omega = \frac{k_y v}{4\omega} dk_y \quad (2.63)$$

Substituting (2.63) for $d\omega$, (2.62) can be rewritten as

$$f(x, y, z, t = 0) = \frac{v}{4} \iiint \frac{k_y}{\omega} U(k_x, k_z, y = 0, k) e^{-j(k_x x + k_y y + k_z z)} dk_x dk_y dk_z \quad (2.64)$$

Equation (2.64) is the Fourier transform of $\frac{k_y}{\omega} U(k_x, k_z, y = 0, k)$ with respect to k_x , k_y , and k_z . However, $U(k_x, k_z, y = 0, k)$ is usually given in an even grid of k but uneven in k_y , which hinders the application of the 3-D inverse fast Fourier transform. To overcome this problem, a variable change from k to k_y is needed to transform $U(k_x, k_z, y = 0, k)$ to $\tilde{U}(k_x, k_y, k_z, y = 0)$. This can be implemented by Stolt interpolation which is a 1-D interpolation from uneven data to even data [8]. By properly warping the scattered data in the spatial Fourier domain, the Stolt interpolation accurately corrects the wavefront curvature of the wave fields scattered from the scatterers. Finally, the migrated image can be expressed as

$$f(x, y, z, t = 0) = \iiint \tilde{U}(k_x, k_y, k_z, y = 0) e^{-j(k_x x + k_y y + k_z z)} dk_x dk_y dk_z \quad (2.65)$$

Due to the Stolt interpolation, the range migration is also known as the Stolt migration. The range migration can be used to migrate the radar data collected in a (quasi-)monostatic configuration. Its implementation steps are briefly described as

- (1) Applying the Fourier transform to the scattered data in the cross-range directions to obtain $U(k_x, k_z, y = 0, k)$;
- (2) Scaling $U(k_x, k_z, y = 0, k)$ by the factor $\frac{k_y v}{4\omega}$, and then performing the Stolt interpolation with the scaled data to get $\tilde{U}(k_x, k_y, k_z, y = 0)$;
- (3) Taking 3-D IFFT of $\tilde{U}(k_x, k_y, k_z, y = 0)$ to get migrated images.

2.5.2 Inversion-based Approaches

Inversion-based approaches form another important group of the methods for microwave imaging. These approaches address the scattered EM data inversion in many different ways based on the imaging configuration, operation condition and the target itself (i.e., strong or weak scatterers) [9]. For weak scatterers, the Born approximation is usually used to linearize the scattering model and simplify the inversion process. We assume the Born approximation is also valid for the scenarios considered in this thesis.

Combining (2.51) and (2.23), the scattered electric field under the Born approximation can be written as

$$\begin{aligned}\hat{\mathbf{E}}^s(\mathbf{r}) &= j\omega\mu_0 \int_V \tau(\mathbf{r}') \bar{\mathbf{G}}(\mathbf{r}, \mathbf{r}') d\mathbf{r}' \cdot j\omega\mu_0 \int_{V^s} \mathbf{J}_0(\mathbf{r}^s) \bar{\mathbf{G}}(\mathbf{r}', \mathbf{r}^s) d\mathbf{r}^s \\ &= -\omega^2\mu_0^2 \int_V \tau(\mathbf{r}') \bar{\mathbf{G}}(\mathbf{r}, \mathbf{r}') d\mathbf{r}' \int_{V^s} \mathbf{J}_0(\mathbf{r}^s) \bar{\mathbf{G}}(\mathbf{r}', \mathbf{r}^s) d\mathbf{r}^s\end{aligned}\quad (2.66)$$

where V represents the domain occupied by the scatterers and V^s denotes the volume of the source. Meanwhile, $\hat{\mu} = 1$ has been used to consider the nonmagnetic media.

In practice, microwave imaging systems generally illuminate the region of interest with some isolated sources and accordingly measure the scattered fields at some discrete positions in the observation domain. In this thesis, we consider the configuration in which both the electric field sources and the receivers are placed on a plane, for instance, xoz plane, and y points towards the region of interest. Assume a point source $\mathbf{J}_\beta = w(\omega)\mathbf{b}_\beta$, where $w(\omega)$ is the source wavelet spectrum and \mathbf{b}_β denotes the orientation of the source antennas, is located at \mathbf{r}' , the scattered field acquired by a receiver at \mathbf{r}^r with the orientation \mathbf{b}_α can be obtained from (2.66) as

$$\begin{aligned}E_{\alpha\beta}^s(\mathbf{r}^r, \mathbf{r}', \omega) &= -\omega^2\mu_0^2 \int_V \tau(\mathbf{r}') \mathbf{b}_\alpha \bar{\mathbf{G}}(\mathbf{r}^r, \mathbf{r}') d\mathbf{r}' \int_{V^s} \delta(\mathbf{r}^s - \mathbf{r}') \mathbf{J}_\beta \bar{\mathbf{G}}(\mathbf{r}', \mathbf{r}^s) d\mathbf{r}^s \\ &= -\omega^2\mu_0^2 w(\omega) \int_V \tau(\mathbf{r}') \mathbf{b}_\alpha \bar{\mathbf{G}}(\mathbf{r}^r, \mathbf{r}') \bar{\mathbf{G}}(\mathbf{r}', \mathbf{r}') \mathbf{b}_\beta d\mathbf{r}'\end{aligned}\quad (2.67)$$

By introducing

$$S(\omega) = -\omega^2\mu_0^2 w(\omega) \quad (2.68)$$

$$D_{\alpha\beta}(\mathbf{r}^r, \mathbf{r}'; \mathbf{r}', \omega) = \mathbf{b}_\alpha \bar{\mathbf{G}}(\mathbf{r}^r, \mathbf{r}') \bar{\mathbf{G}}(\mathbf{r}', \mathbf{r}') \mathbf{b}_\beta \quad (2.69)$$

Then (2.67) can be rewritten as

$$E_{\alpha\beta}^s(\mathbf{r}^r, \mathbf{r}', \omega) = \int_V D_{\alpha\beta}(\mathbf{r}^r, \mathbf{r}'; \mathbf{r}', \omega) \tau(\mathbf{r}') S(\omega) d\mathbf{r}' \quad (2.70)$$

where $D_{\alpha\beta}(\mathbf{r}^r, \mathbf{r}^t; \mathbf{r}', \omega)$ represents the wave-field extrapolator propagating from a \mathbf{b}_β -polarized transmitter at \mathbf{r}' to a scatterer at \mathbf{r}' and then to a \mathbf{b}_α -polarized receiver at \mathbf{r}^r . For numerical processing, (2.70) can be discretized as

$$E_{\alpha\beta}^s(\mathbf{r}^r, \mathbf{r}^t, \omega) = S(\omega) \cdot \Delta V \cdot \sum_{i=1}^N D_{\alpha\beta}(\mathbf{r}^r, \mathbf{r}^t; \mathbf{r}'_i, \omega) \tau(\mathbf{r}'_i) \quad (2.71)$$

where N is the number of discrete cells included in the investigation domain, and ΔV is the volume of each cell. Considering all the measurements acquired over P discrete frequencies by M transceivers/transmitter-receiver pairs in the observation domain, one can obtain

$$\mathbf{s} = \mathbf{D} \cdot \chi \quad (2.72)$$

where

$$\mathbf{s} = \text{vec}([\mathbf{s}_1, \mathbf{s}_2, \dots, \mathbf{s}_M]) \quad (2.73)$$

$$\mathbf{s}_m = [E_{\alpha_m\beta_m}^s(\mathbf{r}_m^r, \mathbf{r}_m^t, \omega_1), E_{\alpha_m\beta_m}^s(\mathbf{r}_m^r, \mathbf{r}_m^t, \omega_2), \dots, E_{\alpha_m\beta_m}^s(\mathbf{r}_m^r, \mathbf{r}_m^t, \omega_P)]^\top, \\ m = 1, 2, \dots, M \quad (2.74)$$

$$\mathbf{D} = [\mathbf{D}_1, \mathbf{D}_2, \dots, \mathbf{D}_M]^\top \quad (2.75)$$

$$\mathbf{D}_m = [\mathbf{D}_m^{(1)}, \mathbf{D}_m^{(2)}, \dots, \mathbf{D}_m^{(P)}], \quad m = 1, 2, \dots, M \quad (2.76)$$

$$\mathbf{D}_m^{(p)} = [D_{\alpha_m\beta_m}(\mathbf{r}_m^r, \mathbf{r}_m^t; \mathbf{r}'_1, \omega_p), D_{\alpha_m\beta_m}(\mathbf{r}_m^r, \mathbf{r}_m^t; \mathbf{r}'_2, \omega_p), \dots, D_{\alpha_m\beta_m}(\mathbf{r}_m^r, \mathbf{r}_m^t; \mathbf{r}'_N, \omega_p)]^\top, \\ p = 1, 2, \dots, P \quad (2.77)$$

$$\chi = [\tau(\mathbf{r}'_1), \tau(\mathbf{r}'_2), \dots, \tau(\mathbf{r}'_N)]^\top. \quad (2.78)$$

In (2.73), $\text{vec}(\mathbf{X})$ represents an $MN \times 1$ vector by stacking the columns of an $M \times N$ matrix \mathbf{X} . Moreover, the term $S(\omega) \cdot \Delta V$ has been suppressed for simplification in (2.72). To reconstruct the contrast function χ in the investigation domain, (2.72) has to be inverted. However, due to the noise and/or measurement errors of the imaging system, the inversion problem of the system (2.72) is generally ill-posed, which may cause the issues related to the existence, uniqueness, and stability of the solution χ . To resolve the nonexistence, non-uniqueness and stability of the solution, many different inversion methods have been proposed, including (truncated) singular value decomposition-type methods and regularization-based methods [9]. The singular value decomposition-type methods provide a generalized solution to (2.72) in the least-squares sense while regularization-based methods enable to incorporate some prior information about the scene to be inspected with the data to get a more stable solution.

2.6 Conclusion

In this chapter, an overview of the mathematical tools that are required in the following chapters is given. Based on Maxwell's equations, the EM wave propagator has been introduced. Then the image reconstruction methods are briefly reviewed. In particular, the radar-based imaging and linear inversion methods are presented. As a rule, all methods are formulated in either space-frequency or wavenumber-frequency domains except Kirchhoff migration which is formulated in the space-time domain. It is also shown that the radar-based imaging methods (such as Kirchhoff and RMA) are typically formulated for backscattered fields, while the inversion methods are generally formulated including multi-static scattering.

References

- [1] J. Van Bladel, *Electromagnetic Fields*. Wiley-IEEE Press, 2007.
- [2] W. Chew, *Waves and Fields in Inhomogeneous Media*. IEEE Press, 1996.
- [3] C.-T. Tai, *Dyadic Green's functions in electromagnetic theory*. The Intext monograph series in electrical engineering, Scranton: Intext Educational Publishers, 1971.
- [4] M. Slaney, A. C. Kak, and L. E. Larsen, "Limitations of imaging with first-order diffraction tomography," *Microwave Theory and Techniques, IEEE Transactions on*, vol. 32, no. 8, pp. 860–874, 1984.
- [5] J. Wiggins, "Kirchhoff integral extrapolation and migration of nonplanar data," *GEOPHYSICS*, vol. 49, no. 8, pp. 1239–1248, 1984.
- [6] P. Morse and H. Feshbach, *Methods of theoretical physics*. International series in pure and applied physics, McGraw-Hill, 1953.
- [7] C. Cafforio, C. Prati, and F. Rocca, "SAR data focusing using seismic migration techniques," *IEEE Transactions on Aerospace and Electronic Systems*, vol. 27, no. 2, pp. 194–207, 1991.
- [8] R. Stolt, "Migration by fourier transform techniques," *GEOPHYSICS*, vol. 43, no. 1, pp. 23–48, 1978.
- [9] M. Pastorino, *Microwave Imaging*. Wiley Series in Microwave and Optical Engineering, John Wiley & Sons, Inc., 2010.

3

Rotated Arrays for Fully Polarimetric Imaging

3.1 Introduction

The synthetic aperture technique achieves a high cross-range resolution by moving a single antenna/small antenna array to simulate a large array aperture. The antenna (array) is generally linearly translated over the array aperture and the EM signals are collected at each spatial position. Then the acquired EM signals are focused with scalar-wave based imaging algorithms [1, 2]. For fully polarimetric measurements, the co-pol and cross-pol signals can also be jointly migrated via a matrix inversion to merge all the polarimetric information in one image [3]. All of these algorithms assume that the polarizations of the signals acquired within the aperture are constant. However, for rotated antenna arrays, the motions of the antennas contain not only linear translations but also rotations in space. Due to the rotation, the orientations (i.e., polarizations) of linearly polarized antennas are changed and thus the polarizations of the EM signals acquired by the rotated arrays are varying within the synthetic aperture, which violates the assumption of traditional scalar-wave based imaging algorithms. If these algorithms are still used to process the

Part of this chapter was published as: J. Wang, P. Aubry, and A. Yarovoy, "A Novel Approach to Full-Polarimetric Short-Range Imaging With Copolarized Data," *IEEE Transactions on Antennas and Propagation*, 64 (11), pp. 4733-4744, 2016. J. Wang, P. Aubry, and A. Yarovoy, "A Novel Rotated Antenna Array Topology for Near-Field 3-D Fully Polarimetric Imaging," *IEEE Transactions on Antennas and Propagation*, 66(3), pp. 1584-1589, 2018.

polarization-varied EM data directly, the quality of the resultant images could be degraded and the polarimetric information of targets is destroyed. Although more advanced imaging algorithms can be developed to process the polarization-varied EM data by considering full-wave radiation patterns of antennas, which will be discussed in Chapter 4, scalar-wave based imaging algorithms (e.g., migration methods) are more efficient compared to them.

The aim of this chapter is to explore the possibility to circumvent the polarization variations of the EM signals acquired with rotated arrays by specifically designing the array topologies, and then to utilize traditional scalar-wave based algorithms for image formation. Firstly, the effects of the variations of antenna orientations (i.e., polarizations) on the recorded EM signals are investigated. Then a novel approach to fully polarimetric imaging with rotated antenna arrays, which includes rotated array design and full-pol signal reconstruction, is proposed to overcome the effects of the polarization variations of the acquired EM signals. Two approaches for rotated antenna array design are proposed. The proposed rotated arrays collect either three co-polarized or two co-pol and one cross-pol measurements in a “local” polarization coordinate system at each position. Then the full-pol signals in the aligned H/V polarization bases can be retrieved from the three “locally” polarized measurements at each position through a simple linear transformation. So they facilitate the applicability of traditional scalar-wave based imaging algorithms for polarimetric image formation and targets’ full-pol feature extraction with rotated arrays.

The rest of the chapter is organized as follows. In section 3.2, the scattering formalism is briefly reviewed. The scattered wave field extrapolator for a rotated antenna is discussed in section 3.3. Two approaches to design rotated arrays for fully polarimetric imaging are proposed in the same section. Section 3.4 shows two examples of rotated array design with the proposed approaches. Then in sections 3.5 and 3.6 the effectiveness and accuracy of the rotated arrays for fully polarimetric imaging are demonstrated through numerical simulations and experiments. Finally, conclusions are drawn in section 3.7.

3.2 Scattering Formulation

Here the monostatic radar configuration is considered. We assume the antennas are deployed on the x_1 - x_2 plane, and the x_3 -axis points towards the observation scenario and forms a right-hand coordinate system. Based on the Born approximation, the

scattering process can be represented by a linear expression [3]

$$E_{\alpha\beta}^s(\mathbf{x}^R, \mathbf{x}^T, \omega) = \int_{V(\mathbf{x}^c)} D_{\alpha\beta}(\mathbf{x}^R, \mathbf{x}^T | \mathbf{x}^c, \omega) \chi(\mathbf{x}^c) J_\beta(\mathbf{x}^T, \omega) dV \quad (3.1)$$

where $\omega = 2\pi f$ is the angular frequency and $\mathbf{x} = (x_1, x_2, x_3)$ collects the spatial coordinates. The superscripts R and T refer to the receiving and transmitting antennas while the subscripts α and β take values $\{1, 2\}$ and represent, respectively, the receiving and transmitting antennas' orientations along the x_1 or x_2 direction. $\chi(\mathbf{x}^c)$ is the contrast function in the position \mathbf{x}^c , $J_\beta(\mathbf{x}^T, \omega)$ is the point source located at the position \mathbf{x}^T , and $D_{\alpha\beta}(\mathbf{x}^R, \mathbf{x}^T | \mathbf{x}^c, \omega)$ is the forward wavefield extrapolator from the transmitting antenna at \mathbf{x}^T to the scatter at \mathbf{x}^c and then to the receiving antenna at \mathbf{x}^R . The contrast function χ is defined as $\chi(\mathbf{x}^c) = \hat{\eta}^s - \hat{\eta}$, which is the difference of the physical properties of the scatter $\hat{\eta}^s$ and the background $\hat{\eta}$. The physical property $\hat{\eta}$ is defined as $\hat{\eta} = \sigma + j\omega\epsilon$, where $j = \sqrt{-1}$, σ is the conductivity, ϵ is the permittivity. The point source $J_\beta(\mathbf{x}^T, \omega)$ can be denoted as

$$J_\beta(\mathbf{x}^T, \omega) = S(\omega) b_\beta(\mathbf{x}^T) \quad (3.2)$$

where $S(\omega)$ is the source wavelet radiated by the source antenna and b_β indicates its orientation along the x_1 - or x_2 -direction. The forward wavefield extrapolator $D_{\alpha\beta}(\mathbf{x}^R, \mathbf{x}^T, \omega)$ is defined by an inner product

$$D_{\alpha\beta}(\mathbf{x}^R, \mathbf{x}^T | \mathbf{x}^c, \omega) = \sum_{\ell=1}^3 G_{\alpha\ell}(\mathbf{x}^R | \mathbf{x}^c, \omega) G_{\ell\beta}(\mathbf{x}^c | \mathbf{x}^T, \omega) \quad (3.3)$$

where $\ell \in \{1, 2, 3\}$ denotes the electric field directions along the axes. Green's function $G_{\ell\beta}(\mathbf{x}^c | \mathbf{x}^T, \omega)$ describes the propagation of an electromagnetic wave from the source at \mathbf{x}^T to the scatterer at \mathbf{x}^c and Green's function $G_{\alpha\ell}(\mathbf{x}^R | \mathbf{x}^c, \omega)$ expresses the propagation from the scatterer in the position \mathbf{x}^c to the receiving antenna at \mathbf{x}^R . The forward wavefield extrapolator shown in (3.3) describes the scattering process with x_β -oriented transmitting antenna and x_α -oriented receiving antenna. Hence (3.1) gives the scattered wave from an illuminated volume acquired with an x_α -oriented receiving antenna related to an x_β -oriented transmission. Accounting for a pair of orthogonal orientations of the receiving antennas on the acquisition plane, the observed waves in the two directions can be arranged as a vector

$$\begin{bmatrix} E_1^s(\mathbf{x}^R, \mathbf{x}^T, \omega) \\ E_2^s(\mathbf{x}^R, \mathbf{x}^T, \omega) \end{bmatrix} = S(\omega) \cdot \int_{V(\mathbf{x}^c)} \mathbf{D}(\mathbf{x}^R, \mathbf{x}^T | \mathbf{x}^c, \omega) \begin{bmatrix} b_1(\mathbf{x}^T) \\ b_2(\mathbf{x}^T) \end{bmatrix} \chi(\mathbf{x}^c) dV \quad (3.4)$$

where $[E_1^s, E_2^s]^\top$ is a measured vector by two receiving antennas with orthogonal orientations corresponding to two orthogonally polarized transmission, and the superscript \top refers to matrix transpose operation. It is given by

$$\begin{bmatrix} E_1^s(\mathbf{x}^R, \mathbf{x}^T, \omega) \\ E_2^s(\mathbf{x}^R, \mathbf{x}^T, \omega) \end{bmatrix} = \begin{bmatrix} E_{11}^s(\mathbf{x}^R, \mathbf{x}^T, \omega) + E_{12}^s(\mathbf{x}^R, \mathbf{x}^T, \omega) \\ E_{21}^s(\mathbf{x}^R, \mathbf{x}^T, \omega) + E_{22}^s(\mathbf{x}^R, \mathbf{x}^T, \omega) \end{bmatrix} \quad (3.5)$$

and \mathbf{D} represents the forward wavefield extrapolator that is given by

$$\begin{aligned} \mathbf{D} &= \begin{bmatrix} D_{11}(\mathbf{x}^R, \mathbf{x}^T | \mathbf{x}^c, \omega) & D_{12}(\mathbf{x}^R, \mathbf{x}^T | \mathbf{x}^c, \omega) \\ D_{21}(\mathbf{x}^R, \mathbf{x}^T | \mathbf{x}^c, \omega) & D_{22}(\mathbf{x}^R, \mathbf{x}^T | \mathbf{x}^c, \omega) \end{bmatrix} \\ &= \begin{bmatrix} G_{11}^R & G_{21}^R & G_{31}^R \\ G_{12}^R & G_{22}^R & G_{32}^R \end{bmatrix} \begin{bmatrix} G_{11}^T & G_{12}^T \\ G_{21}^T & G_{22}^T \\ G_{31}^T & G_{32}^T \end{bmatrix} \end{aligned} \quad (3.6)$$

where G^R is short for $G^R(\mathbf{x}^R | \mathbf{x}^c, \omega)$ and G^T for $G^T(\mathbf{x}^c | \mathbf{x}^T, \omega)$. We focus on the monostatic configuration here, so transmitting and receiving antennas are located at the same position \mathbf{x}^A , i.e., $\mathbf{x}^T = \mathbf{x}^R = \mathbf{x}^A$ for each observation. Consequently, Green's functions of transmitting and receiving antennas are equal in the corresponding electric field directions. Meanwhile, using the reciprocity properties of propagation, the elements of \mathbf{D} can be explicitly written as

$$\begin{cases} D_{11} = G_{11}^2 + G_{21}^2 + G_{31}^2 \\ D_{12} = G_{11}G_{12} + G_{21}G_{22} + G_{31}G_{32} \\ D_{21} = G_{11}G_{12} + G_{21}G_{22} + G_{31}G_{32} \\ D_{22} = G_{12}^2 + G_{22}^2 + G_{32}^2 \end{cases} \quad (3.7)$$

where Green's functions G are functions of \mathbf{x}^c , \mathbf{x}^A , and ω . From (3.7), it can be observed that D_{12} equals D_{21} in the monostatic configuration, which is the result of the reciprocity theorem.

3.3 Wavefield Extrapolator for Rotated Antennas

The variation of the orientations of transmitting/receiving antennas changes the polarizations of the radiated/received electromagnetic fields. In the monostatic configuration, simultaneously rotating the orientations of the transmitting and receiving antennas equivalently rotates the polarization coordinate system of measurement.

Assume the new polarization coordinate system is rotated with an angle θ in a clockwise direction with respect to the original one [e.g., (b_1, b_2) base], then the received signal in the new polarization bases can be related to the measurements before rotation at the same position through the rotation matrix

$$\begin{aligned} \begin{bmatrix} E_1^s(\mathbf{x}^R, \mathbf{x}^T, \omega) \\ E_2^s(\mathbf{x}^R, \mathbf{x}^T, \omega) \end{bmatrix} &= R \begin{bmatrix} E_\theta^s(\mathbf{x}^R, \mathbf{x}^T, \omega) \\ E_{\theta_\perp}^s(\mathbf{x}^R, \mathbf{x}^T, \omega) \end{bmatrix} \\ \begin{bmatrix} b_1(\mathbf{x}^T) \\ b_2(\mathbf{x}^T) \end{bmatrix} &= R \begin{bmatrix} b_\theta(\mathbf{x}^T) \\ b_{\theta_\perp}(\mathbf{x}^T) \end{bmatrix} \end{aligned} \quad (3.8)$$

where R is the rotation matrix and is expressed as

$$R = \begin{bmatrix} \cos \theta & \sin \theta \\ -\sin \theta & \cos \theta \end{bmatrix} \quad (3.9)$$

Inserting (3.8) into (3.4) and performing a simple algebraic manipulation result in

$$\begin{bmatrix} E_\theta^s(\mathbf{x}^R, \mathbf{x}^T, \omega) \\ E_{\theta_\perp}^s(\mathbf{x}^R, \mathbf{x}^T, \omega) \end{bmatrix} = S(\omega) \int_{V(\mathbf{x}^c)} R^{-1} \mathbf{D}(\mathbf{x}^R, \mathbf{x}^T | \mathbf{x}^c, \omega) R \begin{bmatrix} b_\theta(\mathbf{x}^T) \\ b_{\theta_\perp}(\mathbf{x}^T) \end{bmatrix} \chi(\mathbf{x}^c) dV \quad (3.10)$$

where R^{-1} is the inverse matrix of R . Equation (3.10) formulates the scattering process in the polarization bases (θ, θ_\perp) . Compared to (3.4), in the polarization bases (θ, θ_\perp) the forward wavefield extrapolator, denoted by $\hat{\mathbf{D}}$, can be defined as

$$\hat{\mathbf{D}} = R^{-1} \mathbf{D}(\mathbf{x}^R, \mathbf{x}^T | \mathbf{x}^c, \omega) R \quad (3.11)$$

Equation (3.11) describes the relationship between the forward wavefield extrapolators in two different polarization bases (b_1, b_2) and (θ, θ_\perp) . Substituting (3.9) for R , $\hat{\mathbf{D}}$ can be explicitly written as

$$\hat{\mathbf{D}} = \begin{bmatrix} \hat{D}_{11} & \hat{D}_{12} \\ \hat{D}_{21} & \hat{D}_{22} \end{bmatrix} \quad (3.12)$$

where

$$\begin{cases} \hat{D}_{11} = \cos^2 \theta \cdot D_{11} - \sin \theta \cos \theta \cdot D_{21} - \sin \theta \cos \theta \cdot D_{12} + \sin^2 \theta \cdot D_{22} \\ \hat{D}_{12} = \sin \theta \cos \theta \cdot D_{11} - \sin^2 \theta \cdot D_{21} + \cos^2 \theta \cdot D_{12} - \sin \theta \cos \theta \cdot D_{22} \\ \hat{D}_{21} = \sin \theta \cos \theta \cdot D_{11} + \cos^2 \theta \cdot D_{21} - \sin^2 \theta \cdot D_{12} - \sin \theta \cos \theta \cdot D_{22} \\ \hat{D}_{22} = \sin^2 \theta \cdot D_{11} + \sin \theta \cos \theta \cdot D_{21} + \sin \theta \cos \theta \cdot D_{12} + \cos^2 \theta \cdot D_{22} \end{cases} \quad (3.13)$$

In practice, quad-polarimetric radar systems radiate two orthogonally polarized electric fields separately in time or with orthogonal waveforms for identification; then for each polarized transmission, two orthogonally polarized components are collected. This operation can be represented by setting the vector $[b_\theta(\mathbf{x}^T), b_{\theta_\perp}(\mathbf{x}^T)]^\top$ as $[1, 0]^\top$ or $[0, 1]^\top$ for the two orthogonally polarized transmissions. Utilizing the four combinations of the polarizations of transmitting and receiving antennas, the acquired polarimetric measurements are

$$\left\{ \begin{array}{l} E_{\theta\theta}^s(\mathbf{x}^R, \mathbf{x}^T, \omega) = S(\omega) \int_{V(\mathbf{x}^c)} \hat{D}_{11}\chi(\mathbf{x}^c) dV \\ E_{\theta_\perp\theta}^s(\mathbf{x}^R, \mathbf{x}^T, \omega) = S(\omega) \int_{V(\mathbf{x}^c)} \hat{D}_{12}\chi(\mathbf{x}^c) dV \\ E_{\theta\theta_\perp}^s(\mathbf{x}^R, \mathbf{x}^T, \omega) = S(\omega) \int_{V(\mathbf{x}^c)} \hat{D}_{21}\chi(\mathbf{x}^c) dV \\ E_{\theta_\perp\theta_\perp}^s(\mathbf{x}^R, \mathbf{x}^T, \omega) = S(\omega) \int_{V(\mathbf{x}^c)} \hat{D}_{22}\chi(\mathbf{x}^c) dV \end{array} \right. \quad (3.14)$$

Applying (3.1) and (3.13) to (3.14), we can get

$$\left\{ \begin{array}{l} E_{\theta\theta}^s(\mathbf{x}^R, \mathbf{x}^T, \omega) = \cos^2\theta \cdot E_{11} - \sin\theta\cos\theta \cdot E_{21} \\ \quad - \sin\theta\cos\theta \cdot E_{12} + \sin^2\theta \cdot E_{22} \\ E_{\theta_\perp\theta}^s(\mathbf{x}^R, \mathbf{x}^T, \omega) = \sin\theta\cos\theta \cdot E_{11} - \sin^2\theta \cdot E_{21} \\ \quad + \cos^2\theta \cdot E_{12} - \sin\theta\cos\theta \cdot E_{22} \\ E_{\theta\theta_\perp}^s(\mathbf{x}^R, \mathbf{x}^T, \omega) = \sin\theta\cos\theta \cdot E_{11} + \cos^2\theta \cdot E_{21} \\ \quad - \sin^2\theta \cdot E_{12} - \sin\theta\cos\theta \cdot E_{22} \\ E_{\theta_\perp\theta_\perp}^s(\mathbf{x}^R, \mathbf{x}^T, \omega) = \sin^2\theta \cdot E_{11} + \sin\theta\cos\theta \cdot E_{21} \\ \quad + \sin\theta\cos\theta \cdot E_{12} + \cos^2\theta \cdot E_{22} \end{array} \right. \quad (3.15)$$

As $E_{21} = E_{12}$ in the monostatic configuration, (3.15) can be further simplified as

$$\left\{ \begin{array}{l} E_{\theta\theta}^s(\mathbf{x}^R, \mathbf{x}^T, \omega) = E_{11}\cos^2\theta - E_{12}\sin 2\theta + E_{22}\sin^2\theta \\ E_{\theta_\perp\theta}^s(\mathbf{x}^R, \mathbf{x}^T, \omega) = \frac{(E_{11} - E_{22})}{2} \sin 2\theta + E_{12}\cos 2\theta \\ E_{\theta\theta_\perp}^s(\mathbf{x}^R, \mathbf{x}^T, \omega) = \frac{(E_{11} - E_{22})}{2} \sin 2\theta + E_{12}\cos 2\theta \\ E_{\theta_\perp\theta_\perp}^s(\mathbf{x}^R, \mathbf{x}^T, \omega) = E_{11}\sin^2\theta + E_{12}\sin 2\theta + E_{22}\cos^2\theta \end{array} \right. \quad (3.16)$$

In (3.16), $E_{\theta_1\theta}^s$ is equal to $E_{\theta\theta_1}^s$, which agrees with the reciprocity theorem. Another fact one can observe is that the measurement $E_{\theta\theta}^s$ should be obtained by turning 90° (or 270°) clockwise the orientations of the transmitting-receiving antennas for $E_{\theta_1\theta_1}^s$. This can be demonstrated by replacing θ in the last line of (3.16) with $\theta+90^\circ$ (or $\theta+270^\circ$) such that the first line in (3.16) arrives. It shows the self-consistency of the derivation.

The equations in (3.16) give the relationships among the polarimetric measurements in two sets of polarization bases, i.e., (θ, θ_\perp) and (b_1, b_2) . So one can see that as long as we get the fully polarimetric measurements with respect to a rotated polarization coordinate system, the fully polarimetric signals in terms of the aligned polarization bases, for example, (b_1, b_2) , can be reconstructed via (3.16). This provides the first method to design a rotated array for fully polarimetric imaging.

Moreover, the equations in (3.16) reveal that each polarimetric measurement in the (θ, θ_\perp) bases is a function of the fully polarimetric signals in the (b_1, b_2) bases at the same position. Taking the first equation in (3.16) as an example, it shows that the θ co-polarized scattered waves, which are acquired with transmitting and receiving antennas with orientations of θ from the x_1 -axis, contain both the co-polarized (i.e., E_{11} and E_{22}) and cross-polarized (i.e., E_{12}) information that are measured by b_1 - or b_2 -polarized antennas. Therefore, to extract or reconstruct the fully polarimetric information of targets with rotated antennas, a second approach is to take three co-polarized measurements with antennas of three different orientations. Then, the application of the relation in (3.16) helps to reconstruct the full-polarized scattered signals that could be observed by b_1 - or b_2 -polarized antennas. More specifically, assume the three antennas for co-pol measurements are oriented with angles of θ_1 , θ_2 , and θ_3 from the x_1 -axis, then this approach can be expressed as

$$\begin{cases} E_{\theta_1\theta_1}^s(\mathbf{x}^R, \mathbf{x}^T, \omega) = \cos^2\theta_1 \cdot E_{11} - \sin 2\theta_1 \cdot E_{12} + \sin^2\theta_1 \cdot E_{22} \\ E_{\theta_2\theta_2}^s(\mathbf{x}^R, \mathbf{x}^T, \omega) = \cos^2\theta_2 \cdot E_{11} - \sin 2\theta_2 \cdot E_{12} + \sin^2\theta_2 \cdot E_{22} \\ E_{\theta_3\theta_3}^s(\mathbf{x}^R, \mathbf{x}^T, \omega) = \cos^2\theta_3 \cdot E_{11} - \sin 2\theta_3 \cdot E_{12} + \sin^2\theta_3 \cdot E_{22} \end{cases} \quad (3.17)$$

which gives the relations of three co-pol measurements with orientations of θ_1 , θ_2 and θ_3 with the fully polarimetric measurements E_{11} , E_{12} and E_{22} in the linear polarization bases (b_1, b_2) . Solving the system of linear equations in (3.17) reconstructs the observables E_{11} , E_{12} and E_{22} in the linear polarization bases (b_1, b_2) required by the conventional fully polarimetric imaging approaches. Then, the reconstructed measurements E_{11} , E_{12} , and E_{22} can be processed by employing either the scalar-wave based imaging algorithms or the matrix-based inversion algorithm.

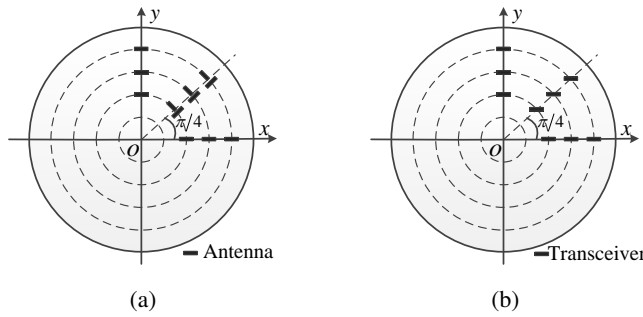


Figure 3.1: Topologies of the rotated arrays for fully polarimetric imaging designed with (a) the first approach based on (3.16) (referred to as Rotated Array I), and (b) the second approach based on (3.17) (referred to as Rotated Array II).

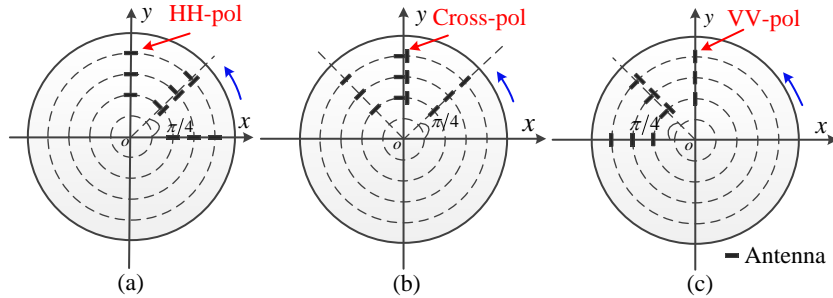


Figure 3.2: Operation Scheme of the Rotated Array I to acquire two “local” co-pol and one cross-pol measurements. (a), (b) and (c) illustrate the two co-pol and one cross-pol measurements at a position on the y-axis acquired sequentially by three antennas on the same circle.

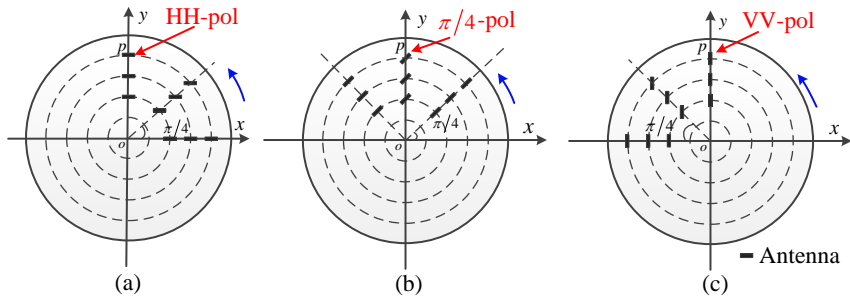


Figure 3.3: Operation scheme of the Rotated Array II to acquire three co-pol measurements. (a), (b) and (c) illustrate the three different co-pol measurements at a sampling position on the y-axis acquired sequentially by three antennas on the same circle.

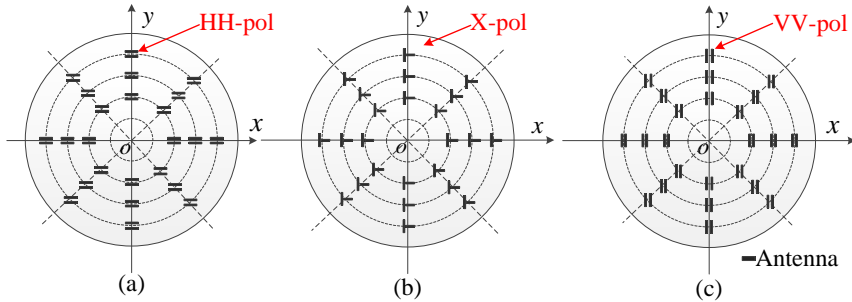


Figure 3.4: Topologies of traditional fully polarimetric imaging arrays: (a) HH copol array, (b) HV cross-pol array, and (c) VV copol array.

3.4 Rotated Antenna Arrays Design

3.4.1 Array Topologies

In this section, the proposed approaches to full-polarized signal acquisition above are applied to design rotated antenna arrays which could be used in, for example, the GPR systems for the TBM applications.

Firstly, one rotated array topology can be proposed based on the first approach, which measures two co-pol and one cross-pol signals at each position with respect to the “local” polarization coordinate system. Assume the antenna elements are distributed along three radial directions over several concentric circles. The antennas on two of the radial directions are placed along the “local” polarization bases to collect the two co-pol components while the transmitting and receiving antennas on the third radial directions are placed orthogonally at each position to take the cross-pol measurements. Figure 3.1(a) illustrates such a topology, where the “local” polarization bases are defined as the vectors parallel and perpendicular to the local radius. For convenience, this rotated array is referred to as Rotated Array I in the following. Its operation scheme is shown in Figure 3.2. With its rotation, the Rotated Array I collects two “local” co-pol and one cross-pol EM signals when the antennas pass by the same sampling positions. As an example, the polarizations of the three measurements acquired by the Rotated Array I at a position on the y-axis are indicated in Figure 3.2.

Next, utilizing the second approach proposed above, another rotated array topology can be designed for full-pol imaging by just recording three co-pol measurements at each position. Similar to the Rotated Array I, the antennas are placed in

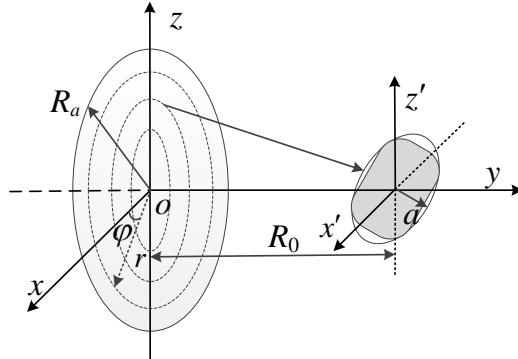


Figure 3.5: Geometry configuration for rotated array imaging.

three radial directions over a series of concentric circles. The antennas in the same radial direction are set with the same orientation but in different radial directions the antenna orientation angles formed with respect to the corresponding radius are different. Figure 3.1(b) shows an example of a rotated array when the three angles formed between antenna axis and the corresponding radius are 0° , 45° and 90° , which is referred to as Rotated Array II. With the rotation of the circular disc, three co-polarized measurements are acquired when the three antennas on the same circle sequentially pass by one particular sampling position. This operation mechanism for the signal acquisition at a point on the y -axis is shown in Figure 3.3. One may note that polarizations of the three measurements with both Rotated Array I and II are still distinct at different spatial points as the antenna array rotates circularly. But employing (3.16) and (3.17), the full-pol signals in an aligned polarization coordinate system can be reconstructed from the measurements of Rotated Array I and II, respectively. Furthermore, to get sufficient spatial observations within the aperture, the radii of concentric circles and the azimuthal sampling intervals with the rotation are determined by the sampling criteria and will be discussed in next section.

3.4.2 Sampling Criteria

The rotated antenna array synthesizes a planar circular aperture (i.e., RadSAR) for the 3-D imaging and takes spatial samples over a polar grid, as shown in Figure 3.5. The numbers of antennas along a radial direction and azimuthal samples can be determined based on the polar sampling analysis. To avoid aliasing, it is derived for narrowband (or monochromatic) systems in [4] that regular sampling is performed

along the radial direction and equi-arc-length sampling in azimuth. The azimuthal sampling interval is

$$\Delta\varphi = 2\pi/(2N + 1), \quad N = \lceil K_a r \rceil \quad (3.18)$$

where K_a is the maximum wavenumber related to the scenario, r denotes the radius and N is the smallest integer larger than or equal to $K_a r$. The radial sampling constraint can be obtained in a similar way to the linear arrays. Based on the Nyquist criterion, it should satisfy

$$\Delta r \leq \lambda \sqrt{(R_a + a)^2 + R_0^2} / [4(R_a + a)] \quad (3.19)$$

where λ is the wavelength of the highest frequency of the signal, R_a is the radius of the antenna aperture, R_0 is the distance from the target to antenna aperture, and a is the radius of the smallest sphere circumscribing the object. For typical imaging systems, the values of the radius of the antenna aperture, the extension of the object, and the distance between antenna aperture and the object are comparable; thus the radial sampling interval is on the order of $\lambda/2$.

In addition, we have to mention that combining ultra-wideband (UWB) techniques these sampling constraints could be relaxed to take sparse measurements without causing aliasing, especially when the fractional bandwidth is larger than 100%. This is due to the limited interference region of UWB pulses in the space domain [5]. To design a particular sparse sampling strategy for UWB systems involves the spatial sampling (or antenna array) optimization, which will be discussed in Chapter 5. For simplicity, in the following examples and analyses, we will use the equal-angular sampling strategy according to Nyquist criterion.

3.5 Numerical Simulation

In this section, numerical electromagnetic simulations were performed to demonstrate the effectiveness of the proposed approaches to fully polarimetric information retrieval and imaging. The simulation models were implemented with the applied EM simulation software FEKO in which the Method of Moments (MoM) solver is utilized to solve the integral equations. In the models, Hertz dipoles were used as transmitting and receiving antennas. The operational signal bandwidth was from 2 to 10 GHz. For comparison, simulations were carried out for both the proposed rotated arrays [Figures 3.1(a) and (b)] and their traditional counterpart (Figure 3.4) for fully polarimetric imaging. Due to the feature of the MoM solver, the EM simulations were implemented in the frequency domain. The synthetic data were

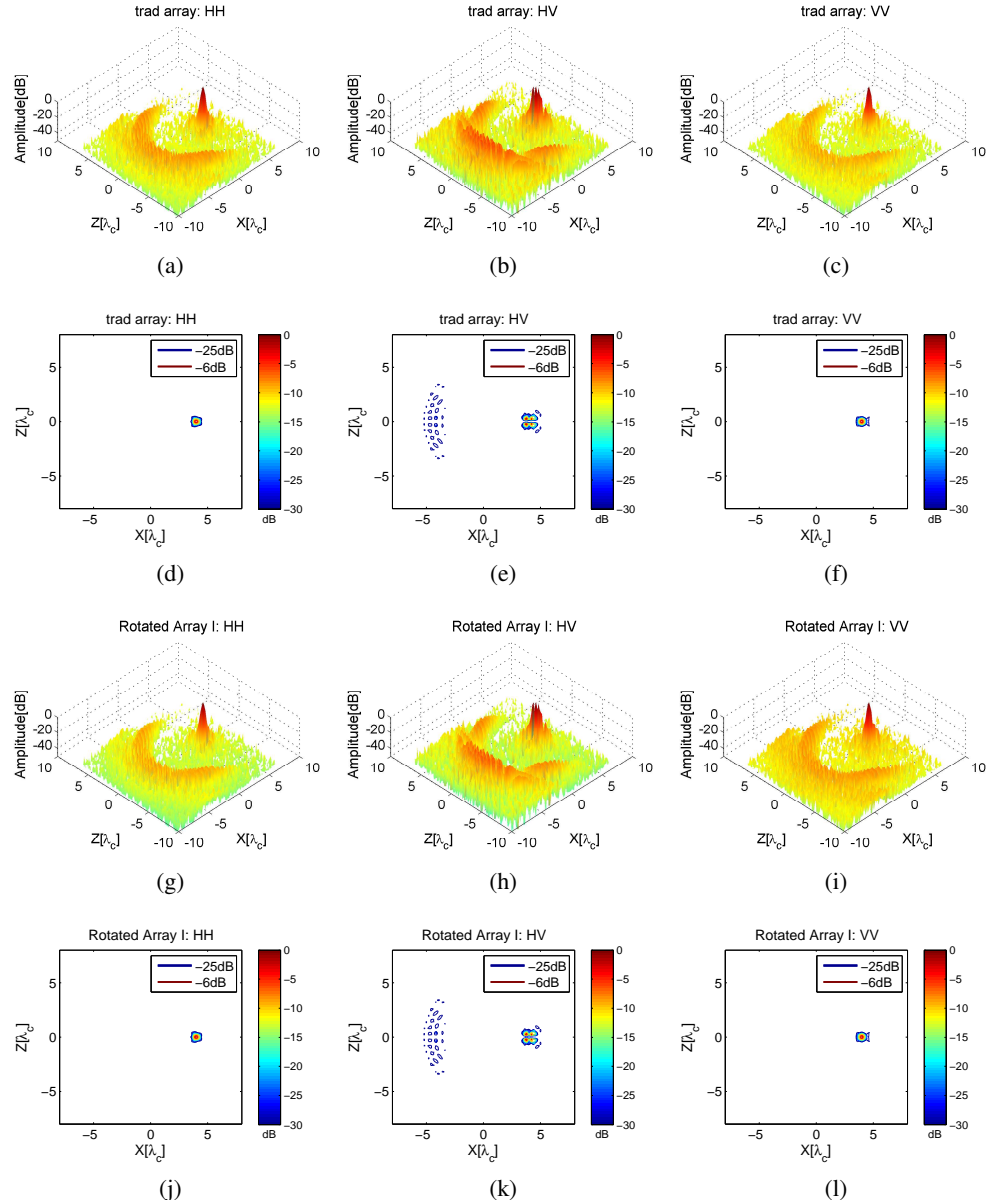
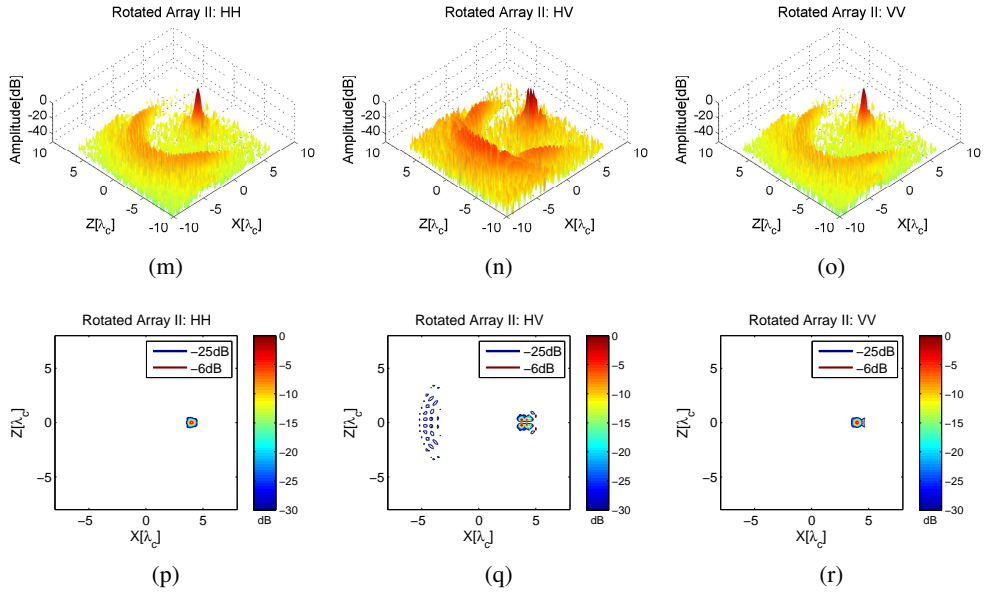


Figure 3.6: The normalized focused patterns of traditional and rotated arrays with focal point at $(4\lambda_c, 10\lambda_c, 0)$ for differently polarized signals. The focusing patterns of traditional array for: (a) HH polarization, (b) HV polarization, (c) VV polarization. (d), (e), and (f) Corresponding contour plots at -25 dB beamwidths. The focused patterns of Rotated Array I for: (g) HH polarization, (h) HV polarization, and (i) VV polarization. (j), (k), and (l) Corresponding contour plots at -25 dB beamwidths. (Legend of Fig 3.6 continued on next page)



(Legend continued from previous page)

The focusing patterns of Rotated Array II for: (m) HH polarization, (n) HV polarization, (o) VV polarization. (p), (q), and (r) Corresponding contour plots at -25 dB beamwidths. The ratios between the maximums of focused HH and HV patterns and between the maximums of focused VV and HV patterns are 16.4 and 16.6, respectively.

converted to the time domain by using the Fast Fourier Transform (FFT) after applying a Hanning window. Then the time-domain polarized data were focused using Kirchhoff migration (2.57) to obtain the fully polarimetric images of objects.

Both the traditional fully polarimetric arrays and the rotated arrays performed the same spatial sampling. In the rotated arrays, the antennas were placed on a series of concentric circles with the topologies in Figure 3.1. The radii of these concentric circles varied from 0.02 m to 0.5 m with intervals of 2 cm (i.e., $0.4\lambda_c$, where λ_c is the wavelength of the center frequency). In azimuth, the samples were taken every 4° over each circle. Then it resulted in a circular antenna aperture of radius 0.5 m (i.e., $10\lambda_c$). With the same spatial sampling intervals, the simulations were also conducted for the traditional fully polarimetric arrays (Figure 3.4). For convenience, the simulation parameters are summarized in Table 3.1.

To evaluate the imaging performance, the Point Spread Functions (PSF) of the traditional and rotated arrays for differently polarized signals are obtained by focus-

Table 3.1: Parameters for numerical simulations

Parameter	Value
Radius of antenna aperture	0.5 m
Sampling interval in radial direction	2 cm
Sampling interval in azimuth	4°
Operational frequencies	2–10 GHz
Frequency steps	100 MHz
Distance between target and antenna array	0.5 m

ing the scattered signals from a point-like target (i.e., a small sphere), and shown in Figure 3.6. The polarization effects on the focused patterns are noticeable. For all HH, HV and VV polarized signals, the nearly same PSFs were obtained for the three arrays. The sidelobes of the PSFs for differently polarized signals are all lower than -25 dB. However, slightly stronger sidelobes around the focal point can be seen in the PSFs of HV-pol signals [Figures 3.6(e), (k) and (q)]. As the cross-pol radiation pattern does not have main lobe but sidelobes, the cross-pol antenna picks up scattered energy via sidelobes when scatterers are off the broadside direction of the antennas. Thus, it results in relatively stronger sidelobes of the cross-pol PSF compared to that of the co-pol components. In addition, we have to mention that the equal-angle sampling of rotated arrays causes a non-uniform distribution of the samples in the synthetic aperture where the sampling distance depends on the radius. The non-uniform distribution of samples inherently introduces a space-tapering and may influence the resolutions of a target. To tackle this effect, the samples were weighted by the effective area (e.g., the areas of Voronoi cells) surrounding them within the aperture in the imaging process. That is to say, smaller weighting factors were imposed on the densely sampled region while larger weighting factors were used for relatively sparse samples within the aperture. This technique has been utilized for image formation in all experiments in this chapter.

Next, a numerical simulation was performed for a complex “E”-shaped perfect electric conductor (PEC) object that was placed in front of the antenna array at a distance of 0.5 m (i.e., $10\lambda_c$) in free space. The “E”-shaped object is illustrated in Figure 3.7, which contains a vertical column of the length 15 cm, a horizontal bar of the length 10 cm in the middle and two inclined bars joined with the vertical column at the two ends. The two inclined bars were 10 cm in length and rotated 30° away from the horizontal direction. The width and thickness of all the parts

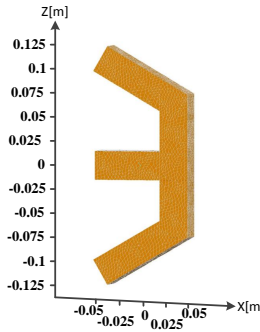


Figure 3.7: The “E”-shaped object used in the simulation

of the “E”-shaped object were 3 cm. The synthetic data with rotated arrays and traditional arrays at 2 GHz are shown in Figure 3.8. For simplicity of notation, the polarizations of the measurements of rotated arrays at each spatial position are defined with respect to the local radius: (1) PP, where the antenna axis is parallel to the radius; (2) NN, where the antenna axis is perpendicular (normal) to the radius; (3) DD, where the antenna axis forms an angle of 45° with the radius; (4) LX, i.e., the local cross-pol measurements which are only acquired by Rotated Array I.

3.5.1 Full-polarimetric Imaging with Rotated Arrays and Traditional Polarimetric Arrays

Using (3.16) and (3.17), the polarimetric (i.e., HH, HV(VH), and VV-pol) signals were retrieved from the synthetic signals collected by rotated arrays and denoted as E_{HH}^{rti} , E_{HV}^{rti} and E_{VV}^{rti} , where the superscript rt refers to “retrieved” signals and $i \in \{1, 2\}$ indicates Rotated Array I or II. Arbitrarily choosing a spatial sample position within the aperture, the retrieved time-domain signals are shown in Figure 3.9. Here the selected spatial position is (0.3 m, 236°). In addition, the polarimetric signals E_{HH}^m , E_{HV}^m and E_{VV}^m acquired with traditional arrays are displayed as references. The differences between the retrieved signals and their corresponding references are presented in Figures 3.9(d), (e) and (f).

Firstly, from Figures 3.9(a)–(c), one can see that the retrieved polarimetric signals with both Rotated Array I and II agree very well with their references at all three positions. It is confirmed by the small differences between the retrieved and reference signals in Figures 3.9(d) till (f) where the relative differences observed are generally smaller than 0.5%. So both Rotated Array I and II provide the capability

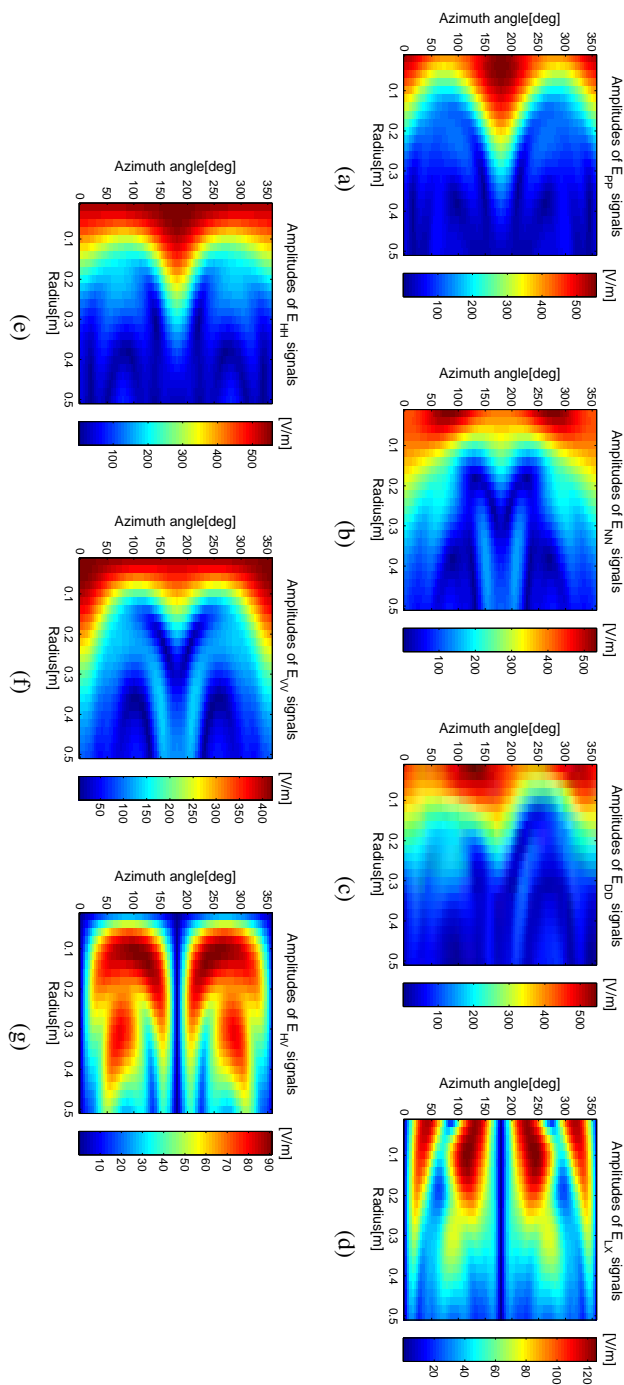


Figure 3.8: Amplitudes of the signals acquired with rotated arrays and traditional polarimetric arrays at $f = 2\text{ GHz}$: (a), (b) and (d) show the amplitudes of PP-, NN- and LX-pol measurements obtained with Rotated Array I; (a), (b) and (c) show the amplitudes of PP-, NN- and DD-pol signals acquired with Rotated Array II; and (e), (f) and (g) are the amplitudes of HH, VV and HV signals obtained with traditional polarimetric arrays.

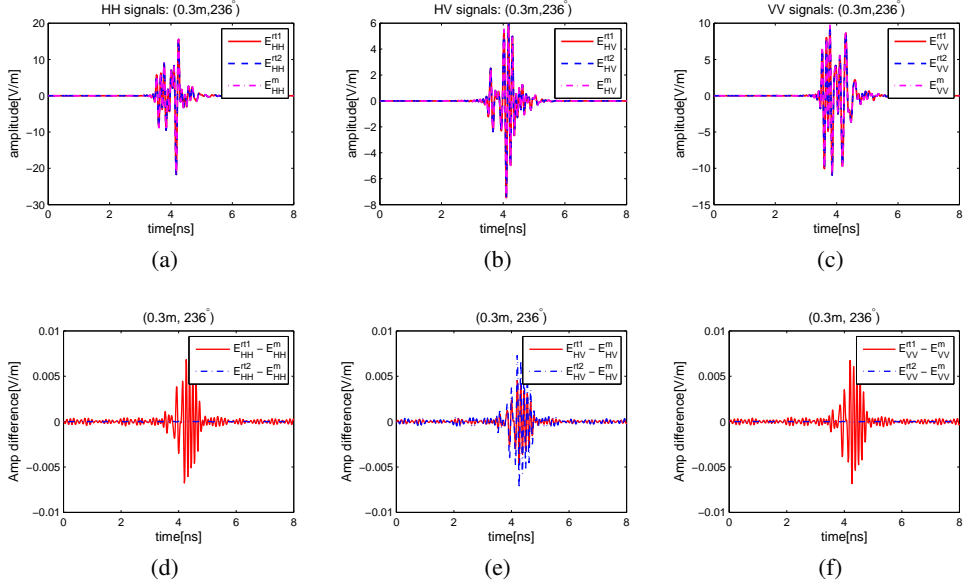


Figure 3.9: Comparison of the retrieved signals with the rotated arrays and the measured signals with traditional array at the position (0.3 m, 236°). (a), (b) and (c) show the measured and retrieved signals while their corresponding differences are presented in (d), (e) and (f).

to estimate the full-pol signals from their measurements with sufficient accuracy compared to the traditional full-pol arrays.

However, some subtle differences between the two rotated arrays are also perceived in terms of the accuracies of the retrieved signals. Based on Figures 3.9(d) and (f), one can see that the co-pol (i.e., HH- and VV-) signals retrieved with Rotated Array I exhibit larger differences than those with Rotated Array II relative to the reference signals. On the other hand, the differences between the cross-pol signals retrieved with Rotated Array I and the reference are slightly smaller than that between the cross-pol signal retrieved with Rotated Array II and the reference one at the position (0.3 m, 236°). So Rotated Array I provides slightly better or comparable estimation for the HV-pol signals in contrast to Rotated Array II. Moreover, it can be seen that the differences between the polarized signals retrieved with Rotated Array I and the corresponding references are relatively comparable. By contrast, with the measurements of Rotated Array II, the co-pol signals are more accurately estimated than the cross-pol one.

To quantitatively analyze the accuracy of the retrieved signals, we introduce the

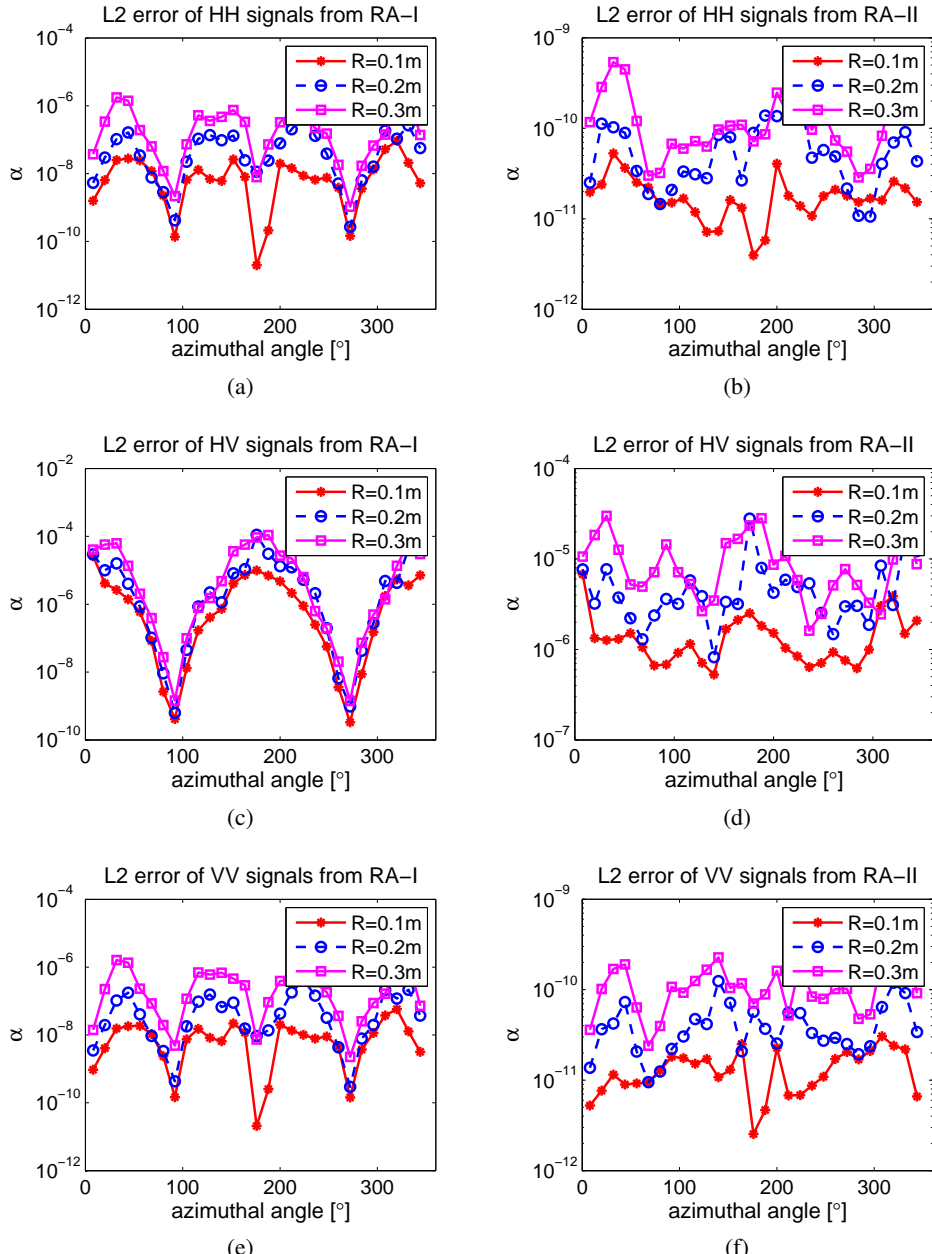


Figure 3.10: Relative errors of the retrieved polarimetric signals on three circles (i.e., $R = 0.1\text{ m}$, 0.2 m and 0.3 m) within the synthetic aperture. (a), (c) and (e) show the L_2 relative errors of the HH-, HV- and VV-signals retrieved with Rotated Array I; (b), (d) and (f) show the L_2 relative errors of the corresponding signals estimated with Rotated Array II.

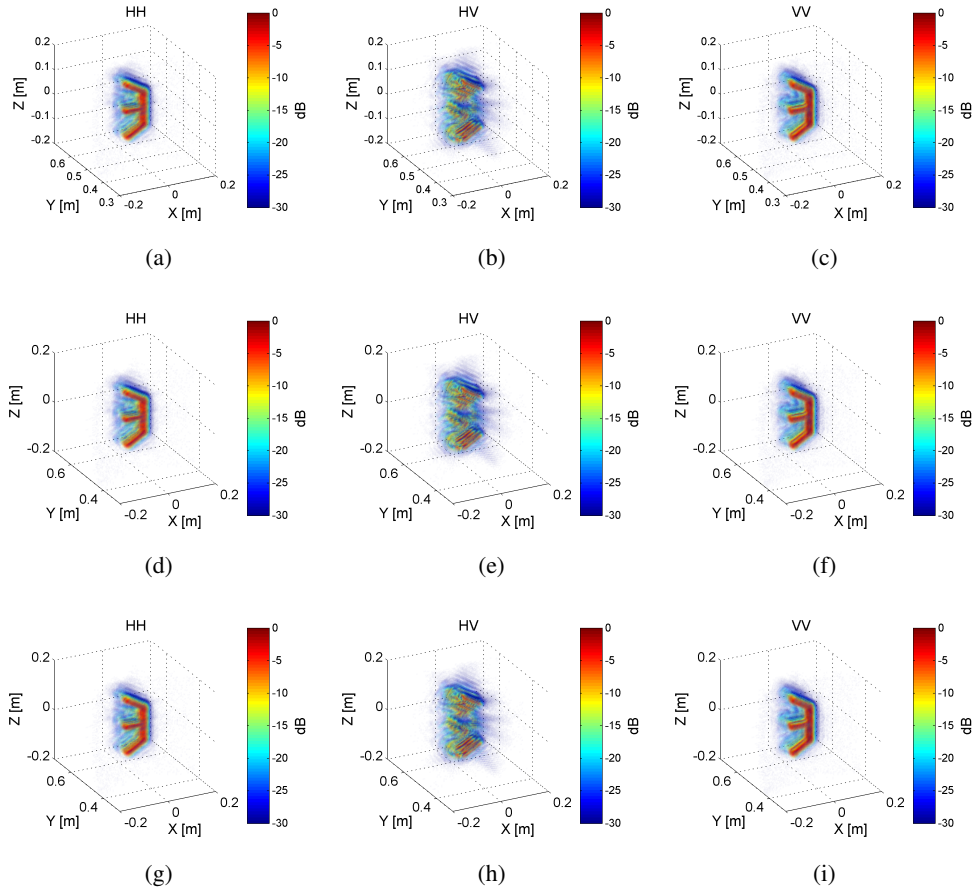


Figure 3.11: Polarimetric images reconstructed from the measurements of the three antenna arrays. (a), (b) and (c) are obtained with Rotated Array I; (d), (e) and (f) are obtained with Rotated Array II; and (g), (h) and (i) are obtained with traditional antenna arrays.

L_2 relative error as a metric that is defined as the energy of the differential signal divided by the energy of the reference signal acquired with traditional arrays

$$\alpha = \frac{\sum_{k=0}^N |E^{rt}(t_k) - E^m(t_k)|^2}{\sum_{i=0}^N E^m(t_i)^2} \quad (3.20)$$

where N is the number of discretized samples of the signal. One can see that the smaller the differences between the retrieved signal $E^{rt}(t)$ and the reference signal

$E^m(t)$, the closer α to zero; thus the more accuracy the retrieved signal.

Figure 3.10 illustrates the relative errors of the full-pol signals estimated from the measurements of Rotated Array I and II on three circles (i.e., $R = 0.1$ m, 0.2 m and 0.3 m) within the synthetic aperture. In general, considerably small relative errors are observed for the polarized signals retrieved with both rotated arrays (i.e., less than 10^{-4}). However, some differences are also found between the relative errors of the signals retrieved with the two rotated arrays as well as among the differently polarized signals. Comparing Figures 3.10(a), (e) with (b) and (f) respectively, one can see that the relative errors of the co-pol signals estimated with Rotated Array II are much (i.e., about two or three orders of magnitude) smaller than that of the co-pol ones retrieved with Rotated Array I. On the other hand, the accuracy of the HV signals estimated with Rotated Array I is slightly better or comparable to that obtained with Rotated Array II.

Moreover, for differently polarized signals obtained with Rotated Array I, their relative errors are more or less at the same level. However, with Rotated Array II, the relative errors of the estimated HV signals are much larger than that of the co-pol ones [see Figures 3.10(b), (d) and (f)], which has been noticed in Figure 3.9 as well. This can be explained as follows. As the relations (3.16) and (3.17) used for full-pol signal retrieval were derived based on the Born approximation, so they are accurate for weak and point-like scatterers. But for distributed targets and strong scatterers, these relations are only approximate. In our simulation, an extended “E”-shaped object was used, which is a strong scatterer. Rotated Array I acquires two co-pol and one cross-pol signal in terms of the ‘local’ polarization basis. Then using (3.16) and algebraic theory, relatively uniform differences result for all retrieved polarized signals. On the other hand, Rotated Array II measures three co-pol signals scattered from the targets. Since two of the co-pol measurements are the same as the co-pol ones measured by Rotated Array I, the third co-pol (i.e., DD) measurement provides some redundancy about the co-pol components scattered from the target. So, applying (3.17) to the measurements of Rotated Array II, relatively higher accuracies are achieved for the co-pol signal estimation than for the cross-pol ones. Furthermore, Rotated Array I takes a local cross-pol measurement instead of a third co-pol one, which improves the accuracies of the HV signal estimations, for instance, at the positions from 60° to 120° and from 240° to 310° in azimuth compared to Rotated Array II [see Figure 3.10 (c)]. But at the positions from 0 to 30° and from 160° to 190° , the accuracies of the signals obtained with Rotated Array I are slightly worse than those acquired with Rotated Array II. So, Rotated Array I is not definitely superior to Rotated Array II in terms of the accuracy of the estimated

Table 3.2: The accuracy of the polarimetric images of “E”-shaped object obtained with the rotated arrays and the traditional arrays.

		HH	HV	VV
Rotated Array I	L_2 error	5.8479e-8	7.5763e-6	6.0008e-8
	L_∞ error	2.5080e-4	2.9873e-3	2.7552e-4
Rotated Array II	L_2 error	1.0163e-12	5.3444e-6	9.8370e-13
	L_∞ error	2.8061e-7	2.8859e-3	3.1629e-7

HV signals but the accuracies of the signals retrieved with Rotated Array I have a relatively larger variation. Nevertheless, with both rotated arrays the relative errors of the estimated signals are sufficiently small [about 10^{-4} in Figure 3.10(c)] so that they are practically negligible for object imaging.

After imaging operation with the Kirchhoff migration [1], the accurately retrieved polarimetric signals lead to almost identical images as those generated by the reference polarimetric signals (Figure 3.11). The images formed with the two rotated arrays and the traditional arrays reveal the similar polarization dependence of different parts of the target. For example, the horizontal bar shows higher amplitudes in the HH-pol images while the vertical column is highlighted in the VV-pol images. In the HV-pol images, the inclined bars are well reconstructed and exhibit stronger scattering properties than other parts. The similarities of the corresponding polarimetric images obtained with the three arrays can also be quantitatively examined via the L_2 and L_∞ relative errors. The L_2 relative error is defined as in (3.20) but the time-domain samples of signals are replaced by the voxels of images. The L_∞ relative error is defined as the maximum difference between the voxel values of a polarimetric image and its reference divided by the maximum voxel value of the reference image. The relative errors for the images of the “E”-shaped object are listed in Table 3.2. According to Table 3.2, one can see that the L_2 and L_∞ errors of the images obtained with the two rotated arrays are smaller than 5×10^{-5} and 5×10^{-3} , respectively. Therefore, both Rotated Array I and II provide sufficient accuracy for fully polarimetric imaging. Moreover, the relative errors of the HV-pol images acquired with both rotated arrays are on the same order of magnitude. For different polarimetric images acquired with Rotated Array I, both L_2 and L_∞ errors are relatively uniform while relative errors with different orders of magnitude are obtained for co-pol and cross-pol images with Rotated Array II, which are consistent with the observations about the differences between the retrieved polarimetric signals and their references.

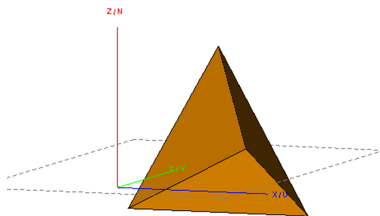


Figure 3.12: Geometrical configuration and corner reflector used for simulation.

Table 3.3: The accuracy of the polarimetric images of the trihedral corner reflector obtained with the rotated arrays and the traditional arrays.

		HH	HV	VV
Roated Array I	L_2 error	1.6374e-6	2.6249e-5	1.6333e-6
	L_∞ error	5.5975e-4	3.89e-3	5.4874e-4
Rotated Array II	L_2 error	2.1335e-13	1.733e-5	2.1401e-13
	L_∞ error	3.0898e-8	3.578e-3	3.2136e-8

In addition, comparing the co-pol measurements of Rotated Array II and the signals recorded by traditional arrays in Figure 3.8, one can see that the amplitudes of co-pol signals measured with Rotated Array II are generally larger than that of cross-polarized signals recorded with the traditional array. So considering the same noise level, Rotated Array II could acquire signals with low susceptibility to noise.

To further examine the accuracy of the full-pol imaging for strong scattering objects with the rotated arrays proposed, one more simulation was carried out with a trihedral corner reflector (TCR) in free space. We took the parameters listed in Table 3.1 for the antenna arrays except that the operational bandwidth was 2–12 GHz. The antenna arrays were located on the xoz plane and centered at the origin. A TCR was placed at a distance of 0.4 m from the corner point to the antenna array. The TCR contains three surfaces that are mutually perpendicular and their intersecting sides are 15 cm in length. Figure 3.12 shows the geometrical configuration. Again, the EM data were synthesized with the EM software FEKO for the three antenna arrays. Then the signals acquired with Rotated Array I and II were used to estimate the fully polarimetric signals via (3.16) and (3.17). Comparing the estimated polarized signals with the references acquired by the traditional full-pol arrays, the similar phenomenon was observed as for the “E”-shaped object: the errors of the co-pol signals estimated with Rotated Array I are larger than those of their counter-

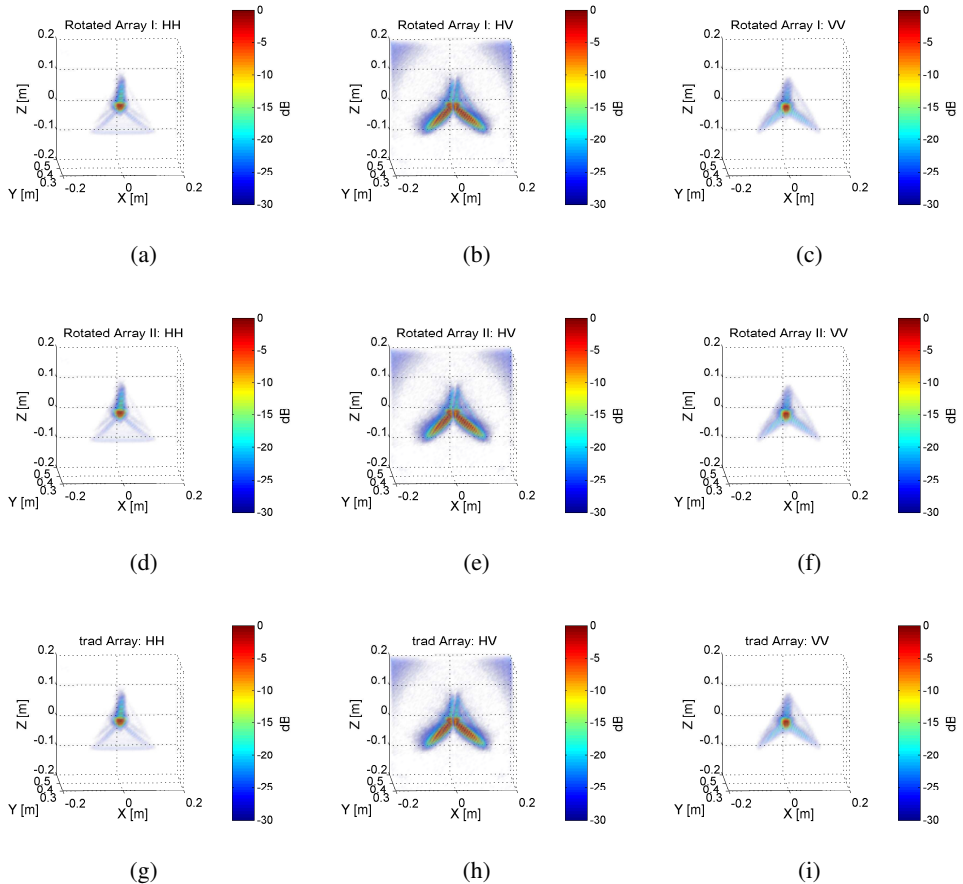


Figure 3.13: Full-polarimetric images reconstructed from the measurements of the three antenna arrays. (a), (b) and (c) are obtained with Rotated Array I; (d), (e) and (f) are obtained with Rotated Array II; and (g), (h) and (i) are obtained with traditional antenna arrays.

parts estimated with Rotated Array II; by contrast, the cross-pol signals estimated with Rotated Array I are slightly more accurate than that with Rotated Array II relative to the references. To make the text compact, these figures are omitted here.

Focusing the polarimetric signals estimated from the measurements of the two rotated antenna arrays as well as collected by traditional full-pol arrays, the polarimetric images of the TCR were reconstructed, as shown in Figure 3.13. Firstly, one can see that in Figure 3.13 all the images are well focused, and different scat-

tering characteristics of the TCR are revealed in the HH-, HV- and VV-polarized images. Specifically, the edge of the bottom surface is well reconstructed in the HH-polarized images while the edges of the two top surfaces are clearly presented in the VV-polarized images. Meanwhile, the HH- and VV-polarized images distinctly show the three intersecting sides of the surfaces and the corner point appears as the brightest spot. In the HV-polarized images, the two bottom intersecting sides demonstrate the strongest cross-polarization effects with the orientation of the TCR placed in the simulation. As its projection on the antenna aperture is a vertical line, the top intersecting side induces negligible cross-polarized signals. Thus, it is missing in the focused HV-polarized images [i.e., the middle gaps in Figures 3.13(b), (e) and (h)]. Comparing the polarized images in each column, the HH-, HV- and VV-polarized images obtained with the two rotated antenna arrays and the traditional arrays are visually equivalent. The relative errors of the reconstructed images were also analyzed with respect to the reference images, and the results are listed in Table 3.3. Similar to the “E”-shaped object case, Rotated Array I achieves roughly similar L_2 and L_∞ errors for different polarimetric images while the relative errors of HH- and VV-pol images obtained with Rotated Array II are much smaller than that of the HV-pol image. But the accuracies of the HV-pol images acquired with Rotated Array I and II are comparable (i.e., about 10^{-5} for L_2 error and 10^{-3} for L_∞ error). Therefore, both Rotated Array I and II achieve sufficient accuracies, even for strong scattering objects, for full-pol imaging although some subtle differences are perceived in the relative errors of their full-pol images.

3.5.2 Polarimetric Imaging vs Scalar-wave-based Processing

In the two proposed antenna arrays, antennas placed on three radii are needed to obtain three differently polarized measurements at each spatial position for the fully polarimetric signal retrieval and imaging. In practical imaging systems, due to the constraints of cost and system complexity, sometimes only the antennas along a single radius can be employed to acquire, for instance, PP- or NN-polarized signals. Thus, the polarizations of the EM signals acquired are varying within the aperture. For these polarization-varied EM data, generally two types of imaging approaches can be applied for image formation: (1) scalar-wave based imaging algorithms, for example, the Kirchhoff migration in (2.57) and the range migration algorithm in (2.62). These algorithms focus the PP (NN)-pol signals recorded by the rotated arrays to form images by ignoring the variations of antenna polarizations during the signal acquisition. They are usually very efficient but assume the polarizations of EM signals are constant within the antenna aperture. So using these algorithms

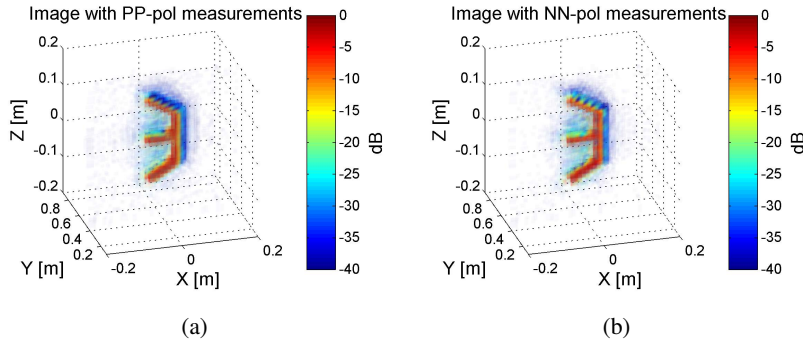


Figure 3.14: Images obtained with scalar wave processing for: (a) measurements acquired with antennas of polarizations parallel to the radius (PP-pol); (b) measurements acquired with antennas of polarizations normal to the radius (NN-pol).

for image formation may lead to the loss of polarimetric information of targets or even degrade the qualities of focused images. (2) inversion based algorithms. Accounting for the vectorial nature of the EM signal, inversion based algorithms could result in better image qualities compared to the scalar-wave based ones, which will be discussed in detail in Chapter 4.

In this section, the scalar-wave based algorithm, i.e., Kirchhoff migration is used to focus PP (NN)-pol signals, and the effects of the variations of signal polarizations on the imaging performance are discussed by comparing the results of fully polarimetric imaging with rotated arrays, scalar-wave based imaging with varied polarizations (SWVP for short), and scalar-wave based imaging with aligned polarizations (SWAP for short). The synthetic data for the ‘‘E’’-shaped object was used.

Figure 3.14 presents the images reconstructed with PP- and NN-polarized signals by Kirchhoff migration. To facilitate the comparison, the HH, HV and VV polarimetric images in Figure 3.11 are integrated by assigning the backscattering matrices HH, HV and VV directly to red, green and blue components (i.e., Lexicographic color coding) to obtain a pseudocolor image. For the convenience of visualization, Figure 3.15 shows the slices at $y = 0.5$ m of the 3-D images obtained by SWAP (i.e., HH and VV), SWVP (i.e., PP and NN) and fully polarimetric imaging. One can see that the shape of the target is relatively well reconstructed in all the slice images. As expected, in the HH- and VV-pol images the horizontal and vertical parts of the targets show higher amplitudes than the rest. In contrast,

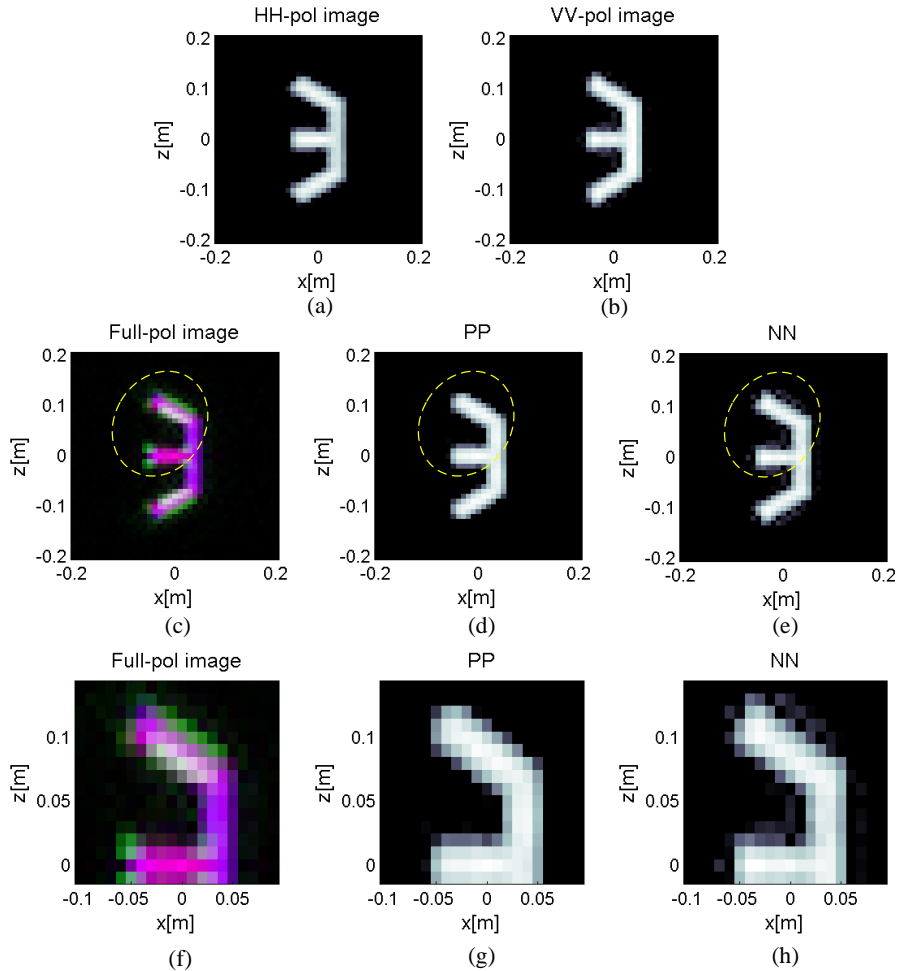


Figure 3.15: Slices of the reconstructed volumetric images at $y = 0.5$ m by fully polarimetric imaging and scalar-wave based imaging. (a) and (b) are the slices of HH- and VV- images with traditional arrays (i.e., SWAP images); (c) is the slice of the integrated polarimetric image obtained with a rotated array; (d) and (e) are the slices of scalar-wave based images with PP- and NN-polarized signals (i.e., SWVP images), respectively; (f), (g) and (h) are the close-ups of the areas indicated by dashed ellipses in (c), (d) and (e).

SWVP with PP- and NN-polarized signals generates more uniform images of targets compared to the SWAP images (i.e., HH and VV images) as the PP- or NN-polarized signals contain various co-pol information scattered from different parts of the target. However, more artifacts are observed surrounding the reconstructed target profile in the image of SWVP with NN-polarized signals. Moreover, as HH, HV and VV images are obtained and integrated into the fully polarimetric image, more scattering features of the target, besides its shape, can be distinguished from the pseudocolor images, e.g., edge and sharp corner diffraction indicated in green. This can be explained by the fact that the edges and corners cause cross-polarization of the incident waves and generate strong cross-polarized (HV) backscattered signals. Comparing Figures 3.15(c), (d) and (e), the pseudocolor image is superior to the SWVP images with PP- and NN-pol signals in terms of some details about the target structure, specifically, the regions circled by dashed ellipses. The edge of the inclined bar is more clearly formed in the pseudocolor image than in the SWVP images [see Figures 3.15(f)–(h)]. The same phenomenon can be observed for the edges of the horizontal bar. In Figure 3.15 (c), the horizontal bar in the middle and the vertical column are displayed in different colors, which also demonstrate the distinct polarization dependence of their scattering properties. So, through different processing and visualization techniques, polarimetric images provide various polarimetric characteristics of targets and abundant scattering information for target discrimination and identification compared to the SWAP and SWVP images.

3.6 Experimental Results

Experimental measurements in free space were also performed to further demonstrate the effectiveness and accuracy of the proposed arrays for fully polarimetric imaging. The experimental setup for the rotated arrays (i.e., Rotated Array I and II) is shown in Figure 3.16(a). To simulate the rotated arrays, a stepper motor was used to drive a vertical column on top of which a polyethylene plastic panel was mounted to support antennas. The stepper motor was precisely controlled by a computer for positioning and rotating the column. Antipodal Vivaldi antennas [6] were used for transmission and reception and connected to a Vector Network Analyzer (VNA) for signal acquisition in the frequency domain. As the monostatic radar configuration was considered, at each spatial sampling position S_{11} was measured to get the co-pol components for all three antenna arrays while S_{21} was measured to get the cross-pol components with a quasi-monostatic configuration where a transmitting antenna and a receiving antenna were placed with a separation of 6 cm. The

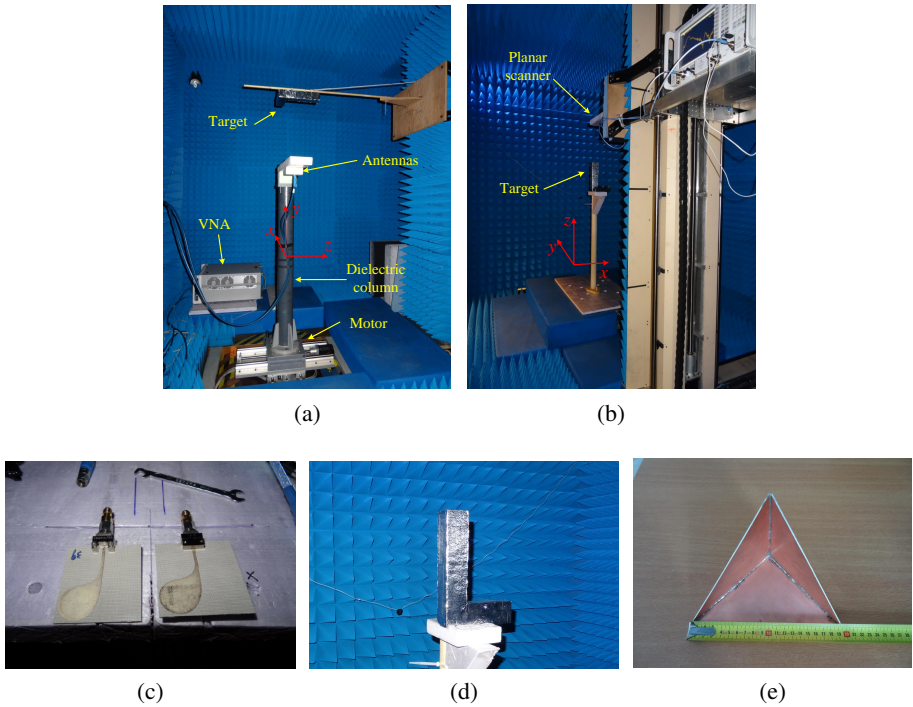


Figure 3.16: The experimental setups for rotated arrays and traditional planar arrays. (a) is the setup for the rotated arrays and (b) for the traditional planar array. (c) shows the employed antipodal Vivaldi antennas. (d) and (e) display the “L”-shaped object and the trihedral corner reflector used for the experiments, respectively.

operational frequencies swept from 3 to 15 GHz with steps of 20 MHz. Through the translation and rotation of the vertical column, the antennas measured the data over 15 circles of the radii ranging from 11 to 53 cm with steps of 3 cm (i.e., $0.9\lambda_c$) and the azimuth sampling interval $d\theta$ along each circle was 1.2° . So a planar circular array of the radius 0.53 m (i.e., $15.9\lambda_c$) was synthesized. An “L”-shaped distributed target which was coated with aluminum foil was placed at a distance of 0.5 m (i.e., $15\lambda_c$) in front of the center of the ‘equivalent’ circular array for the test [Figure 3.16(d)]. The two arms of the “L”-shaped object are about 20 and 30 cm in length, respectively. Their width and thickness are 6 cm and 5.5 cm. Arranging antennas with orientations as required by the two rotated arrays and repeating the measurements over the same sampling grid, then the corresponding polarized signals, i.e., PP-, NN-, DD- and LX-polarized signals were acquired at each sampling

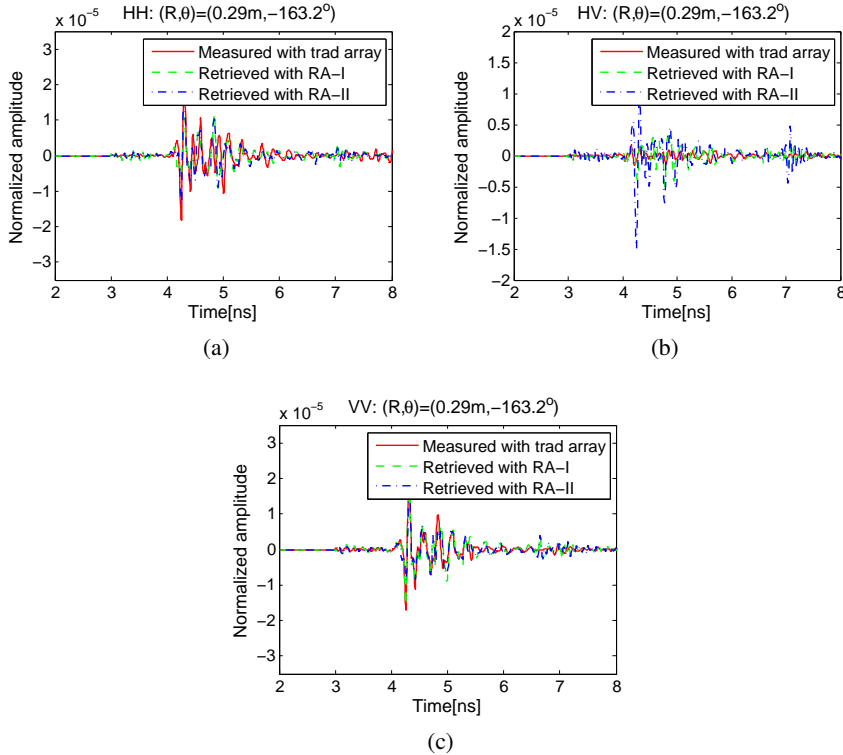


Figure 3.17: Comparison of the retrieved polarimetric signals and the reference ones at the position $(R, \theta) = (0.29 \text{ m}, -163.2^\circ)$. (a) HH-polarized signals, (b) HV-polarized signals, and (c) VV-polarized signals. The scattered signal spectrum was normalized with respect to the transmitted one.

position.

For comparison, the reference HH-, HV- and VV-pol signals were also measured with the traditional polarimetric arrays over the same sampling grid, which was implemented with the planar scanner [Figure 3.16 (b)]. The signals scattered from the background were also measured in the absence of the target with all three arrays. Applying the Hanning window to all the signals measured in the frequency domain and taking the inverse FFT, the time-domain scattered signals were obtained. After background subtraction, the EM signals scattered from targets were extracted.

Taking advantage of (3.16) and (3.17), the HH-, HV- and VV- signals were retrieved from the measurements of the two rotated arrays. As an example, the

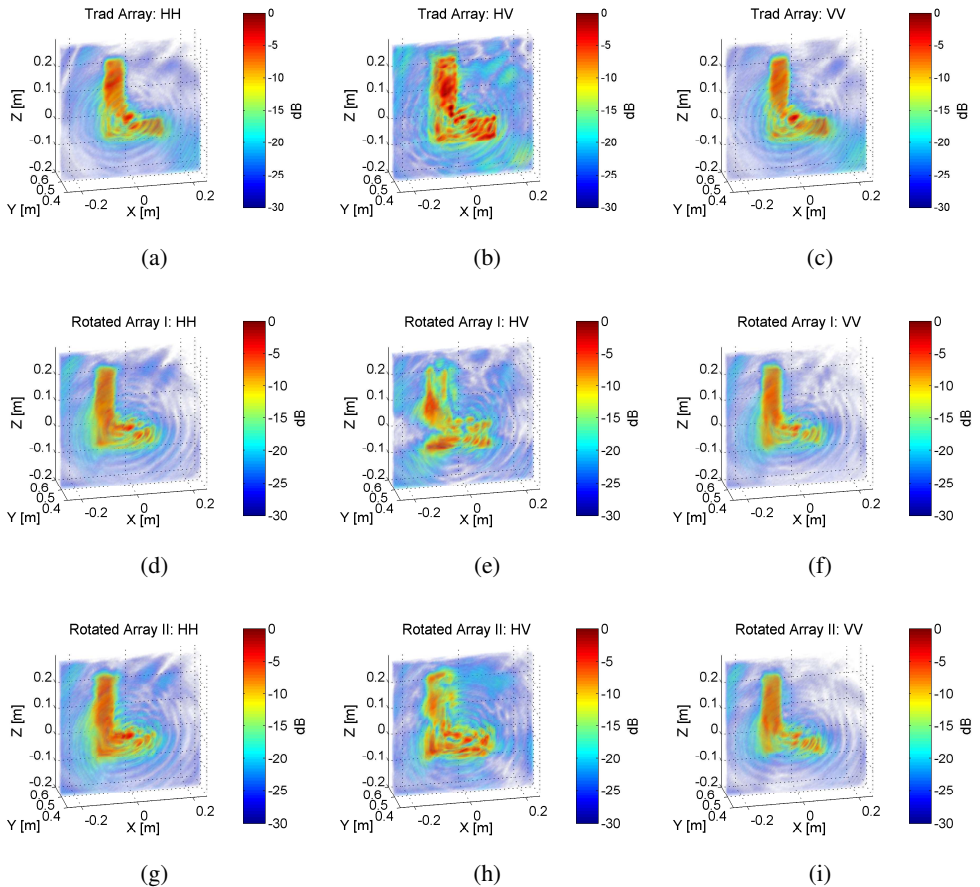


Figure 3.18: The HH, HV and VV polarimetric images obtained with: (a)–(c) traditional array; (d)–(f) Rotated Array I; and (g)–(i) Rotated Array II.

retrieved signals at $(R, \theta) = (0.29 \text{ m}, -163.2^\circ)$, as well as the corresponding reference signals, are shown in Figure 3.17. To suppress the strong antenna reflections, time clipping was used for the signals in the first three nanoseconds. In Figure 3.17, the full-pol signals retrieved with the two rotated arrays have relatively good agreements with the HH-, HV- and VV-polarized reference signals in terms of the wavelets. Focusing both the retrieved and reference polarized signals, the reconstructed polarimetric images are presented in Figure 3.18. It can be seen that the major features of the target are well reconstructed with all the three antenna arrays.

The corresponding polarimetric images are in good agreement. Specifically, the polarization dependence of the horizontal and vertical part of the “L”-shaped target is clearly visible in the HH- and VV-polarized images, respectively. Meanwhile, the edges of the target can be perceived in the HV images.

However, some discrepancies are observed between the amplitudes of the retrieved and reference signals in Figure 3.17 as well as between the images in Figure 3.18. In particular, relatively larger discrepancies between the cross-pol images [i.e., Figures 3.18(b), (e) and (h)] obtained with the traditional arrays and the rotated arrays are seen compared to that between the co-pol images. As the cross-pol signals acquired with traditional full-pol arrays are measured with slightly separated transmitting and receiving antenna pairs (i.e., bistatic configuration), then not only the edges and corners of the target but also the flat surface exhibit high intensity in the reference HV image [Figure 3.18(b)]. By contrast, the HV images obtained with the two rotated arrays demonstrate the cross-polarization features of the target as theoretically expected, where the edges and corners are mainly reconstructed. So the two rotated arrays enable to effectively reconstruct both the co- and cross-pol images of the target. Furthermore, small differences between the HV images acquired with the two rotated arrays [Figures 3.18(e) and (h)] are also noticed. These differences might be induced by the non-purity of the linear polarization of antipodal Vivaldi antenna, especially for high frequencies. Due to this non-purity of the antenna polarization, the HV-polarized signal retrieved with the rotated array II may contain some co-pol components, which leads to its larger amplitude in Figure 3.17(b) (compared to that retrieved with rotated array I) and partially reconstructed flat surface in Figure 3.18(h) [in contrast to Figure 3.18(e)].

To clearly illustrate different polarization features of images in Figure 3.18, the color-coded slice images at the target position are shown in Figure 3.19. The horizontal and vertical bars are displayed in red and pink while the edges of the targets are represented in green where the cross-polarization effect induces the HV polarized signals. According to Figure 3.19, the pseudocolor images obtained with the rotated arrays reveal similar polarimetric features of the targets as that acquired with the traditional full-pol imaging arrays. Hence, the two rotated arrays provide comparable imaging performance as the traditional polarimetric arrays.

Using the same experimental setups for both the rotated and traditional polarimetric arrays, a TCR was used as a strong scattering object for a second experimental measurement. The edges of the TCR are about 19.7 cm in length, as shown in Figure 3.16(e). The TCR was placed in front of the antenna aperture at a distance of 0.5 m. After performing the same experimental measurement operations and image

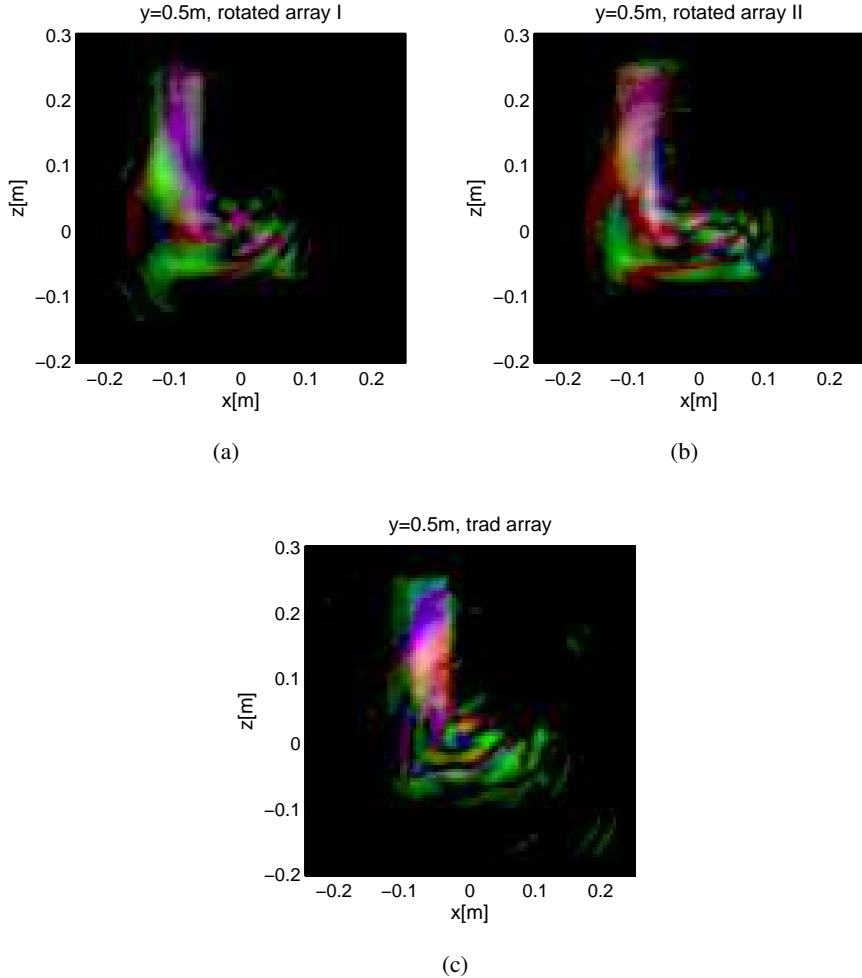


Figure 3.19: Pseudocolor slice images at the target position obtained with (a) rotated array I, (b) rotated array II, and (c) traditional array with dynamic range of 15 dB. Lexicographic color coding is used for visualization (HH: Red; HV: Green and VV:Blue).

formation as for the ‘‘L’’-shaped object, the fully polarimetric images of the TCR with the three antenna arrays are obtained, which are shown in Figure 3.20.

It can be seen that both rotated antenna arrays reconstruct the comparable polarimetric features of the TCR in the corresponding images in contrast to the tra-

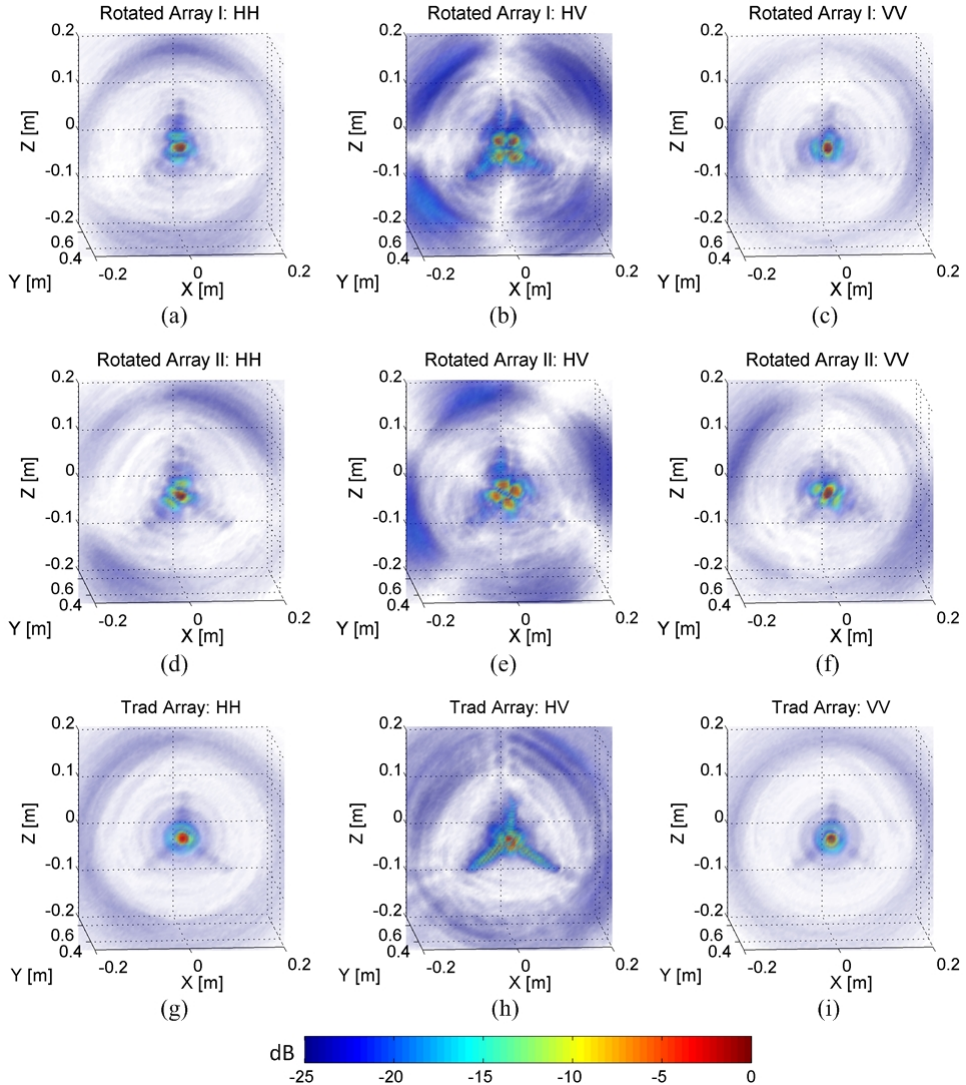


Figure 3.20: Three dimensional polarimetric images of a trihedral corner reflector obtained with the experimental measurements of the three antenna arrays. (a)–(c) are the HH-, HV- and VV-pol images obtained with Rotated Array I; (d)–(f) are obtained with Rotated Array II; and (g)–(i) are obtained with the traditional antenna arrays.

ditional arrays. However, some differences are still noticeable between the polarimetric images formed with the two rotated arrays. Visually, Rotated Array I

achieves slightly better fully polarimetric images in terms of the similarity to those obtained with the traditional arrays. Specifically, in both HH- and VV-pol images obtained with Rotated Array II the edges along the z -axis direction are much weaker than that in the corresponding images of Rotated Array I. Moreover, the cross-pol image focused with Rotated Array II [Figure 3.20(e)] is slightly asymmetric with respect to the xoy plane compared to the one obtained with Rotated Array I [Figure 3.20(b)]. Meanwhile, the sidelobes/artifacts surrounding the images of the TCR seem slightly rotated. These may be caused by non-purity of the linear polarization of the antipodal Vivaldi antenna used for the measurement, as mentioned above. As a consequence, the cross-pol signals were inaccurately estimated with the measurements of Rotated Array II. However, in Rotated Array I, the cross-pol signals were measured with two orthogonally oriented Vivaldi antennas at each spatial position, which to some extent mitigates the effect of the non-purity of their linear polarization on the HV-pol signal estimation.

Furthermore, although a well-reconstructed HV-pol image is obtained with the traditional array through a quasi-monostatic measurement configuration, the HV-pol image obtained with Rotated Array I [Figure 3.20(b)] reveals the slit induced by the intersecting side formed by the two top surfaces in a full agreement with the HV-pol images in Figure 3.13 obtained in the numerical simulations. This demonstrates further the effectiveness and accuracy of Rotated Array I for fully polarimetric imaging and indicates the relatively higher tolerance of Rotated Array I to the quasi-monostatic measurement configuration for full-pol imaging compared to the traditional fully polarimetric imaging arrays and Rotated Array II. This advantage could be very attractive for the implementation of practical full-pol imaging systems, especially in the circumstances where antennas with relatively lower cross-pol isolation are used.

3.7 Conclusion

In this chapter, fully polarimetric imaging with rotated antenna arrays has been investigated. The scattered signals for polarization-varied antennas (i.e., rotated antennas) are formulated under the Born approximation. This formulation reveals that the signals acquired by rotated antennas in a varied-polarization basis can always be expressed as a linear combination of the fully polarimetric signals measured in a fixed polarization basis. Utilizing this fact, two approaches to design rotated antenna arrays for full-pol signal acquisition and imaging are proposed, in which either two co-pol and one cross-pol signals or three co-pol signals are measured at

a sampling position. The rotated arrays designed with both approaches overcome the effects of the polarization variations on the fully polarimetric imaging that are encountered by the traditional rotated imaging arrays.

Numerical simulations and experimental results demonstrate the effectiveness and accuracy of the rotated arrays for fully polarimetric imaging. The numerical results show that the relative errors of all three polarimetric components retrieved with the rotated arrays are generally much smaller than 0.5% compared to their references acquired with traditional arrays, thus resulting in almost identical reconstructed volumetric images (L_2 error is smaller than 10^{-5} and L_∞ error is less than 10^{-3}). Although the rotated array that measures three co-pol signals at each position outperforms the one that records two co-pol and one cross-pol signals at a local polarization coordinate system in terms of the accuracy of the estimated co-pol signals, the rotated array with co- and cross-pol measurements achieves slightly more or equivalently accurate estimation of the cross-pol (i.e., HV) signals. Nevertheless, both rotated arrays provide the capability to retrieve the fully polarimetric (i.e., HH, HV, and VV) signals with sufficient accuracy, which facilitates the fully polarimetric imaging by using traditional scalar-wave-type algorithms on the three sets of polarimetric data. In addition, thanks to the RadSAR implementation, both rotated arrays provide cost-efficient solutions to 3-D fully polarimetric imaging, especially for the observations of small regions/volumes.

References

- [1] J. Wiggins, “Kirchhoff integral extrapolation and migration of nonplanar data,” *GEOPHYSICS*, vol. 49, no. 8, pp. 1239–1248, 1984.
- [2] J. M. Lopez-Sanchez and J. Fortuny-Guasch, “3-D radar imaging using range migration techniques,” *Antennas and Propagation, IEEE Transactions on*, vol. 48, no. 5, pp. 728–737, 2000.
- [3] J. Kruk, C. Wapenaar, J. Fokkema, and P. van den Berg, “Three-dimensional imaging of multicomponent ground penetrating radar data,” *GEOPHYSICS*, vol. 68, no. 4, pp. 1241–1254, 2003.
- [4] J. Wang, H. Cetinkaya, and A. Yarovoy, “On polar sampling of gpr for tunneling boring machine,” in *Ground Penetrating Radar (GPR), 2014 15th International Conference on*, pp. 330–333.

- [5] J. L. Schwartz and B. D. Steinberg, "Ultrasparse, ultrawideband arrays," *Ultrasonics, Ferroelectrics and Frequency Control, IEEE Transactions on*, vol. 45, no. 2, pp. 376–393, 1998.
- [6] X. Zhuge and A. Yarovoy, "Design of low profile antipodal vivaldi antenna for ultra-wideband near-field imaging," in *Antennas and Propagation (EuCAP), 2010 Proceedings of the Fourth European Conference on*, pp. 1–5.

4

Linear Inversion of Polarization-Varied EM Data

4.1 Introduction

The polarization variations of the rotated antenna arrays within the data acquisition aperture have been circumvented by specifically designed array topologies in Chapter 3. In that approach, three differently polarized signals have to be measured at each sampling position [1]. In that case, more antennas are required to construct the array system. However, this is not desirable or even unacceptable for some practical imaging systems (for example, GPR system for TBM) due to the constraint of limited space, cost, mass, etc. Therefore, to tackle the effect of the variation of antenna orientations via post-imaging process is of great importance. To this end, two physical phenomena need to be considered: spatial rotation of the antenna radiation patterns and rotation of the transmitted field polarization. Either both are assumed constant or their variations within array apertures are ignored in traditional scalar-wave-type imaging schemes.

Recently imaging with rotated antenna arrays has been discussed for near-field SAR imaging [2], subsurface object detection [3, 4], etc. However, the effects of the variations of antenna polarizations caused by the rotation were neglected and

Part of this chapter was published as: J. Wang, P. Aubry, and A. Yarovoy, "Efficient Implementation of GPR Data Inversion in Case of Spatially Varying Antenna Polarizations", *IEEE Transactions on Geoscience and Remote Sensing*, 2017, DOI: 10.1109/TGRS.2017.2779788.

the EM signals were treated as the scalar wave for imaging in these works. Considering the vectorial nature of the EM wavefield, in this chapter, the effects of the antenna polarization variations on the microwave imaging are partially overcome by exploiting the exact radiation patterns of the differently oriented antennas within the aperture.

In the past decades, many attempts have been made to get qualitatively improved or quantitatively correct microwave images by considering the effects of antenna radiation patterns and/or vector nature of the electromagnetic waves, especially for subsurface imaging [5–11]. The majority of these approaches are based on the far-field approximation of radiation patterns. For example, the far field radiation pattern of interfacial dipole antenna has been incorporated in Kirchhoff migration [5] and generalized Radon transform [6] for GPR data processing. In [7] and [8], the diffraction tomography is discussed based on the approximated Green’s function in the horizontal wavenumber-frequency domain. These approaches are mainly employed to process the single-component GPR data. Moreover, in [10], a matrix-based inversion approach was proposed to migrate multicomponent GPR data simultaneously by combining the far-field approximation of radiation patterns. Later this approach has been improved through the use of accurate radiation patterns computed with an FFT-based method [11]. However, all the aforementioned imaging approaches assume that the antenna orientations remain constant within the aperture for data acquisition. Namely, their radiation patterns are just linearly translated, i.e., space shift-invariant, which is critical for both radiation pattern computation and the wavenumber domain migration approaches. However, the space shift-invariant property of antenna radiation patterns is spoiled in rotated (or polarization-varied) antenna arrays. Thus, these imaging algorithms are not directly applicable for high-quality imaging with rotated antenna arrays.

In this chapter, microwave imaging with polarization-varied antennas over data acquisition aperture (for example, rotated antenna arrays) is formulated as a linear inverse problem based on the Born approximation. The effects of the variations of antenna polarizations within the aperture are tackled by exploiting the full-wave radiation patterns of antennas. Antennas are assumed to be dipoles (as a majority of widely used GPR antennas demonstrate dipole-like radiation patterns). Two operational circumstances of antennas are considered: free space and half space. In the free-space case, the radiation patterns of differently oriented antennas can be conveniently obtained through the dyadic Green’s function (GF) in the space-frequency domain. In the half-space case, analytically closed Green’s functions of a dipole antenna are not available in the space-frequency domain. The radiation patterns have

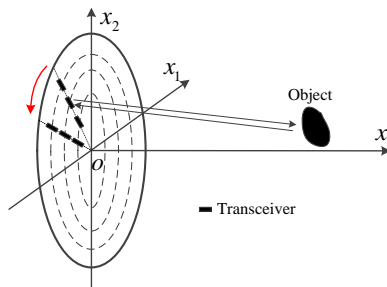


Figure 4.1: Geometrical configuration of 3-D imaging with a rotated antenna array. With the rotation of the linear array, the antenna polarizations constantly change.

to be computed from the wavenumber-frequency domain Green's functions. To get the full-wave radiation patterns (which are valid in near-, intermediate- and far-fields of the dipole) of differently oriented antennas, two methods were suggested to compute the accurate space-frequency domain Green's functions: interpolation based method and Nonuniform fast Fourier transform (NUFFT) based method. Both methods consider the effects of antenna translation and rotation within the aperture and are implemented in the space-frequency and wavenumber-frequency domains, respectively. After obtaining the full-wave radiation patterns for all the antennas, a linear system of equations between the spatial measurements and the scattering coefficients of scatterers can be established for linear inversion.

This chapter is organized as follows. The linear inversion signal model is formulated in section 4.2. In section 4.3, the exact Green's functions computation for rotated antennas are discussed and the fast computing methods are presented. Then some numerical and experimental imaging results are shown in sections 4.4 and 4.5. Finally, the chapter is summarized in the last section.

4.2 Signal Model

Assume the transmitting and receiving antennas (dipoles) are placed along a radial direction of a circular aperture on the vertical plane and their orientations are parallel to the radius, as shown in Figure 4.1. With the rotation of the circular aperture transmitting and receiving antenna arrays, the antennas illuminate the scene of interest and the scattered signals are acquired over the space. As a consequence, an equivalent circular antenna array is synthesized. Using the Born approximation, which we assumed to be valid, the scattered electromagnetic signals for a pair of

transmitting and receiving antennas can be formulated as [10]

$$\begin{aligned} E_{\alpha\beta}^s(\mathbf{x}^R, \mathbf{x}^T, \omega) &= \int_{V(\mathbf{x}^c)} D_{\alpha\beta}(\mathbf{x}^R, \mathbf{x}^T | \mathbf{x}^c, \omega) \chi(\mathbf{x}^c) J_\beta(\mathbf{x}^T, \omega) dV \\ &= S(\omega) \int_{V(\mathbf{x}^c)} D_{\alpha\beta}(\mathbf{x}^R, \mathbf{x}^T | \mathbf{x}^c, \omega) b_\beta(\mathbf{x}^T) \chi(\mathbf{x}^c) dV \end{aligned} \quad (4.1)$$

where $\omega = 2\pi f$ is the angular frequency related to the signal frequency f , $D_{\alpha\beta}$ is the wavefield extrapolator that describes the wave propagation of electric field from a β - polarized point source $J_\beta(\mathbf{x}^T, \omega)$ at \mathbf{x}^T to a scatterer at \mathbf{x}^c and then to a α - polarized receiving antenna at \mathbf{x}^R , $\chi(\mathbf{x}^c) = \hat{\eta} - \eta$ is the contrast function and defined as the difference of the background physical property $\hat{\eta}$ and scatterer's physical property η . Here the electromagnetic physical property η is defined as $\eta = \sigma + j\omega\epsilon$, where σ is the conductivity and ϵ is the permittivity. Moreover, in the last line of (4.1), the expression for a point source $J_\beta(\mathbf{x}^T, \omega) = S(\omega) b_\beta(\mathbf{x}^T)$ is used, where $S(\omega)$ denotes the source wavelet and b_β indicates the source antenna orientation. In space domain, the wavefield extrapolator $D_{\alpha\beta}$ is explicitly represented as an inner product of Green's functions of transmitting and receiving antennas

$$D_{\alpha\beta} = \sum_{l=1}^3 G_{\alpha l} G_{l\beta} \quad (4.2)$$

where $l \in \{1, 2, 3\}$ represents the electric field orthogonal directions. $G_{\alpha l}$ and $G_{l\beta}$ are Green's functions in the l direction for α -pol receiving and β -pol transmitting antennas, respectively. In the discrete form, (4.1) can be written as

$$E_{\alpha\beta}^s(\mathbf{x}^R, \mathbf{x}^T, \omega) = S(\omega) b_\beta(\mathbf{x}^T) \cdot \Delta V \cdot \sum_{k=1}^{N_p} D_{\alpha\beta}(\mathbf{x}^T, \mathbf{x}^R | \mathbf{x}_k^c, \omega) \chi(\mathbf{x}_k^c) \quad (4.3)$$

where N_p is the number of partition cells of the imaging scene and ΔV is the volume of each partition cell. Considering all the transmitting and receiving antenna pairs and all the frequencies of the signals, scattered signals can be represented in a matrix form

$$\mathbf{E}^s = \mathbf{D}_{(N_{tr} \cdot N_f) \times N_p} \cdot \chi(\mathbf{X}^c) \quad (4.4)$$

where N_{tr} is the number of transmitting-receiving antenna pairs, N_f is the number of the discrete frequencies within the operational bandwidth, and \mathbf{E}^s is a $N_{tr} \cdot N_f$ column vector formed by all the measurements. In (4.4), the constant $S(\omega) b_\beta(\mathbf{x}^T) \Delta V$

has been normalized with respect to the signal spectrum of a source at \mathbf{x}^T . $\chi(\mathbf{X}^c)$ is a column vector and represents the contrast functions of the pixels

$$\chi(\mathbf{X}^c) = [\chi(\mathbf{x}_1^c), \chi(\mathbf{x}_2^c), \dots, \chi(\mathbf{x}_{N_p}^c)]^\top \quad (4.5)$$

where superscript \top refers to the matrix transpose operation and $\mathbf{x}_1^c, \mathbf{x}_2^c, \dots, \mathbf{x}_{N_p}^c$ are the positions related to each pixel in the imaging scene. \mathbf{D} is the matrix of the forward wavefield extrapolator and

$$\begin{aligned} \mathbf{D} &= [\tilde{\mathbf{D}}_1, \tilde{\mathbf{D}}_2, \dots, \tilde{\mathbf{D}}_{N_{tr}}]^\top, \\ \tilde{\mathbf{D}}_p &= [\tilde{\mathbf{D}}(\mathbf{x}_p^{TR}, \omega_1), \tilde{\mathbf{D}}(\mathbf{x}_p^{TR}, \omega_2), \dots, \tilde{\mathbf{D}}(\mathbf{x}_p^{TR}, \omega_{N_f})], \\ \tilde{\mathbf{D}}(\mathbf{x}_p^{TR}, \omega_q) &= [D_{\alpha\beta}(\mathbf{x}_p^{TR}|\mathbf{x}_1^c, \omega_q), D_{\alpha\beta}(\mathbf{x}_p^{TR}|\mathbf{x}_2^c, \omega_q), \dots, D_{\alpha\beta}(\mathbf{x}_p^{TR}|\mathbf{x}_{N_p}^c, \omega_q)]^\top \end{aligned}$$

where $p = 1, 2, \dots, N_{tr}$, and $q = 1, 2, \dots, N_f$. \mathbf{x}_p^{TR} denotes the positions of the p -th transmitting-receiving antenna pair, i.e., $(\mathbf{x}^R, \mathbf{x}^T)$.

The objective of imaging process is to retrieve the contrast functions of the targets relative to the background media, which requires solving the large system of linear equations in (4.4). The least squares estimation of the contrast functions of the scatters can be represented as

$$\chi(\mathbf{X}^c) = \mathbf{D}^\dagger \cdot \mathbf{E}^s \quad (4.6)$$

where $\mathbf{D}^\dagger = (\mathbf{D}^H \mathbf{D})^{-1} \mathbf{D}^H$, and the superscript H and $(\cdot)^{-1}$ refer to the Hermitian transpose and the inverse operation of a matrix correspondingly. As the wavefield extrapolator \mathbf{D} is typically a matrix with dimensions of thousands or even more, the inverse operation of $\mathbf{D}^H \mathbf{D}$ is extremely computationally expensive. To save the computational load, (4.6) can be rearranged as

$$\mathbf{D}^H \mathbf{D} \chi = \mathbf{D}^H \mathbf{E}^s \quad (4.7)$$

Then some iterative approaches can be used to solve (4.7). In this chapter, we used the BiConjugate Gradient Stabilized method (BiCGStab). Here, as long as the matrix of the forward wavefield extrapolator \mathbf{D} is computed, (4.7) can be solved to reconstruct the contrast functions of scatterers. Therefore, the other major computational effort has to be spent to compute Green's functions for each transmitting-receiving antenna pair at each frequency with respect to the imaging region. Considering the constant variation of antenna polarizations within the aperture, two approaches are suggested in the following to compute the full-wave Green's functions in the space-frequency and wavenumber-frequency domains, respectively.

4.3 Full-wave Green's Functions of Rotated Antennas

4.3.1 Free-space Dyadic Green's Function

In a Cartesian coordinate system, the free-space dyadic Green's function of an elementary source can be written as [12]

$$\bar{\mathbf{G}}(\mathbf{r}, \mathbf{r}') = \left(\bar{\mathbf{I}} + \frac{1}{k^2} \nabla \nabla \right) G(\mathbf{r} - \mathbf{r}') \quad (4.8)$$

where $\bar{\mathbf{G}}$ denotes a Green's dyadic (i.e., a 3×3 matrix here), $k = 2\pi/\lambda$ is the wavenumber with respect to the wavelength λ in the free space, and $\bar{\mathbf{I}}$ is the identity dyadic (i.e., the identity matrix). $G(\mathbf{r} - \mathbf{r}')$ is the Green's function pertaining to the three-dimensional free-space scalar-wave equation and expressed as

$$G(\mathbf{r} - \mathbf{r}') = \frac{e^{-jk|\mathbf{r} - \mathbf{r}'|}}{4\pi|\mathbf{r} - \mathbf{r}'|} \quad (4.9)$$

where j is the imaginary unit, \mathbf{r}' is the position vector of a point source and \mathbf{r} is the position vector of a field point. After some algebraic manipulations (see the appendix), the free-space dyadic Green's function can be explicitly given by

$$\bar{\mathbf{G}}(\mathbf{r}, \mathbf{r}') = G(\mathbf{r} - \mathbf{r}') \left[\left(1 - \frac{j}{kR} - \frac{1}{k^2 R^2} \right) \bar{\mathbf{I}} + \left(-1 + \frac{3j}{kR} + \frac{3}{k^2 R^2} \right) \hat{\mathbf{R}} \hat{\mathbf{R}} \right] \quad (4.10)$$

where R is the amplitude of the vector $\mathbf{R} = |\mathbf{r} - \mathbf{r}'|$ and denotes the distance between the field point and the point source. $\hat{\mathbf{R}} = \nabla R$ represents the gradient of R , and $\hat{\mathbf{R}} \hat{\mathbf{R}}$ denotes the outer product of itself.

Equation (4.10) gives the vector Green's functions of a field point with respect to the point source with the current component along the three axes in a Cartesian coordinate system, for example, the x_1 -, x_2 - and x_3 -axes, which is a symmetric matrix. For shifted antennas with orientations aligned with one axis, their Green's functions are obtained through the linear translation in space according to space shift-invariant property. However, for the rotated antenna arrays, the antennas within the aperture are not only linearly translated but also rotated. To obtain the corresponding Green's functions, both translation and rotation should be considered.

Assume the rotated antennas are placed on the x_1ox_2 plane, as shown in Figure 4.1. For a rotated antenna, its vector Green's functions in the original coordinate

system can be obtained by combining its current components in the x_1 and x_2 directions or by rotating the source vector of an antenna along, for instance, the x_1 -axis with the corresponding angle. It can be implemented by multiplying the source vector by a rotation matrix. The operation can be expressed as

$$\mathbf{G}_{\text{rot}}^{\theta} = \bar{\mathbf{G}} \cdot \mathbf{R}_{x_3}(\theta) \cdot \mathbf{I}_{x_1} \quad (4.11)$$

where $\mathbf{G}_{\text{rot}}^{\theta}$ is the vector of Green's functions for an antenna rotated by θ with respect to the x_1 -axis. $\mathbf{I}_{x_1} = [1, 0, 0]^T$ denotes the unit current vector along the x_1 -axis, and $\mathbf{R}_{x_3}(\theta)$ is a 3×3 rotation matrix around the x_3 -axis and defined as

$$\mathbf{R}_{x_3}(\theta) = \begin{pmatrix} \cos \theta & -\sin \theta & 0 \\ \sin \theta & \cos \theta & 0 \\ 0 & 0 & 1 \end{pmatrix} \quad (4.12)$$

Accounting for the linear translation and utilizing (4.11), the vector Green's functions for rotated antennas can be obtained.

4.3.2 Half-space Green's Functions

For GPR imaging, the antennas are typically placed on the ground surface. So half-space Green's functions are needed for linear inversion of GPR data. Assume dipole-like GPR antennas are placed on the surface of homogeneous ground, for instance, x_1ox_2 plane in Figure 4.1, with orientations along the x_1 - or x_2 -axis. The related full-wave half-space Green's functions are given in the wavenumber-frequency (k - f) domain by [11]

$$\begin{pmatrix} g_{11} & g_{12} \\ g_{21} & g_{22} \\ g_{31} & g_{32} \end{pmatrix} = -\zeta \begin{pmatrix} k_1^2 V + U & k_1 k_2 V \\ k_1 k_2 V & k_2^2 V + U \\ -jk_1 \Gamma_0 V & -jk_2 \Gamma_0 V \end{pmatrix} \quad (4.13)$$

where g_{mn} represents Green's functions of the electric field component in the x_m direction for the dipole antenna located at the origin with its orientation along the x_n -axis, $m \in \{1, 2, 3\}$ and $n \in \{1, 2\}$. k_n denotes the wavenumber on the aperture plane along the x_n -axis. U and V are written as

$$U = \frac{\exp(-\Gamma_1 x_3)}{\Gamma_0 + \Gamma_1}, \quad V = \frac{\exp(-\Gamma_1 x_3)}{\gamma_1^2 \Gamma_0 + \gamma_0^2 \Gamma_1} \quad (4.14)$$

$$\Gamma_i = \sqrt{\gamma_i^2 + k_1^2 + k_2^2} \quad (4.15)$$

and $\gamma_i^2 = \eta_i \zeta$, where $i \in \{0, 1\}$, denotes the complex propagation constants for air ($i = 0$) and the subsurface ($i = 1$); $\eta_i = \sigma_i + j\omega\epsilon_i$ is the electric material parameters for conductivities σ_i and permittivities ϵ_i ; and $\zeta = j\omega\mu_0$ is the magnetic material parameter with permeability μ_0 .

Taking the inverse Fourier transform (IFT) of Green's functions in (4.13) with respect to k_1 and k_2 , their counterparts in the space-frequency (i.e., x - f) domain are obtained

$$\begin{pmatrix} G_{11}(x_1, x_2, f) & G_{12}(x_1, x_2, f) \\ G_{21}(x_1, x_2, f) & G_{22}(x_1, x_2, f) \\ G_{31}(x_1, x_2, f) & G_{32}(x_1, x_2, f) \end{pmatrix}.$$

Note G_{mn} s give the full-wave Green's functions of an antenna at the origin oriented along the x_1 - or x_2 -axis. For shifted antennas with orientations along the x_1 - or x_2 -axis, the associated half-space Green's functions can be obtained through the linear translation in space. By contrast, to obtain Green's functions for the rotated antennas, both translation and rotation operations are needed in the x - f domain. However, the rotation of the antennas generally spoils the alignment of the computational grid of the Green's functions and the imaging grid, which makes the FFT-based approach to compute GFs with (4.13) no longer straightforwardly applicable. Hence, extremely expensive computations are required if the direct Riemann summation is used to compute the Fourier transform of the k - f domain GFs over the imaging grid, especially for large arrays. To accelerate this computation, two methods are suggested to efficiently compute the exact Green's functions of rotated antennas in the following.

4.3.2.1 Computation of Green's functions via Interpolation

For image reconstruction, Green's functions over a rectilinear grid in the x_1 - x_2 - x_3 coordinate system are required. Let us assume the imaging grid in space at a certain depth is defined as

$$I = \left\{ (x_{1p}, x_{2q}) \middle| \begin{array}{l} x_{1p} = p\Delta x_1; \quad p = 0, 1, \dots, N_{x_1} - 1 \\ x_{2q} = q\Delta x_2; \quad q = 0, 1, \dots, N_{x_2} - 1 \end{array} \right\} \quad (4.16)$$

where Δx_1 , Δx_2 are the grid intervals along the x_1 and x_2 axes and N_{x_1} , N_{x_2} are the associated numbers of sample points. Assume a dipole antenna is placed at $(x_1^a, x_2^a, 0)$ with an orientation angle of θ with respect to the x_1 axis and denote the antenna orientation and its normal direction as x_θ and x_{θ_\perp} . For the convenience of discussion in the following, we define a “local” coordinate system x_θ - x_{θ_\perp} - x_3

with the origin at $(x_1^a, x_2^a, 0)$ and denote k_θ and k_{θ_\perp} as the Fourier counterparts of x_θ and x_{θ_\perp} . As mentioned above, in the “local” k_θ - k_{θ_\perp} - f domain, Green’s functions $g_{\theta\theta_\perp}(k_\theta, k_{\theta_\perp}, f)$ on a grid Φ can be directly calculated via (4.13), and the grid Φ is defined as

$$\Phi = \left\{ (k_{\theta_m}, k_{\theta_\perp_n}) \middle| \begin{array}{l} k_{\theta_m} = m\Delta k_\theta; m = 0, 1, \dots, L_{k_\theta} - 1 \\ k_{\theta_\perp_n} = n\Delta k_{\theta_\perp}; n = 0, 1, \dots, L_{k_{\theta_\perp}} - 1 \end{array} \right\} \quad (4.17)$$

where the sampling intervals Δk_θ and Δk_{θ_\perp} are determined by the field of view of the imaging scene according to the Nyquist criterion. In [11], it suggests that in practical implementation the wavenumber sampling grid should be $4 \sim 16$ times over sampled compared to the Nyquist sampling requirements in order to get accurate radiation properties of antennas, especially for the near-field. Taking the IFFT of $g_{\theta\theta_\perp}(k_\theta, k_{\theta_\perp}, f)$ with respect to k_θ and k_{θ_\perp} , Green’s functions $G_{\theta\theta_\perp}^a(x_\theta, x_{\theta_\perp}, \omega)$ in the x_θ - x_{θ_\perp} - f domain are obtained.

To get Green’s functions on the imaging grid I , a mapping from Green’s functions in x_θ - x_{θ_\perp} has to be made, including both linear translation and rotation operation in space. Explicitly, this mapping can be expressed as

$$G^a(x_1, x_2, f; x_1^a, x_2^a, \theta) = G_{\theta\theta_\perp}^a(\tilde{x}_\theta, \tilde{x}_{\theta_\perp}) \quad (4.18)$$

where

$$\begin{aligned} \tilde{x}_\theta &= (x_1 - x_1^a) \cos \theta + (x_2 - x_2^a) \sin \theta \\ \tilde{x}_{\theta_\perp} &= -(x_1 - x_1^a) \sin \theta + (x_1 - x_2^a) \cos \theta \end{aligned}$$

From (4.18), one can see that Green’s functions over a new grid $(\tilde{x}_\theta, \tilde{x}_{\theta_\perp})$ in the x_θ - x_{θ_\perp} coordinate system are needed to get the corresponding values on the grid I . As the new grid $(\tilde{x}_\theta, \tilde{x}_{\theta_\perp})$ is generally different from that determined by the wavenumber-domain grid Φ , a two-dimensional (2-D) interpolation is required to implement the mapping from a rectilinear grid $(x_\theta, x_{\theta_\perp})$ to the rectilinear grid I . Many interpolation methods, for example, nearest, cubic, spline, are applicable for this operation. Considering both accuracy and efficiency, spline interpolation is used in this chapter.

In addition, we have to mention that instead of taking the interpolation in x - f domain, Green’s function $G^a(x_1, x_2, f; x_1^a, x_2^a, \theta)$ can also be obtained via direct

Fourier summation of $g_{\theta\theta_\perp}(k_\theta, k_{\theta_\perp}, f)$, which is expressed as

$$G^a(x_1, x_2, f; x_1^a, x_2^a, \theta) = \sum_{m=0}^{L_{k_\theta}-1} \sum_{n=0}^{L_{k_{\theta_\perp}}-1} g_{\theta\theta_\perp}(k_{\theta_m}, k_{\theta_\perp_n}, f) \\ \cdot \exp \left\{ -jk_{\theta_m} \cdot [(x_1 - x_1^a) \cos \theta + (x_2 - x_2^a) \sin \theta] \right\} \\ \cdot \exp \left\{ -jk_{\theta_\perp_n} \cdot [-(x_1 - x_1^a) \sin \theta + (x_2 - x_2^a) \cos \theta] \right\} \quad (4.19)$$

The computation of Green's functions via (4.19) is referred to as direct summation method in the following text.

4.3.2.2 Computation of Green's functions with NUFFT

In this section, we propose to take advantage of Nonuniform Fast Fourier Transform (NUFFT) [13] to accelerate the computation of x - f domain Green's functions.

For the interpolation-based method presented in the previous section, linear translation and rotation operations in space are required to obtain the full-wave Green's functions for rotated antennas. Actually, these operations can also be efficiently implemented in the wavenumber domain. According to the properties of two-dimensional (2-D) Fourier transform, the operations in (4.18) can be represented in the wavenumber domain as

$$g_i^a(k_1, k_2, f; x_1^a, x_2^a, \theta) \\ = \mathcal{F}_{2D} [G_i^a(x_1, x_2, f; x_1^a, x_2^a, \theta)] \\ = g_{\theta\theta_\perp}(k_1 \cos \theta + k_2 \sin \theta, -k_1 \sin \theta + k_2 \cos \theta, f) \\ \cdot \exp \left\{ -j[(k_1 \cos \theta + k_2 \sin \theta) x_1^a + (k_2 \cos \theta - k_1 \sin \theta) x_2^a] \right\} \quad (4.20)$$

where G_i^a , as in (4.18), is Green's function of antenna in the x - f domain and g_i^a is its counterpart in the k - f domain in the (k_1, k_2) coordinate system while $g_{\theta\theta_\perp}$ is the 2-D Fourier transform of $G_{\theta\theta_\perp}^a$ in the $(k_\theta, k_{\theta_\perp})$ coordinate system. The subscript $i \in \{1, 2, 3\}$ represents the directions of electric field components. \mathcal{F}_{2D} is the 2-D Fourier transform operator. In (4.20), the exponential terms describe the translation operation in space while the trigonometric terms are related to the rotation.

Then to get the Green's functions G_i^a of a rotated antenna over the grid I , its Fourier counterpart g_i^a should be computed on a rectilinear grid on the k_1 - k_2 plane. According to (4.20), the corresponding values $G_{\theta\theta_\perp}^a$ have to be calculated on a nonuniform grid $(k_1 \cos \theta + k_2 \sin \theta, -k_1 \sin \theta + k_2 \cos \theta)$ in the $(k_\theta, k_{\theta_\perp})$ basis,

which can be obtained directly via (4.13). However, due to the continuously varied antenna orientations, the grid points $(k_1 \cos \theta + k_2 \sin \theta, -k_1 \sin \theta + k_2 \cos \theta)$ change for antennas in different azimuthal positions within the aperture. Hence the point-by-point computation of GFs has to be performed for all antennas with different orientations. This is even more computationally expensive than the interpolation-based method.

One alternative approach to address this problem is to exploit the similar idea as the Stolt interpolation for one-dimensional mapping. Firstly, equations (4.13), (4.14), and (4.15) are used to compute the GFs $g_{\theta\theta_\perp}$ over the grid Φ in the k - f domain. After the k - f domain GF values are obtained point by point, then they can be used to calculate the x - f domain counterparts for every antenna within the aperture. For an antenna at $(x_1^a, x_2^a, 0)$ with orientation of angle θ with respect to the x_1 axis, the pre-computed GFs over the regular grid in the $(k_\theta, k_{\theta_\perp})$ basis that is rotated with θ counter-clockwise with respect to the (k_1, k_2) basis are mapped onto the grid

$$\Phi' = \left\{ (k_1, k_2) \begin{array}{l} | k_1 = k_{\theta_m} \cos \theta + k_{\theta\perp_n} \sin \theta; \\ | k_2 = -k_{\theta_m} \sin \theta + k_{\theta\perp_n} \cos \theta; \\ | (k_{\theta_m}, k_{\theta\perp_n}) \in \Phi \end{array} \right\} \quad (4.21)$$

in the (k_1, k_2) basis. Obviously, after the rotation mapping from $(k_{\theta_m}, k_{\theta\perp_n}) \rightarrow (k_1, k_2)$, the sampling points are located on a rotated rectilinear grid in the (k_1, k_2) basis.

So the problem can be restated as: *Using the pre-calculated k - f domain Green's functions over the rotated rectilinear grid Φ' to reconstruct their counterpart in the x - f domain over the rectilinear grid I.* Apparently, it is a typical non-uniform Fourier transform problem from non-uniform samples in the k - f domain to the uniform grid in the x - f domain. So we can take advantage of NUFFT to efficiently implement it [13]. To compute the Green's functions in a 3-D volume, the wavefield computed in one horizontal plane can be extrapolated to different depth via the derived relation [14]

$$g_{mn}(k_1, k_2, \omega, x_3^{(n)}) = g_{mn}(k_1, k_2, \omega, x_3^{(0)}) \cdot \exp\{-\Gamma_1(x_3^{(n)} - x_3^{(0)})\} \quad (4.22)$$

where $x_3^{(0)}$ is the initial depth of the electric fields computed directly and $x_3^{(n)}$ is the depth of the extrapolated electric fields. As the exponential term in (4.22) is rotationally symmetric around the origin on the k_1 - k_2 plane, so it is directly applicable to extrapolate the wavefield to different depths for antennas with whatever orientations.

Table 4.1: Comparison of three methods for x - f domain Green's function Computation

Method		Direct-sum	Interp	NUFFT
Time [s]		1042.64	4.042	0.553
L_2 Error	G_{11}	-	1.269e-8	1.373e-14
	G_{21}	-	2.034e-8	1.524e-14
	G_{31}	-	2.358e-8	1.827e-14
L_∞ Error	G_{11}	-	1.033e-4	1.255e-7
	G_{21}	-	1.500e-4	1.644e-7
	G_{31}	-	1.655e-4	1.683e-7

4.3.2.3 Sampling Criteria

In the two methods presented above for GF computation (i.e., the interpolation-based method and the NUFFT-based method), the uniform sampling of g_{mn} on a regular grid in the k - f domain is required to facilitate the application of FFT during the GF computation. To avoid the aliasing of the GFs in the x - f domain, the wavenumber-domain sampling spacings can be taken as [11]

$$dk_n = \frac{2\pi}{p \cdot X_n} = \frac{2\pi}{p \cdot N_{x_n} \Delta x_n} \quad (4.23)$$

where p is the oversampling factor, $X_n = N_{x_n} \Delta x_n$ is the dimension of the imaging scene in the x_n direction. Considering the computational accuracy of IFFT-derived Green's functions in the x - f domain, p could empirically take a value of 4 to 16. Moreover, we have to mention that when the interpolation based method is used to compute the GFs, a large enough value should be chosen for p so that the support region of the computed GFs always covers the desired imaging area in the spatial domain even after translation with respect to the most remote antenna from the origin.

4.4 Simulations

4.4.1 Green's Function Computation

In this section, the Green's function computation methods are examined via numerical simulations. In this simulation, the operational frequency was 200 MHz and the relative permittivity of soil medium was 9. Dipole antennas were placed on the x_1 - x_2 plane and their orientation angles were defined as the angle from the

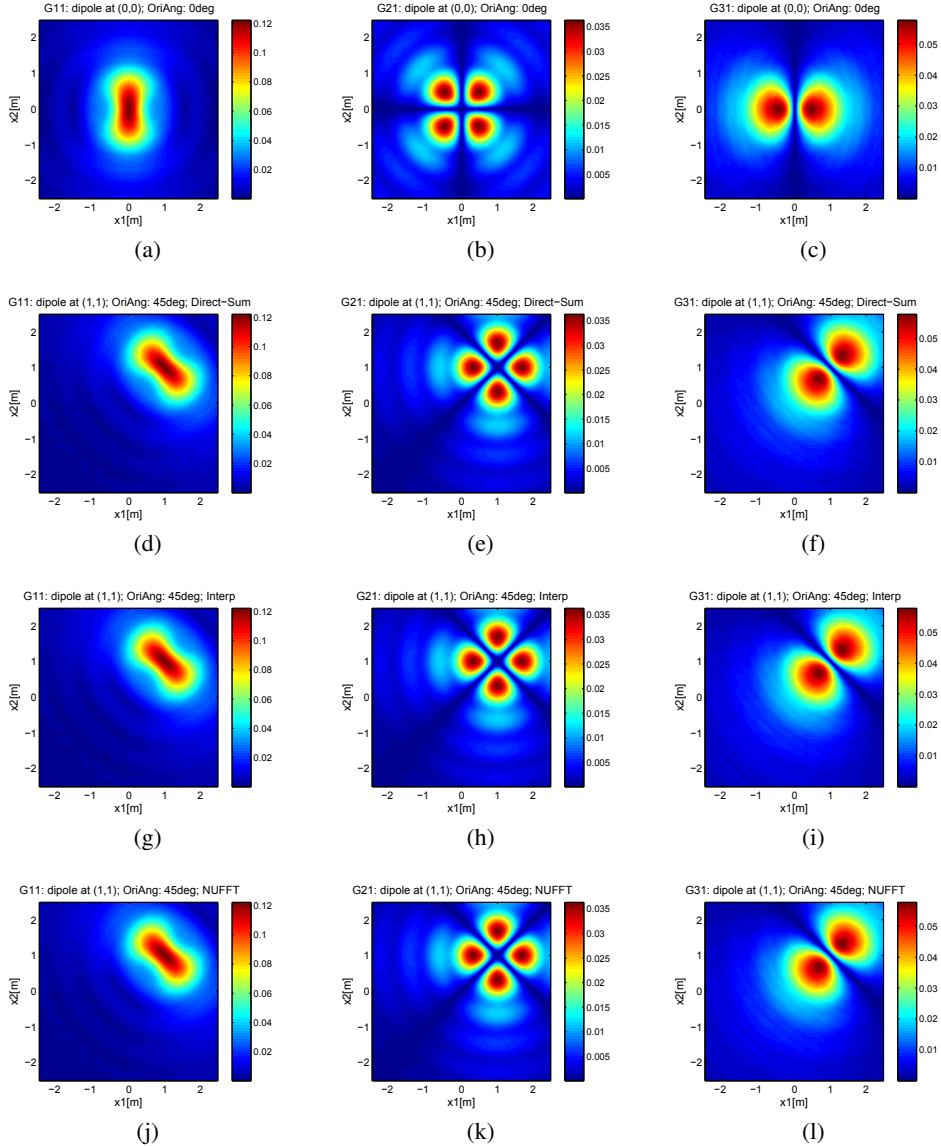


Figure 4.2: Green's functions at the depth of 0.6 m for a dipole antenna located at $(0,0,0)$ with its orientation along the x_1 -axis [(a)–(c)] and a rotated one at $(1,0,1)$ m with its orientation of 45° from the x_1 -axis [(d)–(l)]. (a), (b), and (c) show Green's functions of the dipole antenna at the origin with respect to the electric field components along the antenna axis (i.e., the x_1 component), the direction orthogonal to the antennas axis (the x_2 component), and the propagation direction (the x_3 component here), respectively. (d)–(f), (g)–(i), and (j)–(l) show Green's functions of the rotated dipole antenna at $(1,0,1)$ m obtained with the direct summation, the interpolation-based method, and the NUFFT based method, respectively. The antennas are placed on the ground surface (the x_1 - x_2 plane). The operational frequency is 200 MHz and the relative permittivity of soil $\epsilon = 9$.

x_1 -axis to antenna axis. The x_3 -axis points downward, forming a right-hand coordinate system with the x_1 - and x_2 -axes. Firstly, Green's functions for a dipole antenna at the origin along the x_1 -axis were calculated with the FFT-based method [11]. Then Green's functions for a linearly translated and rotated antenna were computed by the interpolation based method and NUFFT based method proposed in the previous section. In order to get accurate x - f domain Green's functions, four times oversampling in the k - f domain computation was taken for all simulations and the computational accuracy of NUFFT was set to be 10^{-5} . The simulation results are illustrated in Figure 4.2. The GFs at the depth of 0.6 m for a dipole antenna located at the origin are shown in Figures 4.2(a)–(c) while the GFs for a rotated dipole antenna at $(1, 1, 0)$ m with the orientation angle of 45° are displayed in Figures 4.2(d)–(l). Among the plots for the rotated dipole antenna, Figures 4.2(g)–(i) and Figures 4.2(j)–(l) show the GFs obtained with the interpolation based method and NUFFT-based method, respectively. As a reference, the results computed by direct summation are shown in Figures 4.2(d), (e) and (f). According to Figures 4.2(d)–(l), one can see that both the interpolation based method and NUFFT based method obtain the visually equal results as those of direct summation.

The efficiency and accuracy of the two proposed methods were also compared quantitatively and the results are listed in Table. 4.1. The accuracy is indicated by the relative L_2 and L_∞ errors. The relative L_2 error is defined by the norm of the differences between the computed GF with the suggested methods and the reference GF divided by the norm of the reference GF. The relative L_∞ error is defined by the maximum of the differences between the computed GF with the suggested methods and the reference GF divided by the norm of the reference GF. In terms of both relative L_2 error and relative L_∞ error, the NUFFT based method for Green's function computation achieves much higher accuracy than that of the interpolation based one. Although both suggested methods significantly improve the computational efficiency compared to the direct summation method, the NUFFT based method is still more than 7 times faster than the interpolation based method for computing 250×250 points of the x - f domain Green's function.

4.4.2 Imaging with Rotated Antenna Array

To demonstrate the imaging performance of the proposed approach, numerical simulations were performed for dielectric cylinders buried in the soil. GPR data were synthesized with gprMax software, which uses the Finite-Difference Time-Domain (FDTD) method to simulate the electromagnetic wave propagation [15]. The ge-

Table 4.2: Simulation parameters for cylindrical cavities in soil

Parameter	Value
Wavelet	Ricker [900 MHz]
Radial sampling interval	5 cm
Azimuthal sampling interval	3°
Radius of circular antenna aperture	0.5 m
Permitivity of background soil	9.0
Soil conductivity	0.01 S/m
Permitivity of dielectric cylinders	5.0
Conductivity of dielectric cylinders	0.05 S/m
Depth of the cavity	0.4 m

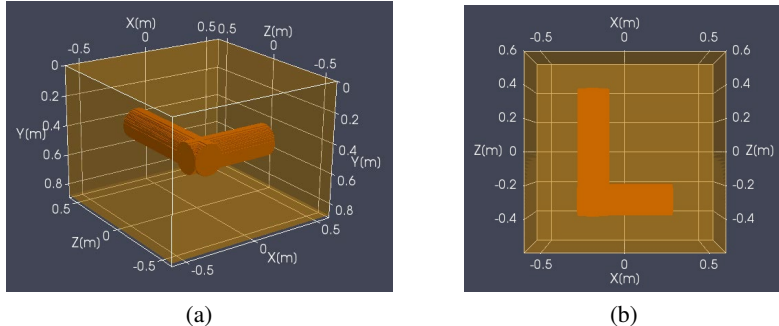


Figure 4.3: Geometrical configuration of dielectric cylinders in soil. (a) is the 3-D geometrical configuration and (b) is its top view against the y axis.

ometrical configuration for the simulation is shown in Figure 4.3. Two cylinders of radius 10 cm were buried at the depth of 0.4 m and they were joined at one end [as shown in Figure 4.3(a)]. The relative permittivity of the cylinders is 5.0 and their conductivity is 0.05 S/m. Meanwhile, the permittivity and conductivity of the background soil are 9.0 and 0.01 S/m, respectively. The elementary dipole antennas were placed on the ground surface (i.e., xoz plane) and the Ricker wavelet of 900 MHz was used as the excitation signal. To emulate the operation of the GPR system used for TBM applications, the dipole antennas were placed with orientations along the radii at different positions. GPR signals were acquired over eight concentric circles whose radii range from 0.15 m to 0.5 m with steps of 5 cm and the azimuthal sampling intervals were 3° . Therefore, in total 960 spatial samples were

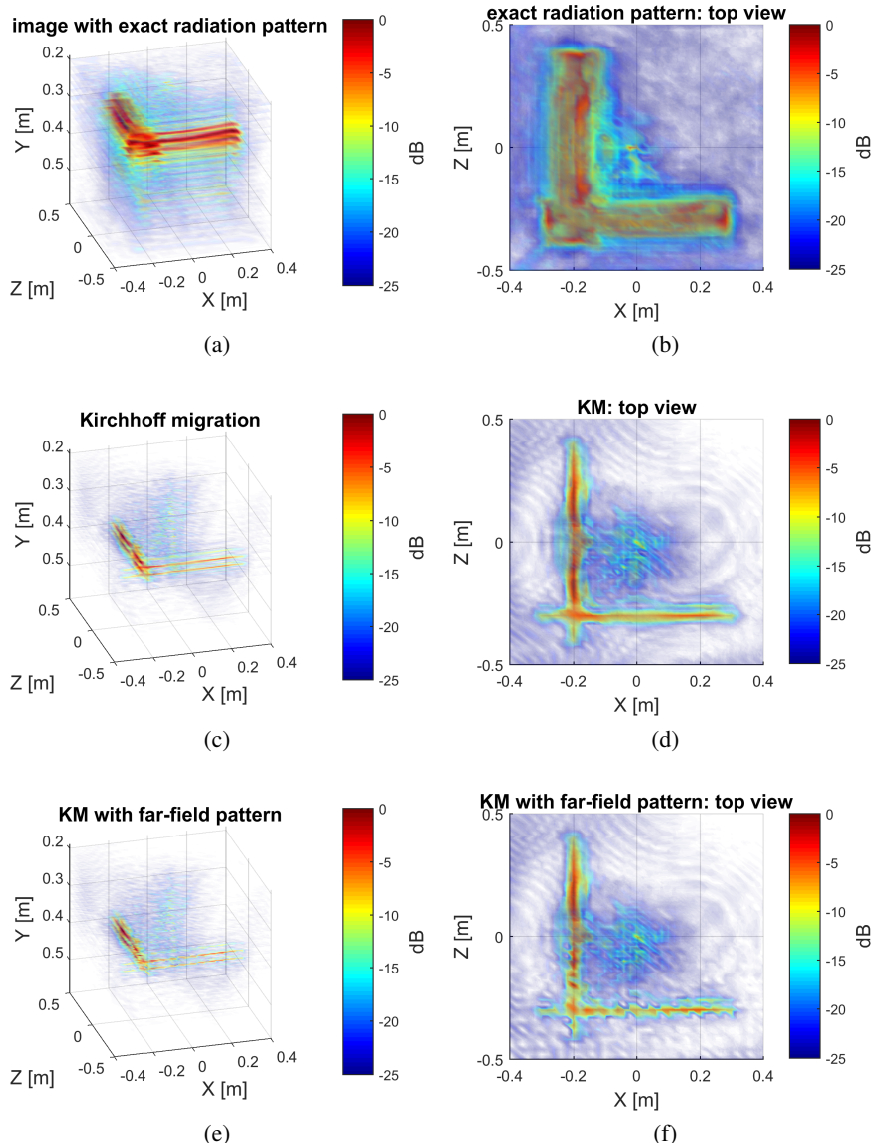


Figure 4.4: Reconstructed images of cylinders buried in the soil with three different imaging approaches: (a), (c), and (e) are the 3-D images obtained by the linear inversion with exact radiation patterns, Kirchhoff migration, and Kirchhoff migration combining the far-field radiation patterns, respectively. (b), (d), and (f) are their corresponding top-view images.

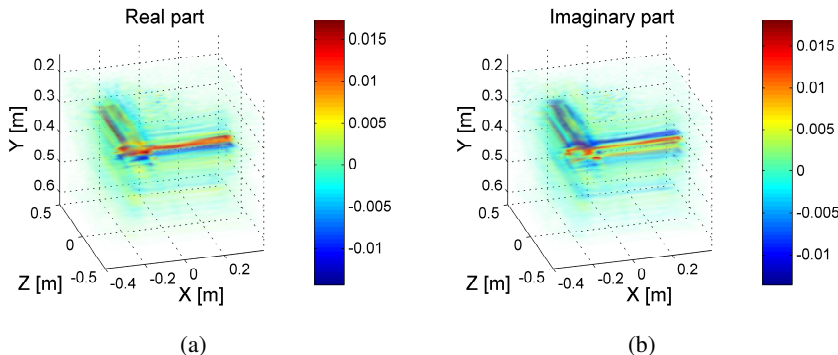


Figure 4.5: Reconstructed image of cylinders with the linear inversion approach. (a) real part, (b) imaginary part.

obtained within the aperture but their polarizations varied in different azimuthal positions. For convenience, the parameters of the GPR system and the media properties are summarized in Table 4.2.

After synthesizing the GPR data, the accurate Green's functions of rotated antennas at each position were computed with the suggested methods in the previous section. Then the synthetic data were focused via the linear inversion method by considering the accurate radiation patterns of the antennas with varied polarizations at different positions (i.e., linear inversion with accurate radiation pattern, referred as LI-AccuRP below). In the implementation, the biconjugate gradients stabilized method (BiCGStab) was exploited to estimate the solution for the linear system of equations. For comparison, the Kirchhoff migration, as well as the Kirchhoff migration combining the far-field approximation of the radiation patterns, was also utilized for image formation. Integrating the far-field radiation pattern aims to correct the angle dependence of the dipole radiation which is generally neglected in the Kirchhoff migration. To avoid the blow-up of the signals after correction caused by the sharp minima in the far-field radiation patterns, only the signals that correspond to the radiation patterns down to -13dB with respect to its maximum were compensated in the third imaging approach.

The images reconstructed with the three approaches are shown in Figure 4.4. In all the images of Figures 4.4(a), (c) and (f), the “L”-shaped profiles of the joint cylinders are more or less reconstructed. However, in Figures 4.4(c) and (e) the reconstructed cylinders are much thinner than that in Figure 4.4(a). This is due to the striking angle dependence of the radiation patterns of the interfacial dipole an-

tennas which significantly affects the strength of the signals observed from different aspects with respect to a target. Although the far field radiation patterns were employed to compensate the angle dependence of the observations in Figures 4.4(e) and (f), the resultant images are visually even worst than that without radiation pattern correction [Figures 4.4(c) and (d)]. Specifically, the image of the cylinder parallel to the x -axis is fractured and in Figure 4.4(f) the joint part of the two cylinders becomes dim compared to that in Figure 4.4(d). This may result from the inadequate approximation of the far-field patterns in this case as well as the truncation effect on the radiation patterns for signal correction. In contrast to Figures 4.4(c)–(f), the images formed with linear inversion are remarkably improved by accounting for the exact radiation patterns of ideal dipole antennas [Figures 4.4(a) and (b)]. Based on Figure 4.4(b), the diameters of the cylinders could be estimated although some artifacts are observed around the object.

Finally, we have to mention that the linear inversion approach in principle has the potential to estimate the contrast function of targets. However, as the Born approximation used in the formulation is invalid in the simulation scenario, the contrast functions of the cylinders relative to the soil background were not correctly estimated. From the reconstructed complex contrast functions (see Figure 4.5), the permittivity difference between the cylinders and the soil background is estimated to be 1.88 while its real value should be 4. Nevertheless, the shapes of the cylinders were properly reconstructed. So one can see that the Born approximation is applicable and robust for reconstructing shapes of targets (at least, for homogeneous objects) but not for estimating the contrast functions.

4.5 Experiments

As the rotated GPR instrument was unavailable, we instead took an experimental campaign in the anechoic chamber for imaging in free space.

A rotated experimental platform was built in the anechoic chamber in the TU Delft to emulate the signal acquisition for rotated arrays, as shown in Figure 4.6(a). Actually, this setup was similar to the one we used in [1]. A column was installed on the base with the three-axis motion (i.e., two-axis translation and one-axis rotation), where a stepper motor was used to drive the base. On the top of the column, a polyethylene plastic panel was mounted as a support for the two antipodal Vivaldi antennas, i.e., one for transmitting and the other for receiving. Both Vivaldi antennas were connected to a vector network analyzer (VNA). By linear translation along the radius and rotation along azimuth, a circular planar array was synthesized. An

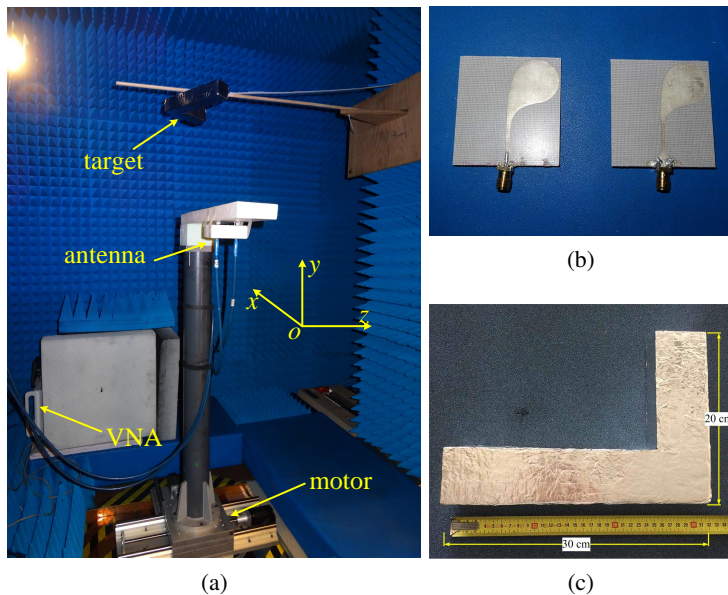


Figure 4.6: The experimental setup in the anechoic chamber. (a) shows the experimental setup for rotated array measurement. (b) displays the antipodal Vivaldi antennas used and (c) is the “L”-shaped target.

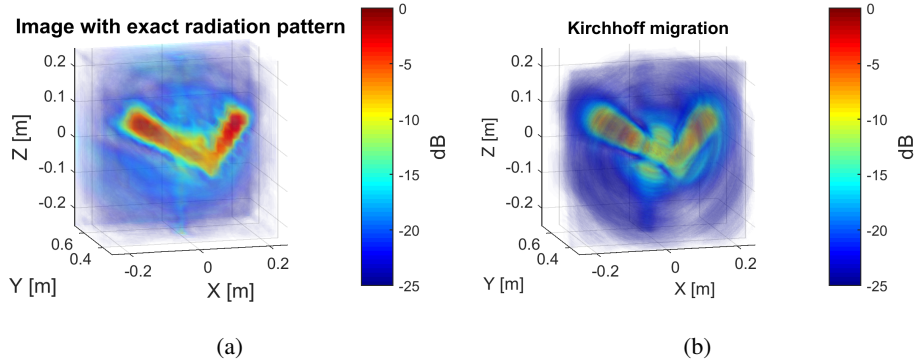


Figure 4.7: Images of experimental measurements reconstructed by: (a) Linear inversion with accurate radiation pattern, (b) Kirchhoff migration.

“L”-shaped object was placed in front of the array at a distance of 0.5 m. The two arms of the “L”-shaped object are about 20 cm and 30 cm in length, respectively,

6 cm in width, and 5.5 cm in thickness [see Figure 4.6(c)]. All the parts of the object was coated with aluminum foil. The spatial measurements were taken over some concentric circles with radii ranging from 11 cm to 53 cm with steps of 3 cm. In azimuth, the sampling interval was 2.4° . The operational frequency of the VNA sweeps from 3 GHz to 6 GHz with steps of 20 MHz.

To consider the direct coupling between the transmitter and the receiver and background reflections, the measurement was also performed with the absence of the object. After background subtraction, the signals reflected from the target were obtained. Then the linear inversion approach with accurate radiation patterns was utilized to reconstruct the target's image from the frequency-domain signals. The reconstructed image is shown in Figure 4.7(a). Note that as the experimental measurement was conducted in free space, the Green's functions for a Hertz dipole in free space instead of half-space were used for linear inversion [12]. For comparison, the signals after applying the inverse Fourier transform (IFT) to the measurements in the frequency domain were focused with the Kirchhoff migration as well and the formed image is presented in Figure 4.7(b). From Figure 4.7, one can see that both linear inversion with accurate radiation patterns and the Kirchhoff migration acquire well-focused images of the target. However, the profile of the target is clearer and sharper in the image formed by linear inversion with accurate radiation pattern [Figure 4.7(a)] compared to that in the image focused by the Kirchhoff migration [Figure 4.7(b)]. Meanwhile, relatively larger artifacts and circularly sidelobes observed in Figure 4.7(b) are noticeably suppressed in Figure 4.7(a). Therefore, by considering the accurate radiation patterns of the rotated antenna arrays, improved images were obtained. As a consequence, in this case the computation time of the linear inversion approach (with 51 frequencies at each spatial position, i.e., the measurements were down-sampled every three frequencies) required ~ 350 s (about 340 s for computing $\mathbf{D}^H\mathbf{D}$ in (4.7)) compared to the ~ 7 s of the Kirchhoff migration on a computer of 3.20 GHz CPU with four cores. The increase of computation time can be considered as a cost to be paid for the improved image quality. To accelerate the linear inversion approach, the matrix $\mathbf{D}^H\mathbf{D}$ can be precomputed and stored before the inversion operation, or more advanced inversion solvers should be exploited to circumvent the computation of $\mathbf{D}^H\mathbf{D}$.

4.6 Conclusion

In this chapter, we have applied a linear inversion approach to microwave imaging with transmitting and receiving antennas which are arbitrarily oriented over the

data acquisition aperture. The approach models the wave propagation process with full-wave Green's functions and the image reconstruction is formulated as a linear inverse problem. Taking advantage of full-wave Green's functions, the polarization and radiation pattern variations of antennas are taken into account and their effects are compensated during the image formation.

In terms of the implementation of the proposed approach, two methods are proposed to compute Green's functions, especially half-space ones: interpolation-based method and NUFFT based method. Compared to the direct summation method, both methods significantly accelerate the Green's function computation and their accuracies were verified through numerical simulations. Besides for the imaging, these two efficient approaches for Green's function calculation can also benefit the investigation of the properties of sensing matrix for near-field imaging which is helpful to optimize the spatial signal sampling and imaging array design. It was shown through both simulations and measurements the proposed approach significantly improves the imaging performance (i.e., the sharpness of the focused image, artifacts suppression) compared to the traditional imaging algorithms, such as the scalar Kirchhoff migration and its combination with far-field radiation patterns. The Born approximation does not seem important for the reconstruction of the shapes of objects. However, reconstructed material parameters of the objects are not correct, as expected. The proposed approach can be used for both free space and subsurface imaging by exploiting the corresponding Green's functions. In particular, the proposed method is very suitable for reconstructing images of polarization independent objects and structures (such as point-like scatterers, spheres, and planar structures). The proposed approach can also be straightforwardly extended to fully polarimetric imaging when the signals are acquired with fully polarimetric antenna arrays and to incorporate with non-linear inversion schemes.

Appendix

As in this chapter Green's function $G(\mathbf{r} - \mathbf{r}')$ with the minus (“−”) sign in the phase terms, instead of “+” sign as used in [12], is used for outgoing waves, so the resultant dyadic Green's function is slightly different, which is derived as follows.

In a Cartesian coordinate system, dyadic Green's function of an elementary source can be written as

$$\bar{\mathbf{G}}(\mathbf{r}, \mathbf{r}') = \left(\bar{\mathbf{I}} + \frac{1}{k^2} \nabla \nabla \right) G(\mathbf{r} - \mathbf{r}') \quad (4.24)$$

where $G(\mathbf{r} - \mathbf{r}')$ is Green's function of the scalar-wave equation, and given by

$$G(\mathbf{r} - \mathbf{r}') = \frac{e^{-jk|\mathbf{r}-\mathbf{r}'|}}{4\pi|\mathbf{r}-\mathbf{r}'|} \quad (4.25)$$

To get the explicit form of dyadic Green's function $\bar{\mathbf{G}}$, we first expand the second term in (4.24) as

$$\begin{aligned} \nabla G &= \nabla \left(\frac{e^{-jk|\mathbf{r}-\mathbf{r}'|}}{4\pi|\mathbf{r}-\mathbf{r}'|} \right) = \nabla \left(\frac{e^{-jkR}}{4\pi R} \right) \\ &= \frac{1}{4\pi R} \nabla e^{-jkR} + e^{-jkR} \nabla \left(\frac{1}{4\pi R} \right) \\ &= \frac{1}{4\pi R} e^{-jkR} (-jk) \nabla R + e^{-jkR} \frac{1}{4\pi} \left(-\frac{1}{R^2} \nabla R \right) \\ &= \left(-jk - \frac{1}{R} \right) G \nabla R = \left(-jk - \frac{1}{R} \right) G \hat{\mathbf{R}} \end{aligned} \quad (4.26)$$

where $R = |\mathbf{r} - \mathbf{r}'|$ denotes the distance between a field point and the point source, and $\hat{\mathbf{R}} = \nabla R$ is used in the last line of the above equation.

Then we can get

$$\begin{aligned} \nabla \nabla G &= \nabla \left[\left(-jk - \frac{1}{R} \right) G \right] \hat{\mathbf{R}} + \left(-jk - \frac{1}{R} \right) G \nabla \hat{\mathbf{R}} \\ &= \left[-jk \nabla G - \nabla \left(\frac{1}{R} G \right) \right] \hat{\mathbf{R}} + \left(-jk - \frac{1}{R} \right) G \nabla \hat{\mathbf{R}} \\ &= \left[-jk \left(-jk - \frac{1}{R} \right) G \hat{\mathbf{R}} - \frac{1}{R} \left(-jk - \frac{1}{R} \right) G \hat{\mathbf{R}} + G \frac{1}{R^2} \hat{\mathbf{R}} \right] \hat{\mathbf{R}} \\ &\quad + \left(-jk - \frac{1}{R} \right) G (\bar{\mathbf{I}} - \hat{\mathbf{R}} \hat{\mathbf{R}}) \frac{1}{R} \end{aligned} \quad (4.27)$$

where

$$\nabla \hat{\mathbf{R}} = \nabla \left(\frac{\mathbf{R}}{R} \right) = \frac{1}{R} \nabla \mathbf{R} - \mathbf{R} \frac{1}{R^2} \nabla R = \frac{1}{R} (\bar{\mathbf{I}} - \hat{\mathbf{R}} \hat{\mathbf{R}}) \quad (4.28)$$

Note that $\mathbf{R} = \mathbf{r} - \mathbf{r}'$ and $\nabla \mathbf{R} = \bar{\mathbf{I}}$ are used, where $\bar{\mathbf{I}}$ is the identity dyadic. So finally dyadic Green's function $\bar{\mathbf{G}}$ is obtained as

$$\bar{\mathbf{G}}(\mathbf{r}, \mathbf{r}') = G(\mathbf{r} - \mathbf{r}') \left[\left(1 - \frac{i}{kR} - \frac{1}{k^2 R^2} \right) \bar{\mathbf{I}} + \left(-1 + \frac{3i}{kR} + \frac{3}{k^2 R^2} \right) \hat{\mathbf{R}} \hat{\mathbf{R}} \right] \quad (4.29)$$

References

- [1] J. Wang, P. Aubry, and A. Yarovoy, “A novel approach to full-polarimetric short-range imaging with copolarized data,” *IEEE Transactions on Antennas and Propagation*, vol. 64, no. 11, pp. 4733–4744, 2016.
- [2] Z. Li, J. Wang, J. Wu, and Q. H. Liu, “A fast radial scanned near-field 3-D SAR imaging system and the reconstruction method,” *Geoscience and Remote Sensing, IEEE Transactions on*, vol. 53, no. 3, pp. 1355–1363, 2015.
- [3] S. Zhu, W. Jian, L. Yu, S. Yi, and M. Sato, “A circular measurement for linearly polarized ground penetrating radar to map subsurface crossing cylinders,” in *Geoscience and Remote Sensing Symposium (IGARSS), 2013 IEEE International*, pp. 1426–1429.
- [4] Z. Min, C. Xiaodong, L. Lei, and C. Parini, “The UWB imaging system with rotating antenna array for concealed metallic object,” in *Antennas and Propagation (EuCAP), 2014 8th European Conference on*, pp. 117–119.
- [5] M. L. Moran, S. A. Arcone, and R. J. Greenfield, “GPR radiation pattern effects on 3D Kirchhoff array imaging,” in *8th International Conference on Ground Penetrating Radar*, pp. 208–212, International Society for Optics and Photonics, 2000.
- [6] T. Wang and M. L. Oristaglio, “GPR imaging using the generalized radon transform,” *GEOPHYSICS*, vol. 65, no. 5, pp. 1553–1559, 2000.
- [7] T. B. Hansen and P. M. Johansen, “Inversion scheme for ground penetrating radar that takes into account the planar air-soil interface,” *Geoscience and Remote Sensing, IEEE Transactions on*, vol. 38, no. 1, pp. 496–506, 2000.
- [8] P. Meincke, “Linear GPR inversion for lossy soil and a planar air-soil interface,” *Geoscience and Remote Sensing, IEEE Transactions on*, vol. 39, no. 12, pp. 2713–2721, 2001.
- [9] J.-P. Van Gestel and P. L. Stoffa, “Migration using multiconfiguration GPR data,” in *8th International Conference on Ground Penetrating Radar*, pp. 448–452, International Society for Optics and Photonics, 2000.
- [10] J. Kruk, C. Wapenaar, J. Fokkema, and P. van den Berg, “Three-dimensional imaging of multicomponent ground penetrating radar data,” *GEOPHYSICS*, vol. 68, no. 4, pp. 1241–1254, 2003.

- [11] R. Streich and J. van der Kruk, “Accurate imaging of multicomponent GPR data based on exact radiation patterns,” *Geoscience and Remote Sensing, IEEE Transactions on*, vol. 45, no. 1, pp. 93–103, 2007.
- [12] C.-T. Tai, *Dyadic Green’s functions in electromagnetic theory*. The Intext monograph series in electrical engineering, Scranton: Intext Educational Publishers, 1971.
- [13] L. Greengard and J.-Y. Lee, “Accelerating the nonuniform fast Fourier transform,” *SIAM Review*, vol. 46, no. 3, pp. 443–454, 2004.
- [14] E. C. Slob, R. F. Bloemenkamp, and A. G. Yarovoy, “Efficient computation of the wavefield in a two media configuration emitted by a gpr system from incident field measurements in the air,” in *Advanced Ground Penetrating Radar, 2003. Proceedings of the 2nd International Workshop on*, pp. 60–65.
- [15] C. Warren, A. Giannopoulos, and I. Giannakis, “An advanced GPR modelling framework: The next generation of gprmax,” in *Advanced Ground Penetrating Radar (IWAGPR), 2015 8th International Workshop on*, pp. 1–4, July 2015.

5

Three-Dimensional Array Design and Optimization

5.1 Introduction

In this chapter, we extend the RadSAR to a new three dimensional SAR modality, termed as the Elevation-RadSAR (E-RadSAR) by exploiting the additional forward movement of the platform in the down-range direction. The E-RadSAR takes the spatial measurements over a volume, i.e., one more degree of spatial freedom used compared to the traditional arrays. An elementary objective of this study is to explore the potential of the 3-D spatial sampling of the E-RadSAR for reducing the number of antennas needed in building a forward-looking short-range imaging system.

5.1.1 Prior Works and Existing Theories

As a cost-efficient array technology, the SAR technique is widely applied to synthesize a large aperture in the cross-range direction for high cross-range resolution. The stripmap, spotlight, and CSAR designed for remote sensing, and the planar scanning array and the RadSAR for short-range imaging are all such modalities.

Part of this chapter was submitted as: J. Wang, and A. Yarovoy,"Sampling design of synthetic volume arrays for three-dimensional microwave imaging," *IEEE Transactions on Computational Imaging*, under review.

Moreover, the SAR technique is also utilized in the down-range direction to extend the CSAR to the E-CSAR [1], which is closely related to our work. Compared to the CSAR, the E-CSAR improves the down-range resolution and provides the 3-D Imaging capability. Although its down-range resolution is still coarser than that achieved by a planar array (e.g., the RadSAR) with the same cross-range dimensions [2], the E-CSAR demonstrates the potential of exploiting SAR technique in the down-range direction for reducing the number of antennas needed for 3-D imaging. Analogously, it inspires the extension of the RadSAR to the E-RadSAR for cost-tight and/or space-limited imaging applications.

The synthetic aperture technique is, in essence, a scheme for spatial signal acquisition. So it involves a signal sampling problem. Specifically, for the E-RadSAR, it relates to a *volume sampling*, i.e., 3-D spatial sampling, of the scattered signals, which is substantially different from the traditional SAR modalities and arrays in which spatial samples are collected along a line or over a surface. Regarding the 3-D or even higher dimensional sampling, the Shannon sampling theorem for frequency-limited signals was extended to functions of multi-dimensional arguments [3], where the samples were taken over a periodic lattice to reconstruct functions with limited spectrum in the wavenumber space. However, the periodic lattice cannot be directly applied to take spatial samples of the wave fields in a volume or to design volume arrays for 3-D imaging. Moreover, Bucci *et al.* [4] studied the bandwidth of the scattered fields and derived the degrees of freedom (DoF), which are equal to the Nyquist number, as a criterion for the sampling representation. But the DoF only provides a guideline for the minimum number of the spatial samples needed to avoid aliasing for the wave field signal reconstruction. Detailed spatial sampling schemes still need to be investigated and elaborately designed for different operational configurations.

Meanwhile, the sampling problem can be transformed to and discretely tackled as a subset selection problem, i.e., selecting a subset of samples as the measurements from a group of candidates. Similar subset selection problems have been formulated for sensor/observation selections in Magnetic Resonance Imaging (MRI) [5–8], sensor management/allocation [9–14], remote sensing [15], etc. The subset selection problem involves a combinatorial optimization problem. If an exhaustive search is used to look for the solution, it requires prohibitively expensive computation, which is impractical, even for a medium-size problem. To accelerate the selection process, plenty of selection methods have been proposed in the related studies, which can be classified into three main categories: heuristic methods [16], greedy methods with various selection criteria [5–8, 10, 12, 15, 17],

and convex optimization methods [9, 11]. Heuristic methods [16] use some general optimization methods, such as the genetic algorithm, particle swarm, etc, to generate (near-)optimal solutions for subset selection. But these kind of algorithms are still prohibitively computational cost and their solutions have no optimality guarantee. Convex optimization methods relax the boolean presentation of discrete sensor/observation selection to a convex set. The optimality of the selected solution can be evaluated through the distance between the primal and dual problem solutions [18]. This approach can be extended by considering some prior information, for instance, sparsity constraints [11]. Greedy methods select the sensors/observations in a one-by-one manner by optimizing some proxies of error of the estimated physical fields or unknowns, such as the trace of $(\mathbf{A}^H \mathbf{A})^{-1}$ (here \mathbf{A} is the observation matrix), the determinant or trace of $\mathbf{A}^H \mathbf{A}$, frame potential or eigenvalues of the observation matrix \mathbf{A} . Accordingly, some selection algorithms have been developed, including the sequential backward selection (SBS), sequential forward selection (SFS), FrameSense, Maximal projection onto minimum eigenspace (MPME), etc. Moreover, when the cost function used for the selection decision is submodular,¹ the resulting combination is guaranteed to be optimal within a certain bound.

5.1.2 Our Contributions

We investigate the volumetric spatial sampling of the E-RadSAR for 3-D short-range imaging. The sampling design of the E-RadSAR for microwave imaging is formulated as a sensor/observation selection problem. Specifically, we assume that the antennas can take measurements within a volume over some grids which form the set of candidate spatial samples. Then the sampling design for the E-RadSAR is converted to the selection of a subset of antennas and their spatial sampling positions. Moreover, if wideband/UWB signals are used, the effect of the signal bandwidth on the array design can be accounted for by taking samples in a series of discrete frequencies in the operational frequency band. Therefore, one antenna gets multiple measurements at each spatial sampling position. So the spatial sample selection, in essence, becomes a vector measurement selection problem. A similar vector measurement selection problem was also considered for sensor selection [9] and sensor array configuration for ionospheric radio tomography [15] based on the convex relaxation and clustered Sequential Backward Selection (CSBS) algorithm,

¹A real-valued function z defined on a finite set \mathcal{N} is called *submodular* if $z(\mathcal{S} \cup \{k\}) - z(\mathcal{S}) \leq z(\mathcal{R} \cup \{k\}) - z(\mathcal{R})$, $\mathcal{R} \subset \mathcal{S} \subset \mathcal{N}$, $k \in \mathcal{N} \setminus \mathcal{S}$. For submodular maximization, submodular set functions exhibit a natural diminishing returns property. More discussions about submodular functions can be referred to [19].

respectively.

To address the vector measurement selection for short-range imaging, we propose two greedy algorithms, i.e., Clustered FrameSense and Clustered Maximum Projection onto Minimum Eigenspace (CMPME). The clustered FrameSense selects the spatial samples by optimizing the frame potential (a surrogate of the estimation error of physical field) of the observation matrix while the CMPME sequentially picks out the sample that brings the maximum complementary information with respect to the existing ones by examining its projection onto the minimum eigenspace. Compared to the convex relaxation method and CSBS, the two proposed algorithms are substantially more computationally efficient and provide near-optimal selections.

Moreover, we have to mention that the linear system formulation of the scattered field inversion also provides a general multi-dimensional sampling model for array-based microwave imaging systems, which enables to explore the impact of spatial-, frequency- and polarization-diversities on the image formation in a unified framework. Based on this general model, we can design more advanced 3-D sampling schemes/arrays, frequency-modulated arrays, as well as polarization-diversified arrays in which the antennas within the aperture are intentionally placed with different polarizations, etc.

5.2 Signal Model

5.2.1 Linear Inversion Problem

Under the Born approximation, the scattered EM field acquired by an array-based imaging system can be expressed as (2.72). For convenience, we rewrite it as

$$\mathbf{s} = \mathbf{D} \cdot \boldsymbol{\chi} \quad (5.1)$$

where $\mathbf{s} \in \mathbb{C}^N$ is a vector formed by N measurements of the imaging system, and $\boldsymbol{\chi} \in \mathbb{C}^m$ is a vector of the scatterers' contrast functions in the investigation domain discretized with respect to a set of unit volume box functions corresponding to a 3-D array of m cubic voxels. $\mathbf{D} \in \mathbb{C}^{N \times m}$, where $N \gg m$, denotes the sensing matrix that relates scattered fields to the targets' contrast functions, and each entry of the matrix \mathbf{D} is a function of operational frequency, the positions of transmitting and receiving antennas, and their polarizations. So it can be seen that different microwave imaging systems lead to distinct sensing matrices and thus affect the information content of the observation datasets. Therefore, the sensing matrix provides important implications on the quality of image reconstruction. Theoretically, to accurately

reconstruct the contrast functions of the targets, a great number of measurements of the scattered fields acquired at different transceiver positions, signal frequencies and polarizations are needed.

However, due to some practical constraints (i.e., cost, space, and bandwidth) of the imaging systems, only a small number of measurements of the scattered EM field can be collected. The measured signals are written as

$$\mathbf{y} = \mathbf{H}\mathbf{s} + \mathbf{n} = \mathbf{A}\chi + \mathbf{n} \quad (5.2)$$

where $\mathbf{H} \in \mathbb{R}^{M \times N}$ is the selection matrix whose rows are the standard bases $\mathbf{e}_{s_i}^T$ s (\mathbf{e}_k is a column vector whose k -th element is non-zero), and $i = \{1, 2, \dots, M\}$. The selected M rows from \mathbf{D} indexed by $\{s_1, s_2, \dots, s_M\}$ form the observation matrix $\mathbf{A} \in \mathbb{C}^{M \times m}$ and each row in \mathbf{A} is an observation vector related to a specific antenna position, frequency and polarization. $\mathbf{n} \in \mathbb{C}^M$ is the measurement error of Gaussian process with zero mean and $\sigma^2 \mathbf{I}$ the covariance matrix. Assuming $M \geq m$ measurements are acquired by the imaging system, the least squares estimate of the contrast function is given by

$$\hat{\mathbf{x}} = \mathbf{A}^\dagger \mathbf{y} = (\mathbf{A}^H \mathbf{A})^{-1} \mathbf{A}^H \mathbf{y} \quad (5.3)$$

where $\mathbf{A}^\dagger = (\mathbf{A}^H \mathbf{A})^{-1} \mathbf{A}^H$ is the pseudo-inverse of \mathbf{A} . The accuracy of the reconstructed $\hat{\mathbf{x}}$ with the observation matrix \mathbf{A} can be examined via the metrics:

- Mean square error (MSE)

$$\begin{aligned} \text{MSE}(\hat{\mathbf{x}}) &= \mathbb{E}[||\hat{\mathbf{x}} - \mathbf{x}||_2^2] \\ &= \sigma^2 \text{tr}(\Gamma^{-1}) = \sigma^2 \sum_{i=1}^m \frac{1}{\lambda_i} = \sigma^2 \|\mathbf{A}^\dagger\|_F^2 \end{aligned} \quad (5.4)$$

where $\Gamma = \mathbf{A}^H \mathbf{A}$, and $\lambda_1 \geq \lambda_2 \geq \dots \geq \lambda_m$ are its non-increasing eigenvalues.

- Worst case error variance (WCEV)

$$\text{WCEV}(\hat{\mathbf{x}}) = \lambda_{\max}(\sigma^2 \Gamma^{-1}) = \sigma^2 \frac{1}{\lambda_m} = \sigma^2 \|\mathbf{A}^\dagger\|_2^2 \quad (5.5)$$

where $\lambda_{\max}(\cdot)$ represents the maximum eigenvalue of a matrix.

In (5.4) and (5.5), notations $\|\cdot\|_F$, $\|\cdot\|_2$ and $\|\cdot\|^2$ represent the Frobenius norm, l_2 norm, and norm square, respectively. From (5.4) and (5.5), One can see that the MSE and WCEV are closely related as $\text{MSE}(\hat{\mathbf{x}}) \leq m \text{WCEV}(\hat{\mathbf{x}})$. By minimizing the

WCEV, the MSE is also minimized. Besides, the condition number of the observation matrix \mathbf{A} is often used to indicate the sensitivity of the estimation of \mathbf{x} with respect to the error of the measurement data and defined by

$$\text{CondNo}(\mathbf{A}) = \sqrt{\lambda_1 / \lambda_m} \quad (5.6)$$

As $\lambda_1 \geq \lambda_m$, the condition number of \mathbf{A} is not less than one. If the condition number is small, then small changes in the measurement data will result in a small error in the estimation of \mathbf{x} . Otherwise, small changes in the measurement data will lead to a large error in the estimation of \mathbf{x} .

According to (5.4)–(5.6), MSE, WCEV, and the condition number are all dependent on the eigenvalues of the matrix Γ , thus fully depending on the observation matrix \mathbf{A} . For microwave imaging, the observation matrix \mathbf{A} is a function of antenna positions, polarizations and frequencies. So the recovery performance of matrix \mathbf{A} can be optimized by properly choosing the antenna positions, polarizations, and the frequencies. Hence, the above linear system formulation provides a unified framework to explore spatial-, polarization- and frequency-diversities for microwave imaging system design.

5.2.2 Problem Statement

Here we assume that the imaging system works over a certain bandwidth and the antenna polarizations are fixed at each position. Only the spatial sampling of synthetic volume array, i.e., E-RadSAR, for 3-D imaging is considered below.

In principle, the 3-D spatial sampling problem of the E-RadSAR can be handled by transforming to a sensor/observation selection problem. As the E-RadSAR is implemented by utilizing synthetic aperture technique in both cross- and down-range directions, the related sensor/observation selection procedure is naturally divided into two steps: (1) selecting a specific number of sensors (antennas); (2) determining the spatial sampling strategy for each antenna performed with a SAR technique in cross- and down-range directions. Actually, both steps can be addressed by searching over a set of candidate positions for sensors/observations to find an optimal or near-optimal subset.

Assume there are L initial candidate positions for the antennas. Taking advantage of the SAR technique, each candidate antenna takes D measurements with respect to q spatial positions in a volume and p discrete frequencies in the operational bandwidth, where $D = p \cdot q$. So $N = L \cdot D$ measurements, in total, can be collected and their corresponding observation vectors form the initial sensing

matrix $\mathbf{D} \in \mathbb{C}^{N \times m}$, which is generally an extremely large matrix. Due to some practical constraints on, for instance, space and weight, only a few (saying M) antennas could be used in the imaging system. So the first step for the sampling design of the E-RadSAR is to select M antennas from the L candidates. As one antenna acquires D measurements, the corresponding observation vectors contribute to D rows in the sensing matrix. Hence, choosing one antenna means selecting D rows in \mathbf{D} . With all the observation vectors related to the M selected antennas, a new matrix, denoted as $\tilde{\mathbf{D}} \in \mathbb{C}^{(M \cdot D) \times m}$, can be constructed. Analogously, the 3-D spatial samples of each antenna are selected in the second step. At each spatial candidate position, a selected antenna collects p measurements over the operational bandwidth. So selecting one spatial position suggests choosing p corresponding observation vectors in $\tilde{\mathbf{D}}$. The observation vectors associated with all selected spatial positions form the final observation matrix \mathbf{A} . Thus, one can see that selecting a position for either antenna or spatial samples from the set of candidates implies to choose multiple observation vector (i.e., a small matrix) from the initial sensing matrix, which is different from the traditional sensor selection problem where one observation vector is typically selected at a time.

Based on the above analysis, both steps of the sampling design for the E-RadSAR can be formulated as a vector measurement selection problem. For the convenience of description, we denote the set of the N candidate positions (for either antenna or spatial samples) as $\mathcal{N} = \{1, 2, \dots, N\}$ and the set of M selected positions $\mathcal{S} = \{s_1, s_2, \dots, s_M\}$. The initial sensing matrix $\tilde{\mathbf{A}} = [\Phi_1, \Phi_2, \dots, \Phi_N]^T \in \mathbb{C}^{(N \cdot Q) \times m}$ (which corresponds to either \mathbf{D} or $\tilde{\mathbf{D}}$ mentioned above), where $\Phi_i^T \in \mathbb{C}^{Q \times m}$ is the submatrix contributed from the i th candidate position and Q is the number of the observation vectors associated. Then, the sensor/observation placement problem with vector measurement can be formally expressed as follows.

Problem 1 *Giving the initial sensing matrix $\tilde{\mathbf{A}} = [\Phi_1, \Phi_2, \dots, \Phi_N]^T \in \mathbb{C}^{(N \cdot Q) \times m}$, where $\Phi_i^T \in \mathbb{C}^{Q \times m}$, select M submatrices of $\tilde{\mathbf{A}}$ indexed with $[s_1, s_2, \dots, s_M]$ in \mathcal{N} to construct an observation matrix $\mathbf{A} = [\Phi_{s_1}, \Phi_{s_2}, \dots, \Phi_{s_M}]^T \in \mathbb{C}^{(M \cdot Q) \times m}$, such that the estimation error is small enough and the number of selected submatrices is minimized.*

It can be found that the *Problem 1* is very similar to the one addressed in [12] except that block submatrices instead of individual rows are selected here. By consecutively tackling the *Problem 1* for antenna and their spatial observation selection, the sampling strategy of the E-RadSAR can be determined. Actually, the *Problem 1* was also considered in [15] and [9]. However, the proposed CSBS and convex re-

laxed methods are still very expensive computationally. To address *Problem 1*, we next present two new algorithms, i.e., clustered FrameSense and clustered MPME, developed for efficiently selecting clustered sensors/observations with sufficient optimality.

5.3 Clustered FrameSense

5.3.1 Frame Potential

Frames are a more general concept than bases [20]. A frame is an over-complete set of vectors which yield expansions that are not necessarily unique for a vector in the finite dimensional space. So a frame must have at least as many vectors as the number of the dimensions of the space.

Frame potential (FP) is a scalar property of the frame and it describes the orthogonality of the frames. For a matrix $\Psi_{\mathcal{L}} = [\psi_1, \dots, \psi_L]^T \in \mathbb{C}^{L \times n}$ and $L > n$, its frame potential is defined as

$$\text{FP}(\Psi_{\mathcal{L}}) = \sum_{i,j \in \mathcal{L}} |\langle \psi_i, \psi_j \rangle|^2 \quad (5.7)$$

where $\psi_i \in \mathbb{C}^n$ whose transpose is the i -th row of $\Psi_{\mathcal{L}}$, and $\mathcal{L} = \{1, 2, \dots, L\}$. $\langle \cdot \rangle$ and $|\cdot|$ represent the inner product and absolute value, respectively. If the rows of $\Psi_{\mathcal{L}}$ have unit norm and form a unit-norm tight frame, then it has the minimum FP compared to other matrices of the same size formed with unit-norm vectors. Thus, the row vectors of $\Psi_{\mathcal{L}}$ are as close to orthogonal as possible. Consequently, the unit-norm tight frame $\Psi_{\mathcal{L}}$ is the matrix that achieves the minimum MSE for each component. In addition, from (5.7), one can see that the FP is defined as the sum of squared modulus of the inner product of the row vectors of a matrix. So minimizing the FP is equivalent to, roughly speaking, minimizing the correlation among the observation vectors.

5.3.2 The Algorithm

By minimizing the FP of the observation matrix, the FrameSense has been proposed for near-optimal sensor selection [10]. Here we apply the FrameSense to optimize spatial sampling positions/sensor with vector measurements (instead of the case of single sensor for single measurement). Based on the FrameSense algorithm, each time, the candidate position that maximally increases the FP of the observation

Algorithm 5.1: Clustered FrameSense

- 1 Input:** Linear model $\tilde{\mathbf{A}} = \{\Phi_1, \Phi_2, \dots, \Phi_N\}^\top \in \mathbb{C}^{(N \cdot Q) \times m}$, where $\Phi_i^\top \in \mathbb{C}^{Q \times m}$; Number of candidate positions N
 - 2 Output:** $\mathbf{A} \in \mathbb{C}^{(M \cdot Q) \times m}$; Selected sample positions \mathcal{S}
 - 3 1) Initialization:** the set of candidate positions $\mathcal{N} = \{1, 2, 3, \dots, N\}$; the set of sample positions $\mathcal{S} = \mathcal{N}$; the set of sample positions to be removed $\mathcal{R} = \emptyset$; $k = 1$
 - 4 2) Determine the M spatial sample positions.**
 - 5** (a) Find the optimal submatrix $i^* = \arg \max_{i \in \mathcal{L}} F(\mathcal{R} \cup i)$.
 - 6** (b) Update the set of removed sample positions $\mathcal{R} = \mathcal{R} \cup i^*$.
 - 7** (c) Update the set of sample positions $\mathcal{S} = \mathcal{S} \setminus i^*$.
 - 8** (d) If $k \leq N - M$, then $k = k + 1$ and repeat the steps (a)-(c); otherwise, stop.
-

matrix is removed. The cost function is written as [10]

$$F(\mathcal{R}) = \text{FP}(\tilde{\mathbf{A}}) - \text{FP}(\tilde{\mathbf{A}}_{\mathcal{N} \setminus \mathcal{R}}) \quad (5.8)$$

where \mathcal{N} is the set of candidate positions with respect to $\tilde{\mathbf{A}}$, \mathcal{R} is the position to be evaluated. Note in our case eliminating one sampling position indicates to remove Q corresponding rows in the observation matrix $\tilde{\mathbf{A}}$. So we name it as Clustered FrameSense (CFS). Its operation steps are shown in Algorithm 5.1.

As indicated in [10], the cost function (5.7) is a submodular function which guarantees that the greedy maximization algorithm returns a solution with a predictable optimality. In CFS the cost function (5.8) is evaluated by removing Q rows, i.e., a small matrix at a time, so the computational cost is reduced compared to the traditional FrameSense method where one observation vector is removed each time. The computational complexity of the clustered FrameSense can be analyzed as follows. As we have an initial sensing matrix $\tilde{\mathbf{A}} \in \mathbb{C}^{(N \times Q) \times m}$ associated with the N candidate positions. To select M positions from the N candidates, then $N - M$ of them should be removed through the “worst-out” strategy of the FrameSense. To determine the k -th position to be removed, the computational cost is $O(2m[(N - k + 1)Q]^2)$. So the total computational complexity can be estimated as $O\left(2 \sum_{k=1}^{N-M} m[(N - k + 1)Q]^2\right) = O\left(\frac{2}{3}(N^3 - M^3)Q^2m\right)$. If the matrix $\tilde{\mathbf{A}}\tilde{\mathbf{A}}^H$ can be stored, then the computational complexity can be reduced to be $O(2mN^2Q^2)$.

5.4 Clustered Maximal Projection on Minimal Eigenspace

The Maximal Projection on Minimal Eigenspace (MPME) approach [12] was proposed to select the minimum number of sensors one by one for linear inversion problems. For convenience, we briefly describe it first. Then the developed clustered MPME as well as its efficient implementation are presented.

5.4.1 MPME

The objective of the MPME algorithm is, in essence, to select the minimum number of sensors such that their observation vectors form an observation matrix with m significant singular values. The basic idea of the MPME algorithm is to select the sensor that brings the most complementary information to that of the existing ones at a time. Assume an observation matrix $\mathbf{A}_{k-1} \in \mathbb{C}^{(k-1) \times m}$ is formed by the observation vectors related to the first $k - 1$ selected samples. Its singular value decomposition (SVD) $\mathbf{A}_{k-1} = \mathbf{U}\Sigma\mathbf{V}^H$, where $\mathbf{U} \in \mathbb{C}^{(k-1) \times (k-1)}$ and $\mathbf{V} \in \mathbb{C}^{m \times m}$ are left and right unitary matrices, and $\Sigma \in \mathbb{R}^{(k-1) \times m}$ is a diagonal matrix with the non-negative real numbers in the diagonal. The column vectors of \mathbf{U} and \mathbf{V} span the data space and the object's space, respectively. So to get an observation matrix for unambiguous reconstruction of the object, the most efficient observations are those that gradually expand the dimension of data space to be close or equal to that of the object's space. So it is better to select as the k th sensor/observation the one that brings the most complementary information with respect to the existing $k - 1$ ones. Specifically, when the number of the sensors/observations is less than that of the unknowns in the beginning, i.e., $k \leq m$, the observation vector that has the largest component (i.e., projection) in the null space of the observation matrix \mathbf{A}_{k-1} expands the dimension of the data space and contributes the most complementary information. Thus, the corresponding sensor/observation should be the k th selection. Inserting the newly selected observation vector into \mathbf{A}_{k-1} , the new observation matrix \mathbf{A}_k is constructed with the row dimension increased by one. Accordingly, it also increases the number of significant singular values of \mathbf{A}_k . When $k > m$, the rows of the observation matrix \mathbf{A}_{k-1} form an over-complete set of bases for its row space and the observation matrix has m non-zero singular values. To reduce the estimation errors of the solution (see (5.4) and (5.5)), the observation vector of a new sensor should increase the minimum singular value of the updated observation matrix \mathbf{A}_k (equivalently, to increase the minimum eigenvalues of the matrix $\mathbf{A}_k^H \mathbf{A}_k$ [12]). This is implemented by selecting the sensor whose observation vector has the largest projection onto the subspace spanned by the eigenvector(s) associated

with the minimum eigenvalue(s) of $\mathbf{A}_{k-1}^H \mathbf{A}_{k-1}$. In [12], the subspace spanned by the eigenvectors associated with the minimum eigenvalues of $\mathbf{A}^H \mathbf{A}$ is defined as its minimum eigenspace.

5.4.2 CMPME Algorithm

In this section, the MPME is further developed to tackle the problem of selecting the sensors/observations with vector measurements, named as clustered MPME (CMPME). In this case, selecting a sensor results in selecting a set of associated observation vectors (Q vectors as indicated above) at a time and these observation vectors are added as rows into the observation matrix \mathbf{A}_{k-1} to form a new one \mathbf{A}_k . To determine the optimal sensor to be selected, it is essential to evaluate how the Q observation vectors affect the eigenvalue system of the “dual observation matrix” $\mathbf{A}_{k-1}^H \mathbf{A}_{k-1}$ (equivalently, the effect on the singular value system of the observation matrix \mathbf{A}_{k-1}), which typically uses the projection of the selected rows onto the minimum eigenspace of the “dual observation matrix” $\mathbf{A}_{k-1}^H \mathbf{A}_{k-1}$ as a metric in MPME. However, besides examining the projection of the selected rows onto the minimum eigenspace of $\mathbf{A}_{k-1}^H \mathbf{A}_{k-1}$, to what extent the rows of the selected small matrix are mutually orthogonal should be checked as well. When the observation vectors associated with two sensors have equal projections onto the minimum eigenspace of “dual observation matrix”, the one with a more mutually orthogonal set of observation vectors is preferred. This can be derived as follows. If we allow the observation vectors associated with a sensor to be selected individually, each time the observation vector that has the largest projection onto the minimum eigenspace of $\mathbf{A}_{k-1}^H \mathbf{A}_{k-1}$ is picked up. If the number of rows of \mathbf{A}_{k-1} is smaller than m , the minimum eigenspace of $\mathbf{A}_{k-1}^H \mathbf{A}_{k-1}$ is the null space of \mathbf{A}_{k-1} . So the newly selected observation vector is always to the largest extent “orthogonal” to the existing rows in the observation matrix. This is also true for the last Q selected observation vectors. However, now we have to select Q vectors as a group at a time. So it is natural that the newly selected Q observation vectors should not only have the largest projection onto the minimum eigenspace of $\mathbf{A}_{k-1}^H \mathbf{A}_{k-1}$ but also be to the largest extent mutually “orthogonal”.

To quantitatively assess the orthogonality among the Q observation vectors of a sensor, the inner products among their corresponding normalized vectors are conducted. As we prefer the sensors whose observation vectors are more close to orthogonal, the inner products among them should be more close to zeros. Combining both the projection of the new observation vectors onto the minimum eigenspace and their orthogonality, the optimal sensor can be selected by maximizing the cost

function

$$\text{Cost}(\Phi_{s_k}) = \|\mathbf{P}_{k-1}\Phi_{s_k}\|_F^2 - \eta \left(\sum_{i,j=1}^Q |\langle \tilde{\varphi}_i, \tilde{\varphi}_j \rangle|^2 \right) \quad (5.9)$$

where Φ_{s_k} is the small matrix formed by the Q observation vectors $\varphi_i, i = 1, \dots, Q$, and $\tilde{\varphi}_i$ is the normalized vector of φ_i . \mathbf{P}_{k-1} is the projection operator onto the minimum eigenspace of $\mathbf{A}_{k-1}^H \mathbf{A}_{k-1}$. η is a regularization(-like) term that controls the importance of the orthogonality among the new observation vectors. Actually, the second term of the cost function is related to the inverse frame potential of the new sensor. Therefore, to some extent, this cost function can be considered as a combination of the projection and the frame potential.

The projection operator at each step can be obtained in a similar way as in [12]. When $k \cdot Q \leq m$, the minimum eigenspace of $\mathbf{A}_{k-1}^H \mathbf{A}_{k-1}$ is the null space of \mathbf{A}_{k-1} . Then the projection matrix \mathbf{P}_{k-1} onto the minimum eigenspace of $\mathbf{A}_{k-1}^H \mathbf{A}_{k-1}$ can be given by

$$\mathbf{P}_{k-1} = \mathbf{I}_{m \times m} - \mathbf{R}_{k-1} \mathbf{R}_{k-1}^H \quad (5.10)$$

where \mathbf{I} is the identity matrix and $\mathbf{R}_{k-1} = \text{orth}(\mathbf{A}_{k-1}^H)$ whose column vectors are obtained through the Gram-Schmidt (G-S) Orthonormalization of all the column vectors of \mathbf{A}_{k-1}^H [21]. When $k \cdot Q > m$, the projection matrix \mathbf{P}_{k-1} is written as

$$\mathbf{P}_{k-1} = \mathbf{U}_m^{(k-1)} (\mathbf{U}_m^{(k-1)})^H \quad (5.11)$$

where $\mathbf{U}_m^{(k-1)} = [\mathbf{u}_{m-\mu_n+1}^{(k-1)}, \mathbf{u}_{m-\mu_n+2}^{(k-1)}, \dots, \mathbf{u}_m^{(k-1)}] \in \mathbb{C}^{m \times \mu_n}$. $\mathbf{u}_{m-\mu_n+1}^{(k-1)}, \mathbf{u}_{m-\mu_n+2}^{(k-1)}, \dots, \mathbf{u}_m^{(k-1)}$ are the eigenvectors of the smallest eigenvalue of $\mathbf{A}_{k-1}^H \mathbf{A}_{k-1}$ with multiplicity μ_n .

After getting the projection matrix in each iteration, the cost function (5.9) can be evaluated for the selection. The detailed CMPME operations are shown in Algorithm 5.2. In its implementation, the cost function evaluation causes the dominant computational cost. To determine the k -th spatial sample position, it costs $O(m^2(N - k + 1)Q + mQ^2(N - k + 1))$. Therefore, the total complexity cost can be estimated as $O((m^2 + mQ)NQM)$.

5.4.3 Efficient Implementation

In Algorithm 5.2, two most computationally expensive steps are to evaluate the cost functions with respect to the observation vectors of each candidate sample (line 6 or 10) and to compute and update the set of orthonormal bases (line 7 or 11). As the cost function of each candidate sample is evaluated with respect to the same set of orthonormal bases, so it can be implemented by parallel computing.

Algorithm 5.2: Clustered Maximal Projection on Minimum Eigenspace

-
- 1 Input:** $\tilde{\mathbf{A}} = \{\Phi_1, \Phi_2, \dots, \Phi_N\}^\top \in \mathbb{C}^{(N \cdot Q) \times m}$, where $\Phi_i^\top \in \mathbb{C}^{Q \times m}$
- 2 Output:** $\mathbf{A} \in \mathbb{C}^{(M \cdot Q) \times m}, \mathcal{S}, M$
- 3 1) Initialization:** $\mathcal{N} = \{1, 2, \dots, N\}, \mathcal{S} = \emptyset$.
- 4 2) Determine the first $n = \lceil \frac{m}{Q} \rceil$ sampling positions:**
- 5 (a) Set $\mathbf{A}_0 = []$, $\mathbf{P}_0 = \mathbf{I}_{n \times n}$ and $k = 1$.
- 6 (b) $\hat{s}_k = \arg \max_{i \in \mathcal{N} \setminus \mathcal{S}} \text{Cost}(\Phi_i)$.
- 7 (c) Update: $\mathcal{S} = \mathcal{S} \cup \{\hat{s}_k\}$, $\mathbf{A}_k = [\mathbf{A}_{k-1}^\top \quad \Phi_{\hat{s}_k}]^\top$, $\mathbf{R}_k = \text{orth}(\mathbf{A}_k^H)$,
 $\mathbf{P}_k = \mathbf{I}_{m \times m} - \mathbf{R}_k \mathbf{R}_k^H$.
- 8 (d) Set $k = k + 1$ and repeat steps (b-c) until $k = n$.
- 9 3) Determine the remaining sampling positions:**
- 10 (a) $\hat{s}_k = \arg \max_{i \in \mathcal{N} \setminus \mathcal{S}} \text{Cost}(\Phi_i)$.
- 11 (b) Update: $\mathcal{S} = \mathcal{S} \cup \{\hat{s}_k\}$, $\mathbf{A}_k = [\mathbf{A}_{k-1}^\top \quad \Phi_{\hat{s}_k}]^\top$, $\mathbf{A}_k^H = \mathbf{U}_k \boldsymbol{\Sigma}_k \mathbf{V}_k^H$,
 $\mathbf{P}_k = \mathbf{U}_m^{(k)} (\mathbf{U}_m^{(k)})^H$.
- 12 (c) If $\lambda_m^{(k)} > \gamma$ return $\mathcal{S}, M = k$ and $\mathbf{A} = \mathbf{A}_k$; else set $k = k + 1$ and repeat
steps (a-b).
-

For the update of the orthonormal bases and projection operator, the computation load can be significantly reduced by iterative computing. More specifically, the orthonormal bases \mathbf{R}_{k-1} (in line 7) are computed through the orthonormalization of the column vectors of \mathbf{A}_{k-1}^H and then expanded to \mathbf{R}_k after appending new observation vectors $\Phi_{\hat{s}_k}$ to \mathbf{A}_{k-1} , which can be expressed as $\mathbf{R}_k = \text{orth}(\mathbf{A}_k^H) = \text{orth}([\mathbf{A}_{k-1}^H \quad \Phi_{\hat{s}_k}^*])$, and the superscript * represents the complex conjugate. As in the previous iteration $\mathbf{R}_{k-1} = \text{orth}(\mathbf{A}_{k-1}^H)$ has been computed and orthonormal column vectors are obtained, \mathbf{R}_k can be updated by only orthonormalizing $\Phi_{\hat{s}_k}^*$ relative to \mathbf{R}_{k-1} via a Gram-Schmidt process. After obtaining \mathbf{R}_k , the projection operator \mathbf{P}_k can also be updated. This update process can be expressed as

$$\begin{aligned} \mathbf{P}_k &= \mathbf{I}_{m \times m} - \mathbf{R}_k \mathbf{R}_k^H \\ &= \mathbf{I}_{m \times m} - \mathbf{R}_{k-1} \mathbf{R}_{k-1}^H - \text{orth}(\Phi_{\hat{s}_k}^*; \mathbf{R}_{k-1}) \text{orth}(\Phi_{\hat{s}_k}^*; \mathbf{R}_{k-1})^H \\ &= \mathbf{P}_{k-1} - \text{orth}(\Phi_{\hat{s}_k}^*; \mathbf{R}_{k-1}) \text{orth}(\Phi_{\hat{s}_k}^*; \mathbf{R}_{k-1})^H. \end{aligned} \quad (5.12)$$

where $\text{orth}(\Phi_{\hat{s}_k}^*; \mathbf{R}_{k-1})$ denotes the new orthonormal bases of $\Phi_{\hat{s}_k}^*$ relative to \mathbf{R}_{k-1} . So one can see that the cost function can be updated by just computing the projections of the observation vectors of the remaining sensors with respect to the second term in the last line of (5.12). As the column dimension of $\text{orth}(\Phi_{\hat{s}_k}^*; \mathbf{R}_{k-1})$ is much

smaller than that of \mathbf{R}_k , i.e., $Q \ll m$, the computational load for the cost function evaluation in line 6 is substantially reduced through a sequential update in each iteration.

In line 11, the column vectors of \mathbf{U} form a set of orthonormal bases, which is obtained through SVD: $\mathbf{A}_k^H = \mathbf{U}_k \boldsymbol{\Sigma}_k \mathbf{V}_k^H$. As the dimensions of matrix \mathbf{A}_k typically are of hundreds and thousands in the imaging case, the SVD of \mathbf{A}_k is very computationally expensive. Considering the fact that \mathbf{A}_k is obtained by appending a small matrix $\Phi_{\hat{s}_k}$ to the row space of \mathbf{A}_{k-1} , then its SVD can be obtained by consecutively performing Q times rank-1 update to the SVD of \mathbf{A}_{k-1} [22, 23]. In addition, we have to mention that these efficient implementation methods can also be used to accelerate the traditional MPME algorithm.

5.5 Imaging Examples

This section presents some examples to show the imaging performance of antenna arrays optimized with the proposed algorithms, i.e., CFS and CMPME. For comparison, the simulations were also carried out with CSBS [15] and the convex relaxed method [9]. The convex relaxed method was solved by using the SDPT3 software package which is a Matlab software for semidefinite-quadratic-linear programming [24].

5.5.1 Planar Array Imaging

Firstly, a circular planar array based imaging in free space is presented to demonstrate the performance of the four methods for antenna array optimization. Assume that a circular planar array of radius 0.5 m is used for signal acquisition and it is located on the xoz plane. The y -axis points towards the illuminated region and forms a right-hand coordinate system with the x - and z -axes. The operational bandwidth is from 2 to 6 GHz. The scene of interest is a volume with the shortest distance of 0.5 m from the array and its dimensions are $0.6 \text{ m} \times 0.2 \text{ m} \times 0.6 \text{ m}$ in the x -, y - and z -axes, respectively. So the cross-range and down-range resolution can be estimated as 2.25 cm and 3.75 cm, respectively. Considering the computational time for the simulation, we divide the scene of interest into voxels with dimensions of $5 \text{ cm} \times 5 \text{ cm} \times 5 \text{ cm}$. So the whole imaging volume contains 845 voxels. In the circular antenna array, the candidate spatial samples of the antennas lie on a series of circles with radii ranging from 0.05 m to 0.5 m with steps of 5 cm. In azimuth, the sampling interval is 6° . Therefore, we have 600 candidate spatial samples within the aperture in total. Moreover, at each spatial sampling position, an antenna takes

41 measurements at the frequencies sweeping from 2 to 6 GHz with steps 100 MHz.

In the simulation, the near-field signal model is used to generate each measurement

$$s(\mathbf{x}_a, f) = \int_V \chi(\mathbf{x}) \cdot \frac{\exp(-j4\pi f R/c)}{4\pi R} dV \quad (5.13)$$

where \mathbf{x}_a and \mathbf{x} represent the antenna's and the scatterers' positions, respectively. c is the wave propagation velocity, f is the signal frequency, $\chi(\cdot)$ is the reflectivity function and $R = |\mathbf{x} - \mathbf{x}_a|$ is the distance between the antenna and the scatterer.

Setting $\chi(\mathbf{x}) = 1$ and applying the spatial box window at each voxel in (5.13), the initial sensing matrix $\tilde{\mathbf{A}} \in \mathbb{C}^{24600 \times 845}$ associated with all the candidate spatial samples can be constructed.

Based on the aforementioned simulation setup, the spatial samples for a circular planar array are selected with CMPME, CFS, CSBS, and convex relaxed method. Here as long as a spatial sampling position is selected, the observation vectors corresponding to all the 41 frequencies are chosen. Assume \mathbf{n} is independent and identically distributed (i.i.d.) Gaussian noise, with the variance $\sigma^2 = 1$. Then the MSE, WCEV and condition numbers achieved by the observation matrices constructed with the observation vectors selected by the four methods are presented in Figure 5.1.

From Figure 5.1(a), it can be seen that the spatial samples selected with CMPME achieve smaller MSE, WCEV and condition numbers compared to CFS. Moreover, with sufficient spatial samples (more than 60 spatial samples), CMPME also leads to slightly better selection than CSBS. However, when the number of selected spatial samples is small (less than 50), CSBS performs slightly better than CMPME. This is because CSBS is, similar to CFS, a greedy ‘worst-out’ algorithm, which gradually removes the least informative spatial samples. Then the most informative ones are selected in terms of MSE. By contrast, CMPME takes a sequential forward selection scheme. It gradually adds to the selection set the sample that is most complementary to the existing ones. So the spatial samples selected by CMPME could be less optimal than that selected by CSBS when the number of samples is small. Nevertheless, 50 spatial samples are not sufficient as the MSEs achieved by the observation matrices obtained with both methods are larger than 10^5 . With the increase of the number of selected spatial samples, CMPME and CSBS achieve equivalent performance in terms of MSE. Meanwhile, CFS reaches a comparable but slightly larger MSE compared to CMPME and CSBS. This is due to the fact that in the simulation scenario the distances from different antenna positions to scatterers have very small differences. Namely, the observation vectors associated with each spatial sample have more or less similar norms, in which case

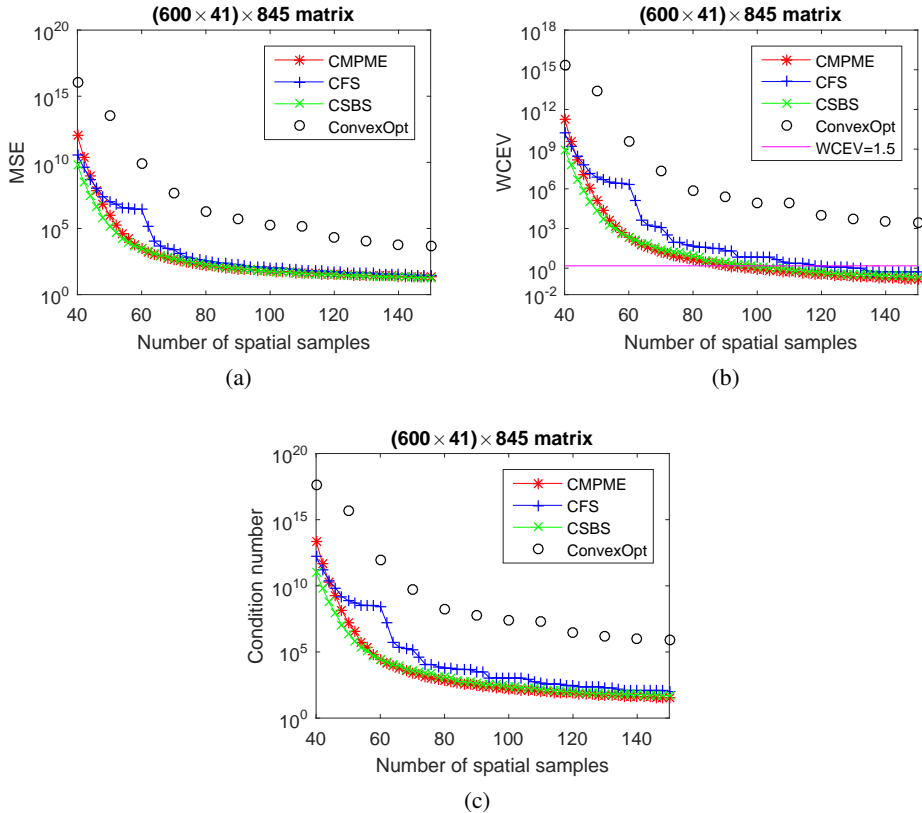


Figure 5.1: Criteria comparison of the three selection approaches. (a) shows the MSEs achieved by the observation matrices with different number of selected spatial sampling positions; (b) for WCEV, and (c) for Condition number.

the frame potential can lead to a near-optimal selection. Therefore, CFS achieves comparable performance as CMPME and a similar phenomenon is also observed for FrameSense and MPME [12]. Furthermore, it is obvious that the observation matrices selected by CMPME, CSBS and CFS arrive at much smaller MSEs than that obtained with the convex relaxed method. So all the CMPME, CSBS, and CFS outperform the convex relaxed method in this case in terms of MSE.

The variations of the WCEVs and condition numbers of the observation matrices obtained with the four methods are shown in Figures 5.1(b) and (c). Similar to the MSE in Figure 5.1(a), the WCEVs and condition numbers rapidly decrease with

the growth of the number of spatial samples. Overall, CMPME and CSBS arrive at better performances than CFS and the convex relaxed method in terms of both WCEV and condition number. Moreover, with sufficient spatial samples, CMPME results in smaller WCEVs and conditions numbers compared to CSBS. If we set the WCEV threshold as 1.5, the numbers of the spatial samples selected by CMPME, CSBS, and CFS are 90, 98 and 118, respectively. Meanwhile, the convex relaxed method leads to more than 150 samples to be selected. Therefore, among the four methods, CMPME selects the minimum number of spatial samples.

To further compare the imaging performance of the arrays obtained with the four methods, we take arrays of 90 spatial samples as an example. The topologies of the circular arrays acquired with the four methods are shown in Figure 5.2. Intuitively, the arrays selected with CMPME and CSBS have a relatively uniform distribution of spatial samples within the aperture while the samples of the array obtained with CFS are mainly located on the circles close to the edge of the aperture. Although the spatial samples selected by the convex relaxed method are also mainly distributed on two circles, they form a smaller effective aperture compared to those acquired with the other three greedy algorithms. Therefore, it would result in, according to array theory, lower cross-range resolution than with the other three arrays.

Imaging simulations were performed for the four arrays with the measurement setup shown in Figure 5.3. Ten point targets were placed on two planes $y = 0.5$ m and $y = 0.7$ m [see Figures 5.3(b) and (c)] and the magnitudes of their reflectivity functions were set to two. The measurement errors and noise were assumed to be zero-mean Gaussian distribution with the variance equal to 1, i.e., $\mathbf{n} \sim \mathcal{N}(0, 1)$ (correspondingly, the signal to noise ratio ≤ 5.6 dB). Taking 50 Monte Carlo simulations each with a different noise realization, the average of the imaging results on the two target planes are presented in Figures 5.4 and 5.5 on a logarithmic scale. For comparison, the truths of the target configurations at the two slices are also shown in Figure 5.4(a) and Figure 5.5(a), respectively. It is obvious that the arrays

Table 5.1: MSEs and WCEVs of the estimated images with the arrays optimized by the four algorithms

Algorithms	CMPME	CFS	CSBS	ConvexOpt
MSE	88.96	185.11	96.06	5.08e+05
WCEV	0.88	2.41	0.96	1.24e+04

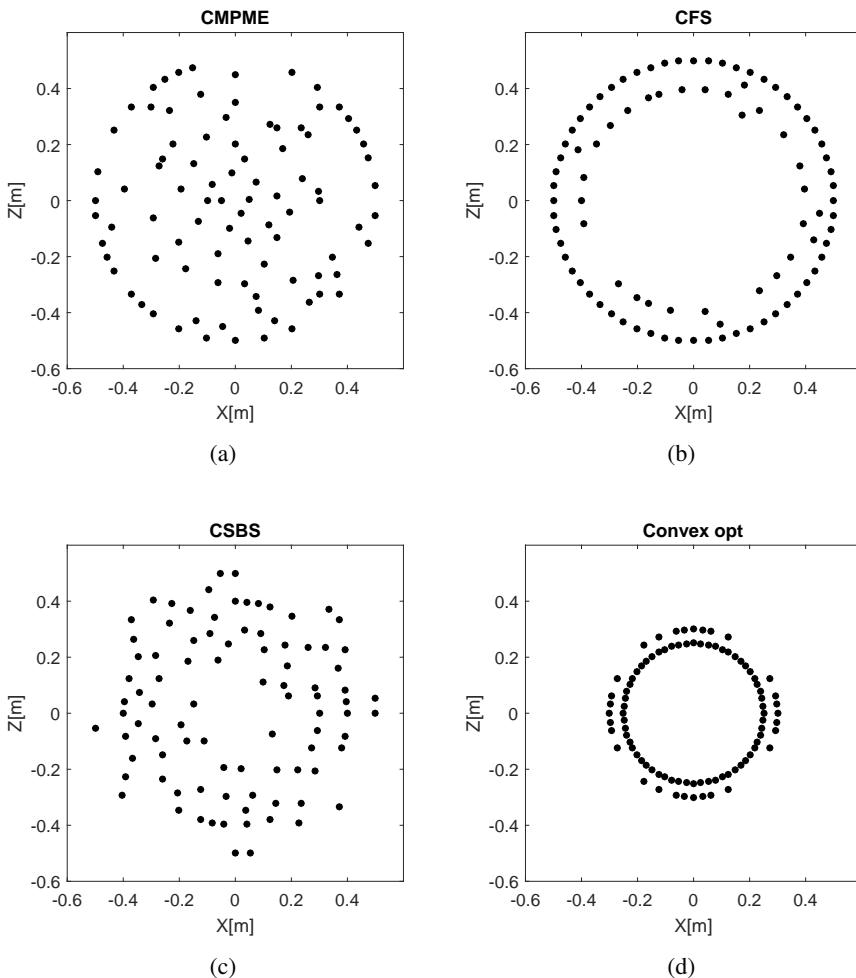


Figure 5.2: Array topologies of 90 selected spatial samples with (a) CMPME, (b) CFS, (c) CSBS, and (d) Convex optimization.

selected with CMPME, CFS, and CSBS result in much better estimations of the imaging scenes in contrast to the array acquired with the convex relaxed method. In the images estimated by the three greedy algorithms, some variations are noticed in the “floor” region compared to their corresponding truths but the differences among them are hard to distinguish visually. The quantitative metrics, i.e.,

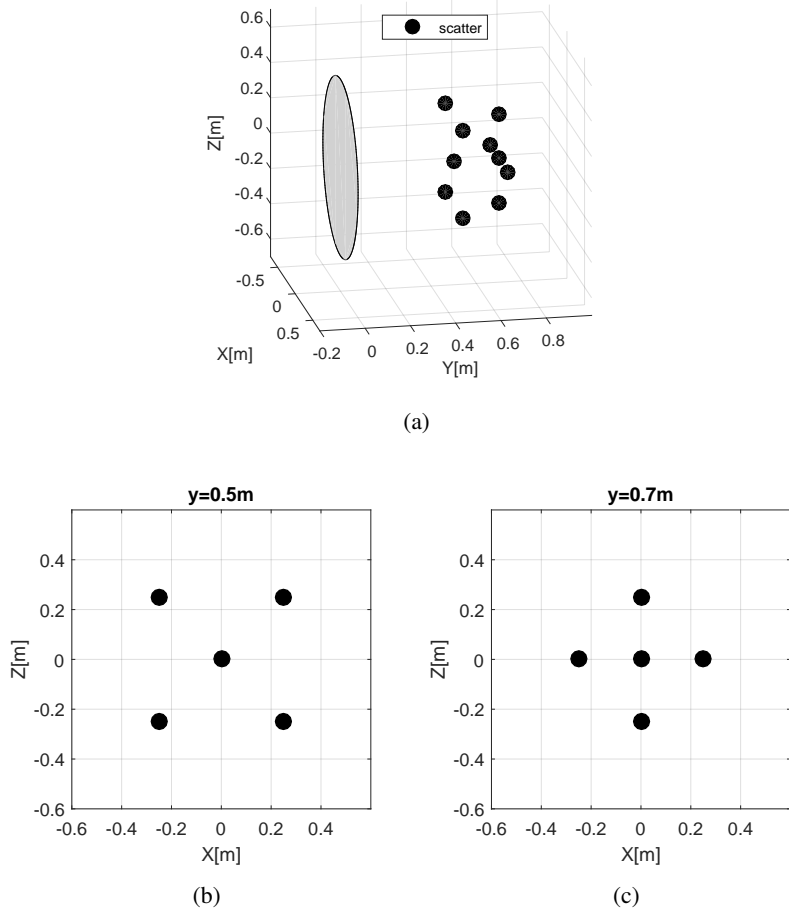


Figure 5.3: Measurement setup for numerical simulations with the four arrays. (a) 3-D view, where the gray area at $y = 0$ indicates the antenna array. (b) slice at $y = 0.5$ m, and (c) slice at $y = 0.7$ m.

MSE and WCEV, of the reconstructed 3-D images were examined and listed in Table 5.1. One can see that the array selected by CMPME achieves the smallest MSE and WCEV for the estimated images while the array obtained with the convex relaxed method leads to the worst estimation of the image. As the $\text{WCEV}=1.5$ (the solid line in Figure 5.1(b)) was used as a threshold to determine the number of spatial samples (i.e., 90 samples), it is indeed achieved with the array designed by CMPME.

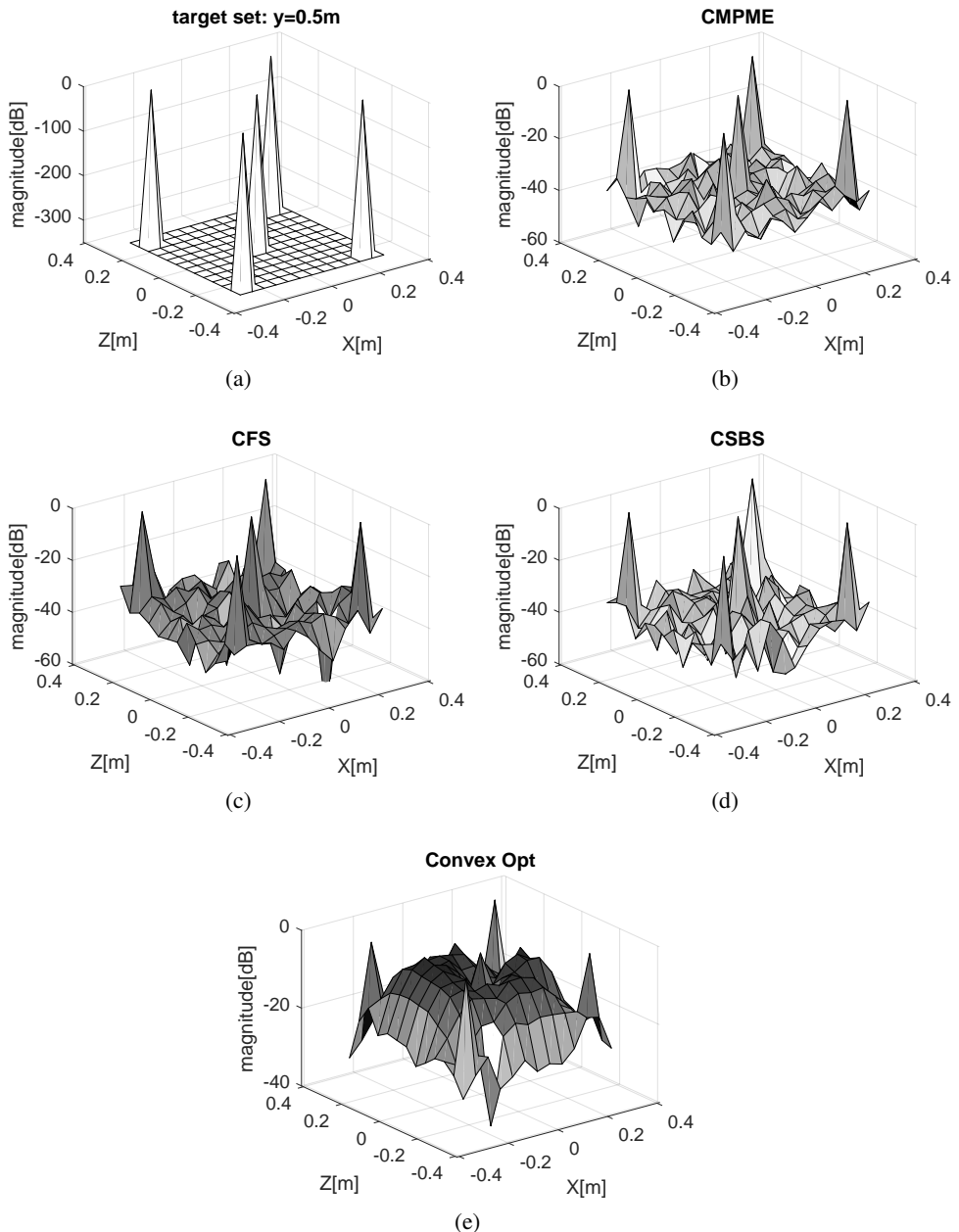


Figure 5.4: Slice images at $y = 0.5$ m for synthetic point scatterer reconstructions. (a) shows the truth, (b) is the slice image estimated with the array optimized using CMPME, (c) is estimated with the array optimized using CFS, (d) is estimated with the array optimized using CSBS, and (e) is estimated with the array optimized using the convex relaxed method.

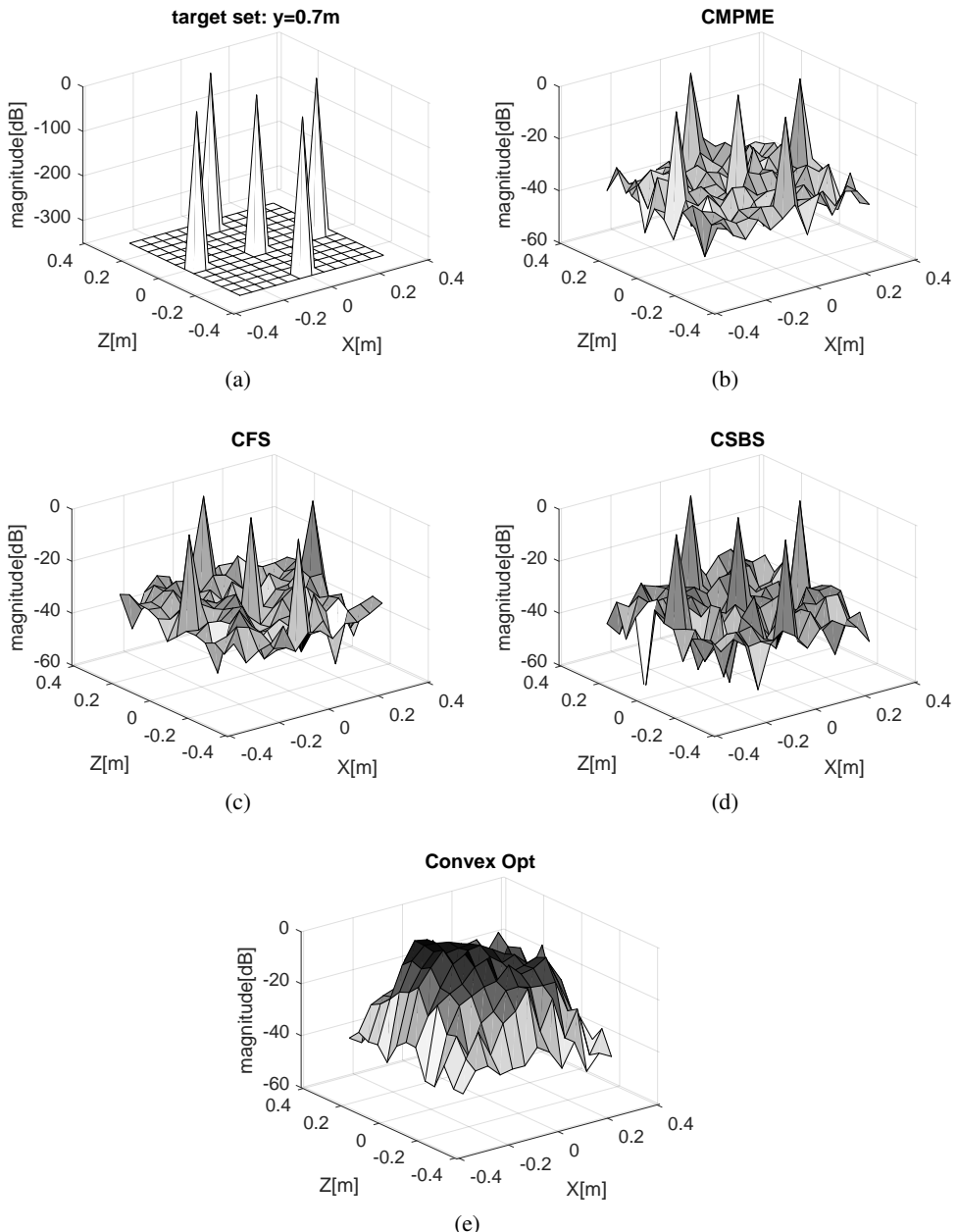


Figure 5.5: Slice images at $y = 0.7\text{ m}$ for synthetic point scatterer reconstructions. (a) shows the truth, (b) is the slice image estimated with the array optimized using CMPME, (c) is estimated with the array optimized using CFS, (d) is estimated with the array optimized using CSBS, and (e) is estimated with the array optimized using the convex relaxed method.

Table 5.2: Computational complexities of the four sensor selection methods

ConvexOpt	CSBS	CFS	CMPME
$O(i_c L^3)$	$O(mNL^2)$	$O(2mL^2)$	$O((m^2 + mQ)ML)$

Table 5.3: Computation time of CMPME, CSBS, CFS and Convex relaxed method to select 90 spatial samples from 600 candidates for planar circular array optimization.

Algorithm	ConvexOpt*	CSBS	CFS	CMPME
Time	4.14h	3.92h	126.4s	91.8s

* 21 iterations were taken.

Finally, the computational complexities of the four sensor/observation selection methods are compared. The computational costs of CFS and CMPME have been discussed in the previous sections. As indicated in [9] and [12], the computational complexity of the convex relaxed method for selecting sensors with vector measurements is $O(i_c N^3 Q^3)$, where i_c is the iterative number of the convex optimization. On the other hand, the CSBS costs $O(mN^3 Q^2)$ [15]. For the convenience of comparison, the computational complexities of the four methods are summarized in Table 5.2, where $L = N \cdot Q$ is used to simplify the notation. As typically $L \gg m, N, Q$, one can see that among the four algorithms, CMPME has the lowest computational complexity followed by CFS. This results from the fact that CMPME is a sequential forward selection approach instead of the sequential backward selection schemes used in CSBS and CFS. This advantage could be even remarkable when the number of selected samples is substantially smaller than that of the candidate samples. For the planar array imaging simulations above, the computational time of the four algorithms also confirms this conclusion, as shown in Table 5.3. In this simulation, the sensor selection simulations were performed on a PC with an Intel Core i5-3470 CPU of 3.2 GHz and 8 GB RAM. All the four methods were implemented in Matlab code. For the convex relaxed method, 21 iterations were automatically performed by the SDPT3 optimization engine. From Table 5.3, one can see that in this simulation CFS and CMPME are more than 100 times faster than the convex relaxed method and CSBS. Moreover, the circular array selected by CMPME achieves a comparable imaging performance as that obtained by CSBS.

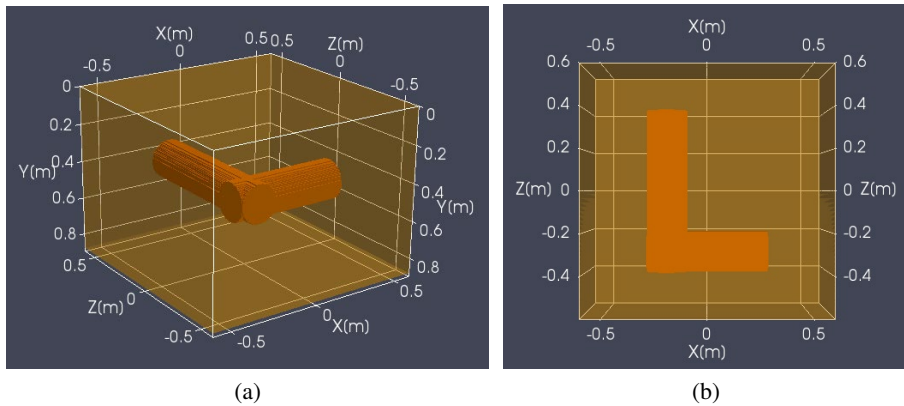


Figure 5.6: Geometrical configuration of GPR numerical simulation. (a) is the 3-D illustration of the simulation setup, and (b) is its xoz -view along the y -axis.

5.5.2 Optimization of the E-RadSAR

In this section, we present the sampling design and optimization of the E-RadSAR for 3-D imaging by using the proposed algorithms. The objective of the sampling design of the E-RadSAR is to explore the potential of utilizing synthetic aperture technique in the down-range direction to reduce the number of antennas needed.

A 3-D subsurface imaging experiment with GPR was performed for illustration of the proposed algorithm for the E-RadSAR design. The experimental configuration is shown in Figure 5.6. Two perpendicularly oriented dielectric cylinders were buried in the soil as the objects and they were joined at one end. The radius of the cylinders is 10 cm and their lengths are 60 cm and 80 cm. The conductivity and relative permittivity of the cylinders are 0.05 S/m and 5.0, respectively. In addition, the permittivity of the background soil is 9.0 and its conductivity 0.01 S/m.² The GPR antennas were placed along a radius of a circle centered at the origin on the ground surface (i.e., xoz -plane in Figure 5.6). The orientations (i.e., polarizations) of the dipole-like antennas were also along the radius. The Ricker wavelet of 900 MHz was used as the excitation signal. To simulate the operation of the GPR system used in the tunnel boring machine (TBM), the GPR signals were acquired over several concentric circles with the rotation of the antennas around the origin. To get

²The dielectric parameters of a few typical geological materials measured at 100 MHz are given by: $\epsilon = 7$ (8), $\sigma = 10^{-8} : 10^{-6}$ ($10^{-2} : 10^{-1}$) for dry (wet) limestone; $\epsilon = 5$ (7), $\sigma = 10^{-8} : 10^{-6}$ ($10^{-3} : 10^{-2}$) for dry (wet) granite; $\epsilon = 5 : 10$, $\sigma = 10^{-4} : 10^{-2}$ for wet sandstone, etc. The dielectric parameters for more materials can be found in [25, 26].

properly focused images of targets at a distance of 0.4 m, a circular planar array aperture of the radius 0.5 m should be used. Based on the polar sampling criteria, eight antennas were placed along a radial direction on eight concentric circles with the radius ranging from 0.15 m to 0.5 m with steps of 5 cm. In azimuth, the signals were sampled every 3° . Therefore, in total 960 spatial samples were obtained over the circular planar array.

To explore the possibility to reduce the number of antennas by taking advantage of the forward motion for 3-D array synthesis, three different depths of the objects, i.e., 0.3 m, 0.4 m, and 0.5 m, relative to the ground surface (i.e., antenna array) were considered to simulate the E-RadSAR. Taking the aforementioned sampling criteria, 2880 spatial samples were acquired over three circular planar arrays at three depths, which form the candidate set for the E-RadSAR sampling design and optimization.

For the convenience of description, let us set $y = 0$ at the closest position of the antenna array to the objects. The imaging volume is a cuboid defined by $[-0.4, 0.4] \text{ m} \times [0.1, 0.5] \text{ m} \times [-0.5, 0.5] \text{ m}$ along the x , y and z directions. The whole volume is discretized as 41820 voxel cells of the dimensions $2 \text{ cm} \times 2 \text{ cm} \times 2 \text{ cm}$ in which the values of voxels represent the reflectivity functions at the corresponding positions. Then the observation vectors of the antenna at each position relative to the imaging volume can be obtained at different frequencies via accurate Green's functions for the scattering process based on the Born approximation [27]. The signal frequencies sweep from 557.8 to 1546.6 MHz with steps of 12.7 MHz to cover the whole bandwidth of the Ricker wavelet. So considering different frequencies, 79 observation vectors are obtained at each sampling position. Stacking all the observation vectors associated with all candidate sampling positions at all frequencies, a candidate sensing matrix $\tilde{\mathbf{A}} \in \mathbb{C}^{(2880 \cdot 79) \times 41820}$ is obtained. The candidate sensing matrix corresponds to the volume array synthesized by using eight antennas, and each antenna contributes 28440 (i.e., $120 \times 3 \times 79$) candidate observation vectors.

To design and optimize the sampling strategy of the 3-D synthetic array, we take two steps: the first step is to select a certain number of antennas from the eight candidate antennas; the second step is to optimize the spatial sampling positions of the selected antennas. Considering the number of voxels in the imaging volume and slight redundancy, at least three antennas should be selected. That is to say, at least three sub-matrices of dimensions 28440×41820 should be chosen. Accounting for the enormous size of the candidate sensing matrix $\tilde{\mathbf{A}}$ and computational time, the first step was implemented by using CFS. The outer-most three antennas within the circular aperture were selected, as shown in Figure 5.7(a).

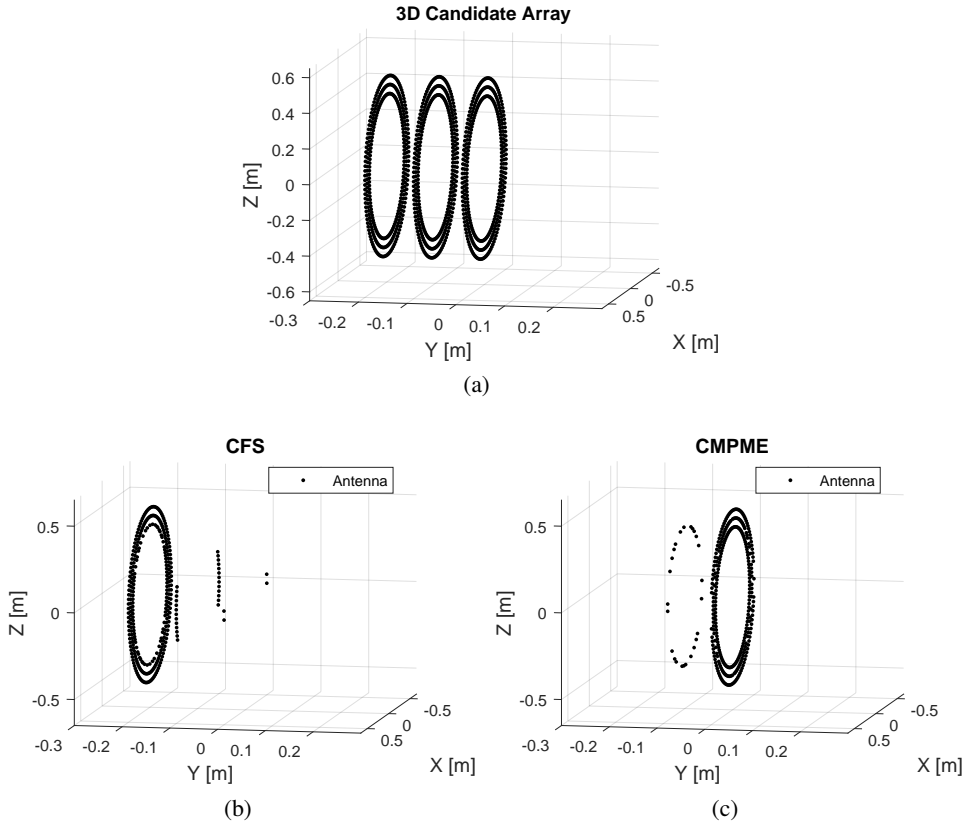


Figure 5.7: Spatial sample selection for 3-D synthetic array. (a) shows the candidate spatial samples of the selected antennas; (b) and (c) show the 350 spatial samples selected for the three antennas with CFS and CMPME, respectively.

Next, the spatial sampling positions of the three selected antennas are selected. Considering both selection performance and computational time, CMPME and CFS were used to select the (near-)optimal spatial samples, and the imaging performance of their selected arrays was compared. In this example, 350 spatial sampling positions were selected for the three antennas. The selected results are shown in Figures 5.7(b) and (c). Comparing Figures 5.7(b) and (c), one can see that the CFS selects mainly the spatial samples that are far from the imaging volume while CMPME selects the nearer ones. This can be explained as follows. CFS gradually eliminates the spatial samples whose observation vectors have the largest frame potential (i.e., correlations) with those of the rest samples, which works optimally for

observation vectors with equal L_2 norms. But for observation vectors with unequal norms, the performance of CFS degrades. Considering attenuation and spreading loss of wave propagation, the observation vectors at the spatial sampling positions closer to the imaging volume have larger L_2 norms than those at a longer distance. So when evaluating the frame potential via the inner product, the observation vectors with larger L_2 norms could lead to larger frame potentials. Thus, the corresponding spatial samples, i.e., those at short range, are discarded, which has been indicated for the traditional FrameSense method in [10]. By contrast, CMPME evaluates the complementary information introduced by the observation vectors associated with a new spatial sample relative to the existing ones, which takes into account the effects of the magnitudes of the vectors. The spatial sampling positions at a shorter distance form relatively diverse observation angles with respect to the imaging volume and their observation vectors have large magnitudes, thus resulting in large projections onto the minimum eigenspace. Consequently, the spatial samples closer to the imaging volume are preferably selected by CMPME algorithm.

To evaluate the imaging performance of the 3-D arrays obtained with the two methods, image reconstruction was carried out as well. The focused images are presented in Figure 5.8. One can see that the images of the cylinders are well reconstructed with both arrays [Figures 5.8(a) and (c)]. From the top-views of the 3-D images [Figures 5.8(b) and (d)], it can be observed that the artifacts in the image obtained with the 3-D array selected with CMPME are considerably suppressed compared to that in the image with the array selected with CFS. So in terms of the overall image quality, the 3-D array selected with CMPME outperforms that obtained with CFS. Moreover, some other differences are also noticed in the focused images with the two 3-D arrays. From Figure 5.8(d), it seems that the focused images of the cylinders are slightly distorted, i.e., curved. This is because the antennas in the array selected with CMPME form relatively large observation angles from the broadside of the antennas. Then due to the weighting effects of the antenna radiation pattern, reflected signals from some scatterers are not well acquired or even missing. Thus it causes slight distortion in the focused images.

Here we have to mention that 350 spatial samples selected in this example lead to an observation matrix $\mathbf{A} \in \mathbb{C}^{27650 \times 41820}$ whose rank is still smaller than the number of voxel cells. This could also be a reason for the distortion of the focused image with the arrays selected with CMPME. By increasing the number of selected spatial samples, the imaging performance of the 3-D array obtained with CMPME could be further improved.

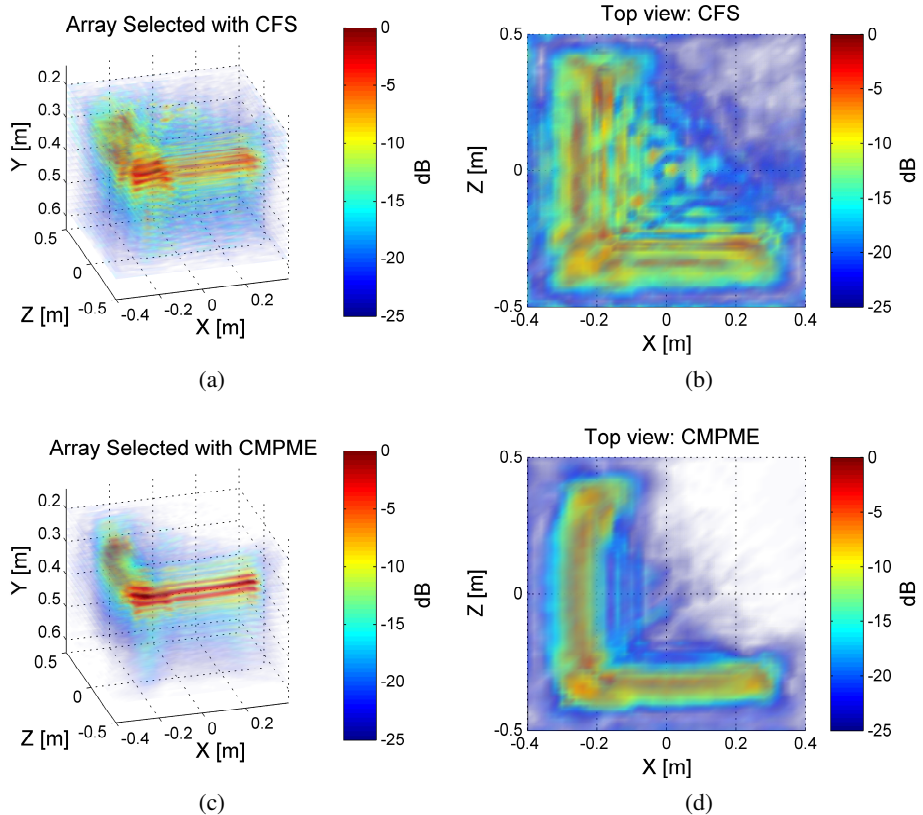


Figure 5.8: Imaging results of the selected 3-D synthetic arrays with CFS and CMPME algorithms. (a) and (c) are the reconstructed 3-D images with the 3-D arrays selected by CFS and CMPME; (b) and (d) display their top-views, respectively.

5.6 Discussion of 3-D Imaging Array

The 3-D synthetic array, i.e., E-RadSAR, provides a novel and flexible spatial sampling strategy, which exploits one more degree of freedom in space compared to the traditional planar array. Nevertheless, topologically we can still consider that the 3-D sampling is performed over a warped surface. For example, a 3-D array synthesized by the E-RadSAR with three antennas is illustrated in Figure 5.9(a), where the spatial samples are located on three cylindrical surfaces formed by the forward movement of the antennas. If we sequentially connect the cylindrical sur-

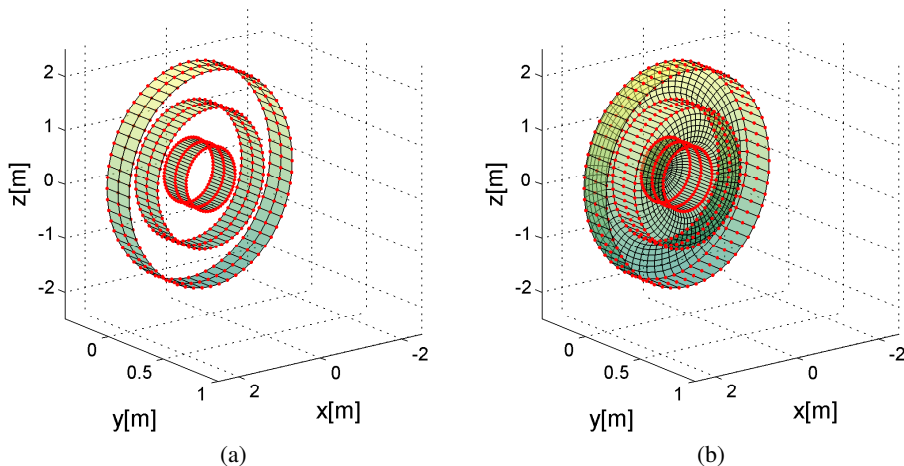


Figure 5.9: (a) Illustration of an E-RadSAR synthesized with three antennas over three cylindrical surfaces; (b) a warped 3-D surface for the E-RadSAR sampling obtained by sequentially connecting the cylindrical surfaces.

faces, a folded surface is constructed in the 3-D space [see Figure 5.9(b)]. Then the E-RadSAR measurements can be regarded as the spatial samples of the scattered field over this folded surface. Taking advantage of the explosive reflector model for the scatterers and Gauss' theorem, the degree of freedom of the scattered field acquired over this folded surface is determined by the dimensions of its flux cross section (i.e., cross-range extension). Therefore, the E-RadSAR provides the similar cross-range resolving capability as a planar array with equal cross-range extension. However, by warping the sampling surface, the E-RadSAR gains more flexibility to take spatial samples of the scattered fields, thus providing a cost-efficient solution for 3-D imaging. This idea can also be applied to develop more sophisticated array/spatial sampling schemes. Regarding the detailed sampling strategy over a warped surface, it can be determined by taking advantage of the algorithms proposed above, which select the most informative samples by optimizing the corresponding observation matrix for accurate image reconstruction. In addition, taking more spatial samples than the degrees of freedom required by resolutions would lead to more accurate image reconstruction.

5.7 Conclusion

In this chapter, we have extended the RadSAR to the E-RadSAR by taking advantage of the SAR techniques in both cross- and down-range directions. To handle the 3-D spatial sampling of the E-RadSAR, the sampling problem is transformed into a sensor/observation selection problem through the linear system formulation, which provides a general frame for multi-dimensional sampling design and facilitates the integral exploration of the spatial, frequency, and polarization diversities for microwave imaging.

Moreover, two approaches, i.e., clustered FrameSense (CFS) and clustered maximum projection onto minimum eigenspace (CMPME), have been proposed for the near-optimal selection of sensors/positions with vector measurements. Both approaches have much higher computational efficiency in contrast to the state-of-the-art. When the set of candidates is moderately larger than or comparable to the selected subset, CFS is slightly faster than CMPME. However, CMPME outperforms CFS in terms of both mean square error (MSE) and worst case error variance (WCEV). Moreover, CMPME is much more efficient than CSBS although they achieve almost identical performance in both MSE and WCEV. Furthermore, as a forward greedy algorithm, CMPME gradually expands the subspace spanned by the observation vectors. So it guarantees the constructed observation matrix to be well conditioned as long as the number of selected sensors/observations is sufficient, which is inherited from MPME. The selection performances of these two approaches have been demonstrated through numerical experiments for imaging array design. Additionally, thanks to the forward selection scheme, CMPME can be used for adaptive sampling point selection during the data acquisition based on the existing measurements, which is its advantage over the backward selection approaches and convex relaxed optimization methods.

Finally, an intuitive physical explanation for the 3-D array sampling is given from the wave field point of view, which connects the spatial sampling over arbitrary surfaces and the degree of freedom of scattered field.

References

- [1] M. L. Bryant, L. L. Gostin, and M. Soumekh, “3-D E-CSAR imaging of a T-72 tank and synthesis of its sar reconstructions,” *Aerospace and Electronic Systems, IEEE Transactions on*, vol. 39, no. 1, pp. 211–227, 2003.

- [2] J. Wang, H. Cetinkaya, and A. G. Yarovoy, “Comparison of CSAR, E-CSAR and planar circular array for 3-D imaging,” in *IET International Radar Conference 2015*, pp. 1–5, Oct 2015.
- [3] D. P. Petersen and D. Middleton, “Sampling and reconstruction of wave-number-limited functions in N-dimensional euclidean spaces,” *Information and Control*, vol. 5, no. 4, pp. 279–323, 1962.
- [4] O. M. Bucci and G. Franceschetti, “On the degrees of freedom of scattered fields,” *Antennas and Propagation, IEEE Transactions on*, vol. 37, no. 7, pp. 918–926, 1989.
- [5] Y. Gao and S. J. Reeves, “Optimal k -space sampling in MRSI for images with a limited region of support,” *IEEE Transactions on Medical Imaging*, vol. 19, no. 12, pp. 1168–1178, 2000.
- [6] S. J. Reeves and L. P. Heck, “Selection of observations in signal reconstruction,” *IEEE Transactions on Signal Processing*, vol. 43, no. 3, pp. 788–791, 1995.
- [7] S. J. Reeves and Z. Zhao, “Sequential algorithms for observation selection,” *IEEE Transactions on Signal Processing*, vol. 47, no. 1, pp. 123–132, 1999.
- [8] R. Broughton, I. Coope, P. Renaud, and R. Tappenden, “Determinant and exchange algorithms for observation subset selection,” *Image Processing, IEEE Transactions on*, vol. 19, no. 9, pp. 2437–2443, 2010.
- [9] S. Joshi and S. Boyd, “Sensor selection via convex optimization,” *IEEE Transactions on Signal Processing*, vol. 57, no. 2, pp. 451–462, 2009.
- [10] J. Ranieri, A. Chebira, and M. Vetterli, “Near-optimal sensor placement for linear inverse problems,” *IEEE Transactions on Signal Processing*, vol. 62, no. 5, pp. 1135–1146, 2014.
- [11] S. P. Chepuri and G. Leus, “Sparsity-promoting sensor selection for non-linear measurement models,” *IEEE Transactions on Signal Processing*, vol. 63, no. 3, pp. 684–698, 2015.
- [12] C. Jiang, Y. Soh, and H. Li, “Sensor placement by maximal projection on minimum eigenspace for linear inverse problems,” *IEEE Transactions on Signal Processing*, vol. 64, no. 21, pp. 5595–5610, 2016.

- [13] I. Ivashko, G. Leus, and A. Yarovoy, “Radar network topology optimization for joint target position and velocity estimation,” *Signal Processing*, vol. 130, pp. 279–288, 2017.
- [14] C. Rusu, J. Thompson, and N. M. Robertson, “Sensor management with time, energy and communication constraints,” *CoRR*, vol. abs/1702.04927, 2017.
- [15] B. Sharif and F. Kamalabadi, “Optimal sensor array configuration in remote image formation,” *Image Processing, IEEE Transactions on*, vol. 17, no. 2, pp. 155–166, 2008.
- [16] W. Hanbiao, G. Pottie, Y. Kung, and D. Estrin, “Entropy-based sensor selection heuristic for target localization,” in *Third International Symposium on Information Processing in Sensor Networks, 2004. IPSN 2004*, pp. 36–45.
- [17] G. Yun and S. J. Reeves, “Efficient computation for sequential forward observation selection in image reconstruction,” in *Image Processing, 1998. ICIP 98. Proceedings. 1998 International Conference on*, pp. 380–384 vol.3.
- [18] S. Boyd and L. Vandenberghe, *Convex Optimization*. Cambridge University Press, 2004.
- [19] G. L. Nemhauser, L. A. Wolsey, and M. L. Fisher, “An analysis of approximations for maximizing submodular set functions—I,” *Mathematical Programming*, vol. 14, pp. 265–294, Dec 1978.
- [20] J. Kovacevic and A. Chebira, “Life beyond bases: The advent of frames (part i),” *IEEE Signal Processing Magazine*, vol. 24, no. 4, pp. 86–104, 2007.
- [21] G. Golub and C. Van Loan, *Matrix Computations*. Johns Hopkins University Press, 1996.
- [22] M. Brand, “Fast low-rank modifications of the thin singular value decomposition,” *Linear Algebra and its Applications*, vol. 415, no. 1, pp. 20–30, 2006.
- [23] P. Stange, “On the efficient update of the singular value decomposition,” *PAMM*, vol. 8, no. 1, pp. 10827–10828, 2008.
- [24] K. C. Toh, M. J. Todd, and R. H. Tütüncü, “SDPT3 – A Matlab software package for semidefinite programming, version 1.3,” *Optimization Methods and Software*, vol. 11, no. 1-4, pp. 545–581, 1999.

- [25] J. L. DAVIS and A. P. ANNAN, “Ground-penetrating radar for high-resolution mapping of soil and rock stratigraphy1,” *Geophysical Prospecting*, vol. 37, no. 5, pp. 531–551, 1989.
- [26] D. Daniels and I. of Electrical Engineers, *Ground Penetrating Radar*. No. v. 1 in Electromagnetics and Radar Series, Institution of Engineering and Technology, 2004.
- [27] J. Wang, P. Aubry, and A. Yarovoy, “Linear inversion of polarization-varied GPR data based on exact radiation pattern,” *Geoscience and Remote Sensing, IEEE Transactions on*, 2017.

6

Signal Fusion for Enhanced Imaging

6.1 Introduction

High-resolution microwave imaging typically requires broad operational signal bandwidth to get fine down-range resolution. For example, to achieve a cm/sub-cm level resolution in the down-range direction, several GHz or even larger operational bandwidth is essential. To radiate and receive such wideband signals, ultrawideband (UWB) antennas are usually needed. However, designing an antenna operating over such a wide band is challenging due to some practical constraints (such as dimensions, cost), especially for subsurface imaging systems (e.g., GPR). To circumvent this problem, the ultrawide bandwidth might be split into several sub-bands and then relatively narrow-band antennas are used to work at each sub-band for signal acquisition. Furthermore, for long-range radar systems the existing spectrum regulations [e.g., Federal Communications Commission (FCC) radio spectrum allocation] may make the continuous wide/UWB spectrum unavailable for the desired applications. In such circumstances, only some separate spectral bands can be used. So to get high-resolution images, one can see that the narrow subband signals have to be coherently stitched to get an equivalent UWB one.

Part of this chapter was published as: J. Wang, P. Aubry, and A. Yarovoy, "Wavenumber Domain Multiband Signal Fusion With Matrix-Pencil Approach for High Resolution Imaging", *IEEE Transactions on Geoscience and Remote Sensing*, 2018, accepted.

In this chapter, we aim at developing a coherent-fusion approach to resolution-improved microwave imaging by making use of multiple narrowband signals. In the open literature, many studies have been carried out to improve the range resolution of radar profiles by coherently extrapolating and/or interpolating the signal spectrum [1–7]. The basic ideas of these approaches are to model the f^α -type scattering behaviors of canonical scatterer centers over a wide bandwidth with the autoregressive (AR) or autoregressive moving average (ARMA) signal models, and then use different parametric estimation methods to get an estimated signal model for incoherence correction and coherent fusion of the separate subband signals. The parameter estimation algorithms used in these approaches include the modified root-MUSIC algorithm [1], Burg’s method [6] and the matrix-pencil approach [2]. Moreover, for the deramped signals in different subbands, the all-phase fast Fourier transform (apFFT) is suggested to estimate phase differences for incoherence compensation and then the iterative adaptive approach (IAA) is employed to fuse multiband radar signals to obtain high-resolution range profiles of targets [5]. However, all these methods fuse the multiband signals that are acquired in (quasi) monostatic/collocated radar configurations. For array-based microwave imaging, the signals at different subbands are generally acquired with different spatial sampling intervals, i.e., non-collocated data in different frequency bands. Therefore, these approaches cannot be directly used to fuse such EM datasets. For high-resolution microwave imaging, we propose to coherently fuse the EM data at different subbands in the wavenumber domain (i.e., k -space) based on the matrix-pencil approach (MPA), named as k -MPA. Taking advantage of the wavenumber-domain signal properties, the algorithm is suitable to fuse either collocated or non-collocated radar data in different subbands to get high-resolution images.

The remainder of this chapter is organized as follows. In section 6.2, the signal model in the k -space is formulated and analyzed for microwave imaging. Then, the k -space signal fusion is discussed in detail based on the matrix-pencil approach in section 6.3, which includes both signal incoherence correction and multiband signal fusion. To demonstrate the effectiveness and accuracy of the proposed approach, numerical simulations and experimental results of multiband fusion are presented in sections 6.4 and 6.5. Finally, some conclusions are drawn in section 6.6.

6.2 k -space Signals for Array Based Imaging

Many imaging algorithms have been developed for microwave imaging, which are implemented in either time-space domain or frequency-wavenumber domain. Due

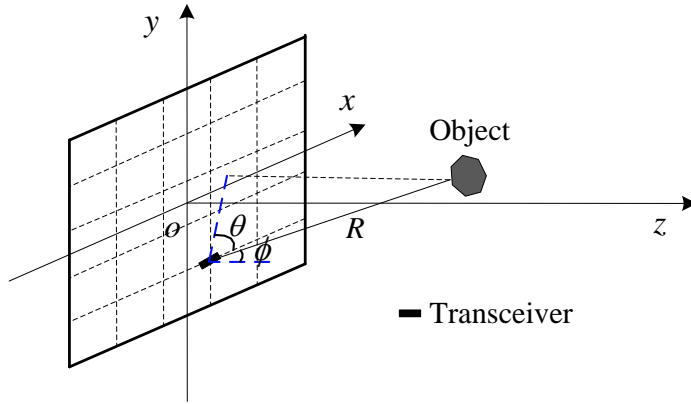


Figure 6.1: Geometrical configuration of 3-D imaging.

to the high computational efficiency, frequency-wavenumber domain imaging algorithms become more and more popular, especially, in real-time/near real-time imaging systems. One typical frequency-wavenumber domain imaging approach is the range migration algorithm [8], which is used for image formation in the following.

Let us consider the geometrical configuration shown in Figure 6.1. A rectilinear planar antenna array is placed on the xoy plane and the object is located in the near field of the array. The transceiver position is denoted as $(x_a, y_a, 0)$. The radiated signals by the antenna array can be continuous wave, pulse signal or step-frequency signal, denoted as $p(t)$ in the time domain.

Assuming that the Born approximation is applicable, the signal measured by an antenna at $(x_a, y_a, 0)$ is given by

$$s(x_a, y_a, t) = \iiint_{o(x,y,z)} \frac{f(x, y, z)}{4\pi R} \cdot p(t - 2R/c) dx dy dz \quad (6.1)$$

where $f(x, y, z)$ is the reflectivity coefficient of a scatterer at (x, y, z) , $o(x, y, z)$ is the space formed by all the scatterers, and $R = \sqrt{(x - x_a)^2 + (y - y_a)^2 + z^2}$ is the distance between a scatterer and the antenna. Taking the FT of $s(x_a, y_a, t)$ with respect to time and two cross-range directions, the frequency-wavenumber (i.e., f -

k) domain signal $S_{fk}(k_{x_a}, k_{y_a}, k)$ is obtained

$$\begin{aligned} & S_{fk}(k_{x_a}, k_{y_a}, k) \\ &= \iiint_{o(x,y,z)} f(x, y, z) P(\omega) dx dy dz \iint \frac{\exp[-jkR]}{4\pi R} \exp[-j(k_{x_a}x_a + k_{y_a}y_a)] dx_a dy_a \\ &= P(\omega) \iiint_{o(x,y,z)} f(x, y, z) \exp[-j(k_{x_a}x + k_{y_a}y + k_z z)] \frac{j}{2k_z} dx dy dz \end{aligned} \quad (6.2)$$

where $k = 2\omega/c$ is the wavenumber with respect to the angular frequency $\omega = 2\pi f$, k_{x_a} and k_{y_a} are the wavenumber counterparts of x_a and y_a , and $k_z = \sqrt{k^2 - k_{x_a}^2 - k_{y_a}^2}$. $P(\omega)$ is the spectrum of $p(t)$. In the derivation of (6.2), the method of stationary phase is used [9].¹

After correcting the spectrum weighting of the radiated wavelet and compensating the wave propagation effect (i.e., propagation spreading loss) and the wavefront curvature [8], then the resulting signal spectrum in k -space can be represented as

$$S(k_{x_a}, k_{y_a}, k_z) = \iiint_{o(x,y,z)} f(x, y, z) \exp[-j(k_{x_a}x + k_{y_a}y + k_z z)] dx dy dz \quad (6.3)$$

In a spherical coordinate system, the wavenumbers k_{x_a} , k_{y_a} , and k_z are given by

$$\begin{cases} k_{x_a} = k \cos \theta \sin \phi \\ k_{y_a} = k \sin \theta \sin \phi \\ k_z = k \cos \phi \end{cases} \quad (6.4)$$

where θ and ϕ are the observation angles of the antenna with respect to a scatterer in the spherical coordinates (see Figure 6.1) and are defined as

$$\begin{cases} \phi = \arccos\left(\frac{z}{R}\right) \\ \theta = \arctan\left(\frac{y - y_a}{x - x_a}\right) \end{cases} \quad (6.5)$$

From (6.4) and (6.5), one can see that the point (k_{x_a}, k_{y_a}, k_z) is located on a sphere of the radius k (also known as, Ewald sphere [11]), and for a specific frequency the

¹Here the spectrum of $\frac{\exp[-jkR]}{4\pi R}$ can also be accurately evaluated by using the Weyl identity of the plane-wave representations [10]. Then, the term $\frac{j}{2k_z}$ in (6.2) should be replaced by $\frac{j}{4\pi k_z}$.

signal spectra of a point target lie on an arc spanned by the observation angles of the antennas with respect to the target. Meanwhile, from (6.4), one can see that with the increase of the radar signal frequency the signal spectrum of a point target expands along a radius of the spherical coordinate system at a specific observation angle. For 2-D imaging scenarios, a similar feature can also be observed for the 2-D signal spectrum of a point target in the polar coordinate system, which can be obtained by setting θ to zero in (6.4). Then, the support area of the target 2-D spectrum becomes a sector of a circular ring. For example, Figure 6.2 shows the 2-D signal spectra of two point targets in k -space with different frequency subbands. The combined spectrum of these two point targets is presented in Figure 6.3 [Note in Figures 6.2 and 6.3, k_x and k_y are used to denote the two dimensions of the 2-D k -space instead of k_x and k_z obtained from (6.4)].

Substituting (6.4) for k_{x_a} , k_{y_a} , and k_z , (6.3) can be rewritten as

$$\begin{aligned} S(k_{x_a}, k_{y_a}, k_z) &= \iiint_{o(x,y,z)} f(x, y, z) \exp[-jkx \sin \phi \cos \theta] \\ &\quad \times \exp[-jk(y \sin \phi \sin \theta + z \cos \phi)] dx dy dz \\ &= S(k, \theta, \phi) \end{aligned} \quad (6.6)$$

In a discrete form, the target signal spectrum along a particular radial direction from the origin in the k -space can be represented as

$$\begin{aligned} S(k, \theta, \phi) &= \sum_{n=1}^N f(x_n, y_n, z_n) \exp[-jk \cdot x_n \sin \phi \cos \theta] \\ &\quad \times \exp[-jk(y_n \sin \phi \sin \theta + z_n \cos \phi)] \\ &= \sum_{n=1}^N f(x_n, y_n, z_n) \exp[-jk \cdot d_n(\theta, \phi)] \end{aligned} \quad (6.7)$$

where

$$d_n(\theta, \phi) = x_n \sin \phi \cos \theta + y_n \sin \phi \sin \theta + z_n \cos \phi \quad (6.8)$$

and $f(x_n, y_n, z_n)$ is the reflectivity function of a point-like scatterer at (x_n, y_n, z_n) , N is the number of point-like scatterers that contribute to the signal spectrum at (k, θ, ϕ) in the k -space. Note that the summation cell $\Delta V = \Delta x \Delta y \Delta z$ has been omitted in (6.7) for simplification. According to (6.5), the observation angles are just determined by the relative geometry between antennas and scatterers, which are independent of the signal frequencies. We assume that, at a specific aspect

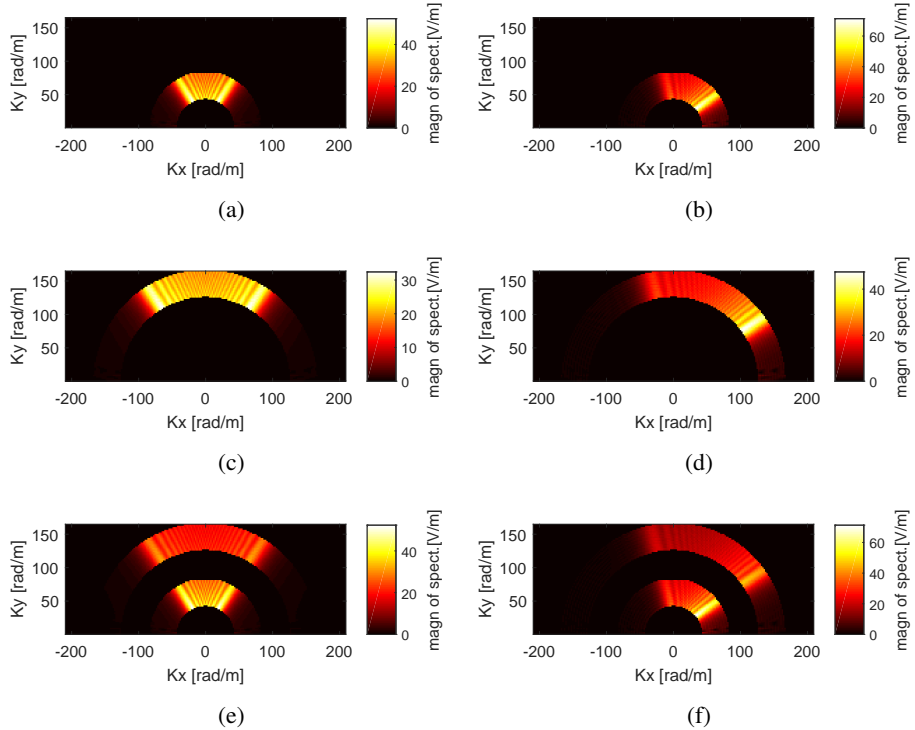


Figure 6.2: Spectra of point targets in k -space. (a), (c) and (e) are the k -space spectra of a point target opposite to the center of linear array at the low-frequency subband (1–2 GHz), high-frequency subband (3–4GHz) and their superposition, respectively; (b) (d) and (f) show the corresponding k -space spectra of a point target which is offset with respect to the center.

(θ, ϕ) , the number of scatterers N is constant over all the frequencies (assume the antenna beam is wide enough compared to the target). Then the signals in different frequency bands share the same form and order of the signal models as in (6.7) where the signal is expressed as a superposition of exponential components. Therefore, the multiband signal fusion can be converted to parameters estimation of exponential damped/undamped sinusoids. By estimating the number of scatterers and the reflectivity function $f(x_n, y_n, z_n)$, the signal model in (6.7) is obtained for a specific aspect (θ, ϕ) . Then the signal can be extrapolated based on the estimated signal model. Such a model takes into account the interference between the fields scattered by different voxels of the scatterer but ignores multiple scattering between different voxels. Note that the complex reflectivity function $f(x_n, y_n, z_n)$

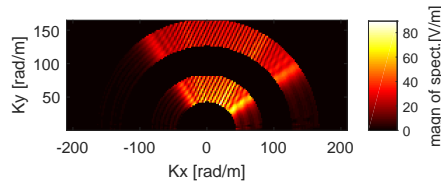


Figure 6.3: The k -space spectrum summation of two point targets with both low- (1–2 GHz) and high-frequency (3–4 GHz) subbands.

can be modeled using different tools (for example, geometrical theory of diffraction (GTD) models and exponential models) according to different scenarios. Also, the frequency dependence of the material parameters of the target can be considered by the reflectivity function.

6.3 *k*-space Signal Fusion

Based on the discussion on the k -space signal models in the previous section, one can see that the signals in different frequency bands can be coherently fused along each radius of the Ewald sphere (circle). The detailed operations of the k -space signal fusion are discussed in the following. Without loss of generality, the fusion principle is illustrated in Figures 6.4 and 6.5 for, as an example, a 2-D imaging case. In Figure 6.4, the effective regions of signal spectra of two point targets, i.e., P_1 and P_2 , are sketched. One can see that the signal spectrum of a point target in k -space occupies an angular segment of a ring defined by the minimum and maximum radiated frequencies. The angular range of this segment is determined by the observation angles of the target with respect to the antenna array. For different point targets, different observation angles are formed and then the signal spectrum in k -space slides along the ring according to the corresponding observation angles. Combining the signal spectra of all the individual scatterers in k -space, we get the signal spectra for the whole imaging scene. As extended targets can be roughly considered as a composition of a group of point scatterers (voxels), a similar approach can also be used to synthesize their signal spectra in k -space.

In terms of different radiated frequencies, the resultant signal spectrum of a point target expands along the radius within a conical sector. Figure 6.5 shows the signal spectra of two point targets in two different frequency bands. Although the signal spectra of different targets occupy different regions in k -space (see Figures 6.4 and 6.5), as mentioned above, the signal spectra along a radial direction are

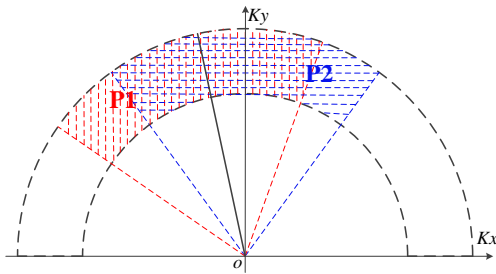


Figure 6.4: Illustration of the signal spectrum in k -space related to two point targets P1 and P2. The red-shadowed area is related to the spectrum of P1 while the blue-shadowed area is related to the spectrum of P2.

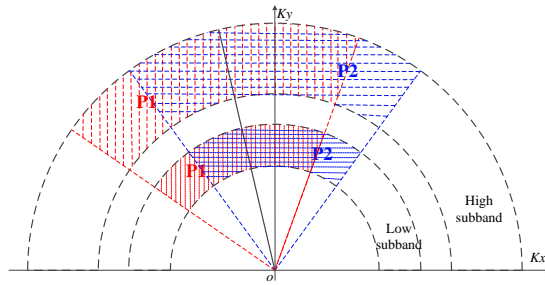


Figure 6.5: Illustration of the signal spectrum in k -space for two point targets (P1 and P2) with two subband signals. The outer angular sector is attributed to the high frequency subband and the inner angular sector is associated with the low frequency subband.

attributed to the same group of scatterers for all the radiated frequencies. This lays the foundation for the k -space signal fusion to improve the image resolution. As the signals in multiple frequency bands can be acquired with different radar systems, the acquired signals may not be coherent, which could result in increased artifacts in the integrated images. Therefore, incoherence compensation is needed before the coherent fusion of the multiband signals.

6.3.1 Signal Incoherence Compensation

In this section, the signal model for multi-band fusion is formulated. Without loss of generality, two subband signals are considered below. According to (6.7), the

k -space signals at the low- and high-frequency subbands are given by

$$S_1(k_1 + m\Delta k, \theta, \phi) = \sum_{n=1}^N f(x_n, y_n, z_n) \exp[-j(k_1 + m\Delta k) d_n(\theta, \phi)] + n_1(m), \\ m = 0, 1, \dots, M_1 - 1 \quad (6.9)$$

$$S_2(k_2 + m'\Delta k, \theta, \phi) = \sum_{n=1}^N f(x_n, y_n, z_n) \exp[-j(k_2 + m'\Delta k) d_n(\theta, \phi)] \\ \times \exp[j(\alpha + \beta m')] + n_2(m'), \quad m' = 0, 1, \dots, M_2 - 1 \quad (6.10)$$

where $\Delta k = 4\pi\Delta f/c$ is the wavenumber counterpart of the frequency sampling interval Δf , M_1 and M_2 are the numbers of frequency samples in the two subbands, $k_1 = 4\pi f_1/c$ and $k_2 = 4\pi f_2/c$ are the wavenumbers associated with the starting frequencies f_1 and f_2 of the low- and high-frequency subbands, respectively, and $k_2 > k_1 + M_1\Delta k$. n_1 and n_2 are with zero-mean Gaussian distribution and represent measurement errors and noise. In (6.10), the first exponential term $\exp[j(\alpha + \beta m')]$ accounts for the phase incoherence between the two subbands. To simplify the notation, we use $S_1(m)$ and $S_2(m')$ to denote $S_1(k_1 + m\Delta k, \theta, \phi)$ and $S_2(k_2 + m'\Delta k, \theta, \phi)$ in the following. After some simple algebraic operations, the signals in both subbands can be rewritten as

$$S_1(m) = \sum_{n=1}^N f_n^{(1)} Z_n^m + n_1(m), \quad m = 0, 1, \dots, M_1 - 1 \quad (6.11)$$

$$S_2(m') = \sum_{n=1}^N f_n^{(2)} Z_n'^{m'} + n_2(m'), \quad m' = 0, 1, \dots, M_2 - 1 \quad (6.12)$$

where

$$f_n^{(1)} = f(x_n, y_n, z_n) \exp[-jk_1 \cdot d_n(\theta, \phi)] \quad (6.13)$$

$$Z_n = \exp[-j\Delta k \cdot d_n(\theta, \phi)] \quad (6.14)$$

$$f_n^{(2)} = f(x_n, y_n, z_n) \exp[j\alpha] \cdot \exp[-jk_2 \cdot d_n(\theta, \phi)] \quad (6.15)$$

$$Z'_n = \exp[-j\Delta k \cdot d_n(\theta, \phi) + j\beta] \quad (6.16)$$

From (6.13) to (6.16), one can see that the phase differences between the two subbands affect both the signal poles and their coefficients in (6.11) and (6.12). More

specifically, the constant phase difference influences the coefficients while the linear phase difference term causes the rotation of signal poles over the unit circle in the complex plane. Therefore, to compensate the phase differences between the two subbands, both signal poles and their coefficients have to be estimated.

To get the signal poles and their coefficients in (6.11) and (6.12), the signal model order should be estimated first. In practice, it can be estimated by using the Akaike Information Criterion (AIC) or Bayesian Information Criterion (BIC) [12]. After obtaining the signal model order estimation \hat{N} , the signal poles can be estimated via the root-MULTiple Signal Classification (MUSIC), ESPRIT [13], the matrix-pencil approach (MPA), etc., while their coefficients are solved through a least squares estimation. Considering the estimation accuracy and computational efficiency, we take advantage of the MPA for signal pole estimation in this chapter. To implement the MPA, two Hankel matrices are formed in each subband, where the measurement data, for example, S_1 are organized as

$$\mathbf{P}_1 = [\mathbf{D}_0, \mathbf{D}_1, \dots, \mathbf{D}_{L-1}] \quad (6.17)$$

$$\mathbf{P}_2 = [\mathbf{D}_1, \mathbf{D}_2, \dots, \mathbf{D}_L] \quad (6.18)$$

where $\mathbf{D}_i = [S_1(i), S_1(i+1), \dots, S_1(M_1-L-1+i)]^T$ and the superscript T represents the matrix transpose. L is the matrix pencil parameter, which satisfies $\hat{N} < L < M_1 - L$. Following the suggestion in [14], we choose $L = \text{round}(M_1/3)$ here. Taking the singular value decomposition (SVD) of \mathbf{P}_1 and \mathbf{P}_2 [2], we get

$$\mathbf{P}_1 = [\mathbf{U}_1 \quad \mathbf{U}'_1] \begin{bmatrix} \Sigma_{1,\hat{N}} & \mathbf{0} \\ \mathbf{0} & \Sigma_{1,L-\hat{N}} \end{bmatrix} [\mathbf{V}_1 \quad \mathbf{V}'_1]^H \quad (6.19)$$

$$\mathbf{P}_2 = [\mathbf{U}_2 \quad \mathbf{U}'_2] \begin{bmatrix} \Sigma_{2,\hat{N}} & \mathbf{0} \\ \mathbf{0} & \Sigma_{2,L-\hat{N}} \end{bmatrix} [\mathbf{V}_2 \quad \mathbf{V}'_2]^H \quad (6.20)$$

where the superscript H denotes Hermitian transpose, $\Sigma_{1,\hat{N}}$ and $\Sigma_{2,\hat{N}}$ are the diagonal matrices of the \hat{N} dominant singular values in the two subbands. \mathbf{U}_1 , \mathbf{U}_2 , \mathbf{V}_1 , and \mathbf{V}_2 are the matrices with the columns as the left and right singular vectors related to the dominant singular values. On the other hand, $\Sigma_{1,L-\hat{N}}$ and $\Sigma_{2,L-\hat{N}}$ are the diagonal matrices of the near-zero singular values, which represent the noise information. \mathbf{U}'_1 , \mathbf{V}'_1 , \mathbf{U}'_2 , and \mathbf{V}'_2 are the matrices with the columns as the noise-associated left- and right-singular vectors. Taking the “pre-filtering” operation, then \mathbf{P}_1 and \mathbf{P}_2 can be approximated by their truncated SVD’s denoted as \mathbf{P}_{1T} and \mathbf{P}_{2T} , which are given

by

$$\mathbf{P}_1 \approx \mathbf{P}_{1T} = \mathbf{U}_1 \boldsymbol{\Sigma}_{1,\hat{N}} \mathbf{V}_1^H \quad (6.21)$$

$$\mathbf{P}_2 \approx \mathbf{P}_{2T} = \mathbf{U}_2 \boldsymbol{\Sigma}_{2,\hat{N}} \mathbf{V}_2^H \quad (6.22)$$

Then we can estimate the signal poles $\{Z_n\}_{n=1}^{\hat{N}}$ of S_1 by solving the generalized eigenvalue problem $\mathbf{P}_{2T} - \lambda \mathbf{P}_{1T}$, which is also equivalent to

$$\mathbf{P}_{2T} - \lambda \mathbf{P}_{1T} \Leftrightarrow \boldsymbol{\Sigma}_{1,\hat{N}}^{-1} \mathbf{U}_1^H \mathbf{U}_2 \boldsymbol{\Sigma}_{2,\hat{N}} \mathbf{V}_2^H \mathbf{V}_1 - \lambda \mathbf{I} \quad (6.23)$$

where \mathbf{I} is the $\hat{N} \times \hat{N}$ identity matrix. The coefficients $\{f_n^{(1)}\}_{n=1}^{\hat{N}}$ can be obtained via the least squares method to approximately solve the following linear system

$$\mathbf{S}_1 = \mathbf{A}_1 \mathbf{f}_1 \quad (6.24)$$

where

$$\begin{aligned} \mathbf{S}_1 &= [S_1(0), S_1(1), \dots, S_1(M_1 - 1)]^T \\ \mathbf{A}_1 &= [\mathbf{a}_1, \mathbf{a}_2, \dots, \mathbf{a}_{\hat{N}}] \\ \mathbf{a}_n &= [1, Z_n, \dots, Z_n^{M_L-1}]^T \\ \mathbf{f}_1 &= [f_1^{(1)}, f_2^{(1)}, \dots, f_{\hat{N}}^{(1)}]^T \end{aligned}$$

The estimation of the coefficients is explicitly written as $\mathbf{f}_1 = (\mathbf{A}_1^H \mathbf{A}_1)^{-1} \mathbf{A}_1^H \mathbf{S}_1$.

Repeating the same operations with the signal S_2 , its signal poles $\{Z'_n\}_{n=1}^{\hat{N}}$ and $\{f_n^{(2)}\}_{n=1}^{\hat{N}}$ can also be estimated. Then according to (6.14) and (6.16), the linear phase difference parameter β can be obtained as

$$\beta = \frac{1}{\hat{N}} \sum_{n=1}^{\hat{N}} [\text{angle}(Z'_n) - \text{angle}(Z_n)] \quad (6.25)$$

According to (6.13) and (6.15), the constant phase difference parameter α is obtained through

$$\alpha = \frac{1}{\hat{N}} \sum_{n=1}^{\hat{N}} [\text{angle}(f_n^{(2)}) - \text{angle}(f_n^{(1)})] + \frac{k_2 - k_1}{\hat{N}} \sum_{n=1}^{\hat{N}} d_n(\theta, \phi) \quad (6.26)$$

where

$$\sum_{n=1}^{\hat{N}} d_n(\theta, \phi) = -\frac{1}{\Delta k} \sum_{n=1}^{\hat{N}} \text{angle}(Z_n) \quad (6.27)$$

Then combining (6.25) and (6.26), the incoherence phase differences of the high-frequency subband from the low subband can be compensated by

$$S'_2(k_2 + m \cdot \Delta k, \theta, \phi) = S_2(k_2 + m \cdot \Delta k, \theta, \phi) \exp[-j(\alpha + m\beta)] \quad (6.28)$$

Thus, the signal $S'_2(k_2 + m \cdot \Delta k, \theta, \phi)$ in the high-frequency subband is coherence-aligned with S_1 in the low-frequency subband. Note that we explicitly write $S_2(m)$ as $S_2(k_2 + m \cdot \Delta k, \theta, \phi)$ to emphasize that S'_2 is also a function of θ and ϕ .

6.3.2 Subband Signal Fusion

This section presents the method to fuse the multiband signals in each radial direction [i.e., (θ, ϕ)] in k -space. Generally, the coherence-aligned subband signals can be integrated by estimating a unified signal model which then is used to extrapolate the missing data in the frequency gap between the low and high subbands. Many approaches used to fill the gap of time sequences can also be adapted to extrapolate the k -space signals. Here we take the MPA based iterative method [2] to fuse the k -space multiband signals. To be clear, we briefly introduce the fusion processing as follows.

After incoherence correction, the k -space coherent multiband signals, i.e., S_1 and S'_2 , are obtained. For the convenience of notation, S'_2 will be replaced by S_2 in the following. The common signal model of the S_1 and S_2 can be expressed as

$$\tilde{S}(k_1 + m\Delta k, \theta, \phi) = \sum_{n=1}^N \tilde{f}_n \tilde{Z}_n^m + b(m) \quad (6.29)$$

where $\{\tilde{f}_n\}_{n=1}^N$ and $\{\tilde{Z}_n\}_{n=1}^N$ are the coefficients and the signal poles, respectively. b is the Gaussian noise. The signal poles and their coefficients in (6.29) can be estimated with the MPA based on the S_1 and S_2 . However, as a frequency gap exists between the two subbands, the two data matrices should be constructed by vertically cascading two corresponding Hankel matrices formed by the data at two subbands, which is given by

$$\mathbf{Y}_1 = \begin{bmatrix} \mathbf{P}_1^{(1)} \\ \mathbf{P}_1^{(2)} \end{bmatrix} \quad \mathbf{Y}_2 = \begin{bmatrix} \mathbf{P}_2^{(1)} \\ \mathbf{P}_2^{(2)} \end{bmatrix} \quad (6.30)$$

where

$$\mathbf{P}_1^{(p)} = [\mathbf{D}_0^{(p)}, \mathbf{D}_1^{(p)}, \dots, \mathbf{D}_{L-1}^{(p)}] \quad (6.31)$$

$$\mathbf{P}_2^{(p)} = [\mathbf{D}_1^{(p)}, \mathbf{D}_2^{(p)}, \dots, \mathbf{D}_L^{(p)}] \quad (6.32)$$

and $\mathbf{D}_q^{(p)} = [S_p(q), S_p(q+1), \dots, S_p(M_p - L - 1 + q)]^T$, $p = 1, 2$ and $q = 0, 1, \dots, L$. Taking advantage of the MPA as presented above, the signal poles $\{\tilde{Z}_n\}_{n=1}^N$ and their coefficients $\{\tilde{f}_n\}_{n=1}^N$ can be obtained. Then utilizing the acquired full-band signal model in (6.29), the full-band signal $\tilde{S}(m)$, $m = 0, 1, \dots, M - 1$, can be estimated, where M is the number of samples in the full band with sampling intervals of Δk . To refine the estimation of the full-band signal, the same iterative scheme as in [2] can be used. For conciseness, the iterative scheme is omitted here.

Repeating the fusion processing in all the radial directions, coherent wideband signals are obtained in k -space. Finally, the image reconstruction operations can be performed to get a focused image with improved resolutions.

6.3.3 More Remarks on the Implementation

The complete processing flowchart for multiband fusion imaging is shown in Figure 6.6. In principle, the processing operations are divided into three major parts: (1) preprocessing for the k -space data preparation, (2) k -space signal fusion and (3) image reconstruction, all of which are indicated on the left side of the flowchart. The main operations for the k -space signal fusion part have been discussed in the previous two subsections. The operations for the other two parts as well as some key points for the k -space fusion part are given in the following.

In the preprocessing part, as mentioned before, spectrum weighting effects, propagation spreading loss and the wavefront curvature are corrected. Firstly, the spectrum weighting effect $P(\omega)$ should be compensated in the frequency domain, which is caused by the wavelet itself and the antenna transfer functions. The spectrum weighting effect introduced by the wavelet itself can be removed by multiplying the inverse of the corresponding weighting factors. The amplitude weighting effect and phase shift resulting from the antenna transfer function can be obtained by measuring the S -parameters in the calibration process and then compensated through inverse filtering. Next, the cross-range processing is performed to correct the wavefront curvature and propagation spreading loss. The operations are as follows. Applying the FT with respect to the cross-range, the weighting-corrected signals are transformed into the frequency-wavenumber (i.e., f - k) domain. Then the propagation spreading loss is compensated through a high-pass filter $-j2k_z$ and the

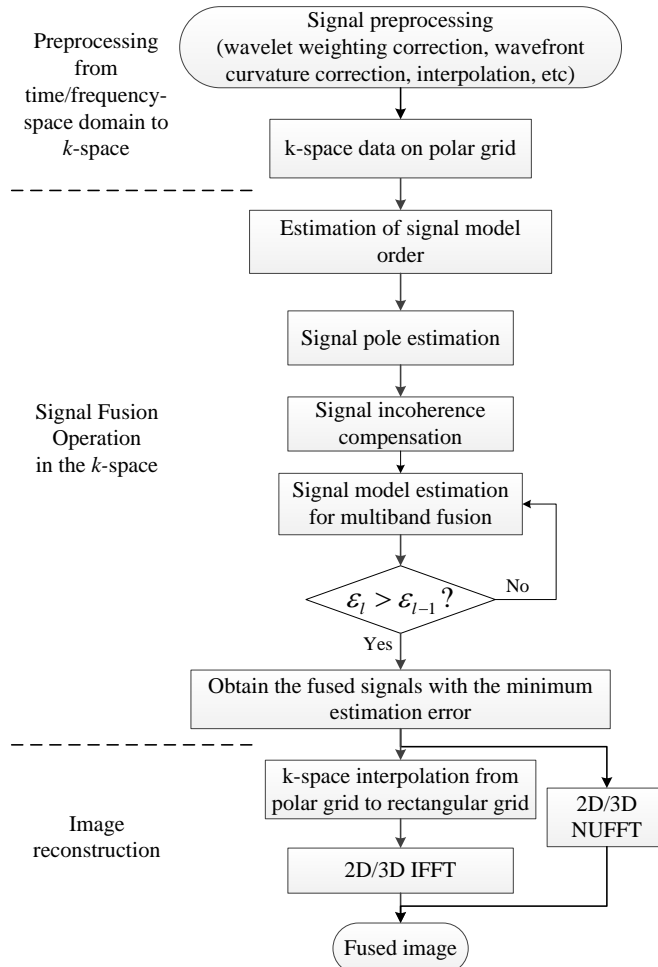


Figure 6.6: Flowchart of the k -space subband fusion for imaging.

wavefront curvature is corrected by the Stolt interpolation [8]. Hence, the k -space signals $S(k_{x_a}, k_{y_a}, k_z)$ for one subband are obtained. Repeating the preprocessing operations for all the subband signals, we get all their k -space counterparts. Putting all the k -space spectra in a unified coordinate system, the spectra resulting from all the subbands are obtained.

The next step is to convert the spectral data at each subband from rectilinear

grid to an aligned polar grid via an interpolation, and the polar grid is given by

$$I = \begin{cases} (k_x, k_y, k_z) & \begin{aligned} k_x &= k \cos \theta \sin \phi \\ k_y &= k \sin \theta \sin \phi \\ k_z &= k \cos \phi \end{aligned} \end{cases} \quad (6.33)$$

where $k = k_1 + m\Delta k$ and $m = 0, 1, \dots, M_1 - 1$ for the low subband while $k = k_2 + m'\Delta k$ and $m' = 0, 1, \dots, M_2 - 1$ for the high subband. Meanwhile, $k_2 = k_1 + (M_1 + h)\Delta k$ and $h > 0$ is an integer. The observation angles θ and ϕ take uniform discrete samples, i.e., $\theta = \{\theta_0, \theta_0 + \Delta\theta, \dots, \theta_1\}$ and $\phi = \{\phi_0, \phi_0 + \Delta\phi, \dots, \phi_1\}$, where θ_0 and θ_1 , ϕ_0 and ϕ_1 are the minimum and maximum values of the observation angles θ and ϕ , respectively; $\Delta\theta$ and $\Delta\phi$ are their corresponding sampling intervals. To avoid aliasing of the focused image in the space domain, the sampling intervals Δk , $\Delta\theta$ and $\Delta\phi$ should satisfy

$$\begin{cases} \Delta k \leq 2\pi/d_{\max} \\ \Delta\theta \leq \lambda_{\min}/(4r) \\ \Delta\phi \leq \lambda_{\min}/(4r) \end{cases} \quad (6.34)$$

where d_{\max} is the largest dimension of the imaging scene in the range direction. λ_{\min} is the wavelength corresponding to the highest frequency, and r is the maximum cross-range radius of the imaging scene (i.e., the minimum radius of a cylinder with its axis along the down-range that encloses the imaging scene).

In addition, we have to mention that the cross-range focusing can also be implemented in the time-space domain via the Kirchhoff migration [15] which actually leads to focused images. Then applying the IFT to the focused images, the *k*-space spectra associated with each subband are obtained. The rest of the operations remain the same.

After getting the *k*-space spectra on an aligned polar grid (as illustrated in Figure 6.3 or Figure 6.5), the *k*-space signal fusion is carried out along each radial direction with the matrix pencil based approach presented in the previous section. After obtaining the fused signals in *k*-space, a 2-D/3-D interpolation is needed to convert the data from the polar grid to a rectilinear grid. Then an inverse FT is applied to the *k*-space data to reconstruct an image in space. Furthermore, to improve the computational efficiency, the interpolation operation and the inverse FT can be replaced by a 2-D/3-D Nonuniform fast Fourier transform operation (NUFFT) [16, 17], which was actually used for the image formation in this chapter.

Table 6.1: Simulation parameters for point targets

Parameter		Value
Low-frequency band		2–4 GHz
High frequency band		6–8 GHz
Antenna aperture		2 m
Case 1	Element spacing of low-freq antenna	1 cm
	Element spacing of high-freq antenna	1 cm
Case 2	Element spacing of low-freq antenna	2 cm
	Element spacing of high-freq antenna	1 cm

6.4 Numerical Simulations

Without loss of generality, in this section we use two subband signals to demonstrate the proposed fusion approach for improved microwave imaging via both numerical simulations and experimental measurements.

6.4.1 Point Targets

Firstly, a numerical simulation was performed for point targets with two-band signals. The simulation parameters are listed in Table 6.1. Assume the antenna array was placed on the x -axis with its center at the origin and the y -axis pointing towards the illuminated scene. The antenna array was 2 m in length and operated in two separate subbands, i.e., 2–4 GHz and 6–8 GHz. Four point targets were placed in front of the antenna array at the positions $(-0.5, 1)$ m, $(0, 0.95)$ m, $(0, 1.05)$ m and $(0.4, 1.2)$ m, respectively. The Hertz dipole was used as the radiator in the antenna array, and the interelement spacings of antennas were 1 cm at both bandwidths (see Case 1 in Table 6.1). The electromagnetic (EM) data at the two bandwidths were synthesized by the Commercial EM software FEKO with the Method of Moments solver in the frequency domain with frequency steps of 20 MHz.

Taking advantage of the range migration algorithm [8], two images were reconstructed with the EM data at the low- (i.e., 2–4 GHz) and high-frequency (i.e., 6–8 GHz) subbands, which are shown in Figures 6.7(a) and (b). As in both cases the same antenna aperture was used for signal acquisition, the high-frequency band signal results in finer cross-range resolution of the focused image compared to the low-frequency band one. In the range direction, similar resolutions are obtained in both cases as their signal bandwidths are equal. Due to their “low” down-range res-

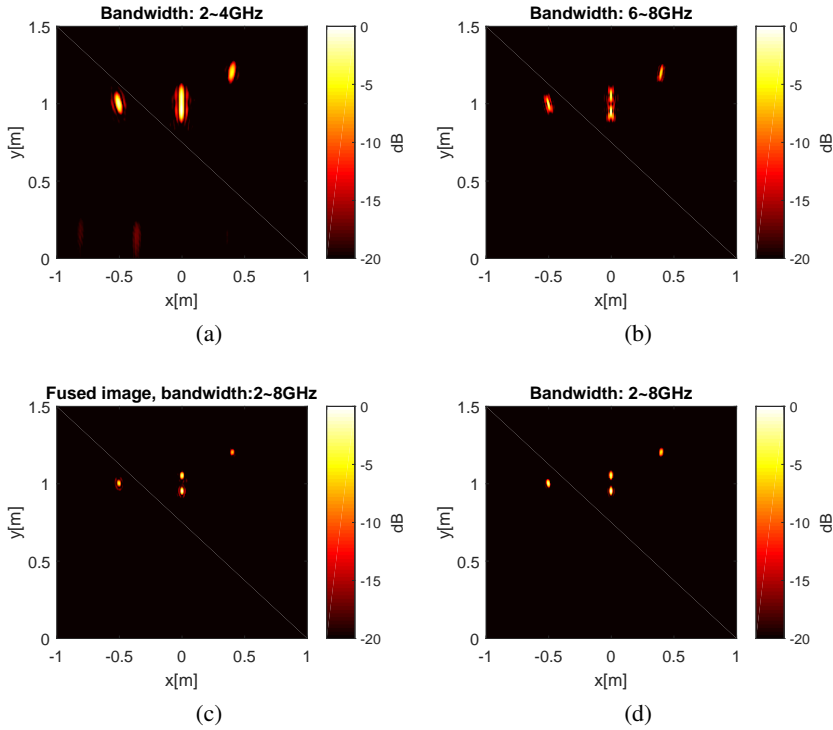


Figure 6.7: Fused images (normalized amplitude) of point targets: (a) and (b) are the images of point targets with bandwidths of 2–4 GHz and 6–8 GHz, respectively. (c) is the fused image with bandwidth of 2–8 GHz and (d) is the reference image obtained with bandwidth of 2–8 GHz.

olution, the two point-targets on the y -axis (i.e., $x = 0$) cannot be well resolved in both cases. To improve the down-range resolution, the signals acquired at the two subbands were fused by using the proposed fusion approach and the focused image is shown in Figure 6.7(c). As an equivalent bandwidth of 2–8 GHz is achieved in the fused image, one can see that in Figure 6.7(c) the two point-targets on the y -axis are more clearly resolved than those in the two individual subband images [Figures 6.7(a) and (b)]. For comparison, the focused image with the real full-band (i.e., the bandwidth of 2–8 GHz) signal is shown in Figure 6.7(d). It can be seen that the fused image obtains comparable spatial resolution as the real full-band image.

In practical imaging systems, the inter-element spacing in a low-frequency antenna array is generally larger than that in a high-frequency one. That is to say, the antenna arrays in different frequency bands are usually non-collocated. To emulate

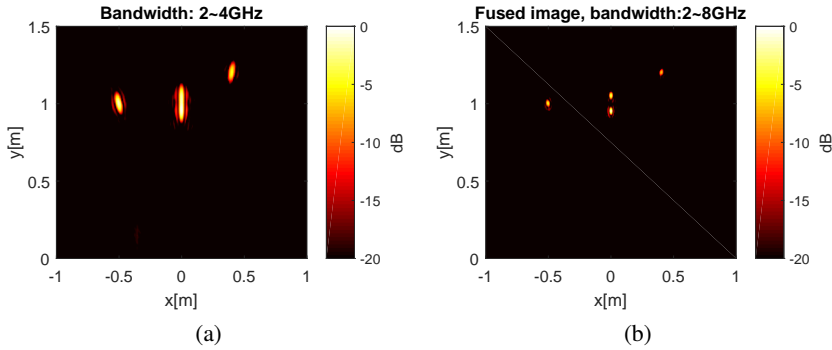


Figure 6.8: Signal fusion of point target with non-collocated antennas in the low- and high-frequency subbands. (a) is the low-frequency images acquired with a down-sampled linear array and (b) the fusion image with the signals collected by down-sampled low-frequency array and the same high-frequency array as in Figure 6.7.

this, we kept the element spacing in the high-frequency antenna array but doubled the sampling intervals (i.e., down-sampled the spatial samples by a factor of two) of the low-frequency array for a second experiment (Case 2 in Table 6.1). Taking the imaging process, the signals collected with the down-sampled low-frequency array were focused and the formed image is shown in Figure 6.8(a). As the inter-element spacing of the low-frequency array in case 2 still satisfies the Nyquist criterion, the focused image in Figure 6.8(a) is comparable to that in Figure 6.7(a). Moreover, in Case 2 the signals synthesized with the high-frequency antenna array were the same as that in Case 1; so the same image as Figure 6.7(b) was obtained, which is omitted here. Applying the proposed fusion approach to the signals in the low- and high-frequency subbands, a fused wideband image was obtained again, as shown in Figure 6.8(b). It can be seen that the image in Figure 6.8(b) is nearly identical to that in Figure 6.7(b) and the two point-targets on the y-axis are better resolved again, compared to those in the two subband images.

6.4.2 Extended Object

An extended target was also used for a numerical simulation to further validate the proposed approach. The extended target was a “V”-shaped perfect electric conductor (PEC) object (see Figure 6.9). The two bars of the object are 20.16 cm in length and 5 mm in both width and thickness, and they form an obtuse angle of 120.5°. A linear antenna array formed by elementary dipoles was used as the radiator. Here

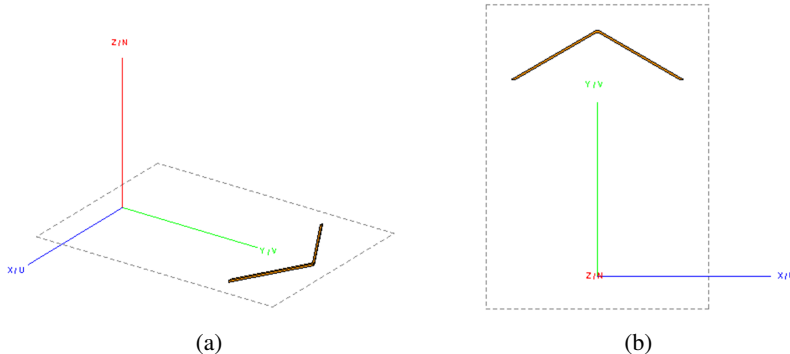


Figure 6.9: Geometrical configuration for extended target simulation. (a) is the 3-D geometry; (b) is the top view against z -axis.

we consider the 2-D imaging scenario. The linear antenna array was set along the x -axis with its center at the origin and the “V”-shaped object was placed on the xoy plane at a distance of 0.4 m from the array, as shown in Figure 6.9. The linear array was 1 m in length with inter-element spacings of 1 cm. The operational bandwidths, i.e., 2–5.5 GHz and 8.5–12 GHz, were used as the low- and high-frequency signal bands. The EM synthetic data at the two operational subbands were generated by using the commercial EM software FEKO with the Method of Moments (MoM) solver in the frequency domain with frequency steps of 100 MHz.

The EM synthetic data in the two operational bands were focused with range migration algorithm [8] and the reconstructed images are shown in Figures 6.10(a) and (b). As for point targets, the down-range resolutions of the two reconstructed subband images are relatively coarse and strong artifacts around the target are also observed in the images.

To improve the spatial resolution and suppress the strong artifacts, the two sub-band signals can be coherently integrated by taking advantage of the proposed fusion approach. Although some fusion results with point targets have been presented above, here more details of the k -space fusion procedure are illustrated to demonstrate the effectiveness and accuracy of the proposed approach by taking the extended “V”-shaped target as an example. Firstly, some preprocessing and the pre-focusing operation in the cross-range direction have been done for the two individual subband signals. The resulting k -space spectra are shown in Figure 6.11, which can be regarded as the 2-D Fourier transform of the images in Figures 6.10(a) and (b), respectively. From Figures 6.11(a) and (b), one can see the k -space spec-

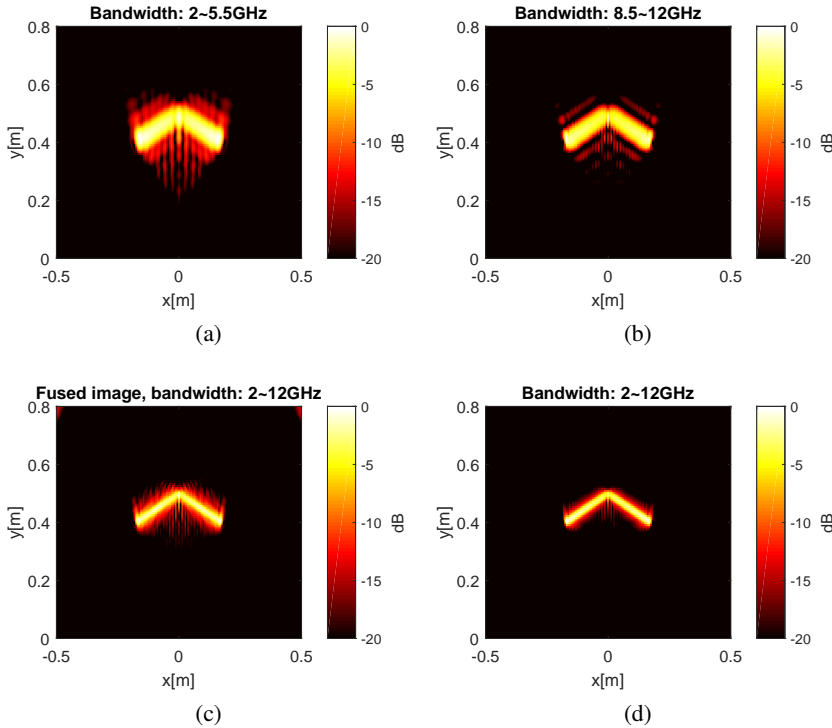


Figure 6.10: Fused images (normalized amplitude) of the extended target. (a) and (b) are the focused images of the “V”-shaped scatterer with bandwidth of 2–5.5 GHz and 8.5–12 GHz, respectively. (c) is the fused image of the “V”-shaped scatterer with bandwidth of 2–12 GHz and (d) is the reference image obtained with bandwidth of 2–12 GHz.

trum at each subband lies in a sector of a circular ring defined by the signal bandwidth and the range of observation angles. Then the k -space spectra resulting from the two subbands were fused in a polar coordinate system. For the convenience of description, we define the k -space polar coordinates as (k, θ) , where k is the polar coordinate from the origin and θ is the angle formed counterclockwise with the positive k_x -axis.

Transforming the k -space data into a polar coordinate system, the signals from the two subbands can be fused along each radial direction. As an example, the complex signals in the two subbands at an aspect angle of $\theta = 94^\circ$ are shown in Figure 6.12. Applying the BIC as a rule to estimate the model orders of the complex signals in both low- and high-frequency subbands, the computed BICs with

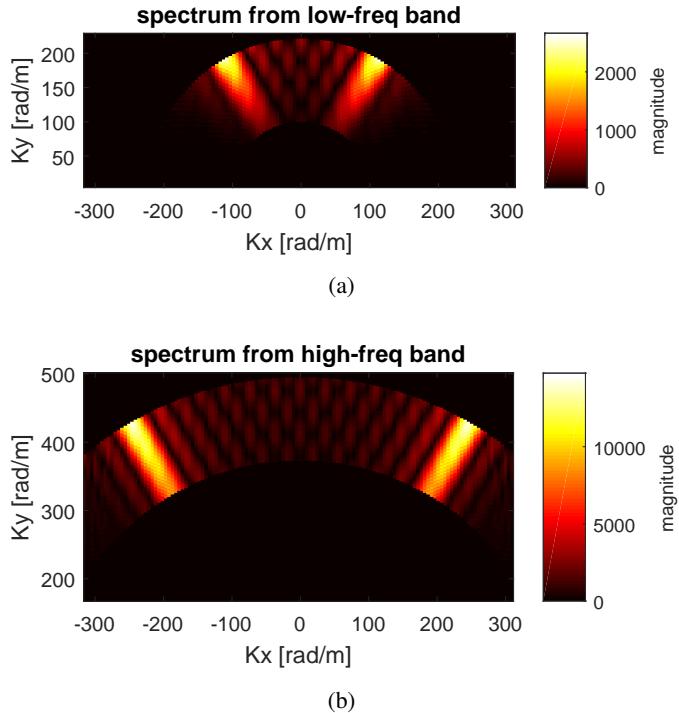


Figure 6.11: The k -space spectra related to the images in Figure 6.10 (a) and (b) obtained with low- and high-frequency bands. (a) low-frequency subband, (b) high-frequency subband.

different model orders are displayed in Figure 6.13(a). From Figure 6.13(a), the BIC for the lower subband signal obtains a first “minimum” with the model order of two while for the high subband signal it arrives at a first minimum with the model order of three. Taking the maximum of the model orders obtained at the two subbands, the model order at this aspect is selected to be three. Correspondingly, from Figure 6.13(b), the first three singular values of a Hankel matrix formed by either the lower or higher subband signal drop sharply (specifically more than one order of magnitude) and with the increase of the indices the singular values decrease relatively slowly. So the model order of three could be a proper selection for the signals at this aspect. Moreover, we want to mention that although some model orders larger than three [for instance, nine in Figure 6.13(a)] could lead to much lower BIC, they may result in severe overfitting for the available data but less predictive to the missing one in the frequency gap.

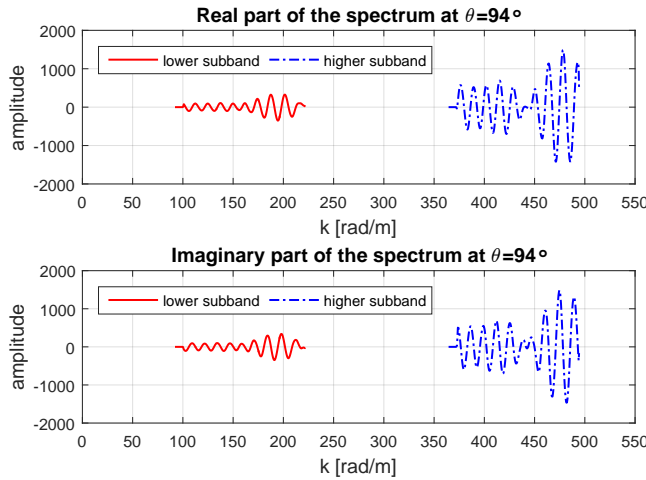


Figure 6.12: The real and imaginary parts of the k -space spectrum at $\theta = 94^\circ$.

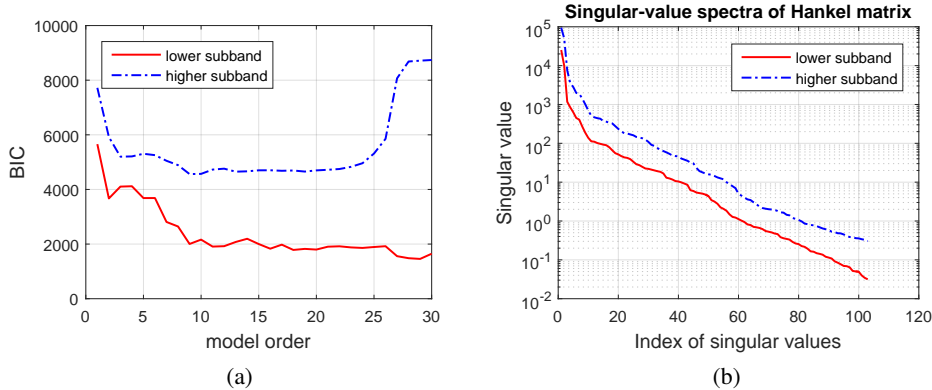


Figure 6.13: The singular-value spectra of the Hankel matrix formed by the spectrum data at $\theta = 94^\circ$ and the related BIC values for model order selection. (b) Singular value spectra in the logarithmic scale, and (a) the BICs with different model orders.

Using the estimated signal model order, the subband signals can be fused with the iterative scheme. Figure 6.14 displays the fused signal and the original one at an aspect angle of $\theta = 94^\circ$, where the original full-band signal is obtained after some preprocessing for the full-band synthetic EM data and the lower and higher subbands are located at the two ends of the full-band spectrum. Although slight

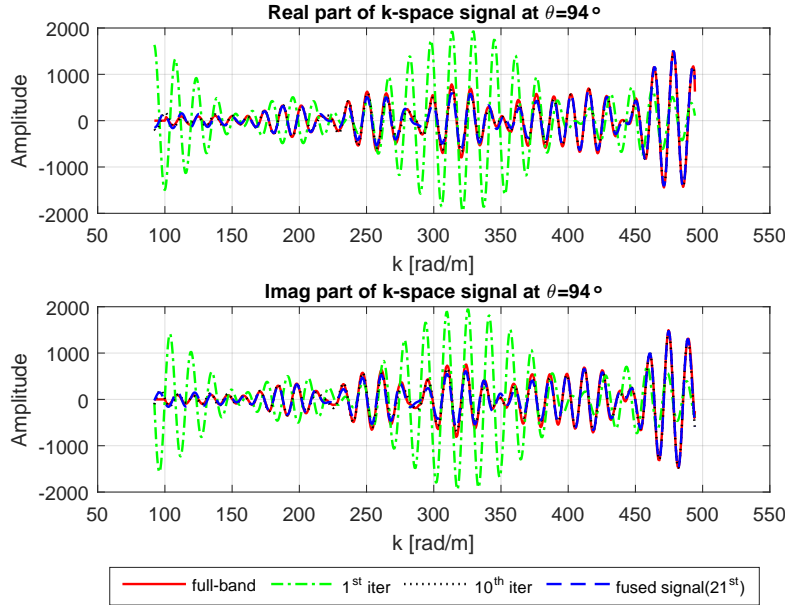


Figure 6.14: The real and imaginary parts of the original k -space signal and the fused signals at the aspect angle $\theta = 94^\circ$. Here the “ i^{th} iter” refers to the estimated signal after the i^{th} iteration.

differences may be noticeable at some points, it can be seen that the fused signal agrees with the original one very well. Moreover, some estimated signals during the iteration are also shown in Figure 6.14 to demonstrate the convergence of the iterative scheme. At the beginning of the iteration, one can see that the estimated signal (i.e., the 1st iteration) oscillates with similar frequencies as the original full-band signal but its amplitude is significantly different from that of the original one. After ten iterations, the amplitude of the oscillating signal converges to the original one (see both the real and imaginary parts of the signals). By minimizing the difference between the estimated and the measured signals, the fused signal at this aspect angle was achieved after 21 iterations. One can see that the signal converges very fast to a relatively accurate signal estimation after the first few iterations but it takes more iterations to reach the minimum difference between the estimated signals and the measured ones at the two frequency subbands.

Taking the fusion operation for the signals in all radial directions, the k -space spectrum corresponding to an equivalent ultra-wide bandwidth were obtained. Then higher down-range resolution is achieved in the fused image [Figure 6.10(c)] where

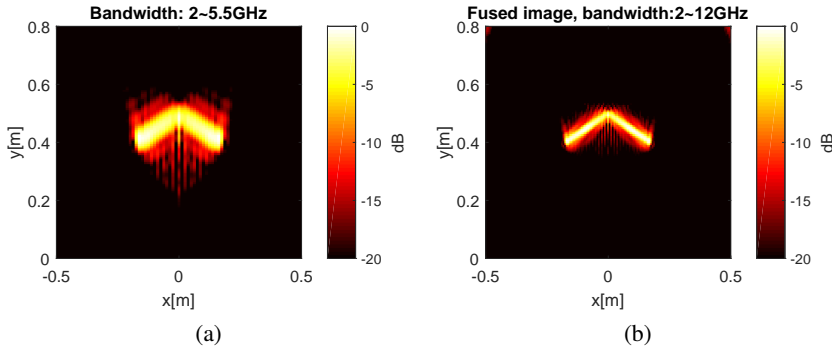


Figure 6.15: Fused images of the extended target acquired by non-collocated low- and high-frequency antennas. (a) is the focused low-frequency image with the antenna element spacing of 2 cm at 2–5.5 GHz, (b) is the fused image with the bandwidth 2–12 GHz.

the strong artifacts perceived in the subband images are significantly suppressed. To examine the quality of the fused UWB image, the focused image with the signals of the entire bandwidth of 2–12 GHz is shown as a reference in Figure 6.10(d). Comparing Figures 6.10(c) and (d), the fused image achieves a similar down-range resolution to that of the reference one. However, slight differences are noticed in the sidelobe levels in the two images. This may be caused by the estimation errors of the fused signals with respect to the real full-band signals in k -space. Nevertheless, these differences in sidelobe levels have little influence on the target detection and recognition. So a satisfactory image was obtained by fusing the data of the two frequency sub-bands.

Similar to the point-targets simulation, we also took every other spatial sample of the linear array (i.e., element spacing of 2 cm) for the low-frequency subband to emulate the non-collocated low- and high-frequency antenna arrays in practical imaging systems. The focused image for the signals acquired with the down-sampled low-frequency linear array is shown in Figure 6.15(a), which is nearly identical to the low subband image in Figure 6.10(a). Again, the same image as that in Figure 6.10(b) was obtained with high-frequency subband signals and we omit it here. Taking the fusion operation for the two subband signals in k -space, a focused image with the enhanced resolution was obtained. Figure 6.15(b) presents the fused image with the bandwidth of 2–12 GHz. It is visually equivalent to that in Figure 6.10(c) fused with the signals acquired by collocated low- and high-frequency antenna arrays. Moreover, this fused image [Figure 6.15(b)] is

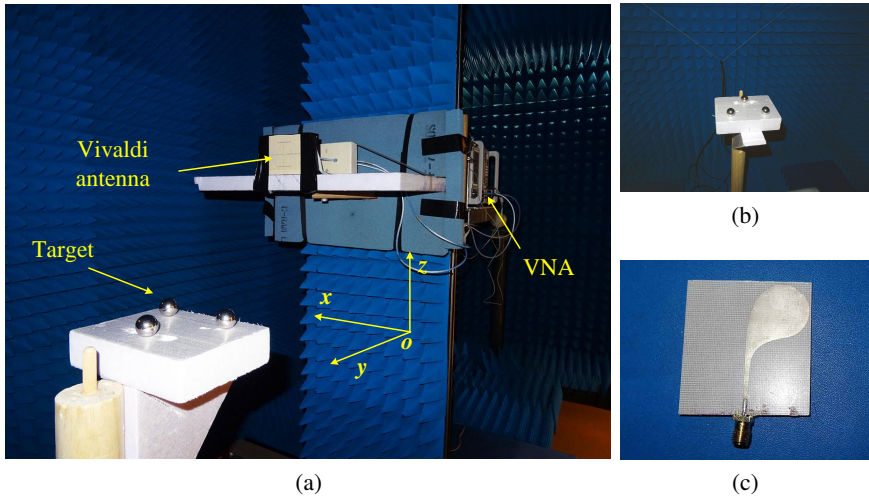


Figure 6.16: (a) Experimental setup, and (b) the metallic sphere targets and (c) the antipodal Vivaldi antenna used for the measurement.

comparable to the fullband image in Figure 6.10(d), especially in terms of the spatial resolution. Therefore, the proposed k -space fusion approach works effectively for multi-band signals acquired with non-collocated antenna arrays as well.

6.5 Experimental Results

Measurements were carried out in the anechoic chamber for further demonstration. The experimental setup is shown in Figure 6.16(a). An antipodal Vivaldi antenna [18] with the operational frequency band from 2.7 till 35 GHz was used as a transceiver, shown in Figure 6.16(c). It was fixed on a planar scanner with polyethylene foam and connected to a Vector Network Analyzer (VNA) [see Figure 6.16(a)]. With the translation of the planar scanner, the transceiver antenna took samples over the xoz plane to synthesize a rectilinear aperture of dimensions of $0.5 \text{ m} \times 0.5 \text{ m}$. The spatial sampling intervals of the antennas in both x and z directions are 1 cm. Three metal spheres of the diameter 2 cm were placed on the xoy plane in front of the array center. The two nearer spheres were separated with an interval of 10 cm and placed at a distance of 54.3 cm away from the antenna aperture. The third sphere was set 7 cm further away than the center of gravity of the other two [Figure 6.16(b)]. Two subband signals with operational frequencies

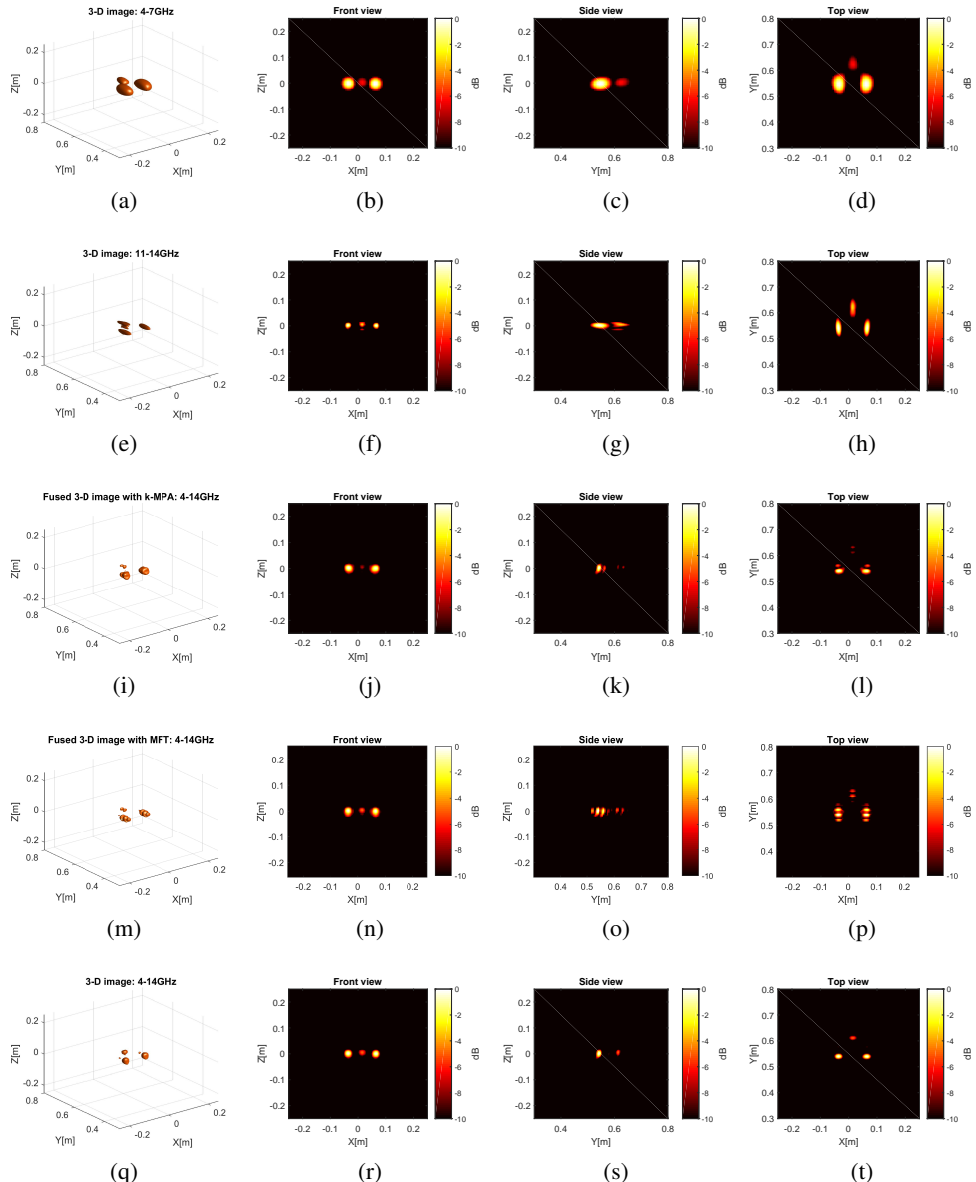


Figure 6.17: Focused images with two subband signals and the whole bandwidth. (a)–(d) are the 3-D image and its projection views on the xoz , yoz and xoy planes for the low frequency signal (4–7 GHz); (e)–(h) are the 3-D image and its projection views on the three planes for the high frequency signal (11–14 GHz); (i)–(l) are the fused 3-D image and its projection views on the three planes for the full-band signal (4–14 GHz); (m)–(p) are the fused 3-D image with the MFT method and its projection views on the three planes for the full-band signal (4–14 GHz); (q)–(t) are the 3-D benchmark image and its projection views on the three planes for the real full-band signal (4–14 GHz). All 3-D images show the isosurfaces of -10 dB in the focused volume.

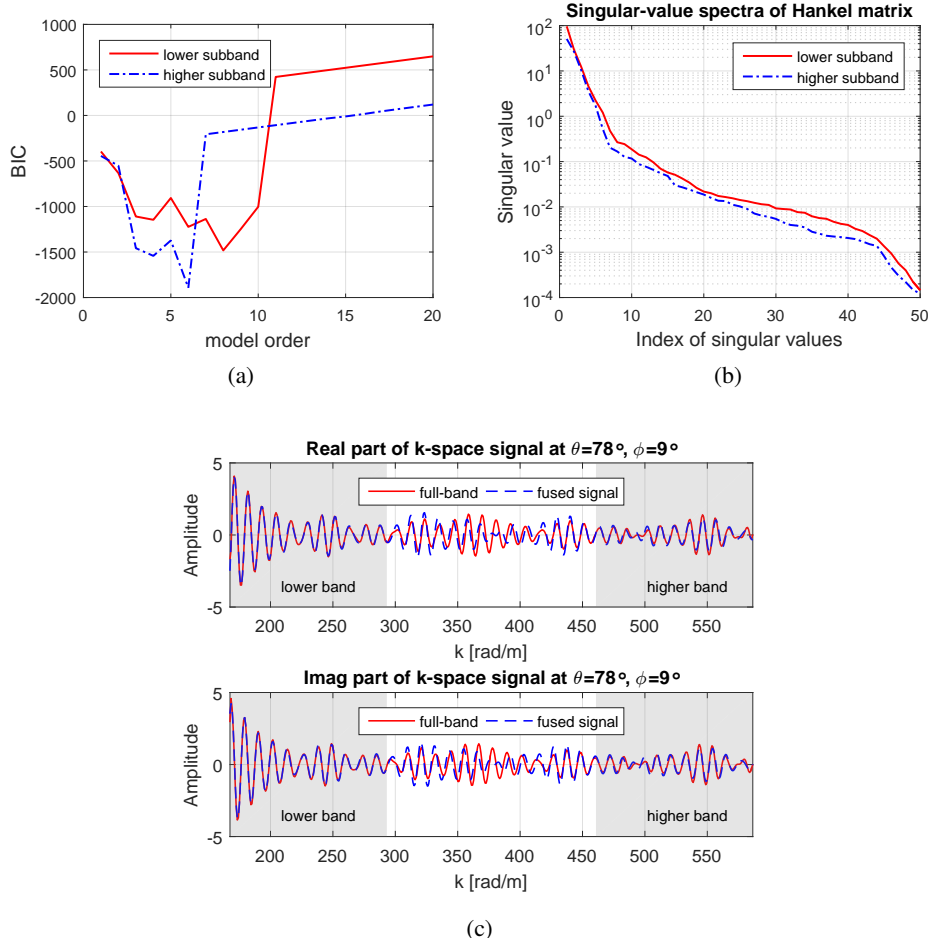


Figure 6.18: Illustration of model order selection and fused experimental signal at the aspect of $(\theta, \phi) = (78^\circ, 9^\circ)$ in the k -space. (a) shows the BICs for different model orders, and (b) shows the singular value spectra of a Hankel matrix formed by the k -space experimental data. (c) displays the real and imaginary parts of the full-band data and the fused signal which are obtained by fusing the signals in the lower and higher subbands in the shaded regions.

ranging from 4 to 7 GHz and 11 to 14 GHz, respectively, were used. The signals were measured in the frequency domain with steps of 20 MHz by the VNA. In addition, calibration was carried out before taking the measurement to eliminate the reflections between the VNA and the antenna.

Then the acquired EM data were focused with the range migration algorithm for the two subband signals, respectively. The formed 3-D images, as well as their projection views, are shown in Figures 6.17(a)–(h). In both low- and high-frequency subbands, the images of spheres are relatively well reconstructed. Thanks to the short wavelengths of the high-frequency signals, finer cross-range resolution is achieved in the image of the high-frequency band [see Figures 6.17(f) and (h)]. On the other hand, the equally lower down-range resolutions were obtained in the images of both subbands due to the equal signal bandwidths (i.e., 3 GHz).

To improve the down-range resolution, the signals acquired in both low- and high-frequency subbands are processed and fused in k -space by using the proposed fusion approach. Similar to the extended target case, the signal model order selection and fusion at an aspect is illustrated first. The k -space counterparts of the spatial coordinates defined in Figure 6.1 are used in the following description. Taking the complex signals at the two subbands [see the shaded regions in Figure 6.18(c)] as an example, the BICs with different model orders were computed, as shown in Figure 6.18(a). Based on the first minima of the BICs at both subbands in Figure 6.18(a), the model order can be chosen to four. Again, a drastic decrease from the first to the fourth singular values of a Hankel matrix constructed by the complex data in either subband is observed [Figure 6.18(b)], which confirms that four could be a proper model order selection in this case. After fusion operation, the complex signal in an equivalently larger bandwidth was obtained, as shown in Figure 6.18(c). For comparison, the k -space complex signal resulting from the full-band measurements from 4 to 14 GHz is also presented in Figure 6.18(c). Clearly, one can see that the signals in the two subbands are well fused. Although slight amplitude differences are observed at some frequencies, the extrapolated data in the frequency gap also demonstrate very good agreement with the real signal.

Applying the proposed fusion approach to the 3-D k -space spectra, a fused image with improved down-range resolution can be acquired, as shown in Figures 6.17(i)–(l). One can see that the images of objects are well focused in the fused image and the down-range resolution along the y -axis is noticeably improved compared to that of the images reconstructed with each individual subband (i.e., 4–7 GHz and 11–14 GHz). For comparison, the two subband signals are also fused with the Matrix Fourier Transform (MFT) approach proposed in [19], and the fused images are displayed in Figures 6.17(m)–(p). One can see that the fused image is focused very well in the cross-range direction [Figure 6.17(n)] and the down-range resolution is improved [Figures 6.17(o)–(p)]. However, split main lobes are observed along the down-range direction. This results from the fact that in the

MFT approach the k -space data from different subbands are only registered in an aligned coordinate system without any operation to deal with the missing data in the frequency gap. Hence, split main lobes are obtained. In contrast, the MPA based method not only coherently registers the k -space data but also extrapolates the missing data to fill the frequency gap, which leads to the sharply focused main lobe and enhances the down-range resolution.

As a benchmark, the images focused with the fully measured data within the bandwidth 4–14 GHz (i.e., full-band images) are also shown in Figures 6.17(q)–(t). Compared with the benchmark images, the fused images achieve comparable image qualities, especially, in terms of the down-range resolution [see Figures 6.17(i)–(l)]. However, relatively high sidelobes are observed in the fused image and the sphere at the further position exhibits weaker intensity in the fused image than that in the full-band benchmark images. This is mainly caused by the differences between the estimated data and the real data in the missing frequency gap. As in the fusion process, the reflectivity functions were assumed to be constant over the entire signal bandwidth, i.e., frequency independent. Based on this assumption, a signal model was estimated with the measured data in the low- and high-frequency subbands. Using the estimated signal model, the missing data in the frequency gap between the low- and high-frequency bands can be extrapolated. Consequently, the equivalent full band data were obtained by combining the low-frequency, high-frequency and the extrapolated data, which leads to resolution-improved images after focusing operation. Nevertheless, the reflectivity function of the practical target can never be absolutely frequency independent. Therefore, extrapolated data in the missing-frequency band may have some differences from the real one, thus resulting in slight differences in the focused image. To be more accurate in capturing the features of the reflectivity functions of targets, a more advanced model should be used to characterize the targets' scattering signatures over a wide bandwidth, e.g. the state-space based modeling [4, 20].

Although the background reflections and clutter were almost perfectly eliminated by taking the experimental measurement in the anechoic chamber, which suppresses their impact on the fusion of the scattered signals from the targets, the suggested fusion method should work as well with their presence. This is because, also for background reflections, the k -space signals along a radial direction from the origin are attributed to a set of scatterers (including the background scatterers) in the imaging scene. With the presence of background reflections, the only consequence is that the signals from background scatterers are also fused. Thus, the corresponding background scatterers also appear in the fused images at appropriate

places (outside the target area) and with improved resolution.

6.6 Conclusion

This chapter has presented a matrix-pencil based approach to fuse multi-band signals in the k -space for high-resolution microwave imaging. This approach works on the k -space data after compensating the spectrum weighting effects, wavefront curvature and propagation spreading loss for raw EM signals. The fusion method is based on the Born approximation of the field scattered from a target resulting in the fact that, in a given direction, the scattered field can be represented over the whole frequency band as a sum of the same number of contributions. By modeling the k -space signals in each radial direction as the sum of exponential/damped exponential sinusoids, the incoherence between the signals in different frequency subbands can be compensated via signal estimation methods, such as the matrix-pencil approach. The missing data in the gap between different frequency bands can be extrapolated using the estimated signal models. Hence, an equivalent wide bandwidth can be synthesized by combining the incoherence corrected data and the extrapolated ones, which lead to resolution-improved images. As the proposed fused method tackles the multiband signals in k -space, it is applicable to multiband data collected over either the same or different spatial sampling grids (i.e., collocated or non-collocated antennas) in different frequency bands.

References

- [1] K. M. Cuomo, J. E. Pion, and J. T. Mayhan, “Ultrawide-band coherent processing,” *Antennas and Propagation, IEEE Transactions on*, vol. 47, no. 6, pp. 1094–1107, 1999.
- [2] Y. Q. Zou, X. Z. Gao, X. Li, and Y. X. Liu, “A matrix pencil algorithm based multiband iterative fusion imaging method,” *Scientific Reports*, vol. 6, p. 19440, 2016.
- [3] L. D. Vann, K. M. Cuomo, J. E. Piou, and J. T. Mayhan, “Multisensor fusion processing for enhanced radar imaging,” tech. rep., DTIC Document, 2000.
- [4] J. E. Piou, K. M. Cuomo, and J. T. Mayhan, “A state-space technique for ultrawide-bandwidth coherent processing,” tech. rep., DTIC Document, 1999.

- [5] J. Tian, J. Sun, G. Wang, Y. Wang, and W. Tan, "Multiband radar signal coherent fusion processing with IAA and apFFT," *IEEE Signal Processing Letters*, vol. 20, no. 5, pp. 463–466, 2013.
- [6] P. v. Dorp, R. Ebeling, and A. G. Huizing, "High resolution radar imaging using coherent multiband processing techniques," in *2010 IEEE Radar Conference*, pp. 981–986.
- [7] F. Ye, F. He, and Z. Sun, "Radar signal level fusion imaging," in *IGARSS 2008 - 2008 IEEE International Geoscience and Remote Sensing Symposium*, vol. 4, pp. IV – 1288–IV – 1291.
- [8] J. M. Lopez-Sanchez and J. Fortuny-Guasch, "3-D radar imaging using range migration techniques," *Antennas and Propagation, IEEE Transactions on*, vol. 48, no. 5, pp. 728–737, 2000.
- [9] A. Papoulis, *Systems and Transforms With Applications in Optics*. Malabar, Florida : Robert Krieger Publishing Company, 1968.
- [10] H. Weyl, "Ausbreitung elektromagnetischer wellen über einem ebenen leiter," *Annalen der Physik*, vol. 365, no. 21, pp. 481–500, 1919.
- [11] A. C. Kak and M. Slaney, *Principles of computerized tomographic imaging*. IEEE press, 1988.
- [12] P. Stoica and Y. Seleny, "Model-order selection: a review of information criterion rules," *IEEE Signal Processing Magazine*, vol. 21, pp. 36–47, July 2004.
- [13] R. Roy and T. Kailath, "Esprit-estimation of signal parameters via rotational invariance techniques," *IEEE Transactions on Acoustics, Speech, and Signal Processing*, vol. 37, pp. 984–995, Jul 1989.
- [14] T. K. Sarkar and O. Pereira, "Using the matrix pencil method to estimate the parameters of a sum of complex exponentials," *Antennas and Propagation Magazine, IEEE*, vol. 37, no. 1, pp. 48–55, 1995.
- [15] J. Wiggins, "Kirchhoff integral extrapolation and migration of nonplanar data," *GEOPHYSICS*, vol. 49, no. 8, pp. 1239–1248, 1984.
- [16] L. Greengard and J.-Y. Lee, "Accelerating the nonuniform fast Fourier transform," *SIAM Review*, vol. 46, no. 3, pp. 443–454, 2004.

- [17] A. Dutt and V. Rokhlin, “Fast Fourier transforms for nonequispaced data,” *SIAM Journal on Scientific Computing*, vol. 14, no. 6, pp. 1368–1393, 1993.
- [18] X. Zhuge and A. Yarovoy, “Design of low profile antipodal Vivaldi antenna for ultra-wideband near-field imaging,” in *Antennas and Propagation (EuCAP), 2010 Proceedings of the Fourth European Conference on*, pp. 1–5.
- [19] Z. Li, S. Papson, and R. M. Narayanan, “Data-level fusion of multilook inverse synthetic aperture radar images,” *IEEE Transactions on Geoscience and Remote Sensing*, vol. 46, no. 5, pp. 1394–1406, 2008.
- [20] K. Naishadham and J. E. Piou, “A robust state space model for the characterization of extended returns in radar target signatures,” *IEEE Transactions on Antennas and Propagation*, vol. 56, no. 6, pp. 1742–1751, 2008.

7

Conclusions

The work described in this dissertation addresses the major problems and challenges of the UWB RadSAR imaging, including both fundamental problems and practical issues of the UWB RadSAR. This work is presented to the radar and remote sensing community to show the latest developments related to microwave imaging with UWB rotated antenna arrays. In particular, the following problems have been considered and solved. Firstly, we addressed the effects of the variation of antenna polarizations in RadSAR in two ways: (1) specifically designing rotated antenna arrays for signal acquisition, and (2) signal processing. Then by utilizing the down-range movement of the radar platform, the RadSAR has been developed to the Elevation-RadSAR, which extends the traditional surface sampling to 3-D sampling schemes and further exploits the spatial diversity for signal acquisition. Considering the effects of UWB signals on the spatial sampling, a unified sampling design approach has been established via a linear formulation. Finally, multiband signal fusion has been addressed through signal processing to circumvent the unavailability of UWB antennas or signals in practical imaging systems, which allows, as an alternative, the use of multiple relatively narrow-band systems to achieve an equivalent UWB imaging. With the works described above, we have demonstrated the potential and feasibility of the UWB RadSAR (and the Elevation-RadSAR) for high-resolution and high-quality polarimetric imaging.

7.1 Results and Novelties of the Research

The major novelties and achievements of this thesis are summarized as follows.

Rotated antenna array design for full-pol imaging. Two novel approaches were proposed for rotated antenna arrays design, which overcomes the effects of polarization variations of the antennas within the aperture and facilitates the extraction of fully polarized scattering properties of objects through traditional scalar-wave based algorithms and polarimetry techniques. The rotated arrays, designed according to the proposed approaches, provide a cost-efficient solution to fully polarimetric imaging array systems.

Efficient implementation of Linear inversion of polarization-varied EM data. A linear inversion approach derived from the Born approximation was applied to address the high-quality image reconstruction from the EM data acquired with arbitrarily oriented antennas based on the full-wave radiation characteristics. *In the numerical implementation, two approaches, i.e., an interpolation based approach and a NUFFT based approach, have been proposed to efficiently compute the accurate Green's functions.* These approaches have significantly accelerated (for instance, from $O(N^2)$ to $O(N \log N)$ for the NUFFT based approach) the observation matrix construction for linear inversion. By taking advantage of the full-wave radiation characteristics of the antennas, the linear inversion approach compensates for the effects of the polarization variations within the array and substantially improves the imaging quality compared to the traditional scalar-wave based algorithms.

Sampling design of three-dimensional arrays for 3-D imaging. A novel concept and design strategies were proposed for three-dimensional arrays, which is, to our best knowledge, the first attempt to investigate three-dimensional arrays for 3-D imaging. Specifically, *we extended the RadSAR to the Elevation-RadSAR (E-RadSAR) by taking advantage of the movement of the radar platform in the down-range direction,* which aimed at reducing the number of antennas needed in the imaging system implementation. To address the 3-D sampling problem of the UWB E-RadSAR, two greedy algorithms, i.e., *the Clustered FrameSense (CFS) and the Clustered Maximal Projection on Minimum Eigenspace (CMPME),* have been proposed to optimize the sampling scheme of the 3-D synthetic arrays of the E-RadSAR. As these two algorithms abstractly tackle the sampling design problem as an observation/sample selection problem with a linear system of equations, they are broadly applicable to high-dimensional sampling problems. In terms of the designed E-RadSAR, its spatial samples are taken over several cylindrical surfaces with a small number of available antennas, which provides a cost-efficient/compact solution to practical imaging systems, though probably at the expense of a slight image quality degradation, as compared to optimal planar arrays with the same number of spatial samples.

Multiband signal fusion. A novel wavenumber domain fusion approach has been proposed to coherently fuse multiple subband signals scattered from targets for radar imaging based on the matrix-pencil method. Using this approach, we compensate the phase incoherence between the different subband signals and extrapolate the missing data in the frequency gap between different subbands. Then the coherence-aligned signals are fused to get an equivalent wideband/UWB signal, which leads to the focused images with enhanced spatial resolution, especially the down-range resolution. Compared to the signal fusion in the space-frequency domain, the wavenumber domain method allows integrating the signals acquired by either collocated or non-collocated arrays (say, different spatial sampling interval) at different frequency subbands. The validity of the proposed fusion approach has been verified through numerical and experimental examples.

7.2 Recommendations

In this section, a few recommendations are given for further research as a continuation of the present work in this thesis. Some of the problems are inspired and identified in the investigation process of the present work while some have not been covered in this thesis. Several possible research directions are listed below.

- Moving target tomography.

In the thesis, we mainly focused on the stationary imaging scenarios with the array-based system and only the motion of the array itself was considered for the synthetic aperture radar imaging. In practice, moving target scenarios may be more general. Simultaneously identifying and reconstructing the images of both stationary and moving targets in a dynamic scenario with microwave imaging provide the spatial-temporal, i.e., four-dimensional (4-D) information about the imaging scene, which will significantly improve the probability of target detection and recognition. This study will definitely boost the development of radar-based autonomous driving, which is one of the hottest interdisciplinary applications in recent years.

- Multiband signal fusion based on matrix completion.

Multiband signal fusion can be considered as an estimation problem which aims at estimating the full signals from the incomplete measurements. For computational microwave imaging, the multiband signal fusion imaging in the wavenumber domain can also be converted to estimate a 2-D matrix/3-D tensor based on part of its entries. In other words, the fusion operation at-

tempts to estimate the unknown entries based on the existing ones so as to get a complete matrix, namely, matrix completion. In terms of implementation, it can be formulated as an optimization problem

$$M : \min \mathcal{F}(M) \quad \text{subject to} \quad M_l = M_l^0$$

where M is the estimated matrix after fusion, M^0 is the initial matrix formed by the measurements for some entries but zeros for others and the subscript l represents the set of indices of the existing entries in matrix M (or M^0). \mathcal{F} is a functional of M , which can be the rank of a matrix, matrix norms, etc.

- Exploration of the potential for enlargement of the class of EM properties to be reconstructed with the rotated array configurations.

Compared to the traditional planar arrays, the rotating antenna array acquires differently polarized EM signals within the aperture. That is, rotated array configurations result in an observation operator different from that with traditional arrays, thus perceiving different information of targets. So one possible question that arises is whether the signals acquired with the rotated arrays combining its observation operator would lead to the enlargement of the class of EM properties to be reconstructed through the inversion process. This question could be a future research topic to further explore the potential of the rotated array configuration.

- Orbital-Angular-Momentum imaging with rotated antenna arrays.

Electromagnetic fields have an angular momentum, which can be decomposed as spin angular momentum (SAM) and orbital angular momentum (OAM) in quantum mechanics [1]. The SAM is associated with the polarization in the classical electromagnetic theory and describes the spin characteristic of the rotational degree of freedom. Meanwhile, the OAM is associated with the spatial distribution and depicts the orbital characteristic of the rotational degree of freedom, which has a helical phase front of $\exp(jn\theta)$, where θ is the azimuthal angle and n is an integer that indicates the index of the OAM mode. For different values of n , the OAM are orthogonal, which provides one more degree of freedom to encode information and has been extensively studied in the optical domain for high-speed communication. In the microwave region, the OAM can be generated by using a circular antenna array with a specific phase for each element. Its application for communications starts to be extended to microwave domain [2–5]. However, the study about the OAM based sensing and imaging is still scarce [6, 7]; this could be a new field for future research.

- Cognitive Sensing for target-matched illumination.

Investigating the possibility to optimize the sequential illumination scheme with respect to targets based on previous observations is very important for efficient sensing. By fully exploiting the spatial-, frequency- and polarization-agilities, a set of operational signals can be generated at different instants, for instance, to avoid the *null-space of the observation operator of targets*. So it can improve the efficiency of signal acquisition about the target and probably also the signal to noise ratio, which will significantly benefit target detection and recognition. Moreover, by improving the efficiency of the information acquisition about the targets, one more straightforward reward is the reduction of the redundancy of the acquired data, thus saving memory requirements for data storage and processing.

- Extension of the 3-D synthetic array technique to automotive radar applications.

Considering the forward motion of a vehicle, it is possible to synthesize a 3-D synthetic array using the forward-looking automotive radar which typically uses a small MIMO planar antenna array for transmission and reception. The 3-D sampling scheme supplements the insufficient samples in the cross-range direction acquired with the real array. Therefore, it will improve the signal-to-noise ratio after coherent processing. Moreover, the MIMO array also introduces extra diversity to the synthesized 3-D array. Consequently, it brings new challenges to the signal processing as well.

References

- [1] A. M. Yao and M. J. Padgett, “Orbital angular momentum: origins, behavior and applications,” *Adv. Opt. Photon.*, vol. 3, pp. 161–204, Jun 2011.
- [2] Y. Yan, G. Xie, M. P. J. Lavery, H. Huang, N. Ahmed, C. Bao, Y. Ren, Y. Cao, L. Li, Z. Zhao, A. F. Molisch, M. Tur, M. J. Padgett, and A. E. Willner, “High-capacity millimetre-wave communications with orbital angular momentum multiplexing,” *Nature Communications*, vol. 5, p. 4876, 2014.
- [3] X. Gao, S. Huang, Y. Wei, W. Zhai, W. Xu, S. Yin, J. Zhou, and W. Gu, “An orbital angular momentum radio communication system optimized by intensity controlled masks effectively: Theoretical design and experimental verification,” *Applied Physics Letters*, vol. 105, no. 24, p. 241109, 2014.

- [4] O. Edfors and A. J. Johansson, “Is orbital angular momentum (OAM) based radio communication an unexploited area?,” *IEEE Transactions on Antennas and Propagation*, vol. 60, no. 2, pp. 1126–1131, 2012.
- [5] T. Fabrizio, M. Elettra, S. Anna, T. Bo, B. Antonio, and R. Filippo, “Encoding many channels on the same frequency through radio vorticity: first experimental test,” *New Journal of Physics*, vol. 14, no. 3, p. 033001, 2012.
- [6] L. Li and F. Li, “Beating the rayleigh limit: Orbital-angular-momentum-based super-resolution diffraction tomography,” *Phys. Rev. E*, vol. 88, p. 033205, Sep 2013.
- [7] T. Yuan, H. Wang, Y. Qin, and Y. Cheng, “Electromagnetic vortex imaging using uniform concentric circular arrays,” *IEEE Antennas and Wireless Propagation Letters*, vol. 15, pp. 1024–1027, 2016.

List of Acronyms

2-D	Two-dimensional
3-D	Three-dimensional
AIC	Akaike Information Criterion
AR	Autoregressive
ARMA	Autoregressive Moving Average
BIC	Bayesian Information Criterion
CFS	Clustered FrameSense
CMPME	Clustered Maximum Projection onto Minimum Eigenspace
CSAR	Circular Synthetic Aperture Radar
CSBS	Clustered Sequential Backward Selection
CT	Computed Tomography
DoF	Degree of Freedom
E-CSAR	Elevation Circular Synthetic Aperture Radar
E-RadSAR	Elevation Radial-scanned Synthetic Aperture Radar
EM	electromagnetic
ERM	Exploding Reflector Model
FCC	Federal Communications Commission
FDTD	Finite-Difference Time-Domain
FFT	Fast Fourier Transform
FP	Frame Potential
GF	Green's Function
GPR	Ground Penetrating Radar
IAA	Iterative Adaptive Approach
IFFT	Inverse Fast Fourier Transform
MFT	Matrix Fourier transform
MIMO	Multiple-Input-Multiple-Output
MoM	Method of Moments
MPA	Matrix-Pencil Approach
MPME	Maximum Projection onto Minimum Eigenspace

MRI	Magnetic Resonance Imaging
MSE	Mean Square Error
MUSIC	MULTiple Signal Classification
NUFFT	Nonuniform fast Fourier transform
OAM	Orbital Angular Momentum
PEC	Perfect Electric Conductor
PSF	Point Spread Function
RadSAR	Radial-scanned Synthetic Aperture Radar
RMA	Range Migration Algorithm
SAM	Spin Angular Momentum
SAR	Synthetic Aperture Radar
SVD	Singular Value Decomposition
TBM	Tunnel Boring Machine
TCR	Trihedral Corner Reflector
UWB	Ultra-wideband
VNA	Vector Network Analyzer
WCEV	Worst Case Error Variance

Summary

The expansion of microwave imaging applications in various fields proposes increasingly higher requirements (including spatial resolution, dynamic range, and signal-to-noise ratio) for microwave imaging systems. To achieve high-quality imaging, microwave imaging systems generally exploit spatial-, frequency- and polarization-diversities to probe objects of interest for information extraction. In practice, they are implemented by using array-, wideband/Ultra-wideband (UWB)- and polarimetry-techniques. So properly exploring these techniques is of great importance to design an advanced microwave imaging system. A motivation for the research presented in the thesis is to develop a ground penetrating radar (GPR) system to predict hazards ahead of tunnel boring machines (TBM) during tunnel excavation. In this circumstance, GPR antennas are mounted on the cutter-head of a TBM. With the rotation of the TBM cutter-head, GPR antennas collect electromagnetic (EM) signals over a synthetic circular aperture, which leads to the Radial-scanned Synthetic Aperture Radar (RadSAR). The rotation of the antenna array benefits the formation of the RadSAR but makes it distinct from traditional SAR modalities as well.

The first part of the thesis focuses on the investigation of the RadSAR for high-quality 3-D imaging by exploring the polarization and spatial diversities. Due to the rotation of the antenna array, EM signals acquired with the RadSAR have various (i.e., misaligned) polarizations over the aperture, which degrades imaging performance of traditional scalar-wave based imaging algorithms. In the thesis, we propose two solutions, i.e., through either antenna array design or image formation, to overcome the effects of polarization misalignment of EM waves on the qualities of formed images. In the first solution, novel antenna array topologies are devised for signal acquisition with the RadSAR. The designed rotated antenna arrays not only enable to overcome the polarization misalignment of EM signals within the aperture but also provide fully polarimetric imaging capability. However, these arrays have higher system complexity (i.e., need maximally two times the number of antennas). As an alternative solution, a linear inversion approach is suggested for image formation by taking advantage of accurate Green's functions of the rotated antennas, which partly compensates the effects of polarization misalignment of EM waves

acquired by the RadSAR. This approach reconstructs the shape of an object with sufficient accuracy for both free-space and subsurface imaging applications, but the computational load significantly increases compared to the first solution. Therefore, some trade-offs between the two solutions should be considered in practical applications.

Moreover, the RadSAR is extended to the Elevation-RadSAR (E-RadSAR) with attempts to further reduce the array system complexity (i.e., fewer antennas) for 3-D imaging. The E-RadSAR exploits a synthetic aperture technique in both cross- and down-range directions; thus it takes a 3-D spatial sampling for signal acquisition. To investigate the 3-D imaging capability of the E-RadSAR, its 3-D spatial sampling is a key problem, which is tackled by converting to a sensor selection problem in the shape of an abstract linear system formulation. This formulation provides a general multi-dimensional sampling framework for microwave imaging systems to exploit spatial-, frequency- and polarization-diversities, that are only partly covered by the traditional monochromatic and UWB array theories. The developed selection tools address the sampling design of a microwave imaging system by optimizing its sensing matrix/operator and also adapt physical constraints for specific tasks. Moreover, these selection tools can also be used for frequency-modulated array design, MIMO array optimization, sensor selection, etc.

The second part of this thesis explores multiband signal fusion for improved microwave imaging. Based on the signal spectrum distribution of focused images, a wavenumber-domain multiband data fusion approach is proposed. Compared to signal-level fusion approaches, the wavenumber-domain fusion strategy facilitates to coherently fuse multiband signals collected by either collocated or non-collocated arrays at different frequency bands. The proposed fusion approach is attractive for high-resolution imaging with multiple narrowband data when UWB data are unavailable due to system constraints, strong interference at a certain frequency within a wide bandwidth, or due to other causes.

Although the research presented in the thesis is triggered by studying the RadSAR related imaging systems, some of the research results can generally benefit the development of more advanced microwave imaging systems by exploiting various signal/system diversities for a wide range of applications.

Samenvatting

De uitbreiding van microgolf beeldreconstructie toepassingen in verschillende omgevingen stelt steeds hogere eisen (met inbegrip van ruimtelijke resolutie, dynamisch bereik, en signaal ruis verhouding) aan microgolf beeldreconstructie systemen. Om hoge kwaliteit beeldreconstructie te bereiken, maken microgolf beeldreconstructie systemen in zijn algemeenheid gebruik van ruimtelijke-, frequentie- en polarisatie- verschillen om informatie van objecten te verkrijgen. In de praktijk, worden deze geïmplementeerd door gebruik te maken van array, wideband/Ultra-wideband (UWB)- en polarimetrische technieken. Dus het op de juiste manier toepassen van deze technieken is van groot belang om een geavanceerd microgolf beeldreconstructie systeem te ontwerpen. Een motivatie voor het onderzoek dat in dit proefschrift wordt gepresenteerd, is om een Ground Penetrating Radar (GPR) systeem te ontwikkelen om gevaren te voorspellen die opdoemen bij Tunnel Boring Machines (TBM) gedurende de uitgraving van een tunnel. In deze omstandigheid worden de GPR-antennes op de snijkop van de TBM gemonteerd. Met de rotatie van de TBM-snijkop verzamelen de GPR-antennes elektromagnetische (EM) signalen met een synthetische circulaire aperture, welke leidt tot de Radiaal opgenomen Synthetic Aperture Radar (RadSAR). De rotatie van het antenne-array komt de formatie van de RadSAR ten goede, maar onderscheidt zich daarmee ook van traditionele SAR modaliteiten.

Het eerste deel van het proefschrift richt zich op het onderzoek van de RadSAR voor hoge kwaliteit 3-D beeldreconstructie door gebruik te maken van polarisatie en ruimtelijke verschillen. Door de rotatie van het antenne array hebben de verkregen EM-signalen met de RadSAR verschillende (bijv. niet uitgelijnde) polarisaties over de aperture, die de werkzaamheid van traditionele op scalaire golven gebaseerde beeldreconstructie algoritmen verminderen. In het proefschrift stellen we twee oplossingen voor, deze zijn, door mogelijk antenne array ontwerp of beeldformatie, het verhelpen van de effecten van niet uitgelijnde polarisatie van EM golven op de kwaliteiten van de geformeerde beelden. In de eerste oplossing worden nieuwe antenne array topologieën toegepast om signalen te verkrijgen voor de RadSAR. De ontworpen roterende antenne arrays maken het mogelijk niet alleen de niet uitgelijnde polarisatie van EM signalen in de aperture te verhelpen, maar ma-

ken ook een volledige polarimetrische beeldreconstructie mogelijk. Deze arrays hebben evenwel een hogere systeem complexiteit (bijv. hebben twee maal zoveel antennes nodig). Als alternatieve oplossing wordt een lineaire inversie benadering voorgesteld voor beeldreconstructie, door gebruik te maken van nauwkeurige functies van Green behorende bij de roterende antennes, die gedeeltelijk het effect van de niet uitgelijnde polarisatie van de verkregen EM golven door de RadSAR compenseert. Deze benadering reconstrueert de vorm van de objecten met voldoende nauwkeurigheid voor zowel de vrije ruimte en ondergrond beeldreconstructie toepassingen, maar de rekenkundige belasting neemt significant toe vergeleken met de eerste oplossing. Daarom zouden bij praktische toepassingen enkele afwegingen tussen de twee oplossingen moeten worden genomen.

Behalve dat is de RadSAR uitgebreid tot de Elevation-RadSAR (E-RadSAR) met pogingen om de complexiteit van het array systeem (bijv. minder antennes) te reduceren voor 3-D beeldreconstructie. De E-RadSAR maakt gebruik van een synthetische aperture techniek in zowel "cross" als "down-range" richtingen; Het meet dus een 3-D ruimtelijke bemonstering voor de signaal acquisitie. Om de 3-D beeldreconstructie mogelijkheden van de E-RadSAR te onderzoeken, is de 3-D ruimtelijke bemonstering het sleutelprobleem welke wordt aangepakt door omzetting naar een sensor selectie probleem in de vorm van een abstracte lineaire systeem formulering. Deze formulering levert een algemeen multi-dimensionaal bemonsterings raamwerk voor microgolf beeldreconstructie systemen om gebruik te maken van ruimtelijke-, frequentie- en polarisatie-verschillen, die alleen gedeeltelijk afgedekt worden door de traditionele monochromatische en UWB array theorieën. De ontwikkelde selectie gereedschappen hebben betrekking op het bemonsteringsontwerp van een microgolf beeldreconstructie systeem door zijn "sensing matrix/operator" te optimaliseren en ook de fysische randvoorwaarden voor specifieke taken aan te passen. Bovendien kunnen deze selectie gereedschappen ook gebruikt worden voor frequentie-gemoduleerd array ontwerp., MIMO array optimalisatie, sensor selectie, etc.

Het tweede gedeelte van dit proefschrift verkent de fusie van multi-band signalen voor verbeterde microgolf beeldreconstructie. Gebaseerd op de distributie van het signaalspectrum van gefocuseerde beelden, wordt een benadering van een fusie van multiband data voorgesteld. Vergelijken met signaal-niveau fusie benaderingen, maakt de golfgetal-domein fusie strategie het mogelijk om coherent multiband signalen te fuseren, die door gecollokeerde of niet-gecollokeerde arrays in verschillende frequentiebanden zijn verkregen. De voorgestelde fusie-benadering is aantrekkelijk voor hoge-resolutie beeldreconstructie bij veel smalbandige data, als

UWB data niet beschikbaar is vanwege systeembeperkingen, sterke interferentie bij een zekere frequentie binnen een brede bandbreedte, of vanwege andere redenen.

Hoewel het onderzoek dat in dit proefschrift wordt gepresenteerd is voortgekomen door de bestudering van RadSAR gerelateerde beeldreconstructie systemen, kunnen enkele van de onderzoeksresultaten in zijn algemeenheid profiteren van de ontwikkeling van meer geavanceerde microgolf beeldreconstructie systemen door gebruik te maken van verscheidene signaal/systeem verschillen voor een uitgebreid aantal toepassingen.

Acknowledgements

I would like to sincerely express my gratitude to all the people who have helped and supported me during the process of my PhD study.

First of all, I would like to express my thanks to my promotor Prof. Alexander Yarovoy. It was him who offered me the opportunity to start my PhD research in TU Delft and made my professional career transition from Australia to the Netherlands smooth. His constructive guidance and insightful comments on my research has helped me gain a lot in the development of my research skills and vision. He always gave me plenty of freedom to my research, which together with his patience and trust on my capabilities has helped me gradually become an independent researcher.

I am glad and lucky to have many good colleagues. Thank Dinh Tran for working together in the NeTTUN project and sharing his knowledge about antennas which really refreshed me. I am also very grateful for Pascal Aubry's technical assistance. I really appreciate his patience to my repeated measurement requests, which happened several times, just for getting satisfactory experimental results. Without his technical assistance, the demonstration for my research results cannot be complete. I would like to thank Harun Cetinkaya for our collaboration in the first two years of my PhD research. I enjoy the time sharing the office with him and our former colleague Dr. Dmitriy Penkin. I also want to thank Dr. Bert-Jan Kooij. A causal talk with him during a lunch time enlightened me on the mathematical analysis used for the electromagnetic theory. I wish to acknowledge the help of Bert-Jan and Dr. Hans Driessen for the Dutch translations of my summary and propositions.

I also give thanks to my PhD committee members: Prof. W. Mulder, Prof. E.Slob, Prof. G. Leus, Prof. P. Hoogeboom, Prof. M. Sato, and Prof. C. Craeye, for their comments for improving my dissertation.

I appreciate Zhiqing Wang who helped me design the nice cover of my book.

I would like to thank Minke van der Put and Minaksie Ramsoekh for their administrative assistance. Special thanks to Minke van der Put for helping me address the housing issues that I met, which really makes my life in the Netherlands comfortable and happy.

I want to thank all the former and present colleagues in MS3 group. I really appreciate working in such an international group. The time we spend for coffee &

lunch broadens my knowledge about different cultures (including Bulgarian, Czech, Dutch, French, German, Greek, Indian, Italian, Japanese, Russian, Saudi, Serbian, Spanish, Turkish, Ukrainian, such a surprisingly long list!) and also makes myself more international. Your companion makes the life beyond research happy and enjoyable.

Finally, my earnest gratitude is given to my parents. Their unconditional love and understanding make it possible for me to concentrate on my work in the past years. Although I am far away from home, their encouragement and support are my constant source of power to go ahead!

Jianping Wang

Delft, February, 2018

List of Publications

Journals

- [1] **J. Wang**, P. Aubry, and A. Yarovoy, "A Novel Rotated Antenna Array Topology for Near-Field 3-D Fully Polarimetric Imaging," *IEEE Transactions on Antennas and Propagation*, vol. 66, pp. 1584-1589, 2018.
- [2] **J. Wang**, P. Aubry, and A. Yarovoy, "A Novel Approach to Full-Polarimetric Short-Range Imaging With Copolarized Data," *IEEE Transactions on Antennas and Propagation*, vol. 64, pp. 4733-4744, 2016.
- [3] **J. Wang**, P. Aubry, and A. Yarovoy, "Efficient Implementation of GPR Data Inversion in Case of Spatially Varying Antenna Polarizations," *IEEE Transactions on Geoscience and Remote Sensing*, to be published, DOI: 10.1109/TGRS.2017.2779788.
- [4] **J. Wang**, P. Aubry, and A. Yarovoy, "Wavenumber Domain Multiband Signal Fusion With Matrix-Pencil Approach for High Resolution Imaging," *IEEE Transactions on Geoscience and Remote Sensing*, 2018, accepted.
- [5] **J. Wang**, and A. Yarovoy, "Sampling Design of 3-D Synthetic Array for Microwave Imaging," *IEEE Transactions on Computational Imaging*, under review.

Conferences

- [6] **J. Wang**, P. Aubry, and A. Yarovoy, "Improved microwave imaging by wavenumber domain multiband data fusion," in *International Conference on Radar 2018, Brisbane, Australia*. submitted.
- [7] **J. Wang**, P. Aubry, and A. Yarovoy, "GPR Measurements Inversion in Case of Spatially Varying Antenna Polarization," *2017 XXXIIInd General Assembly and Scientific Symposium of the International Union of Radio Science (URSI GASS), Montreal, QC*, 2017, pp. 1-4. Note: Invited paper.
- [8] **J. Wang**, and A. Yarovoy, "Near-Optimal Selection of GPR Observations for Linear Inversion," in *Advanced Ground Penetrating Radar (IWAGPR), 2017 9th International Workshop on*, 2017. (**Finalist for the best student paper award**)

- [9] **J. Wang** and A. Yarovoy, "Rotating array design for full polarimetric imaging," in *2016 10th European Conference on Antennas and Propagation (EuCAP)*, 2016, pp. 1-4.
- [10] X. Wang, S. S. Sun, **J. Wang**, A. Yarovoy, B. Neducza, and G. Manacorda, "Real GPR signal processing for target recognition with circular array antennas," in *2016 URSI International Symposium on Electromagnetic Theory (EMTS)*, 2016, pp. 818-821.
- [11] **J. Wang**, H. Cetinkaya, and A. G. Yarovoy, "Comparison of CSAR, E-CSAR and planar circular array for 3-D imaging," in *IET International Radar Conference 2015*, 2015, pp. 1-5.
- [12] **J. Wang**, H. Cetinkaya, A. Yarovoy, I. I. Vermesan, and S. Reynaud, "Investigation of forward-looking synthetic circular array for subsurface imaging in tunnel boring machine application," in *Advanced Ground Penetrating Radar (IWAGPR), 2015 8th International Workshop on*, 2015, pp. 1-4.
- [13] H. Cetinkaya, **J. Wang**, and A. G. Yarovoy, "Investigation of near field beam patterns for rotating arrays," in *Advanced Ground Penetrating Radar (IWAGPR), 2015 8th International Workshop on*, 2015, pp. 1-4.
- [14] A. Yarovoy, H. Cetinkaya, and **J. Wang**, "Sparse MIMO array for short-range imaging," in *Antennas and Propagation (EuCAP), 2015 9th European Conference on*, 2015, pp. 1-4.
- [15] **J. Wang**, H. Cetinkaya, and A. Yarovoy, "On polar sampling of GPR for tunneling boring machine," in *Ground Penetrating Radar (GPR), 2014 15th International Conference on*, 2014, pp. 330-333.
- [16] **J. Wang**, H. Cetinkaya, and A. Yarovoy, "NUFFT based Frequency-Wavenumber Domain Focusing under MIMO Array Configurations," in *International Radar Conference 2014 Lille, France*, 2014.
- [17] D. Tran, V. Paraforou, H. Cetinkaya, **J. Wang**, and A. Yarovoy, "Full-wave characterization of EM transmission and propagation in TBM environment, a temporal and spectral GPR study," in *Ground Penetrating Radar (GPR), 2014 15th International Conference on*, 2014, pp. 391-396.
- [18] H. Cetinkaya, **J. Wang**, D. Tran, and A. G. Yarovoy, "The comparison of the near field beam patterns of 1D-CR MIMO and 2D-CR MIMO arrays," in *Ground Penetrating Radar (GPR), 2014 15th International Conference on*, 2014, pp. 762-766.

About the Author

Jianping Wang was born in Shanxi, China, in 1987. He received the BSc. in Electrical Engineering from North China University of Technology, Beijing, and MSc. in Information and Communication Engineering from Beijing Institute of Technology, in July 2009 and March 2012, respectively. From August, 2012 to May, 2013, he worked on synthetic aperture radar with formation flying satellites as a research assistant in the University of New South Wales, Australia. In July 2013, he joined the Microwave Sensing, Signals & Systems (MS3) group in the Delft University of Technology and started to work on his PhD degree in the field of Ultra-wideband microwave imaging. During his PhD research, he involved in a European project to develop an advanced ground prediction radar system and imaging algorithms used for tunnel boring machine. Now he is working in the same group as a postdoc researcher. His current research interests include computational imaging, signal processing and array design.